



**Some pages of this thesis may have been removed for copyright restrictions.**

If you have discovered material in Aston Research Explorer which is unlawful e.g. breaches copyright, (either yours or that of a third party) or any other law, including but not limited to those relating to patent, trademark, confidentiality, data protection, obscenity, defamation, libel, then please read our [Takedown policy](#) and contact the service immediately (openaccess@aston.ac.uk)

Using Structural Correlations to Inform the Development of Longer Lasting Dental Restorations

SLOBODAN SIROVICA

Doctor of Philosophy

ASTON UNIVERSITY

September 2017

©Slobodan Sirovica, 2017

Slobodan Sirovica asserts his moral right to be identified as the author of this thesis

This copy of the thesis has been supplied on condition that anyone who consults it is understood to recognise that its copyright rests with its author and that no quotation from the thesis and no information derived from it may be published without appropriate permission or acknowledgement.

## **Aston University**

Using Structural Correlations to Inform the Development of Longer Lasting Dental Restorations

Slobodan Sirovica

Doctor of Philosophy

September 2017

### **Thesis Summary**

Photo-initiated dimethacrylate polymers are of great biomedical importance, in orthopaedics and particularly in dentistry where they are used as a matrix to form resin-based-composite (RBC) filling materials. However, the physiochemical properties of these materials are highly sensitive to photo-polymerisation variables, particularly the polymerisation rate, and as a consequence clinical performance is not ideal. Despite extensive mechanical and Infra-red spectroscopic characterisation of the cross-linked polymer resin matrix, the impact of polymerisation rate on the resultant structure is unknown.

Using novel synchrotron FTIR, X-ray and neutron scattering techniques, this study aimed to investigate the effect that polymerisation rate has on the polymer structure, at atomic to micron length scales, of experimental RBCs based on common dimethacrylate resins. Kinetic X-ray scattering measurements demonstrated that polymerisation generates chain segment extension and changes in short range order within the structures of the constituent resin monomers. Accelerating polymerisation confers greater chain extension and reduced short range order, which at extremely fast polymerisation rates may store residual strains within the system. Neutron scattering confirmed that this relationship between polymerisation rate and structure occurs at longer length scales within the polymer, specifically at cross-linking distances.

Synchrotron FTIR micro-spectroscopy showed that the introduction of filler particles into a resin matrix produced local heterogeneity with respect to the degree of monomer-polymer conversion and chemical aromatic bond strain. At nearest neighbour distances, heterogeneity is believed to originate from a lower converted and reduced bond strain boundary layer surrounding each filler particle, whilst light attenuation and likely, relative monomer mobility effects dominate at longer length scales within the resin matrix

This study demonstrates that advanced synchrotron and neutron based characterisation techniques, seldom used in the field of dental materials research, can provide new insight into how the polymerisation rate may impact on the structure of the polymer matrix components of dental RBCs.

## Acknowledgements

I would like to express my deepest gratitude towards my supervisors Dr. Richard Martin, Professor Owen Addison and Dr. Max Skoda for their support during this PhD. I would like to thank them for their constant encouragement, patience, friendship and guidance. I am extremely grateful for their advice and constructive criticism, helping me to develop as a scientist. Their advice on my research and my career has been invaluable and I could not have completed this thesis without them.

I am thankful to Majciek Podgorski for his contributions towards chemical synthesis and I am grateful to the Reece Lillie from the Aston materials workshop for kindly modifying sample holders necessary for several experiments in this thesis. I would also like to thank Dr. Jianguo Lui and Dr. Michael Hoffman at the University of Birmingham Dental School for their help with FTIR and density measurements and Dr. Maisoon Al-Jawad for her guidance with X-ray data. I am also appreciative of the beam line scientists at XMaS, I22, I16, D16, SANS2D, and IRENI for their help during experiments.

I would also like to thank the Science and Technologies Facility Council for providing the funding for this PhD.

During the course of my PhD I have shared in the excellent company of Farah Raja, Karan Rana, Alex Morrell, Chathyan Pararasa, Erin Tse, Ellie Callaghan, Fiona Leahy, Louis Forto-Chungong and Ian Garner. I would like to thank Farah (the 'real' boss), Karan (one half of the world's greatest badminton doubles team) and Alex (my partner in crime) for all of the laboratory and office high jinks. I would also like to thank Ellie, Fiona, Louis and Ian for the copious supply of delicious cakes and doughnuts over the past four years.

Finally, a special thanks to my mum, dad, sister, aunt and grandma who have always encouraged me during this PhD and also throughout my education. They have provided me with love and support that has always kept me going.

“Just one more thing....”

*Columbo*

## List of Abbreviations

|                               |   |
|-------------------------------|---|
| Bis-EMA                       | Ethoxylated bisphenol-A dimethacrylate                          |
| Bis-GMA                       | Bisphenol A glycidyl dimethacrylate                             |
| CQ                            | Camphorquinone  |
| DC                            | Degree of monomer to polymer conversion                         |
| DC <sub>max</sub>             | Maximum/terminal degree of monomer to polymer conversion        |
| DMAEMA                        | Di-methyl-aminoethyl methacrylate                               |
| D-TEGDMA                      | Partially deuterated triethylene glycol dimethacrylate          |
| FTIR                          | Fourier Transform Infrared Spectroscopy                         |
| FT-MIR                        | Fourier Transform Mid Infrared Spectroscopy                     |
| FT-NIR                        | Fourier Transform Near Infrared Spectroscopy                    |
| HF                            | High filler particle fraction                                   |
| RBCs                          | Resin Based Composite   |
| R <sub>p</sub>                | Rate of polymerisation  |
| R <sub>p</sub> <sup>max</sup> | Maximum rate of polymerisation                                  |
| SANS                          | Small angle neutron scattering                                  |
| SAXS                          | Small angle X-ray scattering                                    |
| TEGDMA                        | Triethylene glycol dimethacrylate                               |
| TPO                           | Lucirin TPO or ethyl-2, 4, 6 trimethylbenzoylphenyl phosphinate |
| UDMA                          | Urethane dimethacrylate   |
| XRD                           | X-ray diffraction   |

## Contents

|   |    |
|---|----|
| 1 INTRODUCTION AND LITERATURE REVIEW                                | 1  |
| Literature Review   | 4  |
| 1.1.2 What are Resin Based Composites (RBCs)?                       | 4  |
| 1.1.3 Biomedical Applications of RBCs                               | 6  |
| 1.2 RBC Composition: Historical Development and Current Trends      | 8  |
| 1.2.1 Resin Matrix  | 8  |
| 1.2.2 Filler Particles  | 13 |
| 1.2.3 Photo-initiator Chemistry                                     | 15 |
| 1.2.4 Silane Coupling Agents  | 20 |
| 1.3 Photo-polymerisation Kinetics                                   | 22 |
| 1.4 Origins of Polymerisation Shrinkage                             | 25 |
| 1.5 Determinants of Polymer Formation                               | 27 |
| 1.5.1 Effects of Monomer Structure on Polymer Formation             | 27 |
| 1.5.2 Effects of Light Curing Protocols on Polymer Formation        | 29 |
| 1.5.3 Exposure Reciprocity  | 32 |
| 1.6 Characterisation Techniques                                     | 36 |
| 1.6.1 Fourier Transform Infrared Spectroscopy                       | 36 |
| 1.6.2 Alternative Characterisation techniques                       | 39 |
| 1.6.3 Motivation for Synchrotron X-ray and Neutron Based Techniques | 41 |
| 1.7 X-ray and Neutron Scattering Techniques                         | 42 |
| 1.7.1 Scattering Theory   | 42 |
| 1.7.1.1 Scattering Cross-section                                    | 42 |
| 1.7.1.2 Ideal Elastic Scattering                                    | 43 |
| 1.7.1.3 Scattering from a Group of Atoms                            | 45 |
| 1.7.1.4 Motivation for Using Neutron Scattering                     | 48 |
| 1.8 Neutron Scattering  | 50 |
| 1.9 Summary of Key Aims   | 52 |
| 1.10 References   | 54 |
| <br>  |    |
| 2 MATERIALS AND METHODS   | 77 |
| 2.1 Introduction and Overview                                       | 77 |
| 2.2 Sample Preparation  | 77 |
| 2.2.1 Monomers, Photo-initiators and Filler Particles               | 77 |
| 2.2.2 Synthesis of Partially Deuterated TEGDMA-d <sub>10</sub>      | 79 |

|   |     |
|---|-----|
| 2.2.3 Preparation of Dimethacrylate Resin Blends  | 82  |
| 2.2.4 Preparation of Filled Dimethacrylate Resin Blends   | 83  |
| 2.3 Light Curing Units  | 84  |
| 2.3.1 Lumencor AURA Light Engine – External Polymerisation  | 84  |
| 2.3.2 EMS Swiss Master Light Curing Unit  | 87  |
| 2.4 Production of Resin Test Specimens  | 87  |
| 2.4.1 <i>In-situ</i> Photo – Polymerisation   | 87  |
| 2.4.2 Unfilled Resin Discs – Laboratory   | 89  |
| 2.4.3 Filled Resin Discs – Laboratory   | 90  |
| 2.5 Characterisation  | 91  |
| 2.5.1 Mid FT- IR – Laboratory   | 91  |
| 2.5.2 Near FTIR   | 92  |
| 2.5.3 Density Measurements  | 93  |
| 2.6 Production of X-rays from a Synchrotron Source  | 95  |
| 2.6.1 Production of X-rays at the European Synchrotron Radiation Facility (ESRF)                  | 95  |
| 2.6.2 Production of X-rays at the Diamond Light Source  | 97  |
| 2.7 Production of Neutrons  | 103 |
| 2.7.1 Production of Neutrons at the Institute Laue Langevin (ILL)                                 | 103 |
| 2.7.2 Production of Neutrons at the ISIS Pulsed Neutron Source                                    | 105 |
| 2.8 Data Reduction  | 112 |
| 2.8.1 X-ray Scattering Data Reduction   | 112 |
| 2.9 References  | 118 |
| <br>  |     |
| 3 NOVEL INSIGHTS INTO STRUCTURAL VARIABILITY OF IN-SITU PHOTO-POLYMERISED DIMETHACRYLATE POLYMERS | 122 |
| 3.1 Introduction  | 122 |
| 3.2 Methods   | 126 |
| 3.2.1 Preparation of Photo-Polymerisable Dimethacrylate Resin Blends                              | 126 |
| 3.2.2 Synchrotron X-ray Scattering Measurements   | 127 |
| 3.2.3 <i>Ex-situ</i> Fourier Transform Near Infrared Spectroscopy                                 | 129 |
| 3.2.4 Simultaneous X-ray Scattering and FT-NIR Measurements and Increased Time Resolution         | 129 |
| 3.3 Results   | 132 |
| 3.3.1 De-convolving the Contributions of Monomeric Components to the Scattering Signal            | 132 |
| 3.3.2 Impact of Irradiance on Resultant Polymer Structure of CQ Initiated Resins                  | 136 |

|  |     |
|--|-----|
| 3.3.3 Polymerisation Kinetics of CQ Initiated Resins Blends                                    | 140 |
| 3.3.4 Impact of Irradiance on Resultant Polymer Structure of TPO Initiated Resins              | 142 |
| 3.3.5 Polymerisation Kinetics of TPO Initiated Resin Blends                                    | 146 |
| 3.3.6 The Effect of Polymerisation Rate on the Resultant Polymer Structure                     | 149 |
| 3.3.7 Normalisation of Scattering Data to the Degree of Monomer-Polymer Conversion             | 149 |
| 3.4 Discussion   | 153 |
| 3.4.1 De-convolving the Contributions of Monomeric Components to the Scattering Signal         | 153 |
| 3.4.2 Impact of Irradiance on the Resultant Polymer Structure                                  | 155 |
| 3.4.3 The Effect of Polymerisation Rate on the Resultant Polymer Structure                     | 158 |
| 3.5 Conclusions  | 160 |
| 3.6 References   | 161 |
| <br>   |     |
| 4 RELATIVE ORDERS IN RBC POLYMER NETWORK STRUCTURE DEFINED BY NEUTRON SCATTERING               | 166 |
| 4.1 Introduction   | 166 |
| 4.2 Methods  | 169 |
| 4.2.1 Preparation of Photo-Polymerisable Dimethacrylate Resin Blends                           | 170 |
| 4.2.2 Neutron Scattering   | 171 |
| 4.2.3 Density Measurements   | 177 |
| 4.2.4 Data Analysis  | 177 |
| 4.3 Results  | 178 |
| 4.3.1 Scattering Features Pre and Post Photo-Polymerisation                                    | 178 |
| 4.3.2 Contributions to the Neutron Scattering Spectra  | 180 |
| 4.3.3 The Effect of Relative Differences in Polymerisation Rate on the Final Polymer Structure | 183 |
| 4.3.4 Time Resolved X-ray Scattering Measurements  | 191 |
| 4.4 Discussion   | 194 |
| 4.4.1 Scattering Peak Origins  | 194 |
| 4.4.1.1 Scattering Feature (a)   | 194 |
| 4.4.1.2 Scattering Feature (b)   | 194 |
| 4.4.1.3 Scattering Feature (c)   | 196 |
| 4.4.1.4 Scattering Feature (d)   | 196 |
| 4.4.2 Impact of Irradiance on the Resultant Polymer Structure                                  | 197 |
| 4.5 Conclusions  | 200 |

|  |     |
|--|-----|
| 4.6 References   | 201 |
| <br>   |     |
| 5 MODIFICATION OF POLYMER STRUCTURE THROUGH THERMAL LOADING:<br>A PRELIMINARY STUDY                                  | 207 |
| 5.1 Introduction   | 207 |
| 5.2 Methods  | 208 |
| 5.2.1 Preparation of Photo-Polymerisable Dimethacrylate Resin Blends   | 208 |
| 5.2.2 Synchrotron X-ray Scattering Measurements  | 209 |
| 5.3 Results  | 212 |
| 5.3.1 The Effect of Temperature on Correlation Length  | 212 |
| 5.3.2 The Effect of Temperature on Short Range Order   | 215 |
| 5.4 Discussion   | 217 |
| 5.5 Conclusions  | 220 |
| 5.6 References   | 221 |
| <br>   |     |
| 6 INTER-PARTICULATE SPATIAL VARIABILITY IN DEGREE OF<br>POLYMERISATION OF DIMETHACRYATE DENTAL RBC FILLING MATERIALS | 222 |
| 6.1 Introduction   | 222 |
| 6.2 Methods  | 224 |
| 6.2.1 Preparation of Experimental Resin Based Composites (RBCs)  | 224 |
| 6.2.2 Synchrotron Fourier Transform Mid-Infra-Red Spectroscopy Mapping   | 225 |
| 6.2.3 Data Analysis  | 228 |
| 6.2.3.1 Degree of Conversion   | 228 |
| 6.2.3.2 Measurements of Residual Stress  | 229 |
| 6.3 Results  | 230 |
| 6.3.1 Micro-scale Spatial Variation in Polymerisation  | 232 |
| 6.3.2 Residual Strain  | 234 |
| 6.4 Discussion   | 241 |
| 6.4.1 Understanding Conversion and Strain Profiles Around Filler   | 241 |
| 6.4.2 Understanding Conversion and Strain Profiles Between Particles   | 244 |
| 6.4.3 The Effect of Relative Rate on DC and Aromatic strain  | 245 |
| 6.5 Conclusions  | 247 |
| 6.6 References   | 248 |

|   |     |
|---|-----|
| 7 INTRA-CORONAL STRESS TRANSFER THROUGH ENAMEL FOLLOWING RBC PHOTO-POLYMERISATION   | 252 |
| 7.1 Introduction  | 252 |
| 7.2 Materials and Methods   | 255 |
| 7.2.1 Sample Preparation  | 255 |
| 7.2.2 Synchrotron X-ray Diffraction Mapping   | 255 |
| 7.2.3 Data Processing and Analysis  | 259 |
| 7.3 Results   | 261 |
| 7.3.1 XRD and Orientation   | 261 |
| 7.3.2 Crystallographic Strain   | 265 |
| 7.3.3 Impact of Crystallite Orientation on Resultant Strain                         | 271 |
| 7.4 Discussion  | 276 |
| 7.4.1 Crystallographic Strain and Relief Mechanisms                                 | 276 |
| 7.4.2 The Effect of Relative Polymerisation Rate on Crystallographic Strain         | 277 |
| 7.4.3 Spatial Distribution of Strain and Orientation                                | 278 |
| 7.5 Conclusions   | 282 |
| 7.6 References  | 283 |
| <br>  |     |
| 8 GENERAL DISCUSSION AND FUTURE WORK  | 290 |
| 8.1 General discussion  | 290 |
| 8.1.1 Introduction  | 290 |
| 8.1.2 Effect of Polymerisation Rate on the Polymer Structure                        | 290 |
| 8.1.3 Inter-Particulate Variability in the Degree of Polymerisation                 | 292 |
| 8.1.4 Crystallographic Strain   | 293 |
| 8.2 Future work   | 294 |
| 8.2.1 Effect of Polymerisation Rate on the Polymer Structure                        | 294 |
| 8.2.2 Inter-Particulate Variability in the Degree of Polymerisation                 | 294 |
| 8.2.3 Crystallographic Strain   | 295 |
| <br>  |     |
| 9 CONCLUSIONS   | 296 |
| <br>  |     |
| 10 APPENDIX   | 298 |
| 10.1 Chemical Lot Numbers   | 298 |
| 10.2 Effects of X-ray Beam Damage on the Polymer Structure of Dimethacrylate Resins | 299 |
| 10.3 Publications   | 301 |

|                    |     |
|--------------------|-----|
| 10.4 Conferences   | 301 |
| 10.5 Invited Talks | 302 |
| 10.6 Awards        | 302 |

## List of Tables

| <b>Table no.</b> | <b>Table Description</b>   | <b>Page no.</b> |
|------------------|--|-----------------|
| 1.1              | Summary of common monomers, and some physical properties, used in the formulation of RBCs  | 13              |
| 1.2              | The absorption characteristics of photo-initiators used in in commercial and experimental RBCs.  | 19              |
| 2.1              | Chemicals and suppliers used for the production of experimental, dimethacrylate based, resin blends.   | 78              |
| 2.2              | Weight percentage (wt%) mixing ratios of Bis-GMA and TEGDMA monomers used to formulate each resin blend. Each mixing ratio was combined with a photo-initiator as either 0.2 wt% Camphorquinone (CQ) with 0.8 wt% of its tertiary amine N,N-dimethylaminoethyl-methacrylate (DMAEMA) or 1 wt% Lucirin-TPO photo-initiator. Silica filler particles were added in high (HF) (40/60) and low (50/50) loadings. | 83              |
| 2.3              | A summary of the operating characteristics for the European synchrotron radiation facility compared to those of the smaller Diamond light source synchrotron.  | 97              |
| 2.4              | X-ray and neutron scattering length densities for TEGDMA, Bis-GMA, Deuterium and deuterated TEGDMA (D-TEGDM).  | 114             |
| 2.5              | A summary of monomer formulation ratios, initiation chemistry and photo-polymerisation regime for each pre-cured resin disc sample used for SANS measurements.   | 115             |
| 6.1              | Weight percentage (wt%) mixing ratios of Bis-GMA and TEGDMA monomers used to formulate each resin blend. Each mixing ratio was combined with a photo-initiator as either 0.2 wt% Camphorquinone (CQ) with 0.8 wt% of its tertiary amine N,N-dimethylaminoethyl-methacrylate (DMAEMA) or 1 wt% Lucirin-TPO photo-initiator. Silica filler particles were added in high (HF) (40/60) and low (50/50) loadings. | 224             |
| 7.1              | Strains in the c and a axis for high and low irradiance curing protocols. Here the standard deviation is quoted with the value of strain.  | 269             |
| 10.1             | Lot numbers for monomers and photo-initiators used for resin formulation.  | 298             |

## List of Figures

| Figure no. | Figure Description   | Page no. |
|------------|--|----------|
| 1.1        | Hierarchy of composite classes divided according to matrix material, reinforcement and reinforcement morphology.   | 5        |
| 1.2        | Schematic representation of a resin based composite (RBC). The resin matrix is shown as a light purple background, filler particles are displayed as polygons and radical species are denoted by black dots.   | 6        |
| 1.3        | The chemical structure of monomers commonly used in the formulation of commercial and experimental RBCs.   | 12       |
| 1.4        | The production of free radicals from the excitation of the Camphorquinone photo-initiator species used with an amine reducing agent.   | 17       |
| 1.5        | Chemical structures of Acyl phosphines oxide photo-initiator species <b>(a)</b> Lucirin TPO and <b>(b)</b> Igracure 819.   | 19       |
| 1.6        | Generic structures of functional organosilanes.  | 21       |
| 1.7        | Chemical structure of (3-Mercaptopropyl)trimethoxysilane (MPTMS).  | 21       |
| 1.8        | A simplified schematic showing the formation of cross-links between neighbouring polymer chains to form a three dimensional structure.   | 23       |
| 1.9        | The thermal motions of <b>(a)</b> individual monomers as represented by a Leonard-Jones sphere and <b>(b)</b> a forming polymer chain. Polymerisation reduces the available free volume  | 25       |
| 1.10       | The scattering of an incident X-ray from a given sample into the solid angle, $d\Omega$ in the direction of $\theta$ per unit time.  | 43       |
| 1.11       | Schematic of scattering from a two atom system.  | 45       |
| 1.12       | <b>(a)</b> X-ray scattering cross-sections are proportional to the atomic number whilst <b>(b)</b> neutron scattering cross-sections are erratic.  | 49       |
| 2.1        | <b>(a)</b> Deuterated methacrylic acid combined with phosphorus trichloride in preparation for combining with triethylene glycol. <b>(b)</b> Combining deuterated methacryloyl chloride with hydrogenated triethylene glycol to yield a partially deuterated TEGDMA monomer with 45.5% deuteration by molecular weight of the original hydrogen atoms. | 80       |

|      |   |     |
|------|---|-----|
| 2.2  | FTIR spectra for deuterated undeuterated variants of the TEGDMA monomer. Spectra for the d-TEGDMA at specific steps of purification are also shown and are offset in the absorbance axis for clarity.   | 81  |
| 2.3  | Peak emission irradiance as a function of increasing percentage power output from the light engine for the <b>(Top)</b> blue and <b>(bottom)</b> cyan colour channels.  | 85  |
| 2.4  | Calibration curves to obtain the integrated irradiance of the light engine as a function of the percentage power output for the <b>(top)</b> blue and <b>(bottom)</b> cyan colour channels.   | 86  |
| 2.5  | Liquid containment cells used for <i>in-situ</i> polymerisation simultaneous to X-ray scattering measurements. Liquid resin is stored inside a metal washer with mica windows, which is fixed into a PTFE washer that is housed within a brass annulus.   | 88  |
| 2.6  | An unfilled resin disc test specimen.   | 89  |
| 2.7  | Experimental setup for laboratory based real time FT-NIR measurements. The resin samples were cured for more than 300 s at varying light intensities whilst undertaking FT-NIRS to quantify the degree of conversion.   | 93  |
| 2.8  | Optics of the Bm28 (XMaS) beamline  | 98  |
| 2.9  | Schematic representation of the I16 beam line optics leading to the diffractometer and sample stage (bottom left). The detector arm assembly is displayed in the bottom right, with the vacuum tube and Pilatus 100K detector, shown as the mauve and blue coloured regions respectively, attached.   | 100 |
| 2.10 | Schematic of the I22 beamline, X-rays are generated by an undulator source and subsequently converted to a monochromatic beam. This beam is focussed by toroidal mirrors (27.73 m) and collimated by a series of slits downstream. The scattered X-ray intensity is measured by two detectors near and far from the sample to obtain WAXS and SAXS data respectively. | 102 |
| 2.11 | A slow neutron collides with and is absorbed by a Uranium – 235 nuclei to form an energetically unstable Uranium 236 nucleus. The new nucleus splits into fission products and releases neutrons and gamma rays.  | 103 |
| 2.12 | A schematic diagram of the ISIS pulsed neutron source (Didcot, UK). H <sup>+</sup> ions are accelerated in the LINAC before being stripped of their electrons and accelerated again inside the synchrotron storage ring. These protons are then fired at a  | 106 |

|      |  |     |
|------|--|-----|
|      | Tantalum coated Tungsten target to produce neutrons by spallation. Thermal neutrons are then guided towards beam lines by guide tubes.   |     |
| 2.13 | Diagram showing the entry of neutrons from the beam guide tubes through to the sample face on the D16 neutron diffractometer. The intensity of diffracted neutrons is captured via a $1 \times 1$ m area detector mounted on a moveable semi-circular rail to allow scanning of particular $q$ ranges.   | 107 |
| 2.14 | (top) Impression of the SANS2D beamline from left to right (bottom) a simplified schematic of SANS2D with the bender exit at 7 m (from the guide tube exit), sample at 19m and sample. Detectors may be placed within 2 -12 metres from the sample to provide a $q$ range of $0.0002 \leq q \leq 2.5 \text{ \AA}^{-1}$   | 111 |
| 2.15 | Scattering curves. Broken line: water scattering raw data. Dotted line: blank scattering of the empty capillary. Thick full line: scattering curve of water after subtraction of the blank scattering. Thin full line: horizontal fit.   | 113 |
| 3.1  | Real time SAXS measurements of dental resin composites polymerised in-situ on the I22 beam-line <b>(1)</b> liquid resins loaded in to a sample rack in the path of impinging X-rays, <b>(2)</b> A liquid light guide instigates photo-polymerisation by illuminating the resin sample with visible or UV light and <b>(3)</b> FT-NIR optical fibres are used to quantify real time monomer to polymer conversion.  | 131 |
| 3.2  | <b>(a)</b> X-ray scattering of a 60/40 Bis-GMA/TEGDMA resin blend initiated with TPO using constant light application at an intensity of $450 \text{ mW cm}^{-2}$ for 300 s. Prior to polymerisation (bold black line), a broad Gaussian feature is centred at $q \sim 1.35 \text{ \AA}^{-1}$ which narrows and moves to $q \sim 1.25 \text{ \AA}^{-1}$ (broken black line). <b>(b)</b> Weighted least squares fitting (broken black line) of scattering data from the individual Bis-GMA (red) and TEGDMA (blue) monomers to the 60/40 wt% blend (solid black line) following baseline corrections. Bis-GMA and TEGDMA contribute 30 and 70 % to the signal respectively. | 132 |
| 3.3  | Chemical structures of Bis-GMA and TEGDMA monomers used to formulate each blend. Methacrylic acid (MA) and triethylene glycol (TEG) were used to simulate the chemical structure and dynamic behaviour of the TEGDMA monomer during polymerisation.  | 134 |

- 3.4 WLS fitting of methyl methacrylate (MA) and triethylene glycol (TEG) X-ray scattering to that of TEGDMA. MA and TEG were used to approximate both the structure and X-ray scattering pattern of the TEGDMA monomer. Close to 70% of the shift and narrowing in scattering following polymerisation was attributed to MA with the remainder ascribed to TEG. The fit is not ideal at higher at lower  $q$  values, which may be due to the small  $q$  range which was limited by the sample environment. Additionally, it should be considered that MA and TEG monomers will have different mobility in comparison to the equivalent structures found in the TEGDMA monomer and will therefore show different correlation lengths. 135
- 3.5 Real time evolution of the correlation length observed in CQ initiated resins for **(a)** 70/30, **(b)** 60/40, **(c)** 50/50 and **(d)** 40/60 wt% blends (Bis-GMA/TEGDMA) during 300 s of photo-polymerisation for a range of reaction rates. All resins display an increase in the correlation length which is larger and faster when a high rate of polymerisation is used. For particularly fast reactions, a subsequent relaxation period can be seen after the initial increase in length, although relaxation is negligible in more fluid blends. 137
- 3.6 The relative percentage increase in short range order during photo-polymerisation as a function of polymerisation rate for resin samples initiated with CQ for **(a)** 70/30, **(b)** 60/40, **(c)** 50/50 and **(d)** 40/60 wt% blends. Changes in order are similar and occur simultaneously to those observed in the correlation length for CQ initiated blends. 139
- 3.7 Degree of conversion in real time during illumination of resin samples initiated with CQ for **(a)** 70/30, **(b)** 60/40, **(c)** 50/50 and **(d)** 40/60 wt% blends. Solid black lines correspond to samples irradiated with  $280 \text{ mWcm}^{-2}$  of light whilst the red line indicates an energy output of  $25 \text{ mWcm}^{-2}$ . 141
- 3.8 Time resolved changes in the correlation length as observed in TPO initiated resins for **(a)** 70/30, **(b)** 60/40, **(c)** 50/50 and **(d)** 40/60 wt% blends (Bis-GMA/TEGDMA) during 300s of photo-polymerisation for a range of reaction rates. Initial increases in the correlation length upon illumination and subsequent relaxations are larger and more rapid for TPO initiated resins, corresponding to a faster polymerisation rate. 143
- 3.9 Changes in the relative order throughout photo-polymerisation for TPO initiated **(a)** 70/30, **(b)** 60/40, **(c)** 50/50 and **(d)** 40/60 wt% resin blends. Unlike CQ initiated 145

|      |  |     |
|------|--|-----|
|      | resins, these systems demonstrate a large relaxation feature.  |     |
| 3.10 | Real time degree of conversion during illumination of resin samples initiated with TPO for <b>(a)</b> 70/30, <b>(b)</b> 60/40, <b>(c)</b> 50/50 and <b>(d)</b> 40/60 wt% blends. Solid black lines correspond to samples irradiated with $730 \text{ mWcm}^{-2}$ of light whilst the red line indicates an energy output of $40 \text{ mWcm}^{-2}$ .   | 147 |
| 3.11 | Real time degree of conversion (red line) and scattering length (black line) for a 60/40 wt% blend initiated with TPO. Auto-acceleration in the resin bulk corresponds to a large initial increase in the correlation length. The point of auto-deceleration in the polymer network (the start of the plateau in the <i>DC</i> plot) coincides with the maximum increase in scattering length.   | 148 |
| 3.12 | Maximum chain extension for each resin blend (viscosity) versus polymerisation rate (irradiance). CQ initiated resins are shown by the first four points and are also inset, whilst the other data points refer to TPO initiated resins. Resins polymerised at higher rates display the greatest increase in the correlation length. Data was obtained from BM28 (ESRF).   | 150 |
| 3.13 | Maximum increase in order for each resin blend (viscosity) versus polymerisation rate (irradiance). CQ initiated resins are shown by the first four points, whilst the other data points refer to TPO initiated resins. Resins polymerised rapidly demonstrate the greatest increase in order, although this is likely an artefact of different conversion values, as a more converted system will inevitably be more ordered.   | 151 |
| 3.14 | Normalised maximum increase in relative short range order for each resin blend (viscosity) versus polymerisation rate (irradiance). Data has been normalised to the degree of monomer conversion to determine chain extension and order per converted C=C bond. CQ initiated resins are shown by the first four points, whilst the other data points refer to TPO initiated resins. Systems polymerised at slower rates display the greatest increase in order for a given blend, whilst increasing viscosity decreases short range order. | 152 |
| 4.1  | <b>(a)</b> Fully hydrogenated TEGDMA and <b>(b)</b> partially deuterated TEGDMA where the methyl and methylene groups have had hydrogen exchanged with deuterium.  | 169 |
| 4.2  | Small angle neutron scattering spectra of a 40/60 wt % (Bis-GMA/d-TEGDMA) blend initiated with CQ, prior to photo-   | 179 |

polymerisation (solid line) and after photo-polymerisation (broken line). Three prominent scattering features are located at  $\sim 0.6$ ,  $1.15$  and  $1.4 \text{ \AA}^{-1}$ . The feature at  $\sim 0.2$  may not represent a true structural feature and may instead be a low  $q$  artefact.

|      |   |     |
|------|---|-----|
| 4.3  | SANS spectra of liquid monomers d-TEGDMA (solid black line) and hydrogenated Bis-GMA (broken black line)  | 181 |
| 4.4  | SANS spectra of a completely hydrogenated 60/40 wt% (Bis-GMA/TEGDMA) sample with a CQ initiator system.   | 182 |
| 4.5  | Correlation lengths, corresponding to the scattering peak initially located at $\sim 0.6 \text{ \AA}^{-1}$ , post photo-polymerisation for the respective resin blend test specimens.   | 184 |
| 4.6  | SANS spectra of 60/40 wt % (Bis-GMA/d-TEGDMA) blends utilising either a (a) CQ or (b) TPO photo-initiator. Resin samples polymerised at high irradiance densities are referred to as the fast regimen (broken black line) whilst low irradiance density curing protocols are termed slow regimens (solid black line).                                   | 185 |
| 4.7  | Full width at half maximum (FWHM) for the scattering peak located at $\sim 0.6 \text{ \AA}^{-1}$ , post photo-polymerisation for the respective resin blend specimens.  | 186 |
| 4.8  | Final correlation lengths for peak c ( $q \sim 1.15 \text{ \AA}^{-1}$ ), for each resin formulation and irradiance protocol.  | 187 |
| 4.9  | Final correlation lengths (peak d, $q \sim 1.4 \text{ \AA}^{-1}$ ) for the each resin specimen post-polymerisation  | 189 |
| 4.10 | Density measurements of hydrogenated counterparts to deuterated resin blends used for SANS. Hydrogenated versions were used as each sample formulations could be reproduced several times to gain better statistics, unlike for deuterated samples.   | 190 |
| 4.11 | Real time evolution of the (a) correlation length and (b) relative increase in order for 60/40 wt% (Bis-GMA/TEGDMA) blends. Resins photo-initiated with CQ at high (dotted line) and low (broken line) light irradiance densities are shown in addition to a TPO initiated resin polymerised at a relatively high light irradiance density (solid line) | 193 |
| 5.1  | <b>(left)</b> Two Aluminium plates, mounted onto a heated kinematic stage, heats a resin disc test specimens held between the plates. X-rays impinge normal to the sample face and scatter into a Pilatus 100 K detector mounted onto a 2 $\theta$  | 211 |

- detector arm. **(right)** Top down view of the experimental set-up. The pipe to the left of the image blows cold air ( $20\text{ }^{\circ}\text{C} \pm 1\text{ }^{\circ}\text{C}$ ) to cool the stage after heating.
- 5.2 X-ray scattering of a 40/60 wt % (Bis-GMA/TEGDMA) resin disc sample initiated with TPO. At  $20\text{ }^{\circ}\text{C}$  the scattering peak (black line) is located at approximately  $1.14\text{ \AA}^{-1}$ , but moves to lower  $q$  (red line), indicative of an increase in the correlation length. 213
- 5.3 Correlation length as a function of temperature for **(a)** CQ and **(b)** TPO initiated RBCs. 214
- 5.4 Relative changes in order as a function of temperature for **(a)** CQ and **(b)** TPO initiated RBCs. 216
- 6.1 **(a)** Schematic of the IRENI beamline (Synchrotron Radiation Centre, Wisconsin, U.S.A), where M1 – M4 are mirror sets (adapted from Nasse et al 2011). **(b)** Long-exposure photograph showing the combination of the 12 individual beams to form a  $3 \times 4$  matrix. **(c)** A visible-light photograph of a 60/40 wt% TPO initiated composite, where each map panel measures  $32 \times 32\text{ }\mu\text{m}$ . 227
- 6.2 **(a)** Visible image of a TPO initiated RBC composed of a 60/40 wt % (Bis-GMA/TEGDMA) resin matrix containing 50 wt% of monodisperse  $8\text{ }\mu\text{m}$  silica particles. **(b)** A map of monomer to polymer conversion over the identical area shown in (a). Areas coloured blue and red correspond to regions of relatively low and high conversion respectively. **(c)** A pseudo-coloured map of the aromatic ( $1609\text{ cm}^{-1}$ ) absorption band wavenumber position over the same area, where lower wavenumbers correspond to larger residual strain stored within the polymer (red regions). **(d) (main)** Raw Mid-IR spectra of a TPO initiated composite composed of a 60/40 wt % (Bis-GMA/TEGDMA) resin matrix containing 50 wt % of monodisperse  $8\text{ }\mu\text{m}$  silica particles. The spectra was collected over  $850 - 4000\text{ cm}^{-1}$ , with a  $2\text{ cm}^{-1}$  resolution. **(inset)** Aromatic ( $1609\text{ cm}^{-1}$ ) and aliphatic ( $1637\text{ cm}^{-1}$ ) absorption bands which were used to calculate the degree of monomer to polymer conversion and relative residual strain for each pixel within a map. 231
- 6.3 Degree of conversion is shown as a function of distance from a filler particle centre. Radially averaged conversion (over all particles, centre to edge) is shown to the left of the dashed line, whilst conversion at the midpoint between particle centres is shown to the right. 233

|     |   |     |
|-----|---|-----|
| 6.4 | <p><b>(a)</b> Deconvolution of the aromatic (<math>1609\text{ cm}^{-1}</math>) and aliphatic (<math>1637\text{ cm}^{-1}</math>) absorption bands. <b>(b)</b> The aromatic absorption band taken as a line transect from the centre of a particle into the resin matrix. <b>(c)</b> Loading vectors of the aromatic peak over the aforementioned line transect.</p>  | 236 |
| 6.5 | <p>The aromatic wavenumber for the aromatic group at the centre of the Bis-GMA monomer is shown as a function of distance from a filler particle centre. Radially averaged wavenumber (over all particles, centre to edge) is shown to the left of the dashed line, whilst the wavenumber value at the midpoint between particle centres is shown to the right. <b>(inset)</b> The chemical structure of the Bis-GMA monomer - ring strain was detected in the aromatic core.</p>                                       | 238 |
| 6.6 | <p>The radially averaged decrease in the aromatic wavenumber as a function of monomer to polymer conversion. Each plotting point represents a distance increment of <math>0.54\text{ }\mu\text{m}</math> from the centre of the filler particle, the first point to the left, to the edge of the particle.</p>  | 239 |
| 6.7 | <p>The decrease in the aromatic wavenumber (an increase in residual strain), normalised to the degree of conversion at each distance increment. The generation of residual strain within the RBC is ranked by the relative differences in polymerisation rate.</p>  | 240 |
| 7.1 | <p><b>(a)</b> Schematic of a tooth fin section showing the regions mapped by successive SXRD line scan measurements. <b>(b)</b> A single line scan measurement used to acquire sufficient statistics for each polymerisation regime.</p>  | 258 |
| 7.2 | <p><b>(a)</b> Variation in intensity of the (002) diffraction ring is indicative of texture, whilst <b>(b)</b> a complete ring demonstrates little or no texture. Preferred orientation is defined from <math>0^\circ</math> which points east on the detector face, increasing azimuthally in the counter-clockwise direction. <b>(c)</b> A 1-D diffraction spectra with the (002) and (300) reflections corresponding to peaks located at <math>\sim 10^\circ</math> and <math>\sim 14^\circ</math> respectively.</p> | 263 |
| 7.3 | <p><b>a)</b> A composite image showing individual 2-D diffraction spectra, for each measurement along a track, superimposed on to a schematic of a tooth fin. Bisection of the (002) diffraction ring through points of greatest intensity yields the approximate direction of preferred orientation, which is shown as a red line. <b>(b)</b> Azimuthal integration of the (002) diffraction ring shows that two directions of crystallite/prismatic orientation exist within the tooth enamel.</p>                    | 264 |

|      |   |     |
|------|---|-----|
| 7.4  | Contour maps for the <i>c</i> -lattice parameter for LED and QTH curing. <b>(a)</b> LED before <b>(b)</b> LED after <b>(c)</b> LED % strain; <b>(d)</b> QTH before <b>(e)</b> QTH after <b>(f)</b> QTH % strain   | 267 |
| 7.5  | The percentage change in the <i>c</i> axis length, following the application of an RBC, is shown as a function of the measurement position along the respective track for fast (broken line) or slow (solid line) polymerisation regimes.   | 268 |
| 7.6  | Contour maps for the <i>a</i> -lattice parameter for LED and QH curing. <b>(a)</b> LED before <b>(b)</b> LED after <b>(c)</b> LED % strain; <b>(d)</b> QH before <b>(e)</b> QH after <b>(f)</b> QH % strain   | 270 |
| 7.7  | Changes in crystallite orientation angle post polymerisation, for the low (black solid line) and high (black broken line) angle directions, plotted as a function of track position with strain in the <i>c</i> lattice overlaid (red line). Track position is defined as 0 mm equal to the top of the tooth fin track and 2.4 mm representing the bottom of the fin.   | 272 |
| 7.8  | <b>(a)</b> Relative proportions of two crystallite orientations, red and blue bars, overlaid on to strain data and <b>(b)</b> crystallographic strain in the <i>c</i> axis plotted against the percentage of crystallites in the low angle distribution as a function of track position. The aspect ratio has been altered, blurring the image, to allow for visualisation of orientation bars. Data is taken from the first track of the tooth specimen subjected to the fast polymerisation regime. | 273 |
| 7.9  | <b>(a)</b> Relative proportions of two crystallite orientations, red and blue bars, overlaid on to strain data. The aspect ratio has been altered, blurring the image, to allow for orientation bars. <b>(b)</b> crystallographic strain in the <i>a</i> axis plotted against the proportion of crystallites in a predominantly horizontal orientation as a function of track position. Data is taken from the first track of the tooth specimen subjected to the fast polymerisation regime.         | 275 |
| 10.1 | Real time evolution of the correlation length reported in chapter three when exposed to X-rays for a 60/40 wt% (Bis-GMA/TEGDMA) sample with TPO photo-initiator in the <b>(a)</b> liquid monomer and <b>(c)</b> solid polymer form. Analogous plot for changes in short range order are shown in <b>(b)</b> and <b>(d)</b> .  | 300 |

# 1 INTRODUCTION AND LITERATURE REVIEW

Mercury based amalgams are perhaps the most widely used restorative biomaterials found in orthopaedic and specifically dental applications, with approximately 370 million restorations (fillings) placed each year in Europe alone [1]. Low cost and a relatively long service life have made amalgam, until recently, indispensable in dentistry for over 160 years [2]. However, in 2013 it was agreed by several nations at the Minamata convention [3, 4] that mining [5], export and import, storage [6], and waste management [3] of products containing mercury would be reduced globally to limit health and environmental impacts of mercury pollution [3, 7]. New European legislation heavily restricting the manufacture and disposal of mercury based products has prompted the imminent removal of dental amalgam as a treatment option in several European countries already [8-10], amid mounting environmental and health concerns associated with this global pollutant [1, 11]. Consequently, there is an increasing need to identify a suitable replacement for mercury amalgam dental filling materials. The most promising alternatives are resin based composite (RBC) materials based on dimethacrylate polymer chemistry.

In clinical use for over 30 years, RBCs combine a polymerisable dimethacrylate resin matrix with an inorganic filler phase. Following application to the tooth surface, light excitation of a photo-initiator species dispersed within the resin matrix triggers free radical polymerisation to generate a three-dimensional cross-linked network causing the composite to solidify [12, 13]. Resin based composites offer quicker setting times, are mechanically stronger and demonstrate greater longevity in comparison to competing materials such as glass ionomer cements and giomers. However, a deficiency of RBCs is that the physico-chemical properties of these materials are highly sensitive to setting parameters and as a consequence clinical performance and survival rates are lower in comparison to amalgam fillings [14].

Currently most light curing protocols for RBCs require 40 seconds or more of specified light wavelength exposure at intensities from 400 to 800mW/cm<sup>2</sup> per increment of material (up to 10 increments may be required per filling), to achieve the desired conversion of monomer to polymer [15, 16]. Extensive research is currently being undertaken by academia and industry to develop shorter light curing protocols to reduce treatment times and reduce operator induced curing variability [15, 16]. As a result, high intensity lights are now being advocated and brought to market which enable photo-polymerisation in as short a time as 3 seconds [16], under the assumption that the final properties of an RBC are determined predominantly by the maximum degree of conversion ( $DC_{max}$ ), regardless of the combination of light intensity and exposure time. The effect that photo-polymerisation has on the polymer phase of RBCs has been extensively characterised through the use of FTIR (Fourier transform infra-red spectroscopy) to quantify real time monomer-polymer conversion from which many correlations with bulk material properties have been extrapolated [17-19].

It is widely reported that accelerating polymerisation using high intensity light activation can impact on the tensile strength, toughness, hardness and degree of polymerisation shrinkage and stress of these materials [19-22]. Indeed a parabolic relationship between the reaction rate,  $DC$  and final mechanical properties [23] has been shown to exist [24]. To date these differences in properties have been ascribed to structural differences regarding cross-link density and its effect on polymer network architecture. Faster reactions are believed to reduce the lifetime of radical species with respect to bimolecular termination [22], reducing the degree of cross-linkage.

Previous research has focussed on interpreting differences in polymer network formation from the  $DC$  of RBCs using Fourier Transform Infra-red spectroscopy (FTIR) and indirect measures of cross-link density such as surface hardness. However, the effect that the polymerisation rate has on the resultant polymer structure of the constituent monomers that comprise the resin matrix is surprisingly unknown. This structural information cannot be obtained using conventional laboratory based characterisation techniques.

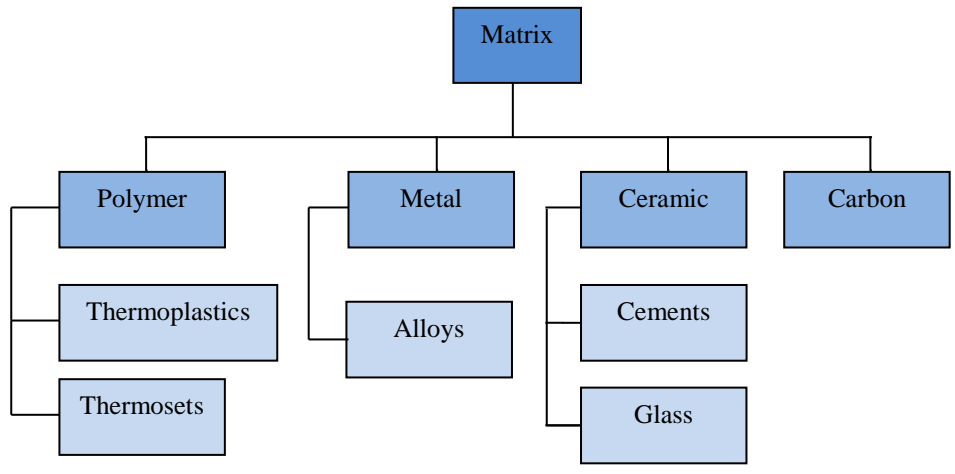
Structural order at atomic length scales in materials can be detected using light and particle scattering methods. Standard scattering measurements using laboratory X-ray sources fail to provide sufficient flux to discern such differences in these materials, especially when dynamic (*in-situ*) curing studies with short measurement times are conducted. Synchrotron light sources however, provide the necessary flux, energy range and flexible sample environment to allow order at intra-monomeric distances to be determined using X-ray scattering methods. Additionally, neutron scattering can provide complimentary structural information at defined length scales. X-ray and neutron scattering techniques are widely used in polymer research to discern evolving polymer structures, including methacrylate functionalised polymers, under dynamic conditions including polymerisation [25, 26], yet these techniques are rarely applied to the study of dental polymers. Application of these techniques therefore has the potential to provide useful complimentary structural information not available through conventional laboratory based characterisation techniques.

This thesis explores the effect that polymerisation rate has on the polymer structure, at atomic to micron length scales, of experimental RBCs based on common dimethacrylate resins using advanced synchrotron and neutron based techniques

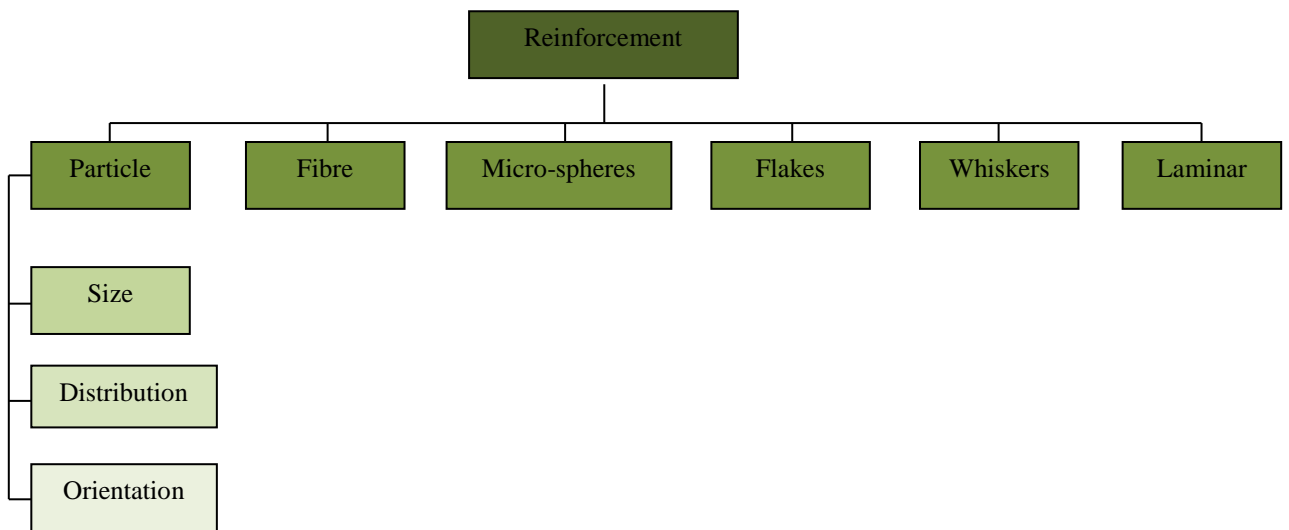
## Literature Review

### 1.1.2 What are Resin Based Composites (RBCs)?

A composite is a compound material formed from the combination of at least two constituent phases bonded together [27]. Each phase has different physical-chemical properties from the other phases and are combined to produce a resultant material with intermediate properties, whilst retaining the macro-structure of the constituent phases [28-32]. Composites typically have three principal phases as a matrix, a higher modulus reinforcement and an interfacial layer acting as a coupling agent between the matrix and reinforcement [28-33]. The role of the matrix is to provide a material into which the second reinforcing phase can be dispersed. The reinforcement material is typically incorporated to confer higher strength and resistance to wear to the final material, whilst the coupling agent bonds the aforementioned phases [28-33]. Composite materials are typically categorised according to the material used for the matrix. Four primary classes exist including organic matrix composites (OMCs), metal matrix composites (MMCs), ceramic matrix composites (CMCs), and carbon matrix composites (CAMCs) [27]. Organic matrix composites are one of the most widely used classes of composites globally and are the focus of this thesis. There are two main classes of polymers used to form the matrix of OMCs as either thermoplastics or thermosets. Thermoplastics may be reformed several times by the application of heat, whilst thermosets form irreversible chemical bonds during a setting or 'curing' process where they transition from a liquid uncured state to a cured solid material. Examples of thermoplastics include polycarbonates, polyamideimides and polyetherimides, whilst thermosets may be based on epoxy or methacrylate polymer chemistry. RBCs are therein classed next by the morphology of the reinforcement phase including particles, fibres and laminates and further by the size, distribution and orientation (Figure 1.1).



(a)



(b)

**Figure 1.1.** (a) Hierarchy of composite classes divided according to matrix material, reinforcement and (b) reinforcement morphology. Adapted from Figure 16.2 Callister 7<sup>th</sup> edition.

### 1.1.3 Biomedical Applications of RBCs

Resin based composites (RBCs) utilising dimethacrylate polymer chemistry matrices are routinely used for biomedical applications, in orthopaedics and in particular in restorative dentistry [34]. Acrylate based composites have been used since the 1940s, predominantly as an alternative to dental amalgam as a tooth filling material [35-37] in addition to dentine bonding agents [38, 39], dental adhesives [40-43] and elastomeric impression materials [44]. Modern commercial dental RBCs typically consist of a dimethacrylate resin matrix [45-47], which can contain one or more monomer species, incorporating an inorganic reinforcing filler fraction in the form of glass particles [48-51] which are bound together by a vinyl silane coupling agent [52-55]. A photo-initiator species is dispersed throughout the resin matrix to instigate free radical polymerisation, when activated by an external visible light source, converting a liquid monomer blend into a three dimensional cross linked polymer network (Figure 1.2).



**Figure 1.2** Schematic representation of a resin based composite (RBC). The resin matrix is shown as a light purple background, filler particles are displayed as polygons and radical species are denoted by black dots.

Consequently, dental RBCs may be manipulated and sculpted to the dimensions of the tooth cavity defect under a relatively long working time, before being polymerised or ‘demand set’ at the discretion of the clinical operator. Dental RBCs can be set in the presence of oxygen and water, have good chemical affinity with tooth tissue [56] and are aesthetically pleasing. Dental composites provide adequate physico-mechanical properties [57], thermal stability and require less dental hard tissue to be removed per restoration in comparison with traditional amalgam fillings. RBCs are currently used for direct restorations in both anterior and posterior teeth, as adhesive cements and as sealants. RBCs can be also used to fabricate indirect restorations including, veneers, crowns and bridges. Resin matrix/glass particle composites are the most widely used material for anterior tooth restorations [58] and are also used for approximately half of posterior restorations [59, 60].

## 1.2 RBC Composition: Historical Development and Current Trends

### 1.2.1 Resin Matrix

Resin based materials have been used in dentistry since the 1850s [61]. Early resin-based dental materials were initially based on Vulcanite [62] however, these were difficult to manipulate and sculpt and often requiring *in-situ* heating. Methyl methacrylate was created in 1931 and by 1936 [36] was being used as a dental restorative material as unfilled (poly) methyl methacrylate (PMMA). Unfortunately, PMMA was unsuitable for dental fillings, suffering from extremely high shrinkage upon polymerisation, typically 20-25 % by volume, resulting in detachment from the tooth substrate and the formation of marginal gaps [63-66]. Quartz filler particles were later added to increase wear resistance, however poor mechanical and wear properties remained [67].

In 1956, the dental resin Bis-GMA was developed by R.L Bowen from the reaction product of bisphenol A and glycidyl ester methacrylate (GMA) [68], and it is still the most widely used constituent monomer in commercial dental RBCs formulations. Bis-GMA is a hybrid monomer which combines the matrix forming potential of epoxy resins with the rapid setting capabilities of acrylic monomers [69]. A relatively large molecular weight in comparison to smaller sized monomers such as PMMA generates less shrinkage, reported to range between 3.3 - 5.2 % by volume [70, 71]. Bis-GMA is a bulky monomer with two centrally located aromatic groups which confer a higher modulus of elasticity and toughness in addition to carbonyl and hydroxyl groups capable of hydrogen bonding, producing a very viscous monomer (Table 1.1). Importantly, Bis-GMA is di-functional, allowing it to bond with two additional monomers per functional group or four bonds in total. This allows the monomer to form cross-links [72], unlike PMMA which may only form linear chains, providing greater structural stability. Unfortunately, the high viscosity of Bis-GMA renders it extremely difficult to handle and to manipulate and severely limits the incorporation of a filler fraction in any useful quantities as to affect mechanical properties [73]. Furthermore, homo-polymerisation of Bis-GMA yields low

terminal monomer to polymer conversion of approximately 36 % [74] and as a consequence a gel is formed instead of a solid polymer.

Bis-GMA is therefore often combined with a reactive and lower molecular weight co-monomer(s) which act as a diluent to reduce the viscosity of the system [45, 75] which affords the incorporation of filler. Triethylene glycol dimethacrylate (TEGDMA) [76-79] is frequently used for this purpose. TEGDMA has a single chain backbone consisting of ester bonds and has a molecular weight that is approximately half that of Bis-GMA (Table 1.1). A lower molecular weight increases the density of polymerisable functional groups and confers greater monomer to polymer conversion i.e. homo-polymerisation of TEGDMA yields more than 60 % conversion. However, increased conversion is accompanied by the deleterious effect of greater polymerisation shrinkage of ~ 12.5 % by volume and a decrease in elastic modulus [70, 80]. Modifications to the chemical structure of these monomers have been made to increase monomer to polymer conversion whilst maintaining similar or reduced degrees of shrinkage [81, 82]. Bisphenol A ethoxylated dimethacrylate (Bis-EMA) [82, 83] is a derivative of Bis-GMA and has an almost identical chemical structure except for the absence of hydroxyl groups. This monomer has a lower viscosity than Bis-GMA, with comparable mechanical properties when polymerised. Less diluent is therefore required to achieve greater terminal conversion, offsetting shrinkage effects. Urethane dimethacrylate (UDMA) (Figure 1.3) is also used as an alternative and/or co-monomer to Bis-GMA [84] within commercial RBCs. Urethane dimethacrylate has similar methacrylate based chemistry to Bis-GMA but with a centrally located urethane group. This affords greater flexibility and reduced viscosity to the monomer, conferring greater monomer to polymer conversion than Bis-GMA, although less than the homo-polymerisation of TEGDMA [35].

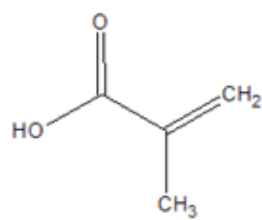
Ultimately though, systems of viscous/diluent dimethacrylate monomers represent antagonistic effects; the viscous monomer(s) confers better mechanical properties but does not reach a high value of terminal monomer to polymer conversion, whilst the diluent achieves higher conversion at the expense of increased shrinkage. Forming a resin matrix from several

constituent methacrylate based monomers requires a compromise between resin viscosity, monomer to polymer conversion, polymerisation shrinkage and resultant physio-mechanical properties. This is not ideal as certain aspects such as polymerisation shrinkage cannot be eliminated and is an inevitable outcome of the radical-mediated chain-growth polymerisation mechanism.

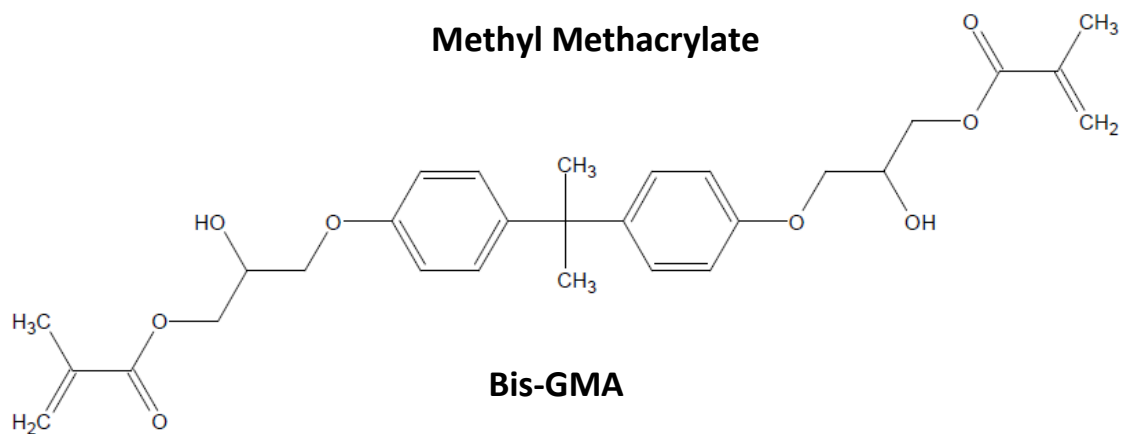
Recent work has focussed on using thiol-ene photo-polymerisation mechanisms to reduce polymerisation shrinkage in dental RBCs. Thiol-enes cure through step growth polymerisation in which propagation and chain transfer alternative, as opposed to chain growth polymerisation displayed by dimethacrylates [79, 85, 86]. The reaction of a thiol-ene monomer creates reactive thiol and vinyl (ene) functional oligomers [87]. This significantly delays the gel point in comparison to dimethacrylates such that the majority of shrinkage stress occurs earlier during polymerisation and can therefore be reduced by viscous flow [88]. It is reported that thiol-ene based RBCs display up to 33 % less shrinkage by volume relative to dimethacrylate control specimens [89, 90] . Upon polymerisation thiol-enes form uniform polymer networks which are less brittle than dimethacrylate based counterparts, also exhibiting higher glass transition temperature, reduced shrinkage and shrinkage stress [78, 91, 92]. However, thiol-ene RBCs display inferior mechanical properties including reduced flexural modulus and strength [93]. Recently, thiol-enes have been combined with methacrylates to combine desirable material properties. It is reported that thiol-ene – methacrylate systems demonstrate comparable strength and flexural modulus to dimethacrylate systems whilst retaining similar shrinkage behaviour to thiol-ene systems [91]. Allyl sulphide moieties have also been incorporated into monomers, which undergo thiol- ene polymerisation [94]. This creates an adaptable covalently bonded polymer network which can undergo addition-fragmentation processes. Chemical bonds therefore remain covalent but are able to break and reform [95, 96]. This novel chemistry has been shown to reduce polymerisation shrinkage stresses by up to 75 % in comparison to monomers without the allyl sulphide moiety [97]. It must be noted however, that despite the use

of novel reaction mechanisms to generate less shrinkage in these materials adhesion to the tooth remains a concern [98].

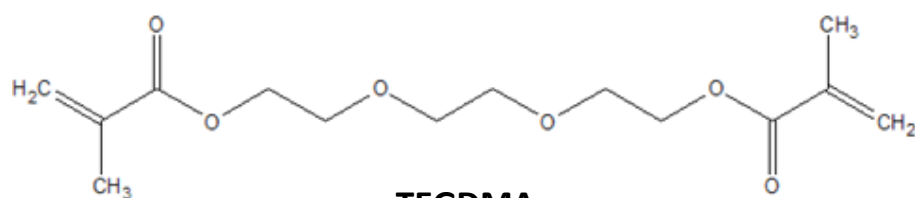
The use of ring opening chemistry has also been explored as a way to reduce polymerisation shrinkage [99, 100]. Ring opening chemistry is an attractive alternative to conventional dimethacrylates as the monomers connect by opening, flattening and extending towards each other, which results in a significantly lower polymerisation shrinkage in contrast to a dimethacrylate based composites in which the monomers are linear and bond by physically moving closer together, conferring a greater loss of volume. Weinmann *et al* [101] reported on the properties of a commercial RBC based on silorane chemistry incorporating a cyclic siloxane core with four oxirane reactive groups, compared to conventional dimethacrylate based RBCs, post-polymerisation. Ring opening siloranes demonstrated comparable elastic modulus and strength to dimethacrylate RBCs, but showed significantly reduced shrinkage values, approximately 1 % by volume. However, studies on bicyclic ring opening monomers have shown that despite demonstrating reduced volumetric shrinkage in comparison to dimethacrylates [102, 103], are highly susceptible to moisture induced reactions, which in an oral environment is not ideal for stable adhesion to hard tissue [104].



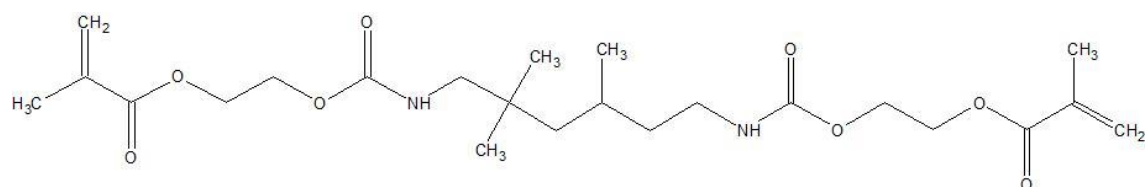
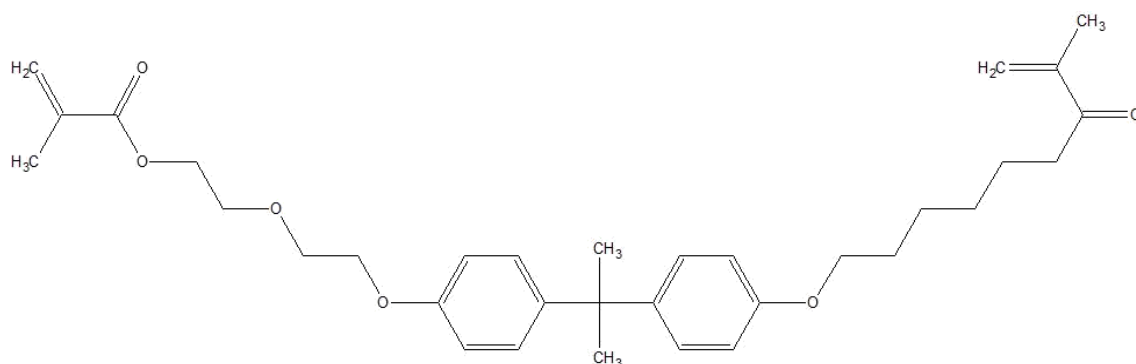
**Methyl Methacrylate**



**Bis-GMA**



**TEGDMA**



**UDMA**

**Figure 1.3.** The chemical structure of monomers commonly used in the formulation of commercial and experimental RBCs.

**Table 1.1.** Summary of common monomers, and some physical properties, used in the formulation of RBCs

| <b>Chemical</b> | <b>Chemical formula</b>                                       | <b>Molecular weight (g/mole)</b> | <b>Density (g/ml)</b> | <b>Viscosity (Pa s)</b> |
|-----------------|---|----------------------------------|-----------------------|-------------------------|
| <b>Bis-GMA</b>  | C <sub>29</sub> H <sub>36</sub> O <sub>8</sub>                | 512.599                          | 1.161                 | 700-1300                |
| <b>TEGDMA</b>   | C <sub>14</sub> H <sub>22</sub> O <sub>6</sub>                | 286.324                          | 1.092                 | 0.05                    |
| <b>Bis-EMA</b>  | C <sub>27</sub> H <sub>24</sub> O <sub>6</sub>                | 444.285                          | 1.120                 | 3                       |
| <b>UDMA</b>     | C <sub>23</sub> H <sub>38</sub> N <sub>2</sub> O <sub>8</sub> | 470.563                          | 1.110                 | 10                      |

### 1.2.2 Filler Particles

Early PMMA based dental resins were combined with quartz filler particles to impart increased wear resistance and hardness [105] to the composite. Combining the resin matrix with filler also increases the composite modulus [106, 107] and radio opacity [108] but decreases thermal expansion [109] and the degree of polymerisation shrinkage [110-112]. These quartz fillers had splint morphology and an average size of 5 - 30  $\mu\text{m}$  in length. Composites containing filler particles belonging to this size regime were classed as macrofilled [113] composites. However, early macrofilled composites were seldom used in this form, as due to the crystalline structure of quartz and the relatively large size of the particles, the composites were highly abrasive to opposing teeth and were difficult to polish. In the case of the latter, polishing often produced rough surfaces from which individual quartz particles would protrude and break away. Macrofilled composites are still currently used although modern versions have an average particle size of 0.2 – 5  $\mu\text{m}$  [105].

Microfilled composites, containing spheroidal amorphous silica particles (0.01 – 1  $\mu\text{m}$  diameter) were introduced to improve polishing and wear abrasion resistance [57]. High filler loads were however limited, as the high surface area to volume ratio produced an extremely

viscous composite that cannot be easily manipulated. Modern commercial RBCs therefore tend to combine a range of particulate sizes in what is known as a hybrid filled system [57, 114]. Hybrid filler allows for higher loading fractions, in terms of volume, as smaller particles fill gaps between larger particles. Hybrids exist in two main classes as either micro or nano hybrids, with sub sets of classification based on whether the filler particles are monodisperse, polydisperse with a continuous or bimodal size distribution [115]. Modern nano hybrids represent a combination of nano-sized (less than 100 nm) and sub-micron sized particles typically within a range of 0.5 – 1 micron, containing a greater proportion of nano sized particles [57, 116]. Nano-filled composites display increased strength, reduced polymerisation shrinkage and a lower viscosity for easier handling in comparison to larger particles for equivalent loading fractions. However, nano-filler particles are prone to agglomeration which predisposes the composite to mechanical failure. Current hybrid filled commercial composites in either micro or nano-hybrid form are often aluminosilicate based, typically including zirconium, strontium or barium to increase X-ray opacity for diagnostic purposes [52, 105] and have typical filler loadings of 70 – 90 wt %.

Recent alternatives to conventional glass based filler particles that are currently being developed include pre-polymerised filler (PPF) particles [117], synthetic calcium phosphates [118, 119], bioactive glasses and quantum dots [120, 121]. Pre-polymerised filler particles are prepared from cured composite that contains sub-micron silicate based particles, ground to micron sizes. Incorporation of PPFs aims to improve the polishability of the composite in comparison to silicate hybrids and to also reduce internal stresses, a by-product of polymerisation [116, 117]. Synthetic calcium phosphates [122-124] including hydroxyapatite, the principal mineral component of tooth enamel, and bioactive glasses treated with coupling agents have been ground to micron dimensions and incorporated with resin matrices to either produce similar mechanical properties to the replaced hard tissue or to induce osteoconductive bone growth to enhance bonding to the tooth [125]. Finally, quantum dots are a colloidal suspension of semi-conductor particles that have been tuned to emit light in the blue visible

region. Quantum dots have been suggested as an alternative filler material [120] as they have the ability to instigate polymerisation from within the material and are able to continue photo-activation after external light sources have ceased sample illumination.

### **1.2.3 Photo-initiator Chemistry**

Chemical initiators were originally used to instigate polymerisation for dental RBCs [126], however relatively fast setting times typically under 5 minutes severely limited the working time available to the clinician to manipulate the composite. In the 1970s [61] photo-initiators, photo-active system that absorbs photons within a specific wavelength range, were first used as an alternative means of initiation for dental RBCs. This technique requires an external light source to activate the initiator species to produce free radicals to start polymerisation. This affords the clinician a longer time to shape the composite as polymerisation commences only when illuminated or 'demand-set'. Photo-initiators that absorbed in the ultra-violet region of light were used at first, although poor penetration depth [127] and potential health hazards by ultraviolet light sources prompted the use of initiators receptive to visible light [128]. Current commercial RBCs utilise photo-initiators which absorb in the blue visible region of light. Photo-initiators are classed according to the mechanism that produces free radicals upon illumination of the initiator species. Norish type I and type II classes refer to photo-initiators that produce radicals either through the photo-fragmentation of the initiator molecule or by hydrogen abstraction from a donor molecule respectively [129].

### 1.2.3.1 Camphorquinone

Camphorquinone (CQ) was first used to photo-initiate dental RBCS in 1978 and remains the most widely used photo-initiator species found in commercial RBCS [130]. Camphorquinone is a Norrish type two initiator species and is used in conjunction with a tertiary aliphatic amine reducing agent [44, 131] to produce radicals. CQ absorbs photons in both the UV (200-300 nm) and also in the blue visible region (400-500, peak = 470 nm) [132]. As current clinical photo-polymerisation regimes use blue visible light for photo-activation this is the only absorption region that will be assumed for the description of this photo-initiator. Energy absorbed from incoming photons promotes the non-binding electron from the carbonyl group (Figure 1.4), to an excited state within the  $\pi^*$  anti-orbital of the double covalent bond. Excited states exist in both singlet and triplet states, and intersystem crossing pumped by the irradiation of the impinging light source, inverts the population from singlet to triplet states [133]. The excited CQ molecule combines with the tertiary amine to form an excited triplet complex or exiplex. Once bound, the exiplex undergoes an internal hydrogen transfer from the amine alpha carbon to the carbonyl of the diketone [134]. This produces two radical species as an amino and cetyl radical. Both of these radicals will remain in the system as due to the preservation of the parallel spin condition neither will undergo bimolecular termination. However, only the amine radical is an active polymerisation species [135]. CQ has a quantum yield of  $0.07 \pm 0.01$  converted CQ per absorbed photon, i.e.  $\sim 14$  photons will on produce one radical from a CQ molecule [136].

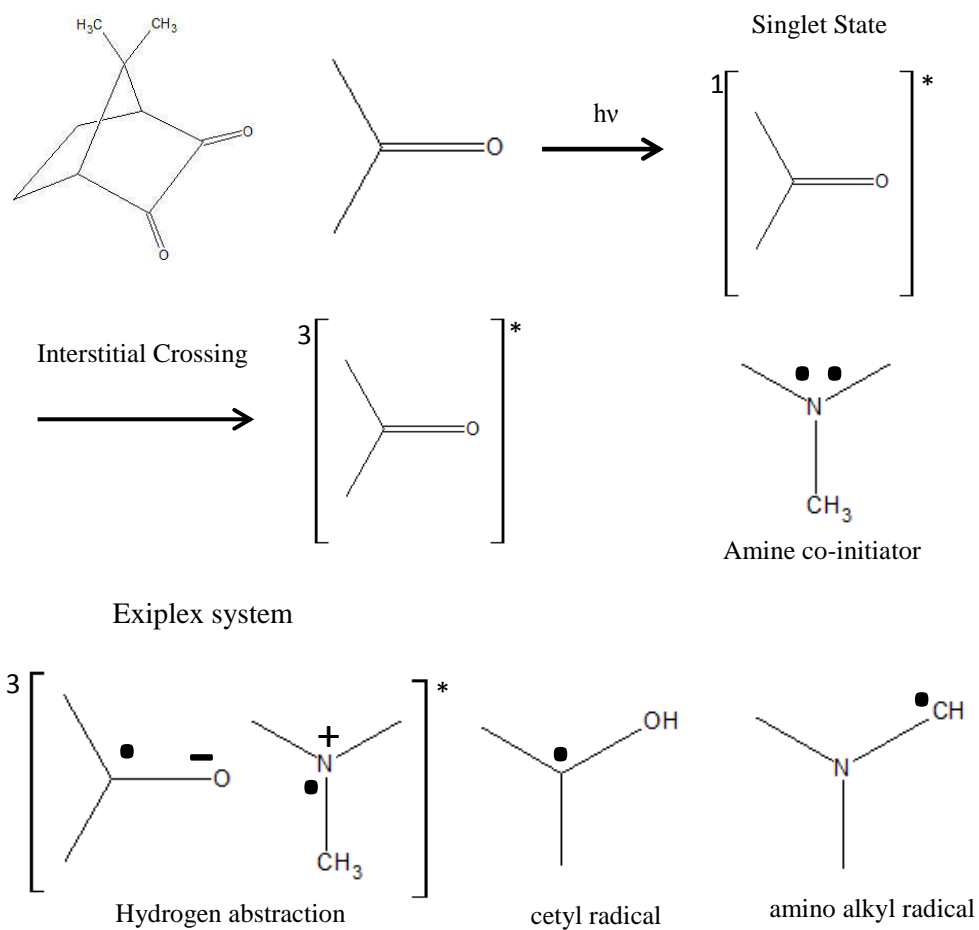


**Figure 1.4.** The production of free radicals from the excitation of the Camphorquinone photo-initiator species used with an amine reducing agent.

### 1.2.3.2 Acyl phosphine oxides

Acyl phosphines oxides are a Norrish type one photo-initiator and have gained recent attention as a more reactive photo-initiator species in comparison with CQ and its ability to drive more efficient polymerisation with respect to polymerisation rate and terminal conversion [137]. Examples include mono (MAPO) [138] and bi-acyl phosphines oxides (BAPO), known commercially as Lucirin TPO (diphenyl(2,4,6-trimethylbenzoyl)phosphine oxide) and Igracure 819 respectively. Acyl phosphines oxides are typically composed of several phenol ring groups connected in a conjugated conformation with a double covalently bonded oxygen (Figure 1.5). Acyl phosphines oxides are photo-lytic initiators and utilise light directly, readily absorbing ultra-violet light near to the blue visible region of the spectrum to split the molecule into two macro-radicals [139]. This will occur if the energy of the incoming photons matches or exceeds the threshold of the central atomic bond arrangement [140] (typically a carbon-carbon or carbon-phosphate bond) [139, 140]. Due to the electron withdrawing tendency of the oxygen atoms present near the phenol rings the sigma bond between the central atoms can be weakened enough to split the molecule (homo-lytic scission), producing two radicals of the acetyl and phosphonyl kind which can produce second generation radicals. Acyl phosphine oxides have a greater molar absorptivity [141] (Table 1.2), quantum yield, produce more primary radicals [142] and the radicals which are produced are more reactive [143] than those generated from a Camphorquinone/amine system.

**Table 1.2.** The absorption characteristics of photo-initiators used in commercial and experimental RBCs.

| Photo-initiator | Absorption Range (nm) | $\lambda_{\max}$ (nm) | Molar extinction coefficient at $\lambda_{\max}$ ( $\text{L}\cdot\text{mol}^{-1}\cdot\text{cm}^{-1}$ ) |
|-----------------|-----------------------|-----------------------|--|
| Camphorquinone  | 400-500               | 470                   | $\sim 35$  |
| Lucirin TPO     | 300-430               | 381                   | $\sim 550$   |
| Igracure        | 300-440               | 370                   | $\sim 300$   |

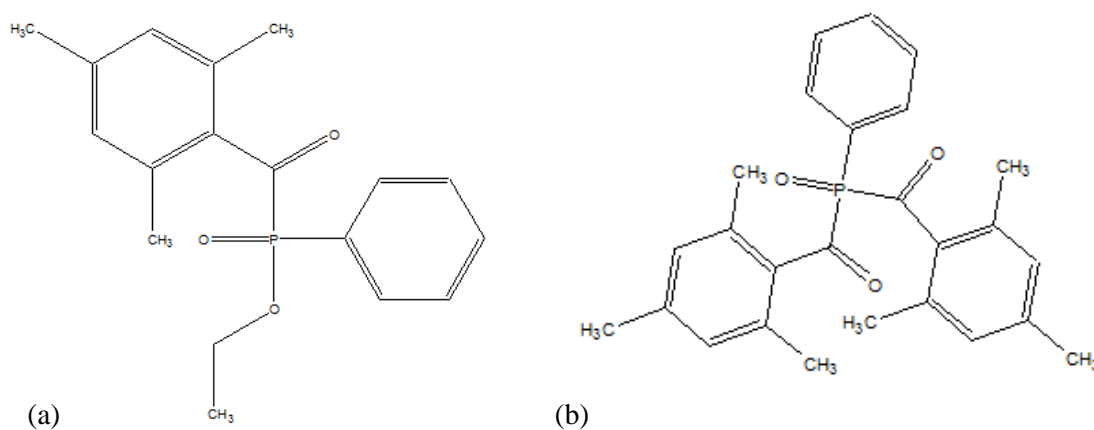


**Figure 1.5.** Chemical structures of Acyl phosphines oxide photo-initiator species (a) Lucirin TPO and (b) Igracure 819.

### 1.2.4 Silane Coupling Agents

Quartz was initially used as a material for filler particles to be combined with methyl methacrylate dental RBCs in the 1930s, however, composites still demonstrated poor mechanical and wear properties. This was partly attributed to poor adhesion between the contiguous resin matrix and the dispersed filler particles. A solution to this problem was to promote adhesion between the two phases through the use of a coupling agent. Coupling agents primarily provide a functional interface for covalent bonding between filler and the resin matrix, but also reduce the surface energy of the filler particle to enhance dispersion of the filler particles throughout the matrix. By 1962 Bowen had prepared composites combining a dimethacrylate resin matrix with a silanised quartz powder [113]. Organosilanes are a class of organic silicon compounds that have a hydrolytically active silicon based functional group and several generic chemical structures for these compounds are illustrated in Figure 1.6. In methacrylate resin based composites, the R group typically represents either a methacrylate or epoxy functional group to achieve adhesion between the resin and filler phases [53, 55, 144]. This coupling has been shown to limit the degradation [145] of the RBC by protecting the filler against fracture [146] and improving the transition and distribution of stresses from the resin matrix to the stronger filler particles[147]. The most widely used organosilane coupling agent for silica/quartz based filler/resin composites is MPTMS (3-Mercaptopropyl)trimethoxysilane) [148, 149] (Figure 1.7). MPTMS is capable of bonding with the resin matrix through covalent carbon-carbon bonds in the methacrylate functional groups [55, 150], bonding with the filler by forming oxane bonds and with itself via siloxane bonds [55]. This chemistry works well when used with a silica/quartz substrate as alcoxy groups may react with the hydroxyl groups of the substrate. However, adhesion to non-silica based filler materials such as zirconia is not satisfactory. Currently, tribological silica coating techniques are used to form a silica layer covering the surface of the filler particle. This provides a substrate to which the silane coupling agent can react chemically to form an oxane bond [55]. More recently, phosphate esters have been used as an alternative to tribological coatings [151-153] due to their ability to bond

directly to non-silica based filler [154-156] in addition to increased hydrolytic stability in comparison to conventional organosilanes [156].

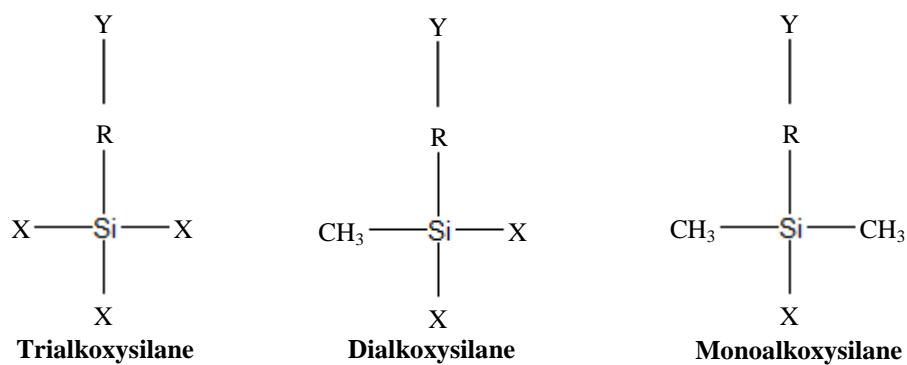


**Figure 1.6.** Generic structures of functional organosilanes.

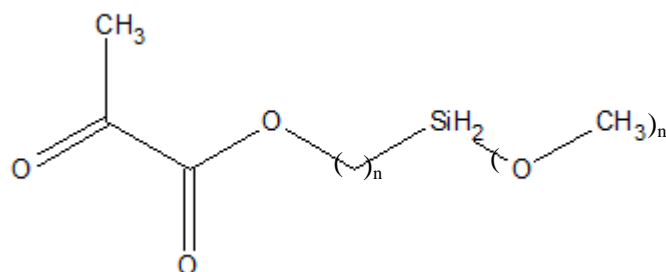


**Figure 1.7.** Chemical structure of (3-Mercaptopropyl)trimethoxysilane (MPTMS).

### 1.3 Photo-polymerisation Kinetics

The process of photo-polymerisation can be simplistically described as being comprised of three distinct kinetic phases; initiation, propagation and termination. Although these processes are statistically sequential, their short reaction time means that they will occur in a quasi-simultaneous fashion i.e. they will co-exist. This results in complex reaction kinetics which are highly susceptible to both resin formulation [35] and polymerisation rate [18] which ultimately govern system mobility. The process begins with the absorption of an impinging photon by a photo-initiator, as described in section 1.2.3 for the relevant photo-initiator, to produce primary radical species (equation 1.1).



Here,  $I$  represents the initiator species,  $h$  is Planck's constant,  $\nu$  is the frequency of the impinging photon and  $R\bullet$  denotes primary radical species. The initiation phase is characterised by the production of radicals and the subsequent opening of vinyl double bonds of the unreacted monomers (equation 1.2). Specifically for di-methacrylate monomers, the radical attacks the double covalently bonded carbon-carbon bond connecting the methylene to the methacrylate functional end group [157]. The incoming radical replaces the existing pi bond by pairing with its electron to form a more stable configuration with the carbon atom. This leaves the remaining sigma bond intact whilst the remaining electron returns to the other carbon [158]. This is the conversion of a double to single covalently bonded carbon, transforming the molecule into a reactive radical. The end of this macro-radical contains a pendant electron which is known as a growth centre and becomes the point of addition for further monomers [159].



It is this conversion process which defines the growth of subsequent polymer chains, termed the propagation phase. The opening of double vinyl bonds is an essential mechanism which is repeated throughout the system to achieve chain growth. The forming polymer can grow

linearly via the addition of individual monomers but may also achieve a three dimensional structure by reacting with another polymer chain, creating a cross link (Figure 1.8).



**Figure 1.8.** A simplified schematic showing the formation of cross-links between neighbouring polymer chains to form a three dimensional structure.

The beginning of the polymerisation reaction is defined by the reaction kinetics of radicals and macro-radicals. Initially, conversion and cross-linking levels are low such that the concentration of free radicals is approximately constant i.e. there is equilibrium between the production and termination of radicals. However, this condition is only true when conversion does not exceed approximately 10 % [160]. The relatively low initial viscosity allows for free radicals to react with each other to form a stable covalent link through bimolecular termination reactions which reduces their numbers and prevents the rapid onset of new growth centres. However, this condition is chemically controlled and therefore is only valid for a very low degree of conversion (~10%) [160]. As the propagation phase continues the DC and extent of cross-linkage inevitably increases, with the resultant polymer chains becoming sufficiently long to demonstrate flexibility to rotate and twist [157] which increases their efficacy to form cross-links. To a lesser extent this also allows for the polymer chains to loop back on to themselves (primary cyclisation) [159] although this only increases the system viscosity and does not contribute towards any desirable network properties e.g. strength and rigidity [159]. The gelation point is defined by the limitation of the free flow of macro-radicals relative to the connected structures. Thus, the diffusivity of the macro-radicals is lower as the activation

energy required for diffusion is higher i.e. termination becomes diffusion limited. Ultimately, this imposes mobility restrictions on radicals located on large growing polymer chains, although small monomer molecules and radicals may still diffuse through the network to proliferate new growth centres [161]. The free radical concentration increases and as a consequence the rate of polymerisation also increases, called *auto-acceleration* [162, 163]. This correlates to a rapid DC through linear growth and cross-linking to form a semi-infinite network. Inevitably, as the degree of conversion reaches a critical limit and the viscosity continues to increase, diffusion for even single monomers will become extremely difficult. Consequently, the system will go through *auto-deceleration* – a rapid decrease in the polymerisation rate [22]. This coincides with a second change of state, from rubber to glass called vitrification. For vitrification to occur, the reaction temperature of the system must match the glass transition temperature whilst simultaneously minimising the free volume between linked polymer chains for molecular motions. This represents an inhibition of diffusion and limits the system reactivity plateaus such that 100% conversion is impossible [164]. Vitrification of the polymer network consequently limits the degree of conversion of typical resins to approximately 75% with a few exceptions achieving only 55% conversion [52, 165-168], with 90 to 95% of the total conversion achieved at this point. It is common however, for additional conversion to take place for several weeks after in the absence of irradiation in what is known as post-cure [18]. The phase change plays an important role in trapping radicals (monomolecular termination) within the polymer network [169], although this is not a permanent form of termination. The trapped radicals remain active and variation in external conditions (temperature change, swelling), common in oral environments, confer additional mobility and therefore allow for continued polymerisation [170-172]. Other active species such as unreacted free monomers, pendent double bonds and traces of photo-initiator remain isolated within the vitrified network which will impact on final bio/mechanical properties. The degree of conversion and the rate of polymerisation are highly susceptible to photo-polymerisation variables, such as the light intensity and the irradiation time used and these factors can significantly impact on mechanical properties and the clinical performance of the RBC filling [173].

## 1.4 Origins of Polymerisation Shrinkage

Polymerisation shrinkage is the most significant constraint associated with dental resins, impacting on the degree of conversion, mechanical strength and ultimately the clinical lifetime of the restoration [174-176]. Shrinkage is an intrinsic consequence of the polymerisation process and expresses itself in two forms throughout the reaction, both originating from a reduction in the free volume [157]. The free volume can be visualised as the interstitial space between neighbouring monomers and forming polymer chains i.e. the difference between the bulk volume of the liquid and the actual total volume of the molecules [157]. At the beginning of the polymerisation reaction each individual monomer has its own thermal motions which allow it to sweep out an effective volume much larger than its own (Figure 1.8).

(a)



(b)

**Figure 1.9.** The thermal motions of (a) individual monomers as represented by a Leonard-Jones sphere and (b) a forming polymer chain. Polymerisation reduces the available free volume [28].

Unbound, the monomers have a large degree of rotational and translational freedom (Figure 1.9, a), which can be ascribed to the ratio of thermal energy to molecular mass. However, as polymerisation advances and the monomers join to form polymer chains, the subsequent motions of these chains become constrained [177]. Specifically, the effective volume for most of the chain is restricted to being swept out over an angle of  $2\pi$  perpendicular to the axis of chain propagation. Between successive monomer additions there is continually a monomer residue (a mer) at the end of the chain i.e. it is unattached at the furthest end [157]. This mer has a reduced effective volume compared to a free monomer, but is still free to sweep out in a conical ‘thrashing circle’ (Figure 1.9, b). Hence, for each successive bond formed the effective free volume is reduced relative to that of the initial monomer phase of the resin. Additionally, for each bond that is formed the exchange of double to single covalent bonds alters the inter-atomic bond distance between monomers (deviating from the initial van der Waals interaction distance to  $1.54 \text{ \AA}$ ) [178], growing the forming polymer chain and increasing the length per unit of addition and further reducing the free volume. This effect is compounded by the formation of cross-links which increase the density of single covalent bonds and hence chain length [157]. Therefore, the progression of polymerisation shrinkage is linked with the degree of conversion. Achieving a critical level of cure will inevitably lead to volumetric shrinkage and subsequent contractive stresses [174].

## 1.5 Determinants of Polymer Formation

### 1.5.1 Effects of Monomer Structure on Polymer Formation

It is known that the molecular weight of a dimethacrylate monomer impacts on the terminal degree of conversion and polymerisation shrinkage. A lower molecular weight monomer, for equivalent weight fractions, will have a greater concentration of methacrylate functional end groups containing polymerisable double bonds in comparison to a larger monomer. Homo-polymerisations of Bis-GMA and an ethylene glycol derivative diluent such as TEGDMA demonstrate terminal conversion values of approximately 30 % and 70 % respectively. However the polymerisation kinetics of monomer homo and co-monomer polymerisations are more complex and are affected by monomer structure and functionality. Cook *et al* [44] used dimethacrylate ethoxylated derivatives of Bisphenol A incorporating increasing units of ethylene glycol situated between the central aromatic phenol groups and the methacrylate functional end groups to alter monomer flexibility and correlate this to terminal conversion. It was shown that greater spacer group flexibility conferred increased terminal conversion. However, conversion values from Bis-GMA homo-polymerisations did not follow this behaviour. This deviation was attributed to the presence of hydroxyl groups that form strong hydrogen bonds which impair mobility of the monomer in the forming network [179], which decreases as a function of monomer to polymer conversion. Strong hydrogen bonds are also reported to impact on the polymerisation kinetics of Bis-GMA [35, 179]. It has been demonstrated that the reduction in monomer mobility promotes rapid onset of diffusion controlled propagation and advances reaction diffusion termination pathways. This drives earlier auto-acceleration through at low conversions ~ 6% [35, 180, 181]. Conversely, Lovell *et al* reported that for ethylene glycol diluent derivatives, the flexible aliphatic structure and the inability to form hydrogen bonds affords greater monomer mobility and extends the time available for segmental motions of macro radicals which delays the onset of auto-acceleration [180]. This allows a TEGDMA homo-polymerisation to reach a greater value of terminal

conversion in comparison to hydroxylated monomers. Despite the delay in auto-acceleration, both Bis-GMA and TEGDMA display similar peak polymerisation rates when polymerised under identical conditions.

Monomer chemical structure and the relative proportion of diluent have been shown to influence polymer network architecture. Molecular simulations by Cook and Bowman [159] demonstrated that increasing the content of diluent raises the likelihood of microgel formation. TEGDMA has a greater potential for primary and secondary cyclisation due to its flexible aliphatic backbone and ether linkages [182] which act as hydrogen bond acceptors. By comparison, the rotationally restricted phenol groups at the centre of Bis-GMA forbid the formation of intra-molecular hydrogen bonds [159]. Although cyclisation contributes to monomer to polymer conversion, it increases the rotational mobility of cross-links and reactive pendent groups occupying more free volume, producing regions of heterogeneity [183, 184] within the polymer network and lowering the packing density of the polymer i.e. reducing the amount of volumetric shrinkage [185, 186]. However, modifications to free volume via cyclisation in systems incorporating a high proportion of TEGDMA do not necessarily offset increased volumetric shrinkage conferred by greater conversion ascribe to a greater concentration of polymerizable functional groups. Conversely, it is reported that the planar structure of Bis-GMA promotes pi – pi stacking [186] of the aromatic groups which affords more efficient packing.

### 1.5.2 Effects of Light Curing Protocols on Polymer Formation

A prerequisite for the photo-polymerisation of RBCs is that the emission spectrum of the light curing unit has a high degree of overlap with the absorption spectra of the photo-initiator species. Ikemura *et al* [139] investigated the degree of conversion of CQ and TPO initiated RBC systems for a fixed curing regime with a halogen LCU. The emission spectra of halogen units cover the visible region of 400 – 500 nm corresponding to the absorption region of CQ. It was reported that under identical curing regimens, the two systems achieved very similar degrees of conversion despite it being acknowledged that TPO is a more efficient photo-initiator than CQ and achieves greater terminal conversion [140] and maximum polymerisation rate [187, 188], typically by an order of magnitude [189] when the emission spectrum of the activating light source is appropriately matched.

Studies have shown that the degree of monomer to polymer conversion of the resin phase of an RBC may be approximated from the product of the exposure time to the activating light source and the irradiance intensity [190]. Similarly, it is well established that the photo-polymerisation rate is proportional to the square root of the light intensity [191], given that more photons per second are impinging on the photo-initiator species. It should be noted that the polymerisation rate is not influenced solely by the number of interacting photons. Temperature increases attributed to either heat from the light source or indeed the exotherm from polymerisation will likely increase the mobility of the system [192]. It has been suggested that this effect may delay auto-acceleration and lead to an Arrhenius-type reaction dependence, increasing polymerization rate and degree of conversion [193].

However, several studies have indicated that the evolution and formation of the polymer network is highly sensitive to the polymerisation rate and that the dynamics of this formation will influence the magnitude and generation rate of internal stresses [194, 195] and polymerisation shrinkage [196]. Supporting studies by Lu *et al* (2004) [197] and Braga *et al* (2002) [174] have shown that greater polymerisation stresses are accrued when polymerisation

is accelerated to greater terminal degrees of conversion and that stress relaxation at macroscopic length scales is significantly reduced or negligible at these rates. It has been proposed that a viscous flow [198, 199] model within the polymer is the most likely mechanism for stress relief in these systems. At lower degrees of conversion, during early polymerisation, primary cyclisation and chain growth dominate over cross-linking and slower rates of polymerisation allow for more time for the microscopic rearrangement of polymer chains [200] and subsequent viscous flow to relieve stresses. Conversely, at faster rates gelation occurs much earlier and time for polymer chain rearrangement is significantly reduced leading to a rigid contraction [201].

A subsequent combined experimental and theoretical approach to understand the rate dependent network formation of a Bis-GMA/TEGDMA model system was reported by Sarkar *et al* 2017 [202]. The experimental aspect of this study simultaneously measured the degree of conversion, temperature change, and observed deformation of a Bis-GMA/TEGDMA system irradiated at light intensities of 100, 500 and 2000 mWcm<sup>-2</sup> and calculated the observed stress during polymerization via a cantilever system as well as the relaxation time of the system. It was found that the conversion values associated with a relaxation time of 1 s were typically higher for high light intensity/fast polymerisation regimes. This research also suggested that increases in the relaxation time is delayed by accelerating polymerisation through high light intensity curing, which was explained in terms of network clustering. Faster polymerisation may result in greater clustering and jamming of growing chains, preventing efficient relaxation and producing a more rigid network than would be observed at lower rates. The theoretical approach of this study focussed on predicting the global cross-link density and local spatial distribution, using a cubic lattice model as described by Camboni *et al* [203]. Accelerating polymerisation increased the density of cross-links, but the cross-links showed significantly greater clustering in comparison to low light intensity photo-polymerisation.

More recently, alternative irradiation modes have been employed to reduce the magnitude of polymerisation stresses. Soft start curing protocols involve the initial use of low light intensities

before gradually increasing the intensity as polymerisation progresses. This approach is proposed to delay the onset of gelation and allow more time for viscous flow, to reduce the build-up of stress. The efficacy of this curing regimen with respect to reducing the generation of polymerisation stress and shrinkage and the resultant polymer network that is formed is still under dispute. Much research suggests that soft start curing regimes reduce shrinkage stresses and volumetric shrinkage through a reduction of the cross-link density [204, 205]. Reduced cross-linking in ‘soft – cured’ RBCs has been demonstrated indirectly through ethanol degradation studies [206-208], despite equivalent degrees of conversion to continuous intensity photo-polymerisation regimes.

### 1.5.3 Exposure Reciprocity

The concept of exposure reciprocity for photo-chemical reactions was first introduced in the field of photography by Bunsen and Roscoe in 1923 [209], where darkening of photographic film was a function of the total energy exposure dose. The concept therefore states that a given property of a photo-active material is dependent only on the total dose, which is equivalent to the product of the exposure time and the intensity of the impinging irradiation, and is independent of the values of exposure time and irradiation intensity and is expressed as

$$It = C \quad (1.3)$$

where  $I$  and  $t$  correspond to the irradiation intensity and exposure time respectively, whilst  $C$  denotes the constant exposure energy dose. This rationale has been applied to photo-activated dental RBCs to predict monomer to polymer conversion for different photo-curing regimens and from which mechanical properties have been correlated. Currently most light curing protocols require 40 seconds or more of specified light wavelength exposure at intensities from 400 to 800mW/cm<sup>2</sup> per increment of material (up to 10 increments may be required per filling), to achieve the desired conversion of monomer to polymer [15, 16], Recently however, the advent of high powered light sources including LEDs and argon ion lasers have promoted rapid photo-polymerisation through the combination of higher light intensities and shorter exposures to reduce chair side operating times. It is reported that photo-polymerisation may be achieved for a RBC with an exposure time of three seconds [16]. Several studies have investigated the validity of the exposure reciprocity law to these materials with respect to monomer to polymer conversion [210-212] modulus [168], flexural strength and hardness [213]. It has been shown that equivalent energy doses may produce very similar terminal degrees of conversion [211, 214], providing support for a total energy concept. Similarly, studies investigating the mechanical properties of RBCs have shown that equivalent fracture toughness [20], flexural strength [20], modulus and hardness are obtained for photo-polymerisation regimens with varying irradiances but with equal total energy doses.

However, numerous studies report contradicting findings and it is widely reported that accelerating polymerisation using high intensity light activation can impact on the tensile strength, toughness, hardness and degree of polymerisation shrinkage of these materials [19, 20, 215]. Peutzfeld and Assmussen demonstrated that greater irradiation intensities for equivalent energy doses, i.e. high energy densities illumination conferred reduced degree of conversion [23]. Additionally, a study by Musanje and Darvell [216] showed that for commercial composites a reciprocal relationship was not observed for most samples with respect to elastic modulus and flexural strength. It was suggested that discrepancies in the exposure reciprocity law for mechanical properties were influenced by the material composition and curing regimen. This is supported by the findings of Dewaele *et al* [24] who found that a parabolic relationship exists between the reaction rate, which had been controlled by different energy densities, and DC, volumetric shrinkage, elastic modulus and glass transition temperature. Hence, it is likely that material composition and photo-polymerisation variables influence the conditions for reciprocity. Work by Hadis *et al* [217] has suggested that exposure reciprocity is an approximation for the behaviour of co-polymerisation and is only valid within certain boundary conditions with respect to system viscosity, irradiance and photo-initiator chemistry and that exceeding these limits may lead to a saturation point for certain material properties [212]. It has been shown that exposure reciprocity is only observed for monomer to polymer conversion when the resin viscosity is relatively high. Conversely, at lower viscosities as the resin becomes more fluid, equivalent conversion was not seen when the energy dose was conserved. This was attributed to a higher system mobility at lower viscosities which affords greater bimolecular termination during an earlier point in polymerisation. Consequently, fewer radical growth centres are generated and conversion is reduced in comparison to a lower intensity, longer exposure time curing regime with an equivalent total energy dose.

Investigations have also shown that exposure reciprocity only exists within certain ranges for irradiance intensity and exposure time. High intensity irradiance coupled with relatively short exposure times have been shown to confer reduced conversion, flexural strength and modulus in

comparison to longer exposure times with lower irradiances. This effect has been explained through radical entrapment [218], polymer chain length and cross-link density. It has been suggested that at lower irradiances, a greater proportion of radicals are trapped within the network as opposed to undergoing bimolecular termination at higher irradiances, which allowing for post cure effects will produce a more converted polymer. More rapid polymerisation may also produce a greater number of growing polymer chains, but with a reduced chain length, which may explain reduced flexural strength and modulus at higher irradiance curing regimens [23].

However, it must be acknowledged that the effects of light intensity and exposure times on photo-polymerisation kinetics are linked to the properties of the photo-initiator species, including the quantum efficiency [136], absorption spectra [141] and molar absorptivity [19]. At high irradiances, photo-initiators with a low molar absorptivity and quantum yield i.e. Camphorquinone may display an irradiance threshold, whereby no additional radicals are produced for increasing light intensities implying that high irradiance has effectively saturated the photo-initiator. Consequently, no additional improvements on reaction rate or terminal conversion are seen.

Even if reciprocity is observed in some properties of the RBC, it is seldom ubiquitous for all physico-chemical properties and the expectation for exposure reciprocity to be valid for these dental materials may be considered to be unreasonable. Numerical kinetic models [159, 219, 220] have been used to understand photo-polymerisation mechanisms for different combinations of irradiation intensity and exposure time. Modelling approaches have shown that only first order reaction process will obey exposure reciprocity. Therefore, the same number of radicals may be liberated from the primary reaction with photo-initiator species for different combinations of irradiance intensity and exposure time however, but secondary processes involving the propagation of these free radicals throughout the polymer network are non-linear and will not follow exposure reciprocity. Instead, properties including terminal

conversion, polymerisation shrinkage and shrinkage rate are dependent on the polymerisation rate as a function of the irradiation intensity.

## 1.6 Characterisation Techniques

This section describes characterisation techniques which are routinely applied to understand the structure of dental RBCs as a function of photo-polymerisation variables and suggests alternative methods which can provide useful complimentary structural information.

### 1.6.1 Fourier Transform Infrared Spectroscopy

Infrared radiation (IR) describes the portion of the electromagnetic spectrum covering the broadband wavelength region from approximately 1-1000 micrometers (1.24 meV). The IR region may be considered to be split into three sections; the near-, mid- and far- IR with respect to the visible part of the spectrum. Several types of excitation may occur when matter is perturbed by radiation with wavelengths corresponding to this region including molecular vibrations which are induced in the chemical bonds. Covalent chemical bonds may be treated simplistically as harmonic oscillators when perturbed, however these vibrational modes occur only if excitation induces a dynamical dipole moment. This selection rule is obtained from Fermi's Golden rule to give the transition rate as;

$$R_{i \rightarrow f} = \frac{2\pi}{\hbar} |\langle f^0 | H' | i^0 \rangle|^2 \delta(E_f^0 - E_i^0 - \hbar\omega) \quad (1.4)$$

Here,  $R_{i \rightarrow f}$  is the transition rate,  $f_0$  and  $i^0$  are the unperturbed initial and final states,  $H'$  is the interaction Hamiltonian,  $E_f$  and  $E_i$  are the final and initial energies for the  $f_0$  and  $i_0$  states and  $\hbar$  is the reduced Planck's constant. The oscillator or bond will therefore only absorb photons whose frequency matches the resonant frequency of a given vibrational mode. Vibrational modes include bond stretching, scissoring, rocking, wagging and twisting and absorption at specific vibrational frequencies can be used to identify functional groups within a molecule.

The modern application of IR spectroscopic techniques is Fourier Transform Infra-red spectroscopy (FTIR). In practice this equipment uses a collimated white light source which is directed into a Michelson interferometer. The light is split into perpendicular directions towards

either a fixed mirror or a moving mirror, which is then reflected back to the beam splitter. Ideally, half of this light is transmitted and half is reflected at the beam splitter, resulting in one beam passing to the detector and the second back to the source. The position of the moving mirror is varied to introduce optical path differences with respect to wave interference. Hence, when the two mirrors are equidistance from the beam splitter the path difference is zero and all wavelengths are in phase. This produces strong constructive interference and a maxima in the light intensity as a function of the optical path difference, known as an interferogram. As the mirror position is altered the optical path difference also changes the intensity of the light varies. Each individual spectral component contributes to this signal a single sinusoid with a frequency inversely proportional to its wavelength. The use of white light allows for the simultaneous measurement of all vibrational modes in the sample, producing a complex interferogram form. The interferogram is therefore Fourier transformed to obtain spectral information in the frequency domain i.e. wavenumber.

Within the context of dental RBCs, FTIR is routinely used to quantify the degree of monomer to polymer conversion using the vibrational signal corresponding to the polymerisable aliphatic  $\text{=CH}_2$  group. Initial measurements utilised the mid-IR region to monitor the decrease in the aliphatic carbon carbon double bond located at  $1637\text{ cm}^{-1}$  before and after polymerisation. Unfortunately, mid-IR measurements are limited to thin samples, typically  $30\text{ }\mu\text{m}$  thickness [221], due to high attenuation which is not ideal given that clinically relevant test specimens usually have a thickness of 1 mm. Thin samples inevitably lead to small variations in sample thickness which will impact on the amplitude of. Internal reference bands are therefore used to normalise for differences in sample thickness. Aromatic groups are typically used for resin blends containing Bis-GMA, located at  $1608$  and  $1583\text{ cm}^{-1}$  for the stretching and twisting modes respectively, whilst resin blends containing UDMA use the N-H vibration. It has previously been suggested that the carbonyl band may be used for normalisation however, the amplitude and position of this peak vary as a function conversion as the bond strength changes

[179]. Mid-IR methods may be applied in transmission [222, 223], reflection and absorption [12] sample geometries.

More recently near infra-red techniques have been employed to measure conversion in samples with thicknesses of clinical relevance. This method uses an overtone of the aliphatic stretching frequency located at  $6170\text{ cm}^{-1}$ , which represents the remaining unreacted =C-H group. The degree of monomer to polymer conversion is quantified from the decrease in the amplitude or integrated amplitude during polymerisation. The NIR method has the advantage of increased sensitivity which affords the measurement of thicker samples (up to 10 mm) without the need for a reference absorption band as the sample thickness can be standardised more easily at thicknesses  $\sim 1\text{ mm}$  or greater. Additionally, the increased sensitivity allows for time resolved studies which can be used to determine curing kinetics, such as auto-acceleration, rate maximum and time to reach maximum rates of polymerisation.

## 1.6.2 Alternative Characterisation Techniques

### 1.6.2.1 Thermal Characterisation

The premise of differential scanning heat calorimetry (DSC) is that when a material undergoes a phase transition or a second order reorganisation of its structure, there is a corresponding change of heat flow either in to or out of the system. In practice this works using two metal plates where one acts as a reference whilst the other is in contact with the sample of interest. Both plates are heated at a constant rate with equivalent temperatures at each thermal increment. Due to the extra flow of heat into the sample, more heat is required to maintain an equivalent temperature in the sample plate in comparison to the reference. The difference in heat is used calculate the specific heat capacity as a function of temperature. From this the glass transition temperature may be identified from changes in the specific heat indicative of changes in free volume. With regards to dental RBCs this has been used to quantify differences in  $T_g$  as a function of monomer chemistry [35], photo-initiator chemistry and photo-curing regimen [224]. This application involves measuring heat flow in to the sample but may also be used to measure exotherm as well. This is important as polymerisation is an exothermic reaction and therefore the degree of polymerisation may be approximated from the heat flow out of the system under the assumption that heat produced during the reaction is proportional to the number of C=C bonds converted to C-C under isothermal conditions [225].

Similar thermal characterisation techniques include differential thermal analysis (DTA) and thermo-mechanical analysis (TMA), from which similar information may be obtained. Differential thermal analysis is a related technique to DSC, but instead of relying on differences in energy required to maintain the sample and reference at an identical temperature, differences in temperature between the sample and reference are used to gain knowledge of the microstructure. DTA requires the heating of a test specimen and of a reference material, typically Alumina, under identical heating conditions. Differences in temperature between the sample and the reference are plotted as a function of temperature and changes of temperature or

temperature gradients may represent phase changes or reorganisation of the polymer microstructure. Similar information may be obtained from this method as from DSC including T<sub>g</sub>, DC and R<sub>p</sub> [74, 226, 227]. Thermal mechanical analysis measures volumetric changes in the bulk material as a function of the sample temperature. This allows for the calculation of the coefficient of thermal expansion and T<sub>g</sub> [228]. Studies have used this technique to also measure T<sub>g</sub>, whilst some authors have used it to study post-cure shrinkage as a function of time [229] or applied heat [230]. The usefulness of this technique towards the study of post cure behaviour as a function of time though is limited as heating the resin sample will increase the mobility of any trapped radicals within the system, increasing conversion [170, 231] and will likely modify the polymer structure.

#### **1.6.2.2 Physical Characterisation**

Indentation tests are often used to characterise the hardness, or the resistance to permanent deformation under a compressive load, for dental RBCs [232-235]. The two main techniques are the Vickers and Knoop hardness tests. The techniques use a square and rectangular based diamond pyramid respectively, which due to its own hardness is highly resistant to deformation, which is pressed into the sample surface. The indentation is observed through a microscope and its dimensions are measured to calculate the surface area of the impression. The hardness number is calculated from the ratio of force to the surface area of the impression. The two techniques are similar although Vickers tests are usually used for thick bulk samples whilst Knoop test are often applied to thin films. FTIR is less sensitive to detecting small changes in DC [236] but can be evaluated using Vickers or Knoop methods [237] to profile the depth of cure [238]. These techniques however are limited by the uncertainty introduced by measuring the impression using a microscope.

### 1.6.3 Motivation for Synchrotron X-ray and Neutron Based Techniques

Infra-red, thermal and physical-mechanical based techniques have played an important role in characterising, understanding and developing dental composite materials. However, the field has become quite dependent on these methods, particularly the use of FTIR to quantify conversion. Complex materials though can seldom, if ever be completely understood at atomic length scales using one technique and using the same techniques will only yield similar results. X-ray scattering methods are sometimes used to characterise dental RBC materials, to identify the presence of amorphous phases [239] whilst structural interpretation of the resin matrix has not been explored further. This is surprising as scattering techniques provide structural information with atomic resolution. Lab based techniques do not allow for time resolved structural measurements of photo-polymerised polymers due to insufficient flux, but this can be easily circumvented by the use of synchrotron X-ray sources to provide a more complete understanding of the structure.

Synchrotron small X-ray and neutron scattering (SAXS and SANS respectively) methods have been used extensively over the past 40 years to characterise the structure of polymers under static and dynamic conditions [240] for a range of chemistries [241-245]. The structure of epoxy resins, which have some similar structural features to common dimethacrylate dental polymers, have been widely characterised using X-ray scattering methods [246, 247] during setting. Methacrylate based polymers have also been studied using X-ray and neutrons since the 1970s [248]. More recently, Peng *et al* [25] used SAXS to investigate structural transitions of methacrylate terminated siloxanes during polymerisation, whilst Genix *et al* [26] used a combination of SAXS and SANS to characterise kinetic changes in the structure of poly(ethyl methacrylate) under thermal load to elucidate chain dynamics below and above the glass transition temperature. Given that X-ray and neutron scattering are routinely used in the field of polymer research, it is surprising that these techniques are seldom applied to the study of polymer based dental materials [239] including RBCs. Application of these techniques therefore has the potential to provide useful complimentary structural information not available through

conventional laboratory based characterisation techniques. In section 1.7 the theory and application of X-ray and neutron scattering techniques is outlined with regards to polymeric systems with similar structures to dimethacrylates used for the formulation of dental RBCs

## **1.7 X-ray and Neutron Scattering Techniques**

### **1.7.1 Scattering Theory**

#### **1.7.1.1 Scattering Cross-Section**

Prior to the examination of the theory of X-ray scattering (SAXS) by electrons in a solid, it is necessary to define the scattering cross-section. For a monochromatic beam of X-rays impinging on a sample containing  $N$  atoms (to be considered as individual scattering centres), the total scattering cross-section is given as [249];

$$\sigma = \frac{N_s}{N\Phi} \quad (1.5)$$

Where  $N_s$  is the number of X-rays scattered per unit time and  $\Phi$  is the flux of the impinging X-rays. In the case of scattering experiments however, it is the differential scattering cross-section that is measured describing the scattering of X-rays into a solid angle  $d\Omega$  per unit time,

$$\frac{d\sigma}{d\Omega} = \frac{N'_s}{N\Phi d\Omega}, \quad (1.6)$$

Here  $N'_s$  represents the number of X-rays scattered into a solid angle of  $d\Omega$ . The scattering process of X-rays is shown schematically in Figure 1.10.



**Figure 1.10.** The scattering of an incident X-ray from a given sample into the solid angle,  $d\Omega$  in the direction of  $\theta$  per unit time.

### 1.7.1.2 Ideal Elastic Scattering

The scattering of either an X-ray photon or a neutron particle may be described by the change in the energy and momentum of the system. Consider an impinging X-ray with an initial wave vector ( $k_i$ ), angular frequency ( $\omega_i$ ) and energy ( $E_i$ ) interacting with a single point scatterer. Prior to the scattering incident the X-rays are coherent and in phase, but are subsequently scattered through an angle of  $2\theta$  with an outgoing wave vector ( $k_f$ ) and energy ( $E_f$ ). Each scattering event therefore represents an exchange in energy and momentum which can be summarised as;

$$\hbar\omega = E_0 - E_f \quad (1.7)$$

$$\hbar\mathbf{Q} = \hbar\mathbf{k}_i - \hbar\mathbf{k}_f \quad (1.8)$$

Equations (3.3) and (3.4) represent the transfer of energy and momentum for elastic and inelastic scattering events [250]. For the ideal case of elastic scattering, when no energy is lost in the interaction between the X-rays and sample,  $\hbar\omega = 0$ . Energy may be defined as

$$E_i = \hbar c |\mathbf{k}_i| \quad (1.9)$$

which dictates that for an elastic scattering event the modulus of the initial and final wavevector must be equivalent.

$$|\mathbf{k}_i| = |\mathbf{k}_f| = \frac{2\pi}{\lambda} \quad (1.10)$$

The wave vector transfer  $\mathbf{Q}$  may be obtained from a vector diagram of the scattering interaction, where an incident particle is deflected through an angle of  $2\theta$ . Each side of the isosceles triangle has a length of  $2\pi/\lambda$ , with the difference between the incident and scattered wave vectors being;

$$\mathbf{k} = \mathbf{k}_i - \mathbf{k}_f = \mathbf{Q} \quad (1.11)$$

where  $\mathbf{Q}$  is the momentum transfer vector. Using a standard vector identity, the magnitude of this momentum transfer can be obtained.

$$\frac{|\mathbf{Q}|}{2} = |\mathbf{k}_i| \sin \theta = \frac{2\pi}{\lambda} \sin \theta \quad (1.12)$$

Substituting the expression for the wave vector  $\mathbf{k}$  into equation (1.12),  $Q$  can be expressed as a function of scattering angle and incident wavelength [250];

$$Q = \frac{4\pi}{\lambda} \sin \theta \quad (1.13)$$

or

$$d = \frac{2\pi}{Q} \quad (1.14)$$

### 1.7.1.3 Scattering from a Group of Atoms

Figure 1.11 illustrates scattering from two arbitrarily placed atoms, with atom B separated from atom A, located at an arbitrary origin O, by a vector distance of  $\mathbf{r}$ . It can be seen that the impinging radiation interacts with atom A first resulting in a phase difference with scattering from atom B. If it is assumed that the scattered radiation is measured at a distance  $\mathbf{R}$  which is significantly greater than the atomic separation distance i.e.  $R \gg r$ , then the phase difference between the two outgoing wave vectors is given as,

$$\varphi = \frac{2\pi (\cos\alpha - r\cos\beta)}{\lambda} \quad (1.15)$$

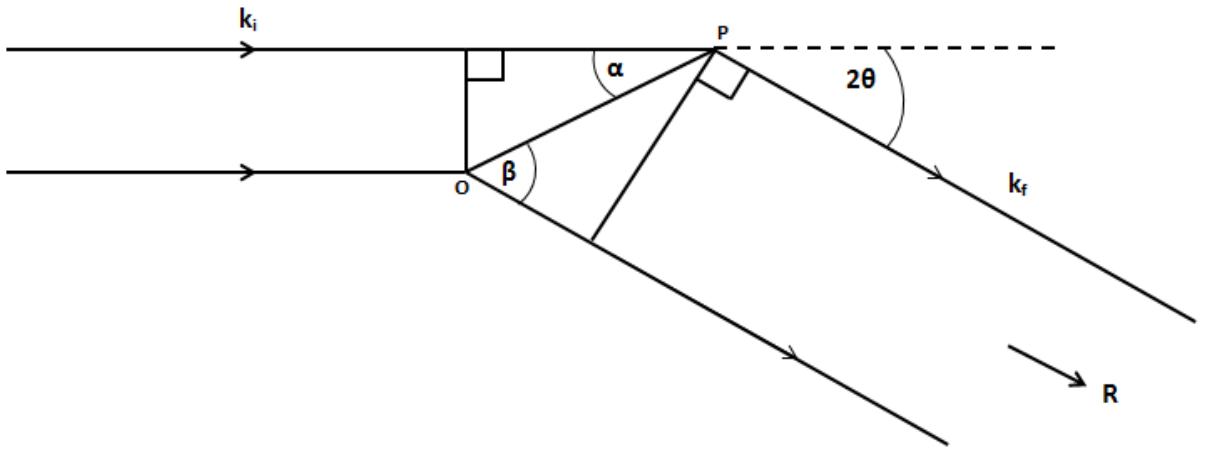


**Figure 1.11.** Schematic of scattering from a two atom system.

This expression for the phase difference can be put in to terms of momentum wave vector by substituting  $\mathbf{r} \cdot \mathbf{k}_i = (2\pi/\lambda)r \cos \alpha$  and  $\mathbf{r} \cdot \mathbf{k}_f = (2\pi/\lambda)r \cos \beta$ , to give

$$\varphi = \mathbf{r} \cdot (\mathbf{k}_i - \mathbf{k}_f) = \mathbf{r} \cdot \mathbf{Q} \quad (1.16)$$

For a scattering experiment it is also necessary to obtain the intensity of the scattered X-rays or neutrons. The intensity of scattered X-rays is dominated by the electron density of the atomic species comprising the material that is being probed. Each electron scatters the incoming beam (approximately) as a dipole proportional to the scattering length of the electron defined as;

$$b_e = \frac{e^2}{m_e c^2} \quad (1.17)$$

where  $m_e$  is the mass of an electron ( $9.11 \times 10^{-31}$ kg),  $e$  the charge of an electron ( $1.6 \times 10^{-19}$ C) and  $c$  is the speed of light ( $3 \times 10^8$  ms<sup>-1</sup>) giving the scattering length for a single electron as  $b_e = 0.282 \times 10^{-4}$  Å. When considering the contribution of a whole atom to the scattering signal, the scattering length of all the associated electrons must be summed together;

$$f(q) = \int b_e \rho(\vec{r}) d^3r \quad (1.18)$$

where  $\rho(\vec{r})$  is the charge distribution within the atom from an arbitrary reference vector. For small angles, where  $\theta$  tends towards zero, the integral reduces to  $f \approx b_e Z$  where  $Z$  is the atomic number. Therefore, the amplitude of the scattered wave for a single atom is the sum of these individual amplitudes and relative phases which is expressed as;

$$A_1(q) = \sum f(q) e^{i(\mathbf{q} \cdot \mathbf{r}_{ij})} = a(q)_i e^{i(\mathbf{q} \cdot \mathbf{r}_{ij})} \quad (1.19)$$

Equation 1.30 represents a general form for the amplitude of scattered light and may therefore represent either the X-ray form factor ( $f(Q)$ ) or the neutron scattering length ( $b$ ) as applicable. For scattering in a system of  $N$  atoms, it is necessary to sum the amplitudes over all atoms for the respective phases.

$$A_N(q) = \sum_n^N a_n(Q) e^{i\mathbf{r}_n \cdot \mathbf{Q}} \quad (1.20)$$

Classically, the intensity is the square of the amplitude, therefore multiplying equation (1.19) by its complex conjugate  $A(q)^*$  will give this value;

$$I_N(Q) = \frac{d\sigma(Q)}{d\Omega} = A_N(Q)A_N(Q)^* = \sum_p \sum_q a_p(Q) a_q(Q) e^{ir_{pq} \cdot Q} \quad (1.21)$$

Equations 1.14 and 1.21 can be applied across a range of materials (crystalline, amorphous liquid etc.) as the derivation has no dependence on atomic arrangements.

#### 1.7.1.4 Motivation for Using Neutron Scattering

Synchrotron X-rays are an extremely powerful tool, providing complimentary structural information to other conventional techniques at atomic length scales. Excellent signal to noise ratio, high  $q$  resolution and high flux allow for time resolved measurements of rapidly evolving structures. However, X-ray scattering does have some drawbacks when studying highly amorphous and in particular highly hydrogenous materials, including dimethacrylates which have been studied in this thesis. The scattering amplitude of an atomic species for impinging X-rays is proportional to the atomic number  $Z$  of the atom [251] (Figure 1.12.a). Therefore, atoms with few or even one electron i.e. hydrogen, have extremely small scattering cross-sections and therefore do not scatter X-rays well. Therefore, correlations lengths existing between two hydrogen atoms or a hydrogen atom and other atomic species are not highlighted. This is not ideal, particularly in systems where order is minimal. Neutron scattering provides a similar technique but becomes far more powerful when combined with isotopic substitution. Neutron scattering lengths vary erratically with atomic species (Figure 1.12.b) but also between isotopes [251]. Hydrogen has a large incoherent neutron scattering cross section in comparison to the coherent contribution. Consequently, heavily hydrogenated materials produce featureless neutron scattering spectra. However, the heavy isotope of hydrogen, deuterium has a larger coherent scattering cross section which allows for much stronger scattering. Hydrogen can therefore be replaced with deuterium to increase the scattering contrast in the system, whilst keeping the chemistry of the molecule mostly intact. This feature allows for specific structures in the system to be highlighted, which would otherwise not be observed using X-ray or conventional neutron scattering techniques. The main limitations though of neutron scattering is that flux is relatively low so time resolved measurements, particularly of structures that change in seconds are not possible. Neutron and X-ray scattering are for this reason used in conjunction to provide complimentary information at a range of length scales. This is particularly useful in polymer systems as this allows for the selected interrogation of polymer segment and cross-link structures.



**Figure 1.12.** (a). X-ray scattering cross-sections are proportional to the atomic number whilst (b) neutron scattering cross-sections are erratic.

## 1.8 Neutron Scattering

Neutron scattering is a related technique to traditional X-ray scattering, although there are some important differences between the two methods. X-rays are scattered by electromagnetic interactions with electrons, whilst neutrons having no charge only interact with the nucleus of an atom, which allows them to penetrate deeper into the sample. Although neutrons are particles they demonstrate wave-particle duality under the de Broglie principle and are therefore able to undergo scattering and interference effects similar to that of X-rays. For this reason a full description of neutron scattering is not given, but an overview of the salient concepts is presented.

Neutrons are scattered by a given atomic nuclei and the strength of this scattering is proportional to the scattering length  $b$ . For several atomic species including carbon and oxygen, this scattering length has real values. This is not ubiquitous for all atoms and there are cases such as hydrogen where the scattering length is complex. The scattering lengths typically depend on the component nuclei and the spin state of the nucleus-neutron combined system. If the impinging neutron has a spin of  $\frac{1}{2}$ , then the combined system may have a spin of  $I \pm \frac{1}{2}$ . Nuclei with non-zero spin have two values of the scattering length,  $b_+$  and  $b_-$ . If the nucleus has zero spin then the nucleus-neutron system can only have spin  $\frac{1}{2}$  and there is only one value of  $b$ .

Similar to X-rays, the aim of neutron scattering is to obtain the differential scattering cross section. However, for neutrons the differential scattering cross section term includes coherent and incoherent contributions. The coherent term originates from correlations between different nuclei at different times and from correlations between a single nucleus and itself at different times and provides structural information of the sample.

$$\left(\frac{d\sigma}{d\Omega}\right)_{coh} = \frac{1}{N} \left\langle \sum_{i,j=1}^N \mathbf{b}_i \mathbf{b}_j e^{i\mathbf{r}_{ij} \cdot \mathbf{Q}} \right\rangle \quad (1.22)$$

Here  $\mathbf{N}$  is the number of atoms,  $\mathbf{b}_i$  is the coherent neutron scattering length for the  $i^{\text{th}}$  atom and  $\mathbf{r}_{ij}$  represents the vector distance between atom  $i$  and  $j$ . As  $\mathbf{Q}$  tends to infinity, the differential coherent cross-section is determined by the total cross section  $\sigma_{\text{coh}}$ :

$$\left(\frac{d\sigma}{d\Omega}\right)_{\text{coh}} = \frac{1}{N} \sum_{i=1}^N \mathbf{b}_i^2 = \frac{\sigma_{\text{coh}}}{4\pi} \quad (1.23)$$

The incoherent contribution ( $\sigma_{\text{inc}}$ ) is related to fluctuations of the scattering lengths in the sample due to the variation of  $b^+$  and  $b^-$  from the mean, isotope mixing and impurities in the sample.

$$\left(\frac{d\sigma}{d\Omega}\right)_{\text{inc}} = \frac{1}{4\pi N} \sum_{i=1}^N \sigma_{\text{inc}}^i = \frac{\sigma_{\text{inc}}}{4\pi} \quad (1.24)$$

## 1.9 Summary of Key Aims

This thesis focuses on the application of advanced synchrotron (X-ray and FTIR) and neutron – based measurements to test conventional wisdom regarding materials determinants of the structure of photo-polymerised biomedical polymers and polymer composites to give a more complete understanding of these materials. These techniques enable advanced characterisation and valuable insight that is not possible through conventional laboratory based techniques. This thesis can be considered to encompass three aims within the framework of the application of these techniques.

The first and most significant aim is to characterise the polymer structure of experimental resin matrices, formulated from clinically relevant monomers, at molecular length scales as a function of the polymerisation rate. This is motivated by reported differences in material properties of similarly converted RBCs which were polymerised at different rates. Previous studies have so far only explained this in terms of radical lifetime, assumed network architecture and most commonly monomer to polymer conversion. However, little is known about the impact that polymerisation rate has on the polymer structure itself. Chapter three presents the results from time resolved *in-situ* X-ray scattering used to resolve the evolving polymer structure during photo-polymerisation for a range of reaction rates. Additionally, chapter four highlights the use of neutron scattering to understand final structural changes at cross-linking distances. Chapter five forms a preliminary investigation to understand the effect that an external perturbation such as temperature can further modify this structure.

The second aim is motivated by current limitations of conventional lab based measurements of monomer to polymer conversion in more complex systems, those representing clinically relevant systems, containing an inorganic filler fraction. Monomer to polymer conversion in filled RBCs is routinely quantified using Fourier transform infra-red (FTIR) spectroscopy. The majority of reported FTIR measurements on RBCs have provided ‘bulk’ averages [6] and fail to identify any differences in the pattern of monomer to polymer conversion at the microscale due to a combination of insufficient spatial resolution and signal to noise ratio. To understand any

microscale variability should it exist, is essential as it is the RBC microstructure which dictates many of its mechanical properties. The aim of chapter six is to identify variability in conversion at inter-particulate length scales through the use of novel synchrotron FTIR microscopy.

Finally, it is known that polymerisation stresses generated by the volumetric shrinkage of the resin matrix transfer stress to the adhered tooth complex. This has been directly demonstrated using cuspal deflection methods to measure strain and indirectly indicated through micro-leakage measurements. However, a deficiency of these techniques is that they are unable to spatially resolve strain. The aim of this study, summarised in chapter seven, was for the first time to empirically measure stresses within the enamel that had been induced by the polymerisation of dental RBCs

## 1.10 References

1. Watkins, E., et al., *USE OF ECONOMIC INSTRUMENTS AND WASTE MANAGEMENT PERFORMANCES* in *European Commission (DG ENV) 2012*, Bio Intelligence Service.
2. Bharti, R., et al., *Dental amalgam: An update*. *Journal of Conservative Dentistry : JCD*, 2010. **13**(4): p. 204-208.
3. Mackey, T.K., J.T. Contreras, and B.A. Liang, *The Minamata Convention on Mercury: Attempting to address the global controversy of dental amalgam use and mercury waste disposal*. *Science of The Total Environment*, 2014. **472**(Supplement C): p. 125-129.
4. Selin, H., *Global Environmental Law and Treaty-Making on Hazardous Substances: The Minamata Convention and Mercury Abatement*. *Global Environmental Politics*, 2014. **14**(1): p. 1-19.
5. Clifford, M.J., *Future strategies for tackling mercury pollution in the artisanal gold mining sector: Making the Minamata Convention work*. *Futures*, 2014. **62**(Part A): p. 106-112.
6. Evers, D.C., et al., *Evaluating the effectiveness of the Minamata Convention on Mercury: Principles and recommendations for next steps*. *Science of The Total Environment*, 2016. **569**(Supplement C): p. 888-903.
7. McNutt, M., *Mercury and Health*. *Science*, 2013. **341**(6153): p. 1430-1430.
8. Lynch, C.D. and N.H.F. Wilson, *Managing the phase-down of amalgam: part II. Implications for practising arrangements and lessons from Norway*. *Br Dent J*, 2013. **215**(4): p. 159-162.
9. Richardson, G.M., et al., *Mercury exposure and risks from dental amalgam in the US population, post-2000*. *Science of The Total Environment*, 2011. **409**(20): p. 4257-4268.

10. Mackey, T.K., J.T. Contreras, and B.A. Liang, *The Minamata Convention on Mercury: Attempting to address the global controversy of dental amalgam use and mercury waste disposal*. Science of The Total Environment, 2014. **472**: p. 125-129.
11. Bose-O'Reilly, S., et al., *Mercury Exposure and Children's Health*. Current problems in pediatric and adolescent health care, 2010. **40**(8): p. 186-215.
12. Stansbury, J.W. and S.H. Dickens, *Determination of double bond conversion in dental resins by near infrared spectroscopy*. Dental Materials, 2001. **17**(1): p. 71-79.
13. Dickens, S.H., et al., *Photopolymerization Kinetics of Methacrylate Dental Resins*. Macromolecules, 2003. **36**(16): p. 6043-6053.
14. Hickel, R., et al., *Longevity of occlusally-stressed restorations in posterior primary teeth*. Am J Dent, 2005. **18**(3): p. 198-211.
15. Jimenez-Planas, A., et al., *Developments in polymerization lamps*. Quintessence Int, 2008. **39**(2): p. e74-84.
16. Rueggeberg, F.A., *State-of-the-art: dental photocuring--a review*. Dent Mater, 2011. **27**(1): p. 39-52.
17. Calheiros, F.C., et al., *Influence of radiant exposure on contraction stress, degree of conversion and mechanical properties of resin composites*. Dent Mater, 2006. **22**(9): p. 799-803.
18. Stansbury, J.W., *Dimethacrylate network formation and polymer property evolution as determined by the selection of monomers and curing conditions*. Dental Materials, 2012. **28**(1): p. 13-22.
19. Ogunyinka, A., et al., *Photoinitiation chemistry affects light transmission and degree of conversion of curing experimental dental resin composites*. Dent Mater, 2007. **23**(7): p. 807-13.
20. Miyazaki, M., et al., *Effect of light exposure on fracture toughness and flexural strength of light-cured composites*. Dent Mater, 1996. **12**(6): p. 328-32.
21. Asmussen, E. and A. Peutzfeldt, *Polymerization contraction of resin composite vs. energy and power density of light-cure*. Eur J Oral Sci, 2005. **113**(5): p. 417-21.

22. Feng, L., R. Carvalho, and B.I. Suh, *Insufficient cure under the condition of high irradiance and short irradiation time*. Dent Mater, 2009. **25**(3): p. 283-9.
23. Peutzfeldt, A. and E. Asmussen, *Resin composite properties and energy density of light cure*. J Dent Res, 2005. **84**(7): p. 659-62.
24. Dewaele, M., et al., *Influence of curing protocol on selected properties of light-curing polymers: degree of conversion, volume contraction, elastic modulus, and glass transition temperature*. Dent Mater, 2009. **25**(12): p. 1576-84.
25. Peng, S., et al., *In Situ Synchrotron SAXS Study of Polymerizable Microemulsions*. Macromolecules, 2011. **44**(8): p. 3007-3015.
26. Genix, A.C., et al., *Neutron Scattering and X-ray Investigation of the Structure and Dynamics of Poly(ethyl methacrylate)*. Macromolecules, 2012. **45**(5): p. 2522-2536.
27. *Comprehensive Composite Materials*, C. Zweben, Editor. 2000, Wiley. p. 402-408.
28. Hull, D. and T.W. Clyne, *An Introduction to Composite Materials*. 1996: Cambridge University Press.
29. Jones, R.M., *Mechanics Of Composite Materials*. 1998: Taylor & Francis.
30. Vinson, J.R. and R.L. Sierakowski, *The behavior of structures composed of composite materials*. 1986: M. Nijhoff.
31. Halpin, J.C., *Primer on Composite Materials Analysis, Second Edition (revised)*. 1992: Taylor & Francis.
32. Kaw, A.K., *Mechanics of Composite Materials, Second Edition*. 2005: CRC Press.
33. Gay, D., *Composite Materials: Design and Applications, Third Edition*. 2014: Taylor & Francis.
34. Moszner, N. and U. Salz, *Recent Developments of New Components for Dental Adhesives and Composites*. Macromolecular Materials and Engineering, 2007. **292**(3): p. 245-271.
35. Sideridou, I., V. Tserki, and G. Papanastasiou, *Effect of chemical structure on degree of conversion in light-cured dimethacrylate-based dental resins*. Biomaterials, 2002. **23**(8): p. 1819-1829.

36. Peyton, F.A., *History of resins in dentistry*. Dent Clin North Am, 1975. **19**(2): p. 211-22.
37. Chesterman, J., et al., *Bulk-fill resin-based composite restorative materials: a review*. Br Dent J, 2017. **222**(5): p. 337-344.
38. Munck, J.D., et al., *A Critical Review of the Durability of Adhesion to Tooth Tissue: Methods and Results*. Journal of Dental Research, 2005. **84**(2): p. 118-132.
39. Craig, R.G. and J.M. Powers, *Restorative Dental Materials*. 2002: Mosby.
40. Silikas, N. and D.C. Watts, *Rheology of urethane dimethacrylate and diluent formulations*. Dental Materials, 1999. **15**(4): p. 257-261.
41. Inoue, S., et al., *Microtensile bond strength of eleven contemporary adhesives to dentin*. J Adhes Dent, 2001. **3**(3): p. 237-45.
42. Van Meerbeek, B., et al., *Adhesives and cements to promote preservation dentistry*. Vol. 26. 2001. 119-144.
43. Meerbeek, B., et al., *Buonocore Memorial Lecture. Adhesion to enamel and dentin: Current status and future challenges*. Vol. 28. 2002. 215-35.
44. Cook, W.D., *Photopolymerization kinetics of dimethacrylates using the camphorquinone/amine initiator system*. Polymer, 1992. **33**(3): p. 600-609.
45. Peutzfeldt, A., *Resin composites in dentistry: the monomer systems*. Eur J Oral Sci, 1997. **105**(2): p. 97-116.
46. Moszner, N. and U. Salz, *New developments of polymeric dental composites*. Progress in Polymer Science, 2001. **26**(4): p. 535-576.
47. Van Landuyt, K.L., et al., *Systematic review of the chemical composition of contemporary dental adhesives*. Biomaterials, 2007. **28**(26): p. 3757-3785.
48. Drummond, J.L., *Degradation, fatigue and failure of resin dental composite materials*. Journal of dental research, 2008. **87**(8): p. 710-719.
49. Moszner, N. and S. Klapdohr, *Nanotechnology for dental composites*. Vol. 1. 2004. 130-156.

50. Söderholm, K.-J., *Degradation of Glass Filler in Experimental Composites*. Journal of Dental Research, 1981. **60**(11): p. 1867-1875.
51. Ruyter, I.E. and I.J. Sjøvik, *Composition of Dental Resin and Composite Materials*. Acta Odontologica Scandinavica, 1981. **39**(3): p. 133-146.
52. Ferracane, J.L., *Current trends in dental composites*. Crit Rev Oral Biol Med, 1995. **6**(4): p. 302-18.
53. Lung, C.Y.K. and J.P. Matinlinna, *Aspects of silane coupling agents and surface conditioning in dentistry: An overview*. Dental Materials, 2012. **28**(5): p. 467-477.
54. Bowen, R.L., *Properties of a silica-reinforced polymer for dental restorations*. The Journal of the American Dental Association, 1963. **66**(1): p. 57-64.
55. Antonucci, J.M., et al., *Chemistry of Silanes: Interfaces in Dental Polymers and Composites*. Journal of Research of the National Institute of Standards and Technology, 2005. **110**(5): p. 541-558.
56. Van Meerbeek, B., et al., *State of the art of self-etch adhesives*. Dental Materials, 2011. **27**(1): p. 17-28.
57. Ferracane, J.L., *Resin composite--state of the art*. Dent Mater, 2011. **27**(1): p. 29-38.
58. Nicholson, J.W., *Adhesive dental materials and their durability*. International Journal of Adhesion and Adhesives, 2000. **20**(1): p. 11-16.
59. Sadowsky, S.J., *An overview of treatment considerations for esthetic restorations: a review of the literature*. J Prosthet Dent, 2006. **96**(6): p. 433-42.
60. Haj-Ali, R., M.P. Walker, and K. Williams, *Survey of general dentists regarding posterior restorations, selection criteria, and associated clinical problems*. General dentistry, 2005. **53**(5): p. 369-75; quiz 376, 367-8.
61. Rueggeberg, F.A., *From vulcanite to vinyl, a history of resins in restorative dentistry*. Journal of Prosthetic Dentistry. **87**(4): p. 364-379.
62. Harris, C.A. and P.H. Austen, *The Principles and Practice of Dentistry: Including Anatomy, Physiology, Therapeutics, Dental Surgery and Mechanism*. 1879: Lindsay and Blakiston.

63. Irie, M., K. Suzuki, and D.C. Watts, *Marginal gap formation of light-activated restorative materials: effects of immediate setting shrinkage and bond strength*. Dental Materials, 2002. **18**(3): p. 203-210.
64. Scheibenbogen, A., et al., *One-year clinical evaluation of composite and ceramic inlays in posterior teeth*. J Prosthet Dent, 1998. **80**(4): p. 410-6.
65. Davidson, C.L., L. Van Zeghbroeck, and A.J. Feilzer, *Destructive stresses in adhesive luting cements*. J Dent Res, 1991. **70**(5): p. 880-2.
66. Frankenberger, R., et al., *Dentin bond strength and marginal adaptation: direct composite resins vs ceramic inlays*. Oper Dent, 1999. **24**(3): p. 147-55.
67. Knock, F.E. and J.F. Glenn, *Dental material and method*. 1951, Google Patents.
68. Bowen, R.L., *Use of Epoxy Resins in Restorative Materials*. Journal of Dental Research, 1956. **35**(3): p. 360-369.
69. Bowen, R.L., *Properties of a silica-reinforced polymer for dental restorations*. J Am Dent Assoc, 1963. **66**: p. 57-64.
70. Munksgaard, E.C., M. Irie, and E. Asmussen, *Dentin-Polymer Bond Promoted by Gluma and Various Resins*. Journal of Dental Research, 1985. **64**(12): p. 1409-1411.
71. Dewaele, M., et al., *Volume contraction in photocured dental resins: the shrinkage-conversion relationship revisited*. Dent Mater, 2006. **22**(4): p. 359-65.
72. Price, C.A., *The Effect of Cross-linking Agents on the Impact Resistance of a Linear Poly(methyl methacrylate) Denture-base Polymer*. Journal of Dental Research, 1986. **65**(7): p. 987-992.
73. Lohbauer, U., et al., *Strength and fatigue performance versus filler fraction of different types of direct dental restoratives*. Journal of Biomedical Materials Research Part B: Applied Biomaterials, 2006. **76B**(1): p. 114-120.
74. Imazato, S., et al., *Degree of conversion of composites measured by DTA and FTIR*. Dental Materials, 2001. **17**(2): p. 178-183.
75. Anseth, K.S., S.M. Newman, and C.N. Bowman, *Polymeric dental composites: Properties and reaction behavior of multimethacrylate dental restorations*, in

- Biopolymers II*, N.A. Peppas and R.S. Langer, Editors. 1995, Springer Berlin Heidelberg: Berlin, Heidelberg. p. 177-217.
76. Geurtsen, W. and G. Leyhausen, *Concise Review Biomaterials & Bioengineering: Chemical-Biological Interactions of the Resin Monomer Triethyleneglycol-dimethacrylate (TEGDMA)*. Journal of Dental Research, 2001. **80**(12): p. 2046-2050.
77. KRISHNAN , V.K., K. MANJUSHA , and V. YAMUNA *Effect of diluent upon the properties of a visible-light-cured dental composite*. Journal of Materials Science: Materials in Medicine, 1997. **8**(11): p. 703-706.
78. Lu, H., et al., *Development of highly reactive mono-(meth)acrylates as reactive diluents for dimethacrylate-based dental resin systems*. Biomaterials, 2005. **26**(12): p. 1329-1336.
79. Podgórski, M., et al., *Ester-free Thiol-ene Dental Restoratives – Part A: Resin Development*. Dental materials : official publication of the Academy of Dental Materials, 2015. **31**(11): p. 1255-1262.
80. Braga, R.R., R.Y. Ballester, and J.L. Ferracane, *Factors involved in the development of polymerization shrinkage stress in resin-composites: a systematic review*. Dent Mater, 2005. **21**(10): p. 962-70.
81. Trujillo-Lemon, M., et al., *Dimethacrylate derivatives of dimer acid*. Journal of Polymer Science Part A: Polymer Chemistry, 2006. **44**(12): p. 3921-3929.
82. Dewaele, M., et al., *Benefits and Limitations of Adding Hyperbranched Polymers to Dental Resins*. Journal of Dental Research, 2012. **91**(12): p. 1178-1183.
83. Ogliari, F.A., et al., *Influence of chain extender length of aromatic dimethacrylates on polymer network development*. Dental Materials, 2008. **24**(2): p. 165-171.
84. Boaro, L.C.C., et al., *Polymerization stress, shrinkage and elastic modulus of current low-shrinkage restorative composites*. Dental Materials, 2010. **26**(12): p. 1144-1150.
85. Reinelt, S., et al., *Synthesis and Photopolymerization of Thiol-Modified Triazine-Based Monomers and Oligomers for the Use in Thiol-Ene-Based Dental Composites*. Macromolecular Chemistry and Physics, 2014. **215**(14): p. 1415-1425.

86. Lu, H., et al., *Investigations of step-growth thiol-ene polymerizations for novel dental restoratives*. Dent Mater, 2005. **21**(12): p. 1129-36.
87. Morgan, C.R., F. Magnotta, and A.D. Ketley, *Thiol/ene photocurable polymers*. Journal of Polymer Science: Polymer Chemistry Edition, 1977. **15**(3): p. 627-645.
88. Cramer, N.B. and C.N. Bowman, *Kinetics of thiol-ene and thiol-acrylate photopolymerizations with real-time fourier transform infrared*. Journal of Polymer Science Part A: Polymer Chemistry, 2001. **39**(19): p. 3311-3319.
89. Carioscia, J.A., et al., *Thiol-ene oligomers as dental restorative materials*. Dental Materials. **21**(12): p. 1137-1143.
90. Patel, M.P., M. Braden, and K.W. Davy, *Polymerization shrinkage of methacrylate esters*. Biomaterials, 1987. **8**(1): p. 53-6.
91. Cramer, N.B., et al., *Investigation of thiol-ene and thiol-ene-methacrylate based resins as dental restorative materials*. Dental Materials, 2010. **26**(1): p. 21-28.
92. Carioscia, J.A., et al., *Thiol-norbornene materials: Approaches to develop high Tg thiol-ene polymers*. Journal of Polymer Science Part A: Polymer Chemistry, 2007. **45**(23): p. 5686-5696.
93. Fairbanks, B.D., et al., *Thiol-Yne Photopolymerizations: Novel Mechanism, Kinetics, and Step-Growth Formation of Highly Cross-Linked Networks*. Macromolecules, 2009. **42**(1): p. 211-217.
94. Park, H.Y., et al., *Covalent adaptable networks as dental restorative resins: Stress relaxation by addition-fragmentation chain transfer in allyl sulfide-containing resins*. Dental Materials, 2010. **26**(10): p. 1010-1016.
95. Kloxin, C.J., et al., *Covalent Adaptable Networks (CANs): A Unique Paradigm in Cross-Linked Polymers*. Macromolecules, 2010. **43**(6): p. 2643-2653.
96. Scott, T.F., et al., *Photoinduced plasticity in cross-linked polymers*. Science, 2005. **308**(5728): p. 1615-7.

97. Kloxin, C.J., T.F. Scott, and C.N. Bowman, *Stress Relaxation via Addition–Fragmentation Chain Transfer in a Thiol-ene Photopolymerization*. *Macromolecules*, 2009. **42**(7): p. 2551-2556.
98. Van Ende, A., et al., *Does a low-shrinking composite induce less stress at the adhesive interface?* *Dental Materials*, 2010. **26**(3): p. 215-222.
99. Bailey, W.J. and T. Endo, *Radical ring-opening polymerization and copolymerization with expansion in volume*. *Journal of Polymer Science: Polymer Symposia*, 1978. **64**(1): p. 17-26.
100. Bailey, W.J., *Cationic Polymerization with Expansion in Volume*. *Journal of Macromolecular Science: Part A - Chemistry*, 1975. **9**(5): p. 849-865.
101. Weinmann, W., C. Thalacker, and R. Guggenberger, *Siloranones in dental composites*. *Dental Materials*, 2005. **21**(1): p. 68-74.
102. Moon, E.J., et al., *Dental restorative composites containing 2,2-bis-[4-(2-hydroxy-3-methacryloyloxy propoxy) phenyl] propane derivatives and spiro orthocarbonates*. *Journal of Biomedical Materials Research Part B: Applied Biomaterials*, 2005. **73B**(2): p. 338-346.
103. Miller, M.D., et al., *A theoretical study of an expanding monomer and an oxirane Part 1: Expanding monomer reactions*. *Journal of Molecular Structure: THEOCHEM*, 2005. **756**(1): p. 185-194.
104. Ge, J., M. Trujillo-Lemon, and J.W. Stansbury, *A Mechanistic and Kinetic Study of the Photoinitiated Cationic Double Ring-opening Polymerization of 2-Methylene-7-phenyl-1,4,6,9-tetraoxa-spiro[4.4]nonane*. *Macromolecules*, 2006. **39**(26): p. 8968-8976.
105. Klapdohr, S. and N. Moszner, *New Inorganic Components for Dental Filling Composites*. *Monatshefte für Chemie / Chemical Monthly*, 2005. **136**(1): p. 21-45.
106. Masouras, K., N. Silikas, and D.C. Watts, *Correlation of filler content and elastic properties of resin-composites*. *Dental Materials*, 2008. **24**(7): p. 932-939.

107. Tanimoto, Y., et al., *Effect of filler content on bending properties of dental composites: numerical simulation with the use of the finite-element method*. J Biomed Mater Res B Appl Biomater, 2004. **71**(1): p. 188-95.
108. van Dijken, J.W., K.R. Wing, and I.E. Ruyter, *An evaluation of the radiopacity of composite restorative materials used in Class I and Class II cavities*. Acta Odontol Scand, 1989. **47**(6): p. 401-7.
109. Soderholm, K.-J.M., *Influence of Silane Treatment and Filler Fraction on Thermal Expansion of Composite Resins*. Journal of Dental Research, 1984. **63**(11): p. 1321-1326.
110. Baroudi, K., et al., *Shrinkage behaviour of flowable resin-composites related to conversion and filler-fraction*. Journal of Dentistry, 2007. **35**(8): p. 651-655.
111. Goncalves, F., et al., *BisGMA/TEGDMA ratio and filler content effects on shrinkage stress*. Dent Mater, 2011. **27**(6): p. 520-6.
112. Jun, S.K., et al., *Investigation of the correlation between the different mechanical properties of resin composites*. Dent Mater J, 2013. **32**(1): p. 48-57.
113. Bowen, R.L., *Dental filling material comprising vinyl silane treated fused silica and a binder consisting of the reaction product of bis phenol and glycidyl acrylate*. 1962, Google Patents.
114. Gladys, S., et al., *Comparative Physico-mechanical Characterization of New Hybrid Restorative Materials with Conventional Glass-ionomer and Resin Composite Restorative Materials*. Journal of Dental Research, 1997. **76**(4): p. 883-894.
115. Randolph, L.D., et al., *Filler characteristics of modern dental resin composites and their influence on physico-mechanical properties*. Dental Materials, 2016. **32**(12): p. 1586-1599.
116. Senawongse, P. and P. Pongprueksa, *Surface Roughness of Nanofill and Nanohybrid Resin Composites after Polishing and Brushing*. Journal of Esthetic and Restorative Dentistry, 2007. **19**(5): p. 265-273.

117. Ferracane, J.L., C.S. Pfeifer, and T.J. Hilton, *Microstructural Features of Current Resin Composite Materials*. Current Oral Health Reports, 2014. **1**(4): p. 205-212.
118. Xu, H.H.K., et al., *Nanocomposite containing amorphous calcium phosphate nanoparticles for caries inhibition*. Dental Materials, 2011. **27**(8): p. 762-769.
119. Skrtic, D., J.M. Antonucci, and E.D. Eanes, *Amorphous Calcium Phosphate-Based Bioactive Polymeric Composites for Mineralized Tissue Regeneration*. Journal of Research of the National Institute of Standards and Technology, 2003. **108**(3): p. 167-182.
120. Garcia, I.M., et al., *Quantum Dots as Nonagglomerated Nanofillers for Adhesive Resins*. Journal of Dental Research, 2016. **95**(12): p. 1401-1407.
121. Kanaparthi, R. and A. Kanaparthi, *The changing face of dentistry: nanotechnology*. International Journal of Nanomedicine, 2011. **6**: p. 2799-2804.
122. Skrtic, D., et al., *Dental composites based on hybrid and surface-modified amorphous calcium phosphates*. Biomaterials, 2004. **25**(7): p. 1141-1150.
123. Yamagishi, K., et al., *Materials chemistry: A synthetic enamel for rapid tooth repair*. Nature, 2005. **433**(7028): p. 819-819.
124. Xu, H.H.K., et al., *Strong Nanocomposites with Ca, PO(4), and F Release for Caries Inhibition*. Journal of Dental Research, 2010. **89**(1): p. 19-28.
125. Chatzistavrou, X., et al., *Sol-gel based fabrication and characterization of new bioactive glass-ceramic composites for dental applications*. Journal of the European Ceramic Society, 2012. **32**(12): p. 3051-3061.
126. Kwon, T.-Y., et al., *Cure mechanisms in materials for use in esthetic dentistry*. Journal of Investigative and Clinical Dentistry, 2012. **3**(1): p. 3-16.
127. Cook, W.D., *Factors Affecting the Depth of Cure of UV -polymerized Composites*. Journal of Dental Research, 1980. **59**(5): p. 800-808.
128. Kopperud, S.E., et al., *Light curing procedures – performance, knowledge level and safety awareness among dentists*. Journal of Dentistry, 2017. **58**(Supplement C): p. 67-73.

129. Gatechair, L.R. and D. Wostratzky, *Photoinitiators: A Review of Mechanisms and Applications*, in *Adhesive Chemistry: Developments and Trends*, L.-H. Lee, Editor. 1984, Springer US: Boston, MA. p. 409-438.
130. Alvim, H.H., et al., *Analysis of camphorquinone in composite resins as a function of shade*. *Dental Materials*, 2007. **23**(10): p. 1245-1249.
131. Jakubiak, J., et al., *Camphorquinone–amines photoinitiating systems for the initiation of free radical polymerization*. *Polymer*, 2003. **44**(18): p. 5219-5226.
132. Kamoun, E.A. and H. Menzel, *HES-HEMA nanocomposite polymer hydrogels: swelling behavior and characterization*. *Journal of Polymer Research*, 2012. **19**(4): p. 9851.
133. Tsai, L. and E. Charney, *Triplet states of .alpha.-dicarbonyls. Camphorquinone*. *The Journal of Physical Chemistry*, 1969. **73**(7): p. 2462-2463.
134. Stansbury, J.W., *Curing dental resins and composites by photopolymerization*. *J Esthet Dent*, 2000. **12**(6): p. 300-8.
135. Stansbury, J.W., *Curing Dental Resins and Composites by Photopolymerization*. *Journal of Esthetic and Restorative Dentistry*, 2000. **12**(6): p. 300-308.
136. Chen, Y.-C., J.L. Ferracane, and S.A. Prahl, *Quantum yield of conversion of the photoinitiator camphorquinone*. *Dental Materials*, 2007. **23**(6): p. 655-664.
137. Jandt, K.D. and R.W. Mills, *A brief history of LED photopolymerization*. *Dental Materials*, 2013. **29**(6): p. 605-617.
138. Palin, W.M., et al., *Reduced polymerization stress of MAPO-containing resin composites with increased curing speed, degree of conversion and mechanical properties*. *Dent Mater*, 2014. **30**(5): p. 507-16.
139. Ikemura, K., et al., *UV-VIS spectra and photoinitiation behaviors of acylphosphine oxide and bisacylphosphine oxide derivatives in unfilled, light-cured dental resins*. *Dental Materials Journal*, 2008. **27**(6): p. 765-774.

140. Schneider, L.F.J., et al., *Curing efficiency of dental resin composites formulated with camphorquinone or trimethylbenzoyl-diphenyl-phosphine oxide*. Dental Materials, 2012. **28**(4): p. 392-397.
141. Neumann, M.G., et al., *Molar extinction coefficients and the photon absorption efficiency of dental photoinitiators and light curing units*. J Dent, 2005. **33**(6): p. 525-32.
142. Janda, R., et al., *Color stability of resin matrix restorative materials as a function of the method of light activation*. European Journal of Oral Sciences, 2004. **112**(3): p. 280-285.
143. Ilie, N. and R. Hickel, *Can CQ Be Completely Replaced by Alternative Initiators in Dental Adhesives?* Dental Materials Journal, 2008. **27**(2): p. 221-228.
144. Karabela, M.M. and I.D. Sideridou, *Effect of the structure of silane coupling agent on sorption characteristics of solvents by dental resin-nanocomposites*. Dental Materials, 2008. **24**(12): p. 1631-1639.
145. Brown, S.K., *Mechanisms of fracture in filled thermosetting resins*. British Polymer Journal, 1980. **12**(1): p. 24-30.
146. Mohsen, N.M. and R.G. Craig, *Effect of silanation of fillers on their dispersability by monomer systems*. J Oral Rehabil, 1995. **22**(3): p. 183-9.
147. Calais, J.G. and K.J. Soderholm, *Influence of filler type and water exposure on flexural strength of experimental composite resins*. J Dent Res, 1988. **67**(5): p. 836-40.
148. Soderholm, K.J., *Degradation of glass filler in experimental composites*. J Dent Res, 1981. **60**(11): p. 1867-75.
149. McDowall, F., *Introduction to dental materials, 4th edition*. Br Dent J, 2013. **215**(2): p. 100-100.
150. Lung, C.Y.K. and J.P. Matinlinna, *Resin Bonding to Silicized Zirconia with Two Isocyanatosilanes and a Cross-linking Silane. Part I: Experimental*. Silicon, 2010. **2**(3): p. 153-161.

151. May, L.G., et al., *Effect of silica coating combined to a MDP-based primer on the resin bond to Y-TZP ceramic*. J Biomed Mater Res B Appl Biomater, 2010. **95**(1): p. 69-74.
152. Tsuchimoto, Y., et al., *Effect of 4-MET- and 10-MDP-based primers on resin bonding to titanium*. Dent Mater J, 2006. **25**(1): p. 120-4.
153. Kim, S.-S., et al., *Effect of adhesive primers on bonding strength of heat cure denture base resin to cast titanium and cobalt-chromium alloy*. The Journal of Advanced Prosthodontics, 2009. **1**(1): p. 41-46.
154. Tanaka, R., et al., *Cooperation of phosphate monomer and silica modification on zirconia*. J Dent Res, 2008. **87**(7): p. 666-70.
155. Yoshida, K., Y. Tsuo, and M. Atsuta, *Bonding of dual-cured resin cement to zirconia ceramic using phosphate acid ester monomer and zirconate coupler*. J Biomed Mater Res B Appl Biomater, 2006. **77**(1): p. 28-33.
156. Kern, M. and S.M. Wegner, *Bonding to zirconia ceramic: adhesion methods and their durability*. Dental Materials, 1998. **14**(1): p. 64-71.
157. Darvell, B.W., *Materials Science for Dentistry*. 9th ed.: Woodhead Publishing Limited. 677.
158. Atai, M. and D.C. Watts, *A new kinetic model for the photopolymerization shrinkage-strain of dental composites and resin-monomers*. Dent Mater, 2006. **22**(8): p. 785-91.
159. Elliott, J.E., L.G. Lovell, and C.N. Bowman, *Primary cyclization in the polymerization of bis-GMA and TEGDMA: a modeling approach to understanding the cure of dental resins*. Dental Materials, 2001. **17**(3): p. 221-229.
160. Anseth, K.S., et al., *The influence of comonomer composition on dimethacrylate resin properties for dental composites*. J Dent Res, 1996. **75**(8): p. 1607-12.
161. Leprince, J.G., et al., *Progress in dimethacrylate-based dental composite technology and curing efficiency*. Dental Materials, 2013. **29**(2): p. 139-156.
162. Leprince, J.G., et al., *Photoinitiator type and applicability of exposure reciprocity law in filled and unfilled photoactive resins*. Dental Materials, 2011. **27**(2): p. 157-164.

163. Goodner, M.D. and C.N. Bowman, *Modeling Primary Radical Termination and Its Effects on Autoacceleration in Photopolymerization Kinetics*. *Macromolecules*, 1999. **32**(20): p. 6552-6559.
164. Finan, L., et al., *The influence of irradiation potential on the degree of conversion and mechanical properties of two bulk-fill flowable RBC base materials*. *Dental Materials*, 2013. **29**(8): p. 906-912.
165. Ruyter, I.E. and H. Øysæd, *Composites for use in posterior teeth: Composition and conversion*. *Journal of Biomedical Materials Research*, 1987. **21**(1): p. 11-23.
166. Ruyter, I.E. and S.A. Svendsen, *Remaining methacrylate groups in composite restorative materials*. *Acta Odontol Scand*, 1978. **36**(2): p. 75-82.
167. Silikas, N., et al., *Surface characterization of modern resin composites: a multitechnique approach*. *Am J Dent*, 2005. **18**(2): p. 95-100.
168. Sakaguchi, R.L. and J.L. Ferracane, *Effect of light power density on development of elastic modulus of a model light-activated composite during polymerization*. *J Esthet Restor Dent*, 2001. **13**(2): p. 121-30.
169. Zhu, S., et al., *Radical trapping and termination in free-radical polymerization of methyl methacrylate*. *Macromolecules*, 1990. **23**(4): p. 1144-1150.
170. Ferracane, J.L. and J.R. Condon, *Post-cure heat treatments for composites: properties and fractography*. *Dental Materials*, 1992. **8**(5): p. 290-295.
171. Bagis, Y.H. and F.A. Rueggeberg, *The effect of post-cure heating on residual, unreacted monomer in a commercial resin composite*. *Dental Materials*, 2000. **16**(4): p. 244-247.
172. Loza-Herrero, M.A., et al., *Effect of Heating Delay on Conversion and Strength of a Post-cured Resin Composite*. *Journal of Dental Research*, 1998. **77**(2): p. 426-431.
173. Ferracane, J.L. and E.H. Greener, *Correlation between Mechanical-Properties and Conversion in Unfilled Bis-Gma Resins*. *Journal of Dental Research*, 1984. **63**: p. 231-231.

174. Braga, R.R. and J.L. Ferracane, *Contraction stress related to degree of conversion and reaction kinetics*. J Dent Res, 2002. **81**(2): p. 114-8.
175. Atai, M., D.C. Watts, and Z. Atai, *Shrinkage strain-rates of dental resin-monomer and composite systems*. Biomaterials, 2005. **26**(24): p. 5015-5020.
176. Dewaele, M., et al., *Volume contraction in photocured dental resins: The shrinkage-conversion relationship revisited*. Dental Materials, 2006. **22**(4): p. 359-365.
177. Darvell, B.W., *Chapter 5 - Acrylic*, in *Materials Science for Dentistry (Ninth edition)*, B.W. Darvell, Editor. 2009, Woodhead Publishing. p. 108-127.
178. Rueggeberg, F.A., K. Tamareselvy, and J.W. Ertle, *Network Conversion and Leachability of Bis-Gma Tegdma Copolymers*. Journal of Dental Research, 1995. **74**: p. 183-183.
179. Lemon, M.T., M.S. Jones, and J.W. Stansbury, *Hydrogen bonding interactions in methacrylate monomers and polymers*. J Biomed Mater Res A, 2007. **83**(3): p. 734-46.
180. Lovell, L.G., et al., *Understanding the kinetics and network formation of dimethacrylate dental resins*. Polymers for Advanced Technologies, 2001. **12**(6): p. 335-345.
181. Lovell, L.G., et al., *Effects of Composition and Reactivity on the Reaction Kinetics of Dimethacrylate/Dimethacrylate Copolymerizations*. Macromolecules, 1999. **32**(12): p. 3913-3921.
182. Kannurpatti, A.R., J.W. Anseth, and C.N. Bowman, *A study of the evolution of mechanical properties and structural heterogeneity of polymer networks formed by photopolymerizations of multifunctional (meth)acrylates*. Polymer, 1998. **39**(12): p. 2507-2513.
183. Lovell, L.G., S.M. Newman, and C.N. Bowman, *The effects of light intensity, temperature, and comonomer composition on the polymerization behavior of dimethacrylate dental resins*. J Dent Res, 1999. **78**(8): p. 1469-76.

184. Poshusta, A.K., C.N. Bowman, and K.S. Anseth, *Application of a kinetic gelation simulation to the characterization of in situ cross-linking biomaterials*. J Biomater Sci Polym Ed, 2002. **13**(7): p. 797-815.
185. Anseth, K.S., et al., *Reaction Kinetics and Volume Relaxation during Polymerizations of Multiethylene Glycol Dimethacrylates*. Macromolecules, 1995. **28**(7): p. 2491-2499.
186. Pfeifer, C.S., et al., *Characterization of dimethacrylate polymeric networks: a study of the crosslinked structure formed by monomers used in dental composites*. European polymer journal, 2011. **47**(2): p. 162-170.
187. Leprince, J.G., et al., *Photoinitiator type and applicability of exposure reciprocity law in filled and unfilled photoactive resins*. Dent Mater, 2011. **27**(2): p. 157-64.
188. Miletic, V. and A. Santini, *Micro-Raman spectroscopic analysis of the degree of conversion of composite resins containing different initiators cured by polywave or monowave LED units*. Journal of Dentistry, 2012. **40**(2): p. 106-113.
189. Randolph, L.D., et al., *Ultra-fast light-curing resin composite with increased conversion and reduced monomer elution*. Dental Materials, 2014. **30**(5): p. 594-604.
190. Emami, N. and K.-J.M. Söderholm, *How light irradiance and curing time affect monomer conversion in light-cured resin composites*. European Journal of Oral Sciences, 2003. **111**(6): p. 536-542.
191. Pearce, E.M., *Principles of polymerization (third edition), by George Odian, Wiley-Interscience, New York, 1991, 768 pp. price: \$59.95*. Journal of Polymer Science Part A: Polymer Chemistry, 1992. **30**(7): p. 1508-1508.
192. Lloyd, C.H., A. Joshi, and E. McGlynn, *Temperature rises produced by light sources and composites during curing*. Dental Materials, 1986. **2**(4): p. 170-174.
193. Lovell, L.G., et al., *The effect of light intensity on double bond conversion and flexural strength of a model, unfilled dental resin*. Dent Mater, 2003. **19**(6): p. 458-65.
194. Bouschlicher, M.R. and F.A. Rueggeberg, *Effect of Ramped Light Intensity on Polymerization Force and Conversion in a Photoactivated Composite*. Journal of Esthetic and Restorative Dentistry, 2000. **12**(6): p. 328-339.

195. Lim, B.S., et al., *Reduction of polymerization contraction stress for dental composites by two-step light-activation*. Dental Materials, 2002. **18**(6): p. 436-444.
196. Ferracane, J.L., *Developing a more complete understanding of stresses produced in dental composites during polymerization*. Dental Materials, 2005. **21**(1): p. 36-42.
197. Lu, H., J.W. Stansbury, and C.N. Bowman, *Towards the elucidation of shrinkage stress development and relaxation in dental composites*. Dental Materials, 2004. **20**(10): p. 979-986.
198. Davidson, C.L. and A.J.D. Gee, *Relaxation of Polymerization Contraction Stresses by Flow in Dental Composites*. Journal of Dental Research, 1984. **63**(2): p. 146-148.
199. R. Kannurpatti, A., et al., *Use of "Living" radical polymerizations to study the structural evolution and properties of highly crosslinked polymer networks*. Vol. 35. 1997. 2297-2307.
200. Feilzer, A.J., A.J. De Gee, and C.L. Davidson, *Quantitative determination of stress reduction by flow in composite restorations*. Dental Materials, 1990. **6**(3): p. 167-171.
201. Calheiros, F.C., et al., *Polymerization contraction stress of low-shrinkage composites and its correlation with microleakage in class V restorations*. Journal of Dentistry, 2004. **32**(5): p. 407-412.
202. Sarkar, S., et al., *Quantifying the sensitivity of the network structure and properties from simultaneous measurements during photopolymerization*. Soft Matter, 2017. **13**(21): p. 3975-3983.
203. Camboni, F., A. Koher, and I.M. Sokolov, *Diffusion of small particles in a solid polymeric medium*. Physical Review E, 2013. **88**(2): p. 022120.
204. Lu, H., J.W. Stansbury, and C.N. Bowman, *Impact of Curing Protocol on Conversion and Shrinkage Stress*. Journal of Dental Research, 2005. **84**(9): p. 822-826.
205. Feitosa, V.P., et al., *Effects of different photo-polymerization protocols on resin-dentine  $\mu$ TBS, mechanical properties and cross-link density of a nano-filled resin composite*. Journal of Dentistry, 2012. **40**(10): p. 802-809.

206. Asmussen, E. and A. Peutzfeldt, *Two-step curing: influence on conversion and softening of a dental polymer*. Dental Materials, 2003. **19**(6): p. 466-470.
207. Moon, H.J., et al., *Effects of various light curing methods on the leachability of uncured substances and hardness of a composite resin*. Journal of Oral Rehabilitation, 2004. **31**(3): p. 258-264.
208. Asmussen, E. and A. Peutzfeldt, *Influence of Pulse-Delay Curing on Softening of Polymer Structures*. Journal of Dental Research, 2001. **80**(6): p. 1570-1573.
209. Bunsen, R.W., Roscoe, H.E, Photochemical Studies. Ann Phys, 1923: p. 108:193.
210. Halvorson, R.H., R.L. Erickson, and C.L. Davidson, *Energy dependent polymerization of resin-based composite*. Dental Materials. **18**(6): p. 463-469.
211. Emami, N. and K.J. Soderholm, *How light irradiance and curing time affect monomer conversion in light-cured resin composites*. Eur J Oral Sci, 2003. **111**(6): p. 536-42.
212. Feng, L. and B.I. Suh, *Exposure Reciprocity Law in Photopolymerization of Multi-Functional Acrylates and Methacrylates*. Macromolecular Chemistry and Physics, 2007. **208**(3): p. 295-306.
213. Price, R.B., C.A. Felix, and P. Andreou, *Effects of resin composite composition and irradiation distance on the performance of curing lights*. Biomaterials, 2004. **25**(18): p. 4465-77.
214. Halvorson, R.H., R.L. Erickson, and C.L. Davidson, *An energy conversion relationship predictive of conversion profiles and depth of cure for resin-based composite*. Oper Dent, 2003. **28**(3): p. 307-14.
215. Stewardson, D.A., et al., *Thermal changes and cure depths associated with a high intensity light activation unit*. J Dent, 2004. **32**(8): p. 643-51.
216. Musanje, L. and B.W. Darvell, *Polymerization of resin composite restorative materials: exposure reciprocity*. Dent Mater, 2003. **19**(6): p. 531-41.
217. Hadis, M., et al., *High irradiance curing and anomalies of exposure reciprocity law in resin-based materials*. J Dent, 2011. **39**(8): p. 549-57.

218. Leprince, J.G., et al., *Irradiation modes' impact on radical entrapment in photoactive resins*. J Dent Res, 2010. **89**(12): p. 1494-8.
219. Goodner, M.D. and C.N. Bowman, *Development of a comprehensive free radical photopolymerization model incorporating heat and mass transfer effects in thick films*. Chemical Engineering Science, 2002. **57**(5): p. 887-900.
220. O'Brien, A.K. and C.N. Bowman, *Modeling Thermal and Optical Effects on Photopolymerization Systems*. Macromolecules, 2003. **36**(20): p. 7777-7782.
221. Stansbury, J.W., et al., *Conversion-dependent shrinkage stress and strain in dental resins and composites*. Dent Mater, 2005. **21**(1): p. 56-67.
222. Ruyter, I.E. and H. Oysaed, *Composites for use in posterior teeth: composition and conversion*. J Biomed Mater Res, 1987. **21**(1): p. 11-23.
223. Gulari, E., K. McKeigue, and K.Y.S. Ng, *Raman and FTIR spectroscopy of polymerization: bulk polymerization of methyl methacrylate and styrene*. Macromolecules, 1984. **17**(9): p. 1822-1825.
224. Soh, M.S. and A.U.J. Yap, *Influence of curing modes on crosslink density in polymer structures*. Journal of Dentistry, 2004. **32**(4): p. 321-326.
225. Tanimoto, Y., T. Hayakawa, and K. Nemoto, *Analysis of photopolymerization behavior of UDMA/TEGDMA resin mixture and its composite by differential scanning calorimetry*. J Biomed Mater Res B Appl Biomater, 2005. **72**(2): p. 310-5.
226. McCabe, J.F., *Cure performance of light-activated composites by differential thermal analysis (DTA)*. Dental Materials, 1985. **1**(6): p. 231-234.
227. Brauer, G.M., D.J. Termini, and C.L. Burns, *Characterization of Components of Dental Materials and Components of Tooth Structure by Differential Thermal Analysis*. Journal of Dental Research, 1970. **49**(1): p. 100-110.
228. Sideridou, I.D. and D.S. Achilias, *Elution study of unreacted Bis-GMA, TEGDMA, UDMA, and Bis-EMA from light-cured dental resins and resin composites using HPLC*. Journal of Biomedical Materials Research Part B: Applied Biomaterials, 2005. **74B**(1): p. 617-626.

229. Truffier-Boutry, D., et al., *A physico-chemical explanation of the post-polymerization shrinkage in dental resins*. Dental Materials, 2006. **22**(5): p. 405-412.
230. Vaidyanathan, J., et al., *Thermoanalytical characterization of visible light cure dental composites*. J Oral Rehabil, 1992. **19**(1): p. 49-64.
231. Bagis, Y.H. and F.A. Rueggeberg, *Effect of post-cure temperature and heat duration on monomer conversion of photo-activated dental resin composite*. Dent Mater, 1997. **13**(4): p. 228-32.
232. DeWald, J.P. and J.L. Ferracane, *A Comparison of Four Modes of Evaluating Depth of Cure of Light-activated Composites*. Journal of Dental Research, 1987. **66**(3): p. 727-730.
233. Harrison, A. and R.A. Draughn, *Abrasive wear, tensile strength, and hardness of dental composite resins—Is there a relationship?* The Journal of Prosthetic Dentistry, 1976. **36**(4): p. 395-398.
234. Kurachi, C., et al., *Hardness evaluation of a dental composite polymerized with experimental LED-based devices*. Dental Materials, 2001. **17**(4): p. 309-315.
235. Ferracane, J.L. and E.H. Greener, *The effect of resin formulation on the degree of conversion and mechanical properties of dental restorative resins*. Journal of Biomedical Materials Research, 1986. **20**(1): p. 121-131.
236. Rueggeberg, F.A. and R.G. Craig, *Correlation of parameters used to estimate monomer conversion in a light-cured composite*. J Dent Res, 1988. **67**(6): p. 932-7.
237. Rueggeberg, F.A., J.W. Ertle, and D.J. Mettenburg, *Polymerization depths of contemporary light-curing units using microhardness*. J Esthet Dent, 2000. **12**(6): p. 340-9.
238. Moore, B.K., et al., *Depth of cure of dental resin composites: ISO 4049 depth and microhardness of types of materials and shades*. Oper Dent, 2008. **33**(4): p. 408-12.
239. Fong, H., S.H. Dickens, and G.M. Flaim, *Evaluation of dental restorative composites containing polyhedral oligomeric silsesquioxane methacrylate*. Dent Mater, 2005. **21**(6): p. 520-9.

240. Mansur, H.S., R.L. Oréface, and A.A.P. Mansur, *Characterization of poly(vinyl alcohol)/poly(ethylene glycol) hydrogels and PVA-derived hybrids by small-angle X-ray scattering and FTIR spectroscopy*. *Polymer*, 2004. **45**(21): p. 7193-7202.
241. Butler, M.F., A.M. Donald, and A.J. Ryan, *Time resolved simultaneous small- and wide-angle X-ray scattering during polyethylene deformation—II. Cold drawing of linear polyethylene*. *Polymer*, 1998. **39**(1): p. 39-52.
242. Cai, J., B.S. Hsiao, and R.A. Gross, *Real-Time Structure Changes during Uniaxial Stretching of Poly( $\omega$ -pentadecalactone) by in Situ Synchrotron WAXD/SAXS Techniques*. *Macromolecules*, 2011. **44**(10): p. 3874-3883.
243. Wilderbeek, H.T.A., et al., *Synthesis and properties of phenyl benzoate-based and biphenyl-based liquid crystalline thiol-ene monomers*. *Liquid Crystals*, 2003. **30**(1): p. 93-108.
244. Waters, D.J., et al., *Morphology of Photopolymerized End-Linked Poly(ethylene glycol) Hydrogels by Small-Angle X-ray Scattering*. *Macromolecules*, 2010. **43**(16): p. 6861-6870.
245. Domján, A., et al., *Structural Studies of Nanophase-Separated Poly(2-hydroxyethyl methacrylate)-*l*-polyisobutylene Amphiphilic Conetworks by Solid-State NMR and Small-Angle X-ray Scattering*. *Macromolecules*, 2003. **36**(24): p. 9107-9114.
246. Kumar, S. and W.W. Adams, *Structural studies of epoxy resins, acetylene terminated resins and polycarbonate*. *Polymer*, 1987. **28**(9): p. 1497-1504.
247. Guo, Q., et al., *Miscibility, crystallization kinetics and real-time small-angle X-ray scattering investigation of the semicrystalline morphology in thermosetting polymer blends of epoxy resin and poly(ethylene oxide)*. *Polymer*, 2001. **42**(9): p. 4127-4140.
248. Yoon, D.Y. and P.J. Flory, *Small angle neutron and X-ray scattering by poly(methyl methacrylate) chains*. *Polymer*, 1975. **16**(9): p. 645-648.
249. Urnes, S., *Modern Aspects of Vitreous State*. 1960, London: Butterworths.
250. Tipler, P.A. and G. Mosca, *Physics for Scientists and Engineers*. 2004: W.H. Freeman.

251. Sivia, D.S., *Elementary Scattering Theory: For X-ray and Neutron Users*. 2011: OUP Oxford.

## **2 MATERIALS AND METHODS**

### **2.1 Introduction and Overview**

In this chapter the materials, generic formulation procedures and analytical techniques used throughout the body of work are outlined. Methods used to address the specific hypotheses are outlined in detail in each experimental chapter.

### **2.2 Sample Preparation**

#### **2.2.1 Monomers, Photo-initiators and Filler Particles**

All experimental resin blends presented in this thesis are based on the combination of triethylene glycol dimethacrylate (TEGDMA) and bisphenol-A-glycidyl-methacrylate (Bis-GMA) monomers. Free radical polymerisation of the dimethacrylate monomer blends was initiated through the use of photo-initiator species dispersed in the resin matrix as either Camphorquinone and its tertiary amine 2-(Dimethylamino)ethyl methacrylate, or Lucirin TPO. A variant of this resin matrix was produced via the synthesis of partially deuterated monomers, described in Section 2.2.2, whilst composites were produced through the combination of the resin matrix with non-silanized monodisperse silica microspheres ( $\rho = 1.8 \text{ g cm}^{-3}$ , mean diameter =  $8.07 \text{ }\mu\text{m}$ , refractive index = 1.54). All chemicals and materials were used as received and were purchased from the companies listed in Table 2.1.

**Table 2.1.** Chemicals and suppliers used for the production of experimental, dimethacrylate based, resin blends. Lot numbers for monomers used in resin formulation are presented in chapter 10, table 10.1.

| <b>Chemical Name/Material</b>        | <b>Formula</b>     | <b>Company</b>                       |
|--------------------------------------|--------------------|--------------------------------------|
| triethylene glycol dimethacrylate    | $C_{14}H_{22}O_6$  | Sigma Aldrich (Dorset, UK)           |
| bisphenol-A-glycidyl-methacrylate    | $C_{29}H_{36}O_8$  | Sigma Aldrich (Dorset, UK)           |
| triethylene glycol                   | $C_6H_{14}O_4$     | Sigma Aldrich (Dorset, UK)           |
| triethylamine                        | $C_6H_{15}N$       | Sigma Aldrich (Dorset, UK)           |
| methacryloyl chloride                | $C_4H_5ClO$        | Sigma Aldrich (Dorset, UK)           |
| sodium sulfate                       | $Na_2SO_4$         | Sigma Aldrich (Dorset, UK)           |
| sodium bicarbonate                   | $NaHCO_3$          | Sigma Aldrich (Dorset, UK)           |
| hydroquinone                         | $C_6H_6O_2$        | Sigma Aldrich (Dorset, UK)           |
| dichloromethane                      | $CH_2Cl_2$         | POCh (Gliwice, Poland)               |
| diethyl ether                        | $(C_2H_5)_2O$      | POCh (Gliwice, Poland)               |
| methanol                             | MeOH               | POCh (Gliwice, Poland)               |
| chloroform                           | $CHCl_3$           | POCh (Gliwice, Poland)               |
| hydrochloric acid                    | HCl                | POCh (Gliwice, Poland)               |
| methacryloyl chloride-d <sub>5</sub> | $C_4D_5ClO$        | Polymer Source, Inc (Quebec, Canada) |
| lucirin TPO                          | $C_{22}H_{21}O_2P$ | Sigma Aldrich (Dorset, UK)           |
| camphorquinone                       | $C_{10}H_{14}O_2$  | Sigma Aldrich (Dorset, UK)           |
| 2-(Dimethylamino)ethyl methacrylate  | $C_8H_{15}NO_2$    | Sigma Aldrich (Dorset, UK)           |
| silica Microspheres (8 μm diameter)  | $SiO_2$            | Cospheric (Santa Barbara, CA, USA)   |

### 2.2.2 Synthesis of Partially Deuterated TEGDMA-d<sub>10</sub>

The synthesis of partially deuterated TEGDMA-d<sub>10</sub> was conducted in collaboration with Dr Majiek Podorski, University of Lublin, Poland. Before the partially deuterated triethylene glycol dimethacrylate (TEGDMA-d<sub>10</sub>) was synthesized, the reaction conditions were optimized with the use of undeuterated precursor compounds. The extent of the reaction was monitored by means of IR spectroscopy by withdrawing aliquots from the reaction mixture during synthesis.

Initially, diol (triethylene glycol) (3.5g, 23 mmol) in 80 mL of methylene chloride and 5.2 g (51 mmol) triethylamine (TEA) were mixed under a nitrogen atmosphere in an ice bath. Subsequently, 5.3 g (51 mmol, 10 % excess with respect to the diol) of undeuterated methacryloyl chloride in 20 mL of methylene chloride was added dropwise to the mixture during 1 h, and the temperature was kept at -5°C. The reaction mixture was allowed to stir for two further hours at room temperature, and then was filtrated and treated with a 1 M HCl solution (2 x 40 mL), a saturated NaHCO<sub>3</sub> solution (2 x 40 mL), and distilled water (1 x 20 mL) as detailed in similar synthetic reports [1]. The organic phase was dried with Na<sub>2</sub>SO<sub>4</sub>, and the solvent was evaporated to obtain a colorless liquid (TEGDMA).

The TEGDMA-d<sub>10</sub> was synthesized according to the above procedure using undeuterated triethylene glycol (3g, 20 mmol), deuterated methacryloyl chloride-d<sub>5</sub> (5g, 45 mmol), and TEA (4.6 g, 45 mmol). Because of the initially low yield (< 20%) the reaction time was extended to 8 h. The raw product was purified using column chromatography (1 x DCM/MeOH, 95/5, v/v, and 1 x chloroform), and then discolored with the use of activated carbon in diethyl ether. The overall yield was 35-40%. The product was stabilized with 100 ppm hydroquinone. The reaction process is summarized in Figure 2.1.

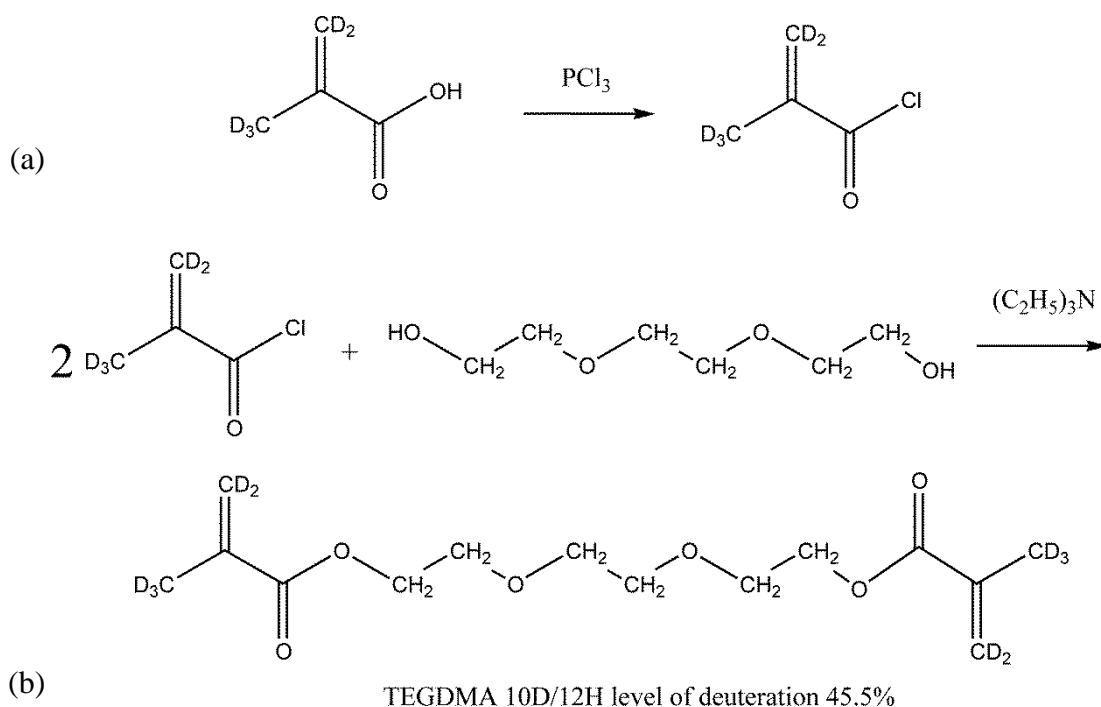


**Figure 2.1.** (a) Deuterated methacrylic acid combined with phosphorus trichloride in preparation for combining with triethylene glycol. (b) Combining deuterated methacryloyl chloride with hydrogenated triethylene glycol to yield a partially deuterated TEGDMA monomer with 45.5% deuteration by molecular weight of the original hydrogen atoms.

The  $^1\text{H}$  NMR ( $\delta$ ) spectrum of the TEGDMA- $\text{d}_{10}$  showed characteristic signals for ethylene protons at  $\delta = 4.31$  (4H), 3.74 (4H), and 3.62 (4H) ppm. Residual peaks of the undeuterated methacrylate moiety were detected (all < 5%) at  $\delta = 1.98$  (3H), 5.61 (1H) and 6.12 (1H) ppm.

FTIR spectra showed peaks at ( $\text{cm}^{-1}$ ): 3010-2775 ( $\text{CH}_{\text{aliphatic}}$ ), 1715 (CO), 1647 (residue  $=\text{CH}_2$ ), 1595 ( $=\text{CD}_2$ ), 1500-775 ( $\text{CH}_{\text{aliphatic}}$ ), 1068 (CD), 745 (residue DCM). No alcohol or chloride IR peaks were detected after purification (Figure 2.2).

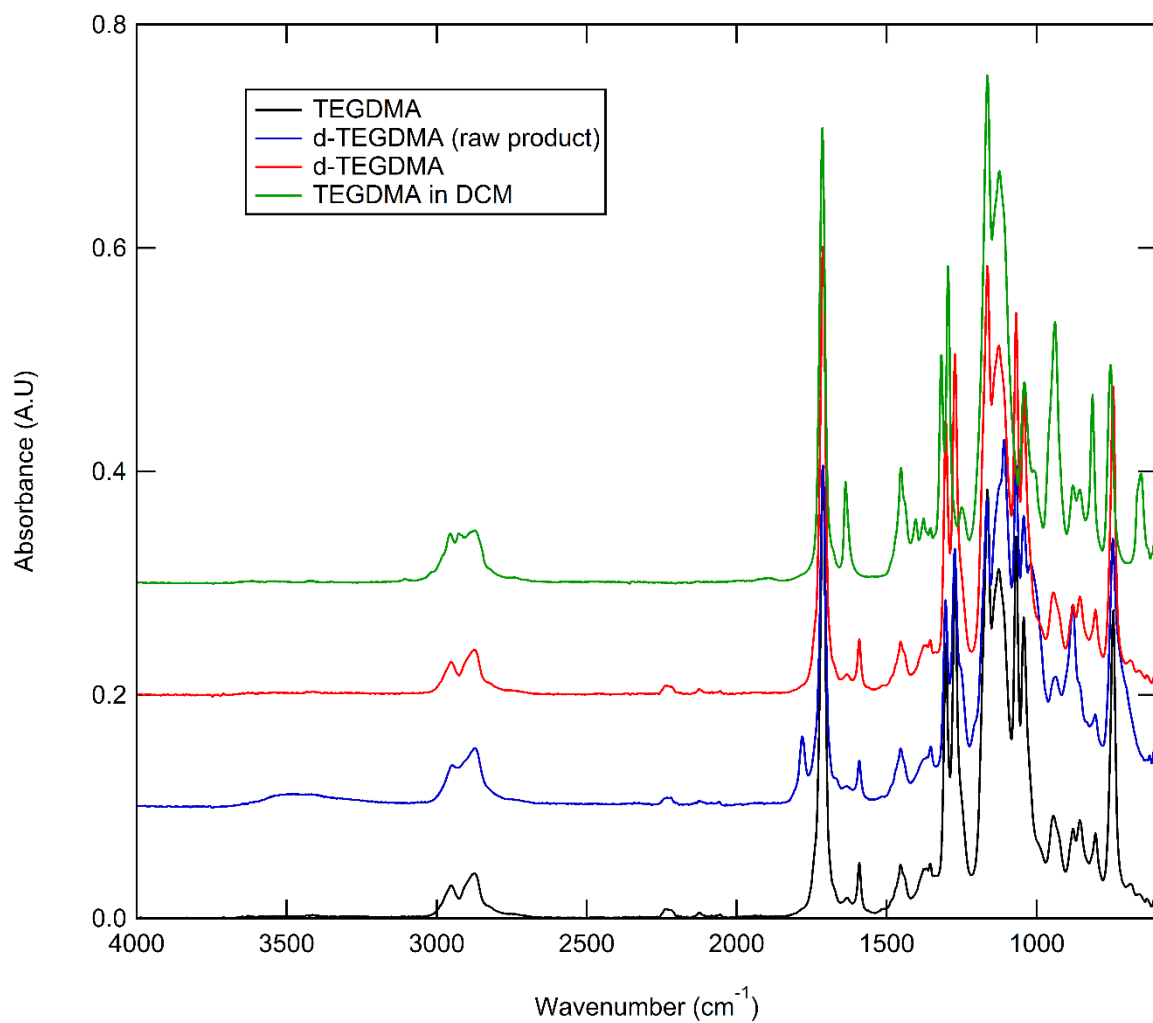


**Figure 2.2.** FTIR spectra for deuterated undeuterated variants of the TEGDMA monomer. Spectra for the d-TEGDMA at specific steps of purification are also shown and are offset in the absorbance axis for clarity.

### 2.2.3 Preparation of Dimethacrylate Resin Blends

Dimethacrylate monomers, bisphenol-A-glycidyl-methacrylate (Bis-GMA) and triethyleneglycol-dimethacrylate (TEGDMA) were proportioned in 70/30, 60/40, 50/50 and 40/60 (Bis-GMA/TEGDMA) weight percentage (wt. %) ratios and combined to produce 10 g mixes. Fresh resin blends were mixed prior to individual experiments. The viscosity of the blend increases with the proportion of Bis-GMA. The monomer blends were combined with a photo-initiator as either 0.2 wt% Camphorquinone (CQ) with 0.8 wt% of its tertiary amine N,N-dimethylaminoethyl-methacrylate (DMAEMA) or 1 wt% of the type 1 photo-initiator, Lucirin-TPO, which does not require a co-initiator. The proportioned monomers and photo-initiators were homogenised in a glass beaker using a magnetic stirrer at  $50 \pm 1^\circ\text{C}$  for 30 min in dark conditions. Deuterated counterparts were produced by similar methods but were stirred by hand due to a limited amount of sample. The resultant resins were stored in dark conditions in sealed containers at  $4 \pm 1^\circ\text{C}$  prior to further use.

## 2.2.4 Preparation of Filled Dimethacrylate Resin Blends

Non-silanized, 8  $\mu\text{m}$  (diameter) silica microspheres (refractive index = 1.54) were added to 70/30 and 60/40 (Bis-GMA/TEGDMA) wt% resin blends in either 50/50 or 40/60 wt% ratios and mixed to form composites. The filler fraction was incorporated into the resin blend using a high speed mixing machine (SpeedMixer™ DAC 150.1 FVZ-K, Synergy Devices Limited, Buckinghamshire, UK) at 1000 rpm for 5 min. The compositions of the filled resin blends are summarised in Table 2.2, where higher filler fractions (40/60 wt%) are referenced as *HF*.

**Table 2.2.** Weight percentage (wt%) mixing ratios of Bis-GMA and TEGDMA monomers used to formulate each resin blend. Each mixing ratio was combined with a photo-initiator as either 0.2 wt% Camphorquinone (CQ) with 0.8 wt% of its tertiary amine N,N-dimethylaminoethyl-methacrylate (DMAEMA) or 1 wt% Lucirin-TPO photo-initiator. Silica filler particles were added in high (HF) (40/60) and low (50/50) loadings.

| <b>Bis-GMA<br/>(wt%)</b> | <b>TEGDMA<br/>(wt%)</b> | <b>Photo-initiator</b> | <b>Resin/filler (wt%)</b> | <b>Sample Code</b>  |
|--------------------------|-------------------------|------------------------|---------------------------|---------------------|
| 70                       | 30                      | CQ                     | 50/50                     | 70/30 CQ            |
| 70                       | 30                      | TPO                    | 50/50                     | 70/30 TPO           |
| 60                       | 40                      | CQ                     | 50/50                     | 60/40 CQ            |
| 60                       | 40                      | TPO                    | 50/50                     | 60/40 TPO           |
| 60                       | 40                      | CQ                     | 40/60                     | 60/40 CQ <i>HF</i>  |
| 60                       | 40                      | TPO                    | 40/60                     | 60/40 TPO <i>HF</i> |

## 2.3 Light Curing Units

Two different light engines were used to photo-polymerise resin blends in this work. An externally controllable light engine was used for all *in-situ* photo-polymerization of test specimens whilst undertaking simultaneous X-ray scattering on a synchrotron beam line. For laboratory based fabrication of pre-cured samples for neutron scattering and ‘off-line’ FTIR measurements, the light engine or a calibrated dental photo-curing unit was used.

### 2.3.1 Lumencor AURA Light Engine – External Polymerisation

Resin blends were photo-polymerised *in-situ* on several X-ray scattering synchrotron beam lines using a multi-channel solid state light engine (Lumencor Aura 3 LCR, serial no. 1321, Oregon, USA) which was controlled through Lumencor software [2]. A 5 mm liquid light guide (part no. 10-10256) was connected to the light engine to direct light towards liquid resin samples. For the TPO initiated resins, the light engine was programmed to emit a peak emission spectrum at 405 nm (FWHM = 20 nm) using a blue filter channel, whilst for CQ based systems a spectral emission maximum located at 465 nm (FWHM = 16 nm) was employed via the cyan colour channel. The wavelengths of light were chosen to match the maxima in the absorption spectra of the Lucirin TPO and camphorquinone photo-initiators centred at 381 nm and 470 nm respectively. The irradiance for the blue and cyan channels are shown in Figure 2.3 as a function of the wavelength of the light engine at increasing power output, defined as the percentage of the maximum output for a given channel. Spectra were collected at increasing power outputs using a UV/visible spectrometer positioned normal to and 10 mm from the tip of the light guide. Calibration plots were obtained for each colour channel by plotting the integrated emission intensities as a function of the corresponding percentage power output which was fit with a linear regression model (Figure 2.4). Light was toggled on and off externally using a TTL pulse command which was incorporated in to control scripts to automate illumination simultaneously to X-ray measurements and to timestamp data files.

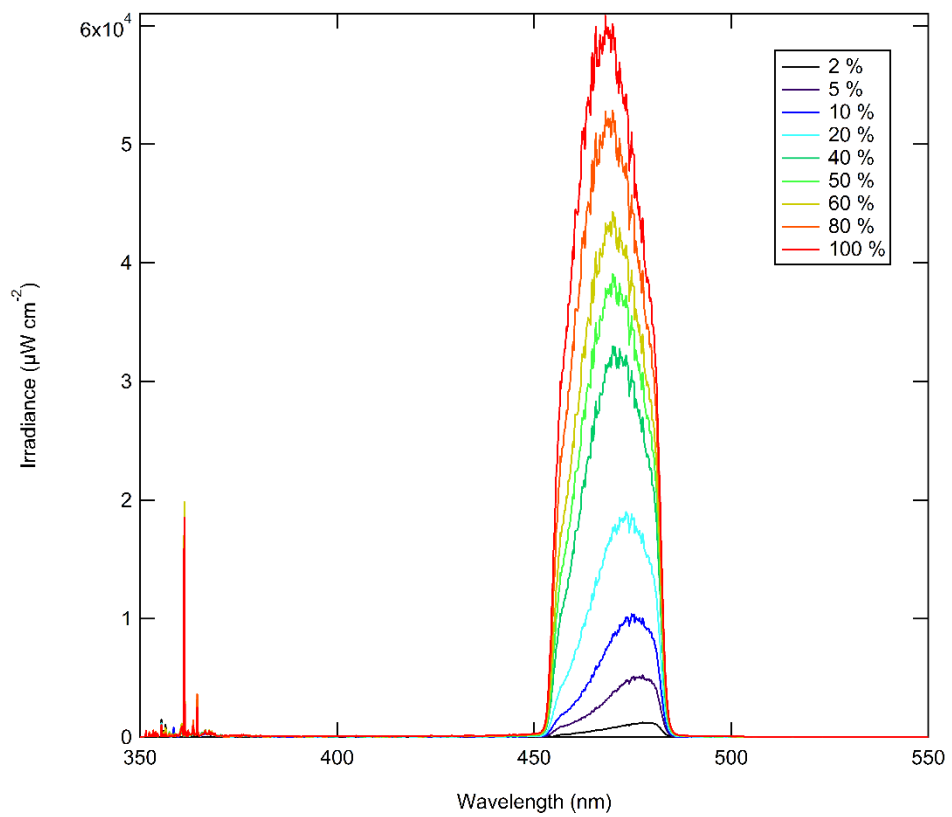
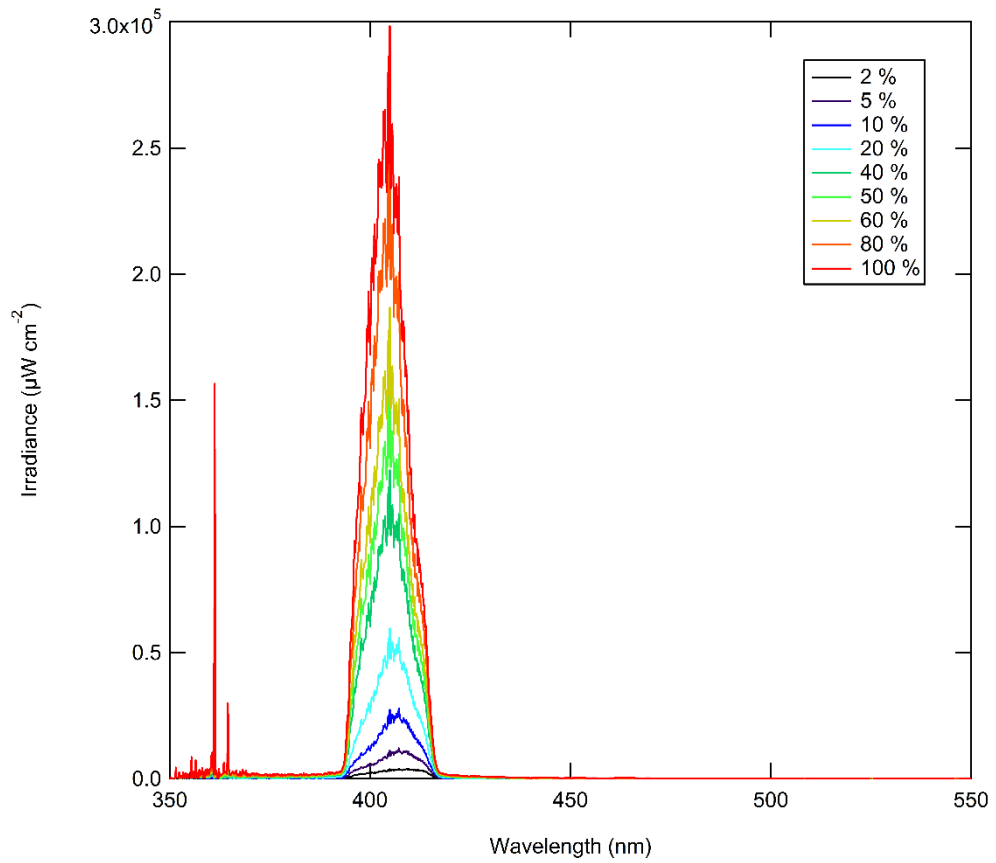


**Figure 2.3.** Peak emission irradiance as a function of increasing percentage power output from the light engine for the **(Top)** blue and **(bottom)** cyan colour channels.

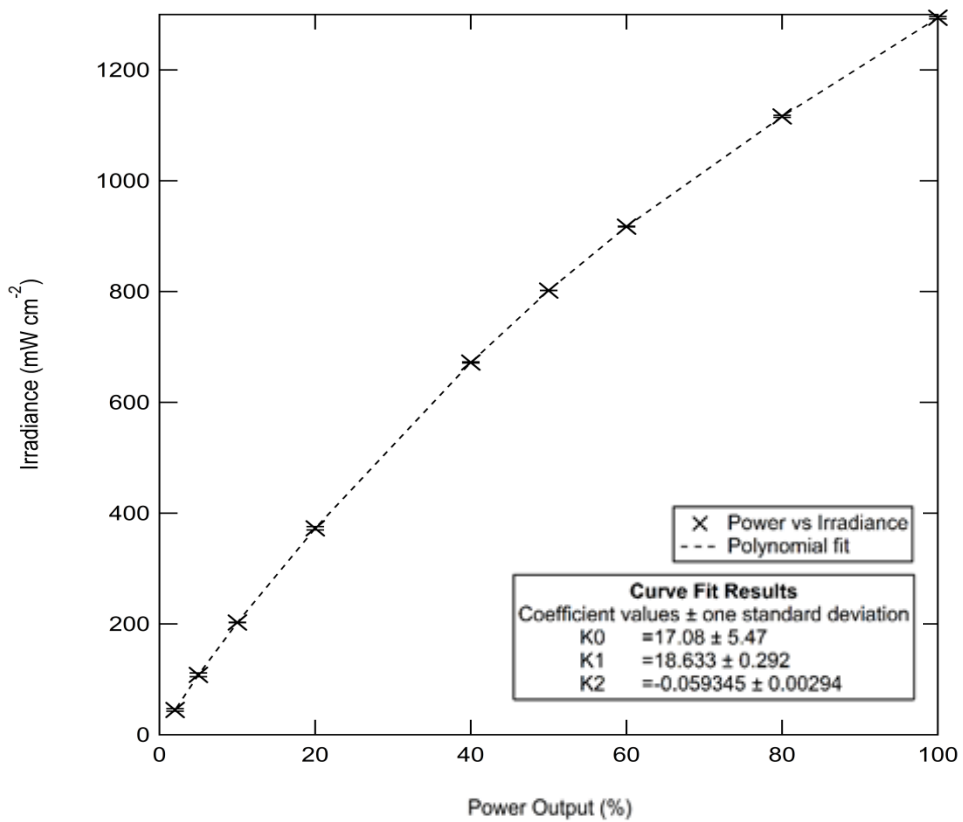
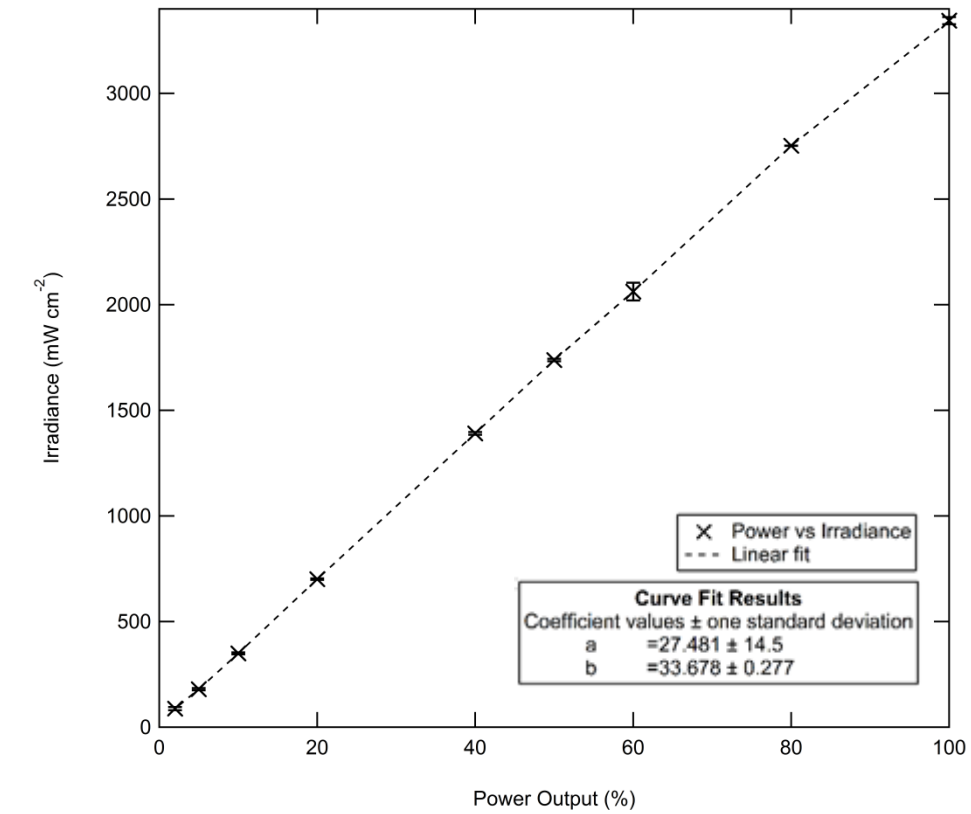


**Figure 2.4.** Calibration curves to obtain the integrated irradiance of the light engine as a function of the percentage power output for the **(top)** blue and **(bottom)** cyan colour channels. Error bars represent the standard deviation for three repeat measurements of the irradiance.

### **2.3.2 EMS Swiss Master Light Curing Unit**

Laboratory based photo-polymerisation of resins was performed using an EMS Swiss master light curing unit (EMS OPTIDENT, electro medical systems, Nyon, Switzerland). The curing unit is a water cooled device with a halogen light source and an 11 mm diameter tip. The spectral range covers 390 – 550 nm with the peak emission located at ~ 490 nm. The device has a maximum irradiance of 3000 mWcm<sup>-2</sup> and the time of illumination can be pre-programmed. The device features an internal photo-diode which is used to calibrate the intensity from the curing tip.

## **2.4 Production of Resin Test Specimens**

### **2.4.1 *In-situ* Photo - Polymerisation**

Unfilled resin disc-shaped specimens were produced *in-situ* on X-ray scattering beam lines by filling a 0.9 mm thick stainless steel ring (RS, Northants, UK) with a 10 mm internal diameter, sealed on both sides by 25 µm mica windows (Attwater Group, Lancashire, UK), with liquid monomer blends (section 2.2.3). Resin filled washers were housed within a brass block annulus and mounted in the path of impinging X-rays (Figure 2.5). Test specimens were photo-polymerised via a liquid light guide (Lumencor, Kent, UK) fixed normal to the resin surface and connected to a multichannel light source (Lumencor Aura Light engine, Lumencor, Kent, UK) to illuminate the sample. The separation distance between the light guide tip and the sample surface was set to either 10 or 15 mm for experiments on the BM28 and I22 beamlines respectively due to unavoidable geometrical constraints imposed by the different sample environments built in to the beam line set up. For each unique composition, monomer blends were photo-polymerised at four different irradiances to introduce a range of polymerisation rates, for the respective colour channel corresponding to either TPO or CQ initiated resins, controlled by the power output of the light engine (5, 20, 60 and 100% power output) for a total

of 300 s. Polymerisation rates for each specific sample geometry are reported in the each data chapter.

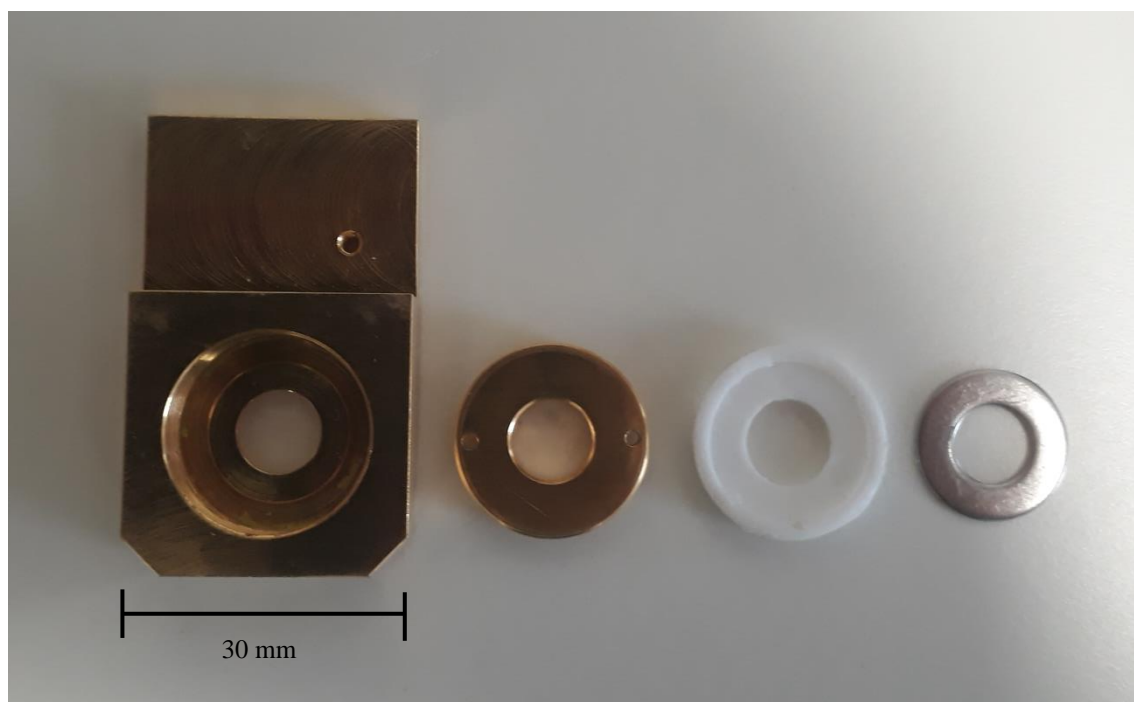


**Figure 2.5.** Liquid containment cells used for *in-situ* polymerisation simultaneous to X-ray scattering measurements. Liquid resin is stored inside a metal washer with mica windows, which is fixed into a PTFE washer that is housed within a brass annulus.

### 2.4.2 Unfilled Resin Discs – Laboratory

Unfilled resin disc-shaped specimens were prepared by filling a circular impression in a dental polyvinylsiloxane mould (11 mm diameter and 1 mm in depth) with liquid monomer blends (Section 2.2.3), and pressed flat with a microscope cover slide to prevent the formation of an oxygen inhibition layer. Resins were photo-polymerised using an EMS Swiss master light curing unit (EMS OPTIDENT, electro medical systems, Nyon Switzerland) which was placed normal to and in contact with the cover slide. For each monomer blend composition, the resin was either photo-polymerised at a relatively high ( $3000 \text{ mW cm}^{-2}$  for 6 s) or low ( $300 \text{ mW cm}^{-2}$  for 60 s) light intensity to introduce extreme rates of polymerisation whilst ensuring matched total energy doses. The resultant specimens were stored in dark conditions in sealed containers at  $4 \pm 1 \text{ }^\circ\text{C}$  prior to further use. A typical resin disc test specimen is shown in Figure 2.6.

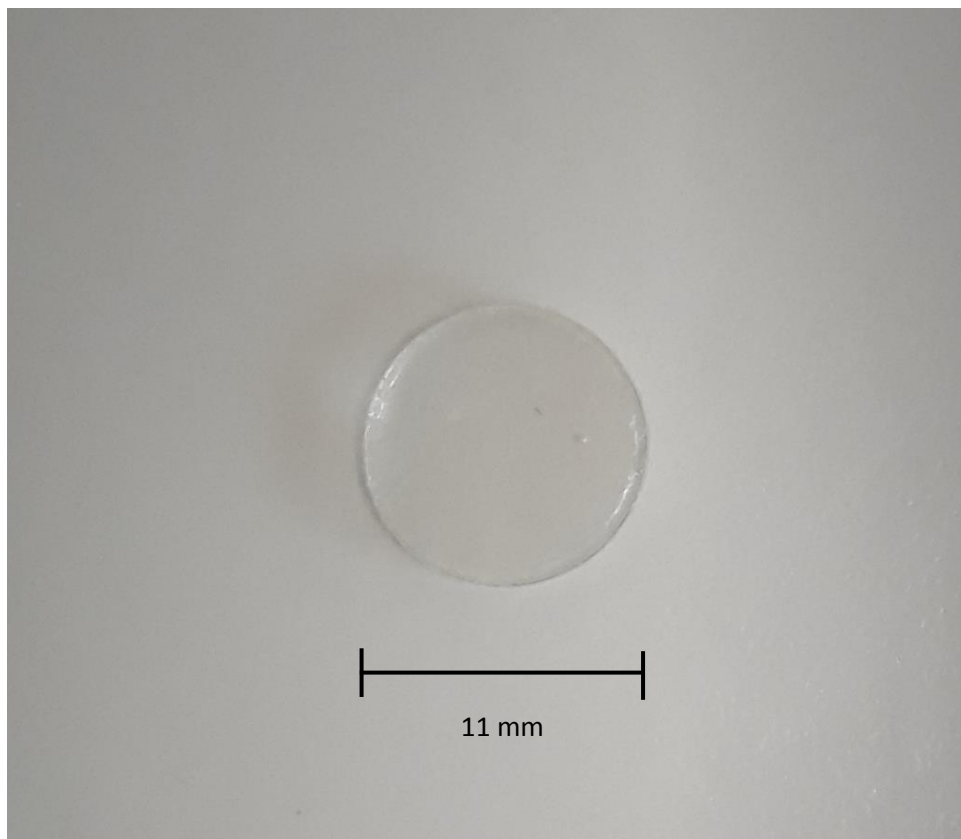


**Figure 2.6.** An unfilled resin disc test specimen.

### **2.4.3 Filled Resin Discs – Laboratory**

For each composition, 0.1 mL of RBC was applied to the surface of a calcium fluoride ( $\text{CaF}_2$ ) (30 mm x 1 mm: diameter x thickness), UV grade polished window (Crystan, Dorset, UK), and gently pressed with a glass microscope cover slide to an approximate thickness of 100  $\mu\text{m}$ . Composites were photo-polymerised using an EMS Swiss master light curing unit (EMS OPTIDENT, electro medical systems, Nyon Switzerland) which was placed normal to and in contact with the cover slide, illuminating the composite for 60 s at an intensity of 300  $\text{mWcm}^{-2}$ . Silicon carbide paper (P4000 roughness, Agar Scientific, Stansted, Essex, UK) was used to polish polymerised composites to a thin layer, approximately 10  $\mu\text{m}$  thick (measured with a digital micrometer) to only a single layer of filler particles, suitable for mid infra-red mapping. The resultant thin composite samples were stored in dark conditions in sealed containers at  $4 \pm 1$   $^\circ\text{C}$  prior to further use.

## 2.5 Characterisation

### Fourier Transform Infrared Spectroscopy

#### 2.5.1 Mid FTIR – Laboratory

The degree of monomer to polymer conversion (DC) was quantified before and after photo-polymerisation using Fourier Transform Mid-Infrared Spectroscopy (FT-MIR). Static measurements were made using a Nicolet 6700 spectrometer (Thermo Scientific, Warrington, UK), operating in attenuated total reflectance (ATR) mode utilising a diamond crystal sample mount through which the sample made contact with the evanescent wave. Liquids were deposited directly on to the ATR crystal whilst pre-cured resin disc specimens (Section 2.2.3) were held in contact with the diamond crystal by a turn screw to allow the evanescent wave to penetrate the sample. Spectra were collected using a white light source and an InGaAs detector over a spectral range of 850 to 4000  $\text{cm}^{-1}$  with a 2  $\text{cm}^{-1}$  spectral resolution. Final spectra were the sum of thirty two scans. Following a baseline correction, the aliphatic (1637  $\text{cm}^{-1}$ ) and aromatic (1608  $\text{cm}^{-1}$ ) absorption peaks were fitted with a Voigt model to determine the peak intensity. The degree of conversion was calculated from the change in the peak intensity of the aliphatic absorption band prior to and following photo-polymerisation as demonstrated in equation (2.1),

$$DC = \left( 1 - \left( \frac{(1637 \text{ cm}^{-1}/1608 \text{ cm}^{-1})^p}{(1637 \text{ cm}^{-1}/1608 \text{ cm}^{-1})^m} \right) \right) \times 100 \quad (2.1)$$

where  $m$  and  $p$  denote the absorption peaks in the monomer and polymer forms respectively. All aliphatic intensity measurements were normalised to the aromatic absorption peak, which is invariant with respect to polymerisation, to correct for variations in sample thickness.

## 2.5.2 Near FTIR

Dynamic measurements of monomer conversion and polymerisation rate were performed using laboratory based Fourier Transform Near Infrared Spectroscopy (FT-NIR). Near IR methods were used as mid-IR transmission techniques necessitates a thin transmission path which would provide insufficient X-ray scattering for kinetic measurements. Sample containment of liquid monomer blends was reproduced according to Section 2.4.1, whilst identical sample geometries, positioning and irradiance protocols as those used for X-ray scattering experiments at the BM28 and I22 beam lines respectively were applied. Optical (emitting and receiving) fibres (0.6 mm core diameter) (Helma Analytics, Essex, UK) were placed either side of the resin test specimen, which was mounted horizontally on a steel ring platform, at a 45° incline relative to the sample face and connected to a Nicolet 6700 spectrometer (Thermo Scientific, Warrington, UK) (Figure 2.7). Spectra were collected in transmission mode using a white light source and an InGaAs detector over a spectral range of 4000 to 10000 cm<sup>-1</sup> (2 cm<sup>-1</sup> spectral resolution) for >360 s with an integration time of 0.1 s. Data acquisition was collected 1 s prior to the initiation and subsequent photo-polymerisation of test specimens using the Lumencor light engine. The degree of conversion was calculated from the decrease in intensity of the aliphatic =CH<sub>2</sub> IR absorption band (6164 cm<sup>-1</sup>), located within the methacrylate functional end groups of the Bis-GMA and TEGDMA monomers,

$$DC = \left( 1 - \left( \frac{=CH_2^p}{=CH_2^m} \right) \right) \times 100 \quad (2.2)$$

where =CH<sub>2</sub><sup>m</sup> refers to the peak intensity of the band prior to polymerisation (in the monomer state) whilst =CH<sub>2</sub><sup>p</sup> corresponds to the peak intensity for the *i*<sup>th</sup> measurement. Additional spectral profiles were taken of the empty cell, mica windows and of the liquid monomer prior to illumination to correct for background subtraction and intensity normalisation. Data were baseline corrected using Omnic software (version 8.0, [www.ThermoScientific.com](http://www.ThermoScientific.com)).

Measurements were repeated three times to calculate averages for the degree of conversion and polymerisation rate. The experimental set up is shown in Figure 2.7.

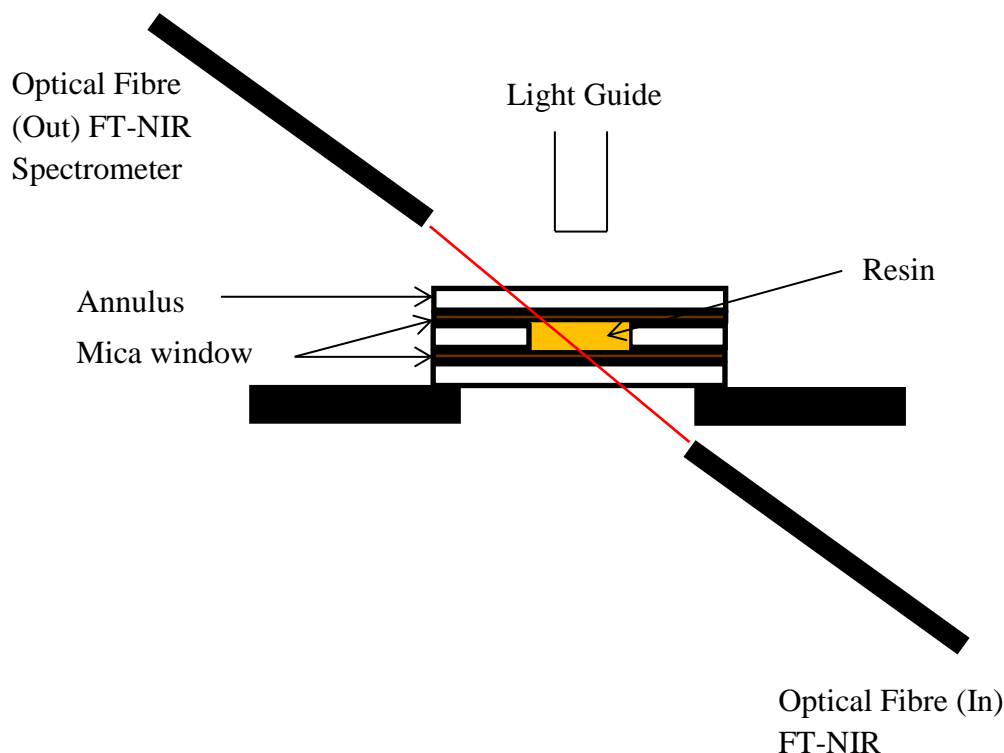


**Figure 2.7.** Experimental setup for laboratory based real time FT-NIR measurements. The resin samples were cured for more than 300 s at varying light intensities whilst undertaking FT-NIRS to quantify the degree of conversion.

### 2.5.3 Density Measurements

For density measurements, pre-cured resin samples were prepared and photo-polymerised in a disc geometry at either relatively fast or slow polymerisation rates as described in Section 2.4.2. Sample density was determined via a helium gas pycnometer (Quantachrome ULTRAPYC 1200e, Hartley Whitney, England). The volumes of the sample ( $V_c$ ) and reference ( $V_r$ ) cells prior to the insertion of the resin disc were calibrated using a 440-C stainless steel sphere with a known volume and mass of  $1.0725 \text{ cm}^3$  and 8.21 g respectively. Disc test specimens were measured inside a micro cell chamber (internal diameter = 15 mm, volume =  $4.25 \text{ cm}^3$ ) where

one measurement constituted the average of five internal automated measurements. The sample volume ( $V_s$ ) was calculated from the ratio of the initial pressure ( $P_1$ ) in the sample chamber, containing the resin disc sample with helium, to the pressure in the combined volume of the sample and reference chambers after being filled with helium ( $P_2$ ),

$$V_s = V_c + \frac{V_r}{1 - \frac{P_1}{P_2}} \quad (2.3)$$

The density was measured five times per disc (with each measurement consisting of five internal measurements) for three disc specimens and these values were used to calculate an average density for a specific blend and polymerisation regimen.

## **2.6 Production of X-rays from a Synchrotron Source**

X-ray scattering results/data presented in this thesis were collected at the European Synchrotron Radiation Facility (ESRF, Grenoble, France) [3] and the Diamond Light Source (DLS, Didcot, UK) [4]. Synchrotrons rely on the principle that an electron accelerated to relativistic velocities will emit Bremsstrahlung radiation when forced into a circular path by magnetic fields. The operation of these synchrotron facilities is outlined in detail in the following section.

### **2.6.1 Production of X-rays at the European Synchrotron Radiation Facility (ESRF)**

A 100 KeV triode gun injects electrons into a LINAC where they are accelerated to 200 MeV [5]. The electrons are then transferred into a small (300 m circumference) [5] internal ‘booster’ ring which precedes the main synchrotron storage ring. This booster ring is typically only active for a few minutes a day but serves to accelerate the electrons to  $\sim 6$  GeV [6] before filling the main storage ring. The booster ring transfers bunches of electrons every 50 ms to the storage ring during beam refills, which occurs twice a day. The main storage ring is a 268 m diameter tube held under vacuum to reduce air scattering. Within the ring the electron bunches are maintained at a working energy of 6 GeV [5], circulating at a revolution frequency of 355 kHz. The storage ring consists of 32 straight and 32 curved [7] sections in alternating order with each section containing magnets designed for specific purposes. The curved sections serve to confine the electron beam to an orbital flight path and consist of focussing magnets and bending magnets placed in a sequential array. The focussing elements are a series of alternating quadrupoles and sextupole [8] magnets which confine the beam transversely and correct for chromatic aberrations caused by the quadrupoles respectively. Bending magnets with a field strength of 0.4 T, curve the electrons flight path and consequently induces the emittance of a fan of X-rays tangentially to the plane of the electron beam [8]. The straight sections of the storage ring similarly contain focussing magnets but also incorporate insertion devices (IDs) to increase

the brilliance of X-rays relative to a bending magnet. Insertion devices come in two varieties – the wiggler and the undulator, both having similar designs and operation. Insertion devices are characterised by an alternating linear sequence of high field dipole magnets. Each dipole effectively behaves as a bending magnet but with a much smaller radius of curvature such that emitted X-rays propagate in the plane parallel to the line of dipoles. This creates a multiplicative effect in the intensity of the emitted X-rays, with the light from each dipole source constructively interfering with that of its neighbour to create a more intense and collimated beam in comparison to a conventional bending magnet. The main difference between the two types of insertion devices is that undulators have a shorter dipole period. Consequently, the radiation generated from an undulator causes sympathetic, resonant oscillations in other electrons, producing more coherent light with a narrower energy distribution. In comparison, wigglers have a broad energy distribution similar to that of a bending magnet but with a greater intensity. The radiation generated from a wiggler scales with the number of dipoles in the ID, whilst the radiation intensity scales with the square of the number of poles in the undulator. Inevitably as the electrons pass through the bending magnets and IDs, emitting X-rays, they lose energy. To compensate, radio-frequency cavities restore any loss and maintain the energy close to the nominal 6 GeV.

## 2.6.2 Production of X-rays at the Diamond Light Source

The Diamond Light Source is a medium energy (3 GeV) [9] synchrotron and has a similar design and operation to that of the ESRF. For this reason, this synchrotron will not be described in as great detail as for the ESRF. Instead, its salient physical and operational features are summarised in Table 2.3.

### ESRF vs Diamond Light Source

**Table 2.3.** A summary of the operating characteristics for the European synchrotron radiation facility compared to those of the smaller Diamond light source synchrotron.

| <b>Physical and Operational Features</b>       | <b>ESRF</b> | <b>Diamond Light Source</b> |
|--|-------------|-----------------------------|
| <b>Triode gun energy (keV)</b>                 | 100         | 90                          |
| <b>LINAC energy (MeV)</b>                      | 200         | 100                         |
| <b>Storage ring energy (GeV)</b>               | 6           | 3                           |
| <b>Storage ring beam current (mA)</b>          | 200         | 300                         |
| <b>Storage ring diameter (m)</b>               | 268         | 179                         |
| <b>Storage ring revolution frequency (kHz)</b> | 355         | 533.8                       |
| <b>No. straight sections</b>                   | 32          | 24                          |
| <b>No. curved section</b>                      | 32          | 24                          |

## Beam lines

Beam lines used predominantly for X-ray and neutron scattering for structural determination are described, whilst other beam lines are described in their respective chapters.

### BM 28 (ESRF)

A 0.4 T dipole bending magnet (bending magnet no.28, BM28) produces a swath of X-rays, from the impinging 6.04 GeV [10] electron beam in the ESRF storage ring, with an energy range of 2.4 – 15 keV [11]. The beam line has three operating modes; focussed monochromatic beam, unfocussed monochromatic beam and unfocussed polychromatic ‘white’ beam [12]. For the purpose of this thesis, operation of the focussed monochromatic beam setup will be discussed only.



**Figure 2.8.** Optics of the Bm28 (XMaS) beamline [10].

The incoming X-rays are collimated by primary slits and a monochromator (Figure 2.8), consisting of two channel cut Si (111) crystals [13], which select the working wavelength which is typically  $\sim 0.82 \text{ \AA}$  for the operation of this beam line. The beam is then focussed in the horizontal and vertical directions by two torroidal mirrors [13] oriented perpendicular to each other. The beam enters a 150 mm air free path modular section containing an intensity monitor, slits and attenuator foils to measure the beam intensity, reduce scatter and control the beam intensity respectively. After exiting this section the beam is collimated to its final dimensions

with vacuum tube slits before interacting with the sample. The slits have a maximum aperture of  $4 \text{ mm} \times 4 \text{ mm}$  with a 1 micron resolution. The beam size is typically defined as  $0.08 \times 0.5 \text{ mm}$  (horizontal  $\times$  vertical) during operation of BM28.

Samples are typically mounted normal to the direction of the impinging X-rays, in transmission geometry, on a motorised xyz stage (Huber 5012.2M mount) [14]. Translation is performed by three separate stepper motors with a  $1 \text{ }\mu\text{m}$  movement tolerance. The xyz stage sits inside a Eulerian cradle, consisting of a goniometer and a detector arm on which to mount a detector for wide angle scattering measurements. The scattered X-ray intensity are measured using a 165 mm diameter charged coupled device (CCD) 2D detector (MAR CCD 165, Rayonix, Norderstedt, Germany), either mounted on the detector arm of the cradle or directly behind the sample on a separate rail. The detector consists of  $2048 \times 2048$  single fibre optic sensor pixels which convert incoming X-rays to photons in the visible region which induces a voltage proportional to the incident X-ray count. The detector is segmented into four quadrants each with a  $4\text{K} \times 4\text{K}$  resolution, with each pixel binned to a  $2 \times 2$  box size to give pixel dimensions of  $80 \text{ }\mu\text{m} \times 80 \text{ }\mu\text{m}$ . The temporal resolution for data acquisition is 1 s in addition to a 4 s readout time. In a WAXS geometry with a small sample to detector distance, the detector can cover a  $2\theta$  region of approximately  $5 - 50^\circ$ . The beamline is not optimised for true SAXS measurements given its relatively small flight path post sample and large beam stops and can therefore achieve measurements in  $q$  as low as  $0.05 \text{ \AA}^{-1}$ .

## I16 (DLS)

X-ray photons are extracted from the Diamond storage ring by insertion device (I) 16 [15], which is a 2 m undulator with a 27 mm dipole period held under vacuum, providing an energy range of 3.5 – 15 keV. The white beam passes through a gas bremsstrahlung collimator before entering a monochromator array, consisting of a pair of Si (111) channel cut crystals to select the beam wavelength. The beam is then focussed vertically and horizontally by a torroidal and flat plate mirror [16] placed in series respectively to a beam width of 290  $\mu\text{m}$ . A further series of slits and attenuator foils are used to control the beam size and intensity depending on the test specimen composition. An ionization chamber is located before the last beam slit to monitor the intensity of the impinging beam, whilst slits define a beam size of 30  $\mu\text{m}$  (vertical)  $\times$  200  $\mu\text{m}$  (horizontal) for typical beam operation. The optical beam line arrangement prior to the sample is shown schematically in Figure 2.9.



**Figure 2.9.** Schematic representation of the I16 beam line optics leading to the diffractometer and sample stage (bottom left). The detector arm assembly is displayed in the bottom right, with the vacuum tube and Pilatus 100K detector, shown as the mauve and blue coloured regions respectively, attached.

Samples are mounted within a six axis kappa diffractometer (Figure 2.9, bottom left image) which offers up to  $100^\circ$  rotation about the sample z axis with a 0.1 mrad resolution. For this thesis, experiments conducted at I16 used a transmission sample geometry with the sample face normal to the direction of the impinging X-rays i.e. rotation of the diffractometer was zero. The diffractometer includes a  $2\theta$  arm rail onto which a Pilatus 100K [17] photon counting area detector is mounted to measure the scattered beam intensity. The detector is a  $487 \times 195$  pixel silicon diode array with a pixel size of  $172 \times 172 \mu\text{m}^2$ . It has an energy resolution of 500 eV and a readout time of 2.3 ms. The  $2\theta$  arm sweeps through angles  $0 - 120^\circ$  at a minimum increment of  $0.2^\circ$ .

## **I22 (DLS)**

I22 is a small angle X-ray scattering beam line [18] that operates with an undulator insertion device held under vacuum (Figure 2.10). The insertion device provides an initial energy range of 3.7 – 20 keV [19], corresponding to a wavelength range of 0.62 – 3.35 Å. The beam enters primary slits before the wavelength is selected via two, liquid nitrogen cooled, Si (111) channel cut crystals [19]. The beam is focussed in the horizontal and vertical dimensions by a set of torroidal Kirkpatrick-Baez geometry torroidal mirrors and further collimated by a series of slits and jaws to produce a  $320 \mu\text{m}$  (horizontal)  $\times$   $80 \mu\text{m}$  (vertical) beam at the exit of the last collimator prior to the sample stage [19]. Samples are mounted  $\sim 1$  m from the final slit on a precision x-y stage which allows for 0.1 m translation in the plane normal to the direction of the impinging X-ray beam. Two dimensional SAXS measurements are made using a silicon pixel Pilatus P3-2M area [20] detector positioned 1.9 – 9.9 m from the sample behind an extendable helium filled flight tube to reduce air scatter. The detector is composed of  $3 \times 8$  stack of individual modules with a total of  $1475 \times 1679$  pixels, a pixel size of  $172 \times 172 \mu\text{m}^2$  and a readout time of 0.95 ms. One dimensional WAXS measurements are performed by an in-house modified L shaped Pilatus P3-2M [21] (termed Pilatus P3-2M DLS – L) mounted in a fixed

position 0.17 m from the sample stage [19]. The modified detector has identical pixel and readout capabilities to the standard Pilatus P3–2M detector model. The combination of the SAXS and WAXS detectors allows coverage for a  $d$  space range of 1- 5000 Å.



**Figure 2.10.** Schematic of the I22 beamline, X-rays are generated by an undulator source and subsequently converted to a monochromatic beam. This beam is focussed by toroidal mirrors (27.73 m) and collimated by a series of slits downstream. The scattered X-ray intensity is measured by two detectors near and far from the sample to obtain WAXS and SAXS data respectively.

## 2.7 Production of Neutrons

Neutron scattering data presented in thesis were collected at the Institute Laue Langevin (ILL) [22] and the ISIS pulsed neutron source [23]. The operation of these two facilities is described in detail below.

### 2.7.1 Production of Neutrons at the Institute Laue Langevin (ILL)

The Institute Laue Langevin (ILL) is a high flux nuclear reactor which uses the fission of  $^{235}\text{U}$  to produce a constant flux of neutrons. The ILL reactor consists of a 10 kg element fuel rod of highly enriched (97 %) Uranium-235 [24]. The core has a diameter of 0.4 m and is controlled by a single, central control rod. Slow neutrons are initially produced by a  $(\gamma, n)$  reaction from Beryllium-9 ( $^9\text{Be}$ ) which coats the Boron control rod. Antimony-124 ( $^{124}\text{Sb}$ ) is used as the  $\gamma$ -emitter, which destabilises the Beryllium nucleus to produce a Beryllium isotope and a neutron in the endothermic reaction shown in equation [25] (2.4)



**Figure 2.11.** A slow neutron collides with and is absorbed by a Uranium-235 nuclei to form an energetically unstable Uranium-236 nucleus. The new nucleus splits into fission products and releases neutrons and gamma rays.

The neutrons produced from this reaction are absorbed by Uranium - 235 nuclei in the reactor core. This compound nucleus fissions into two new atoms and produces on average 2.5 neutrons and releases  $\sim 180$  MeV of energy per fission reaction [25], as shown in Figure 2.11.

During operation, 63 MW of energy is generated by the core in addition to gamma radiation and heat, which is removed by pumping light water ( $\text{H}_2\text{O}$ ) through the fins of the Uranium fuel element. The reactor core is surrounded by a 2.5 m (diameter)  $\text{D}_2\text{O}$  reflector vessel to direct outgoing neutrons back into the core to reduce losses in flux and to maintain the reaction. The  $\text{D}_2\text{O}$  is held at a temperature of 308 K and exchanges heat with  $\text{H}_2\text{O}$  from the nearby Drac river [25]. The reflector is enclosed by a tank of  $\text{H}_2\text{O}$  and a concrete radiation shield. There are also three purpose-built moderators maintained at different temperatures to provide a wide range of neutron spectra for the various instruments. The  $\text{D}_2\text{O}$  doubles as a moderator, producing thermal neutrons whose wavelengths range between 1 - 2 Å and have a Maxwell-Boltzmann distribution [24]. A graphite block heated to 2773 K via collisions with neutrons is used as a hot moderator to produce neutrons with wavelengths less than 1 Å, whilst a spherical 25 L vessel containing liquid deuterium at 20 K [25] generates neutrons with wavelengths between 5 – 20 Å. Neutrons exit the reactor core through helium filled beam tubes made of aluminium [26]. The beam tubes incorporate a slight curvature in their design to allow gamma radiation to escape tangentially through the aluminium walls [26], which are transparent to gamma radiation, to be absorbed by surrounding concrete shields. Neutrons are then transferred to rectangular guide tubes, composed of nickel coated glass [26], which internally reflect neutrons to allow them to propagate along the tube length to the experimental beam line.

### 2.7.2 Production of Neutrons at the ISIS Pulsed Neutron Source

The generation of neutrons at ISIS starts with  $H^-$  ions, which are produced from a plasma discharge ion source and accelerated to an energy of 35 keV [27]. The ions then enter a radio frequency quadrupole which produces an alternating electric field to both focus and accelerate the ions. Discrete bunches of  $H^-$  ions 4.94 ns apart are passed into the linear accelerator (LINAC), where high intensity frequency fields accelerate the ion beam to 70 MeV. The LINAC provides 200  $\mu$ s long, 22 mA  $H^-$  pulses which are transported to the synchrotron [27]. Prior to entry into the synchrotron, the ions are stripped of electrons by an aluminium oxide foil. The synchrotron has a 52 m diameter and consists of 10 dipole bending magnets which confine the protons to a pseudo-circular orbit. The protons are accelerated to 800 MeV [28] in two bunches and extracted from the storage ring at 50 Hz, producing a mean beam current of 200  $\mu$ A [27]. A further series of magnets within a beam pipe direct the ion beam to a target station and ensure that protons are kept in bunches. The proton beam strikes a water cooled non-fissile heavy metal target, which in this case are Tungsten plates coated with Tantalum which sits in a heavily shielded container. At ISIS there are two target stations appropriately named; target station one (TS1) and target station two (TS2). When protons strike the Tungsten, each collision yields  $\sim 15$  neutrons in addition to gamma radiation which are released isotropically. The process of proton production through to neutron spallation is shown schematically in Figure 2.12 [29].



**Figure 2.12** A schematic diagram of the ISIS pulsed neutron source (Didcot, UK).  $H^+$  ions are accelerated in the LINAC before being stripped of their electrons and accelerated again inside the synchrotron storage ring. These protons are then fired at a Tantalum coated Tungsten target to produce neutrons by spallation. Thermal neutrons are then guided towards beam lines by guide tubes.

Neutrons immediately produced following spallation are epi-thermal and have wavelengths too short to be used in scattering experiments. Consequently, moderator materials with similar nuclei mass are used to slow the neutrons down and transfer energy. Neutrons are slowed down to speeds suitable for scattering experiments by four moderators; liquid methane at 100 K, liquid hydrogen at 20 K and two water tanks at 293 K [28]. The moderator units are surrounded by water-cooled beryllium reflectors which are used to scatter neutrons back at the moderators to reduce losses in flux. Moderation results in a wider range of neutron energies, demonstrating a Maxwell-Boltzmann distribution. Following moderation the neutrons are funnelled towards the respective beamlines via beam ports [28].

## D16 (ILL)

Cold neutrons enter the D16 beam line from the guide hall and are horizontally collimated by slits (not shown). A pyrolic graphite (002) monochromator is used to select a neutron wavelength of  $\lambda = 4.5 \text{ \AA} \pm 1\%$  for normal operation modes and  $5.1 \text{ \AA}$  for alternative sample geometries. The beam is collimated by an additional set of slits and passes through a scintillator monitor to record the initial beam intensity, a foil attenuator (depending on the sample, the attenuator may need to be removed) to control the incident intensity at the sample surface and a Beryllium filter to cut off any neutrons with a wavelength below  $\lambda = 3.95 \text{ \AA}$ . The neutrons pass into an evacuated flight tube where the beam intensity is measured prior to the sample via another scintillator monitor. Beam dimensions are defined by a series of slits with a maximum size of  $30 \text{ mm}$  (vertical)  $\times$   $150 \text{ mm}$  (horizontal) and a minimum of  $5 \text{ mm} \times 5 \text{ mm}$ .



**Figure 2.13.** Diagram showing the entry of neutrons from the beam guide tubes through to the sample face on the D16 neutron diffractometer. The intensity of diffracted neutrons is captured via a  $1 \times 1 \text{ m}$  area detector mounted on a moveable semi-circular rail to allow scanning of particular  $q$  ranges.

Samples are mounted within a cadmium rack, to absorb neutrons, which sits on a translation stage [30] allowing movement in the plane perpendicular to the direction of the incoming neutron beam. The scattered intensity is collected by a moveable liquid nitrogen cooled  $^3\text{He}$  area detector mounted on a circular floor rail. The detector has a  $64 \times 16$  (1024) pixel geometry [31] with an individual pixel size of  $2.54 \text{ mm} \times 5.08 \text{ mm}$  [31, 32]. It is possible to vary the sample to detector distance between  $0.5 - 1 \text{ m}$  and rotate the detector up to  $90^\circ$  about the chi axis (see Figure 2.13, top panel left) to provide a  $q$  range of  $0.01 - 2.5 \text{ \AA}^{-1}$ [33].

## SANS2D (ISIS)

Unlike the previous instruments described in this section, SANS2D does not function using a monochromatic light source, operating instead as a time of flight (TOF) instrument. This technique utilises a ‘white’ neutron beam and requires the flight time of a neutron over a fixed path length to be accurately measured to determine its velocity and consequently its wavelength. This can be realised by combining the condition for Bragg scattering with the de Broglie’s equation,

$$\lambda = \frac{h}{mv} \quad (2.5)$$

$$\lambda = 2d\sin\theta \quad (2.6)$$

$$\lambda = \frac{ht}{mL} = 2d\sin\theta \quad (2.7)$$

Here,  $\lambda$  is the wavelength of the neutrons,  $h$  is Planck’s constant,  $m$  is the mass of a neutron,  $L$  is the length of the neutron flight path,  $t$  is the time taken to travel the length of this path and  $d$  is spacing between atomic reflection planes.

At SANS2D neutrons arrive from the source at target station 2 (TS2) where a Ni super mirror bender removes neutrons with a wavelength less than  $\lambda = 1.5 \text{ \AA}$ , producing a white neutron beam with a wavelength range of  $1.5 \leq \lambda \leq 12 \text{ \AA}$  [34]. A high frequency mechanical ‘chopper’ disc rotates at 10 Hz to time slice the beam to establish a start time for the beam pulse (Figure 2.14). The frequency of the chopper is also carefully chosen to prevent frame overlap, whereby fast neutrons overtake slower neutrons from a preceding pulse. A series of five 2 m steel

collimator tubes are used to reduce the beam intensity and define a beam with an 8 mm diameter.

Solid samples are housed within a cadmium rack with a series of circular apertures (15 mm diameter), whilst liquid samples are stored within quartz cuvettes which slot into the rack. The sample rack itself sits on a horizontal translation stage to allow sample changes. The scattered neutrons are recorded by two multi-wire  $^3\text{He} - \text{CF}_4$  area detectors (ORDELA) [35] placed inside a vacuum tank (13 m length, 3.2 m internal diameter) to reduce air scatter. The detectors have dimensions of 96.5 cm  $\times$  96.5 cm [35], a pixel geometry of 64  $\times$  16 (1024) and a pixel size of 5 mm  $\times$  5 mm [35]. The sample to detector position for both detectors can be varied along the 13 m path length of the vacuum tank to provide a  $q$  range [36] of  $0.002 \leq q \leq 3.0 \text{ \AA}^{-1}$ .



**Figure 2.14.** (top) Impression of the SANS2D beamline from left to right (bottom) a simplified schematic of SANS2D with the bender exit at 7 m (from the guide tube exit), sample at 19m and sample. Detectors may be placed within 2 -12 metres from the sample to provide a  $q$  range of  $0.0002 \leq q \leq 2.5 \text{ \AA}^{-1}$

## 2.8 Data Reduction

### 2.8.1 X-ray Scattering Data Reduction

X-ray scattering data was processed using the Fit2D [37] (version 12.077, ESRF) and DAWN [38] [39] (version 2.6.0) software packages for data files collected at the ESRF and Diamond light source respectively. Measured intensities  $I_d$  from the raw detector pixels were corrected for dark current ( $I_{dc}$ ) contributions and normalised to the count time ( $ct$ ) and to the monitor intensity ( $i_0$ ) to correct for variations in the incident beam i.e. during beam decay and refills.

$$I_{\Omega} = \frac{I_d/ct - I_{dc}/ct}{i_0} \quad (2.8)$$

Additional corrections were employed to adjust for differences in spherical angles in detector pixels due to a flat plate detector geometry and the detector quantum efficiency, before the data was azimuthally integrated and reduced to a 1D plot. The background intensity, as measured from the empty sample holder ( $I_{e\Omega}$ ), was subtracted from  $I_{\Omega}$ , after both were corrected for sample thickness ( $d$ ) and transmission factor  $T$ , to give the corrected sample intensity  $I_c$ .

$$I_c = \frac{I_{s\Omega}}{T_s d_s} - \frac{I_{e\Omega}}{T_e d_e} \quad (2.9)$$

Here,  $T_s$  and  $T_e$  correspond to the sample and empty container transmissions respectively, where  $T_e = 1$  and  $T_s$  is calculated via the following equation,

$$T_s = \left( \frac{I_{sf}}{I_{si}} \right) / \left( \frac{I_{ef}}{I_{ei}} \right) \quad (2.10)$$

The  $i$  and  $f$  subscripts refer to the beam intensity as measured by ion chambers before ( $i$ ) and after ( $f$ ) the sample, for the empty container ( $I_e$ ) and sample ( $I_s$ ). The corrected scattering intensity was converted to absolute units by using water as a primary calibration sample [40]. The absolute scattering of water is well characterised and demonstrates a plateau in intensity

between  $0.1 < q < 0.4 \text{ \AA}^{-1}$ , corresponding to an absolute scattering intensity of  $1.632 \times 10^{-2} \text{ cm}^{-1}$  [40] as shown in figure 2.15.



**Figure 2.15.** Scattering curves. Broken line: water scattering raw data. Dotted line: blank scattering of the empty capillary. Thick full line: scattering curve of water after subtraction of the blank scattering. Thin full line: horizontal fit.

A scaling factor ( $SF$ ) was calculated by comparing the intensity from X-ray scattering measurements of water, following data corrections outlined in equations 2.6-2.8, to the known value in absolute units. Water samples were left to acclimate to the temperature of the beam hutch, set to  $22^\circ\text{C}$ , as the compressibility of water varies as a function of temperature [41]. Scattering from experimental measurements of water was fitted with a linear function and extrapolated to  $q = 0$  to obtain an intensity value. Conversion to absolute units was achieved by multiplying the corrected intensity by this factor,

$$\left(\frac{\delta\Sigma}{\delta\Omega}\right)_s(q) = SF I_c \quad (2.11)$$

where the differential term represents the absolute scattering intensity ( $\text{cm}^{-1}$ ).

## 2.8.2 Small-Angle Neutron Scattering/ Neutron Diffraction

For all neutron scattering experiments presented in this thesis, polymer blend samples were prepared by combining a partially deuterated monomer with a completely hydrogenated monomer species. Section 2.2.2 describes a procedure for the isotopic substitution of hydrogen for deuterium in the methacrylic functional groups of the TEGDMA monomer, corresponding to 45.5% substitution of hydrogen by molecular weight. Deuteration serves two purposes for these measurements: deuterium has a larger coherent scattering length in comparison to hydrogen and as a consequence increases the scattering contrast between deuterated and hydrogenated monomers, effectively highlighting the d-TEGDMA monomer over Bis-GMA (Table 2.4). Additionally, by deuterating only the functional end groups of the TEGDMA monomer the functional groups become the predominant contributors to the coherent scattering signal. This allows for the average end to end distance  $\langle R \rangle$  of the TEGDMA monomeric unit to be measured as a function of polymerisation rate.

**Table 2.4.** X-ray and neutron scattering length densities for TEGDMA, Bis-GMA, Deuterium and deuterated TEGDMA (D-TEGDMA).

| Monomer  | X-ray scattering length density ( $10^{-6} \text{ \AA}^{-2}$ ) | Neutron scattering length density ( $10^{-6} \text{ \AA}^{-2}$ ) |
|----------|--|--|
| Bis-GMA  | 10.542   | 1.426  |
| TEGDMA   | 9.978  | 1.048  |
| d-TEGDMA | 9.978  | 3.440  |

Monomer blends were produced in 60/40 and 40/60 wt% formulations of Bis-GMA/d-TEGDMA with either CQ or TPO as photo-initiator and were mixed as described in section 2.2.3. Pre-cured disc-shaped specimens were prepared according to section 2.4.2 and were photo-polymerised at a relatively high ( $3000 \text{ mW cm}^{-2}$  for 6 s) or low ( $300 \text{ mW cm}^{-2}$  for 60 s) light intensity to introduce extreme rates of polymerisation whilst ensuring matched total energy doses. All unique sample compositions for neutron scattering experiments are listed in Table 2.5.

**Table 2.5.** A summary of monomer formulation ratios, initiation chemistry and photo-polymerisation regime for each pre-cured resin disc sample used for SANS measurements.

| <b>Bis-GMA</b> | <b>d-TEGDMA</b> | <b>Photo-initiator</b> | <b>Curing regime</b> | <b>Sample Code</b> |
|----------------|-----------------|------------------------|----------------------|--------------------|
| 60             | 40              | CQ                     | Fast                 | 60/40 CQ F         |
| 60             | 40              | CQ                     | Slow                 | 60/40 CQ S         |
| 40             | 60              | CQ                     | Fast                 | 40/60 CQ F         |
| 40             | 60              | CQ                     | Slow                 | 40/60 CQ S         |
| 60             | 40              | TPO                    | Fast                 | 60/40 TPO F        |
| 60             | 40              | TPO                    | Slow                 | 60/40 TPO S        |
| 40             | 60              | TPO                    | Fast                 | 40/60 TPO F        |
| 40             | 60              | TPO                    | Slow                 | 40/60 TPO S        |

Small angle neutron scattering (SANS) was conducted at the LoQ (ISIS, Didcot, UK), Sans2D (ISIS, Didcot, UK) and D16 (Institute Laue Langevin, Grenoble, France) beam lines. The first two beam lines are time of flight (TOF) SANS instruments and utilise a white beam with a wavelength range of 2.2–10 Å to provide a final  $q$  range of 0.006–1.4 Å<sup>-1</sup> in a single measurement window. The latter is a two-circle diffractometer operating with a monochromatic neutron beam with an energy of 2.755 keV corresponding to a wavelength of 4.5 Å. Consequently, several detector angle positions are required to cover a  $q$  range of approximately  $0.1 < q < 1.5$  Å<sup>-1</sup>. Pre-cured resin disc specimens were wrapped in aluminium foil and mounted in a cadmium sample rack. Liquid monomer blends were contained in quartz cuvettes with a 1 mm path length (Helma, QS/QX) and also wrapped in foil to prevent photo-polymerisation. Samples were measured for 15-25 min per detector bank position, depending on the instrument flux, to accrue sufficient counting statistics. Further details regarding the specific experimental geometry and set up are included in the relevant data chapters. To aid data analysis measurements were taken for the direct beam, empty sample containers (aluminium foil and quartz cuvettes) and sample transmission. Data was converted to scattering cross section using the LoQ and Sans2D plugins for the MantidPlot [42] software package whilst the Large Array Manipulation Program [43] (LAMP) was used to reduce data from D16, ILL. Data was placed on an absolute scale (cm<sup>-1</sup>) using the scattering from either a solid blend of hydrogenous and pre-deuterated polystyrene or a vanadium sample.

### 2.8.3 Data Fitting SAXS and SANS

Scattering peaks from the processed data were fit with Gaussian models to obtain the peak centre and the full width at half maximum (FWHM). The peak centre represents  $q_{max}$ , which for polymeric systems with only short range order corresponds to an average correlation length. Using equation 1.24 this value was used to approximate an average distance  $d$ , between scattering centres. The width of the scattering peak (FWHM) represents the distribution of correlation lengths that the peak denotes. A wider peak corresponds to greater variability in the polymer conformation and reduced correlation for the distances between scattering centres, which would be referred to as having less short range order. Changes in order, under dynamic conditions, were calculated as the absolute percentage change in the FWHM with respect to the initial value. Data fitting was performed using the Python programming language and Mantidplot [42] software for SAXS and SANS analysis respectively.

## 2.9 References

1. Trujillo-Lemon, M., et al., *Dimethacrylate derivatives of dimer acid*. Journal of Polymer Science Part A: Polymer Chemistry, 2006. **44**(12): p. 3921-3929.
2. *Documentation and Software*. [Accessed 2013 November 11]; Available from: <http://lumencor.com/resources/documentation-software/?section=S1>.
3. Bösecke, P., O. Diat, and B. Rasmussen, *High-brilliance Beamline at the European Synchrotron Radiation Facility*. Review of Scientific Instruments, 1995. **66**(2): p. 1636-1638.
4. *Diamond Light Source Home Page*. 2017 [cited 2017 June 29]; Available from: <http://www.diamond.ac.uk/Home.html>.
5. *ESRF Home Page - Parameters*. 2017 [cited 2017 May 6]; Available from: <http://www.esrf.eu/home/UsersAndScience/Accelerators/parameters.html>.
6. *ESRF Home Page - Accelerators*. 2017 [cited 2017 May 17]; Available from: <http://www.esrf.eu/home/UsersAndScience/Accelerators.html>.
7. *ESRF Home Page - What is a Synchrotron*. 2017 [cited 2017 August 8]; Available from: <http://www.esrf.eu/about/synchrotron-science/synchrotron>.
8. *ESRF Home Page - The Accelerator Complex*. 2017 [cited 2017 August 7]; Available from: <http://www.esrf.eu/home/UsersAndScience/Accelerators/the-accelerator-complex.html>.
9. *Diamond Light Source - Machine Status*. 2017 [cited 2017 August 1]; Available from: <http://www.diamond.ac.uk/Science/Machine.html>.
10. *XMaS: The UK Materials Science Facility at the ESRF*. [cited 2017 June 15]; Available from: [http://www2.warwick.ac.uk/fac/cross\\_fac/xmas/](http://www2.warwick.ac.uk/fac/cross_fac/xmas/).
11. Thompson, P., et al., *Optimizing the XMaS Beamline for Low energy Operations to Maximize Benefits from the ESRF Upgrade Program*. Vol. 1234. 2010. 407-410.

12. *BM28 - XMaS*. [cited 2017 June 16]; Available from:  
<http://www.wayforlight.eu/eng/synchrotrons/esrf/esrf-beamlines/bm28-x-ray-magnetic-scattering-beamline.aspx>.
13. Brown, S.D., et al., *The XMaS beamline at ESRF: instrumental developments and high-resolution diffraction studies*. Journal of Synchrotron Radiation, 2001. **8**(6): p. 1172-1181.
14. Thompson, P., et al., *New Developments at the XMaS Beamline For Magnetic and High Resolution Diffraction*. Vol. 705. 2004.
15. Collins, S.P., et al., *Diamond Beamline I16 (Materials & Magnetism)*. AIP Conference Proceedings, 2010. **1234**(1): p. 303-306.
16. Collins, S.P., et al., *The simplest possible design for a KB microfocus mirror system?* AIP Conference Proceedings, 2016. **1741**(1): p. 040018.
17. Marchal, J., N. Tartoni, and C. Nave, *Synchrotron applications of pixel and strip detectors at Diamond Light Source*. Nuclear Instruments and Methods in Physics Research Section A: Accelerators, Spectrometers, Detectors and Associated Equipment, 2009. **604**(1): p. 123-126.
18. Inoue, K., J. Douth, and N. Terrill, *The Current Status of Small-angle X-ray Scattering Beamline at Diamond Light Source*. BUNSEKI KAGAKU, 2013. **62**(6): p. 565-570.
19. *I22: Technical Specifications*. 2017 [cited 2017 August 7]; Available from:  
<http://www.diamond.ac.uk/Beamlines/Soft-Condensed-Matter/small-angle/I22/specs.html>.
20. *Diamond Confluence: Pilatus P3-2M*. 2017 [cited 2017 August 5]; Available from:  
<http://confluence.diamond.ac.uk/display/SCATTERWEB/Pilatus+P3-2M>.
21. *Diamond Confluence: Energy and Camera Length*. 2017 [cited 2017 June 10]; Available from:  
<http://confluence.diamond.ac.uk/display/SCATTERWEB/Energy+and+Camera+Length>

22. *ILL Home Page: What is the ILL?* 2017 [cited 2017 June 3]; Available from:  
<https://www.ill.eu/about/what-is-the-ill/>.
23. *ISIS Home Page* 2017 [cited 2017 May 4]; Available from:  
<https://www.isis.stfc.ac.uk/Pages/home.aspx>.
24. *Advanced Certificate in Powder Diffraction on the Web: Nuclear Reactors*. 2017 [cited 2017 June 12]; Available from: <http://pd.chem.ucl.ac.uk/pdnn/inst3/reactors.htm>.
25. in *Neutron Data Booklet*, G. Lander, Editor. 2003, Old City Publishing.
26. *Advanced Certificate in Powder Diffraction on the Web: Guide Halls and Guide Tubes*. 2017 [cited 2017 Jul 10]; Available from:  
<http://pd.chem.ucl.ac.uk/pdnn/inst3/guides.htm>.
27. *How ISIS works: In depth*. 2017 [cited 2017 June 18]; Available from:  
<https://www.isis.stfc.ac.uk/Pages/How-ISIS-works--in-depth.aspx>.
28. *How ISIS works*. 2017 [cited 2017 June 9]; Available from:  
<https://www.isis.stfc.ac.uk/Pages/How-ISIS-works.aspx>.
29. *Advanced Certificate in Powder Diffraction on the Web: Production of Spallation Neutrons*. 2017 [cited 2017 June 4]; Available from:  
<http://pd.chem.ucl.ac.uk/pdnn/inst3/pulsed.htm>.
30. Büttner, H.G., *New ILL instrumentation*. Neutron News, 1997. **8**(4): p. 21-26.
31. Cristiglio, V., et al., *D16 is back to business: more neutrons, more space, more fun*. Neutron News, 2015. **26**(3): p. 22-24.
32. Stefanescu, I., et al., *Neutron detectors for the ESS diffractometers*. Journal of Instrumentation, 2017. **12**(01): p. P01019.
33. *D16 - Small momentum transfer diffractometer*. [cited 2017 July 8]; Available from:  
<https://www.ill.eu/instruments-support/instruments-groups/instruments/d16/description/instrument-layout/>.
34. Heenan, R., et al., *SANS2D at the ISIS Second Target Station*. 2006.

35. Duxbury, D., et al., *Performance characteristics of the new detector array for the SANS2d instrument on the ISIS spallation neutron source*. Journal of Instrumentation, 2014. **9**(12): p. C12051.
36. *Sans2d technical information [cited 2017 June 6]; Available from: <https://www.isis.stfc.ac.uk/Pages/Sans2d-technical-information.aspx>.*
37. Hammersley, A.P., et al., *Two-dimensional detector software: From real detector to idealised image or two-theta scan*. High Pressure Research, 1996. **14**(4-6): p. 235-248.
38. Basham, M., et al., *Data Analysis Workbench (DAWN)*. Journal of Synchrotron Radiation, 2015. **22**(3): p. 853-858.
39. Filik, J., et al., *Processing two-dimensional X-ray diffraction and small-angle scattering data in DAWN 2*. Journal of Applied Crystallography, 2017. **50**(Pt 3): p. 959-966.
40. Orthaber, D., A. Bergmann, and O. Glatter, *SAXS experiments on absolute scale with Kratky systems using water as a secondary standard*. Journal of Applied Crystallography, 2000. **33**(2): p. 218-225.
41. Fritz, G., G. Scherf, and O. Glatter, *Applications of Densimetry, Ultrasonic Speed Measurements, and Ultralow Shear Viscosimetry to Aqueous Fluids*. The Journal of Physical Chemistry B, 2000. **104**(15): p. 3463-3470.
42. Arnold, O., et al., *Mantid—Data analysis and visualization package for neutron scattering and SR experiments*. Nuclear Instruments and Methods in Physics Research Section A: Accelerators, Spectrometers, Detectors and Associated Equipment, 2014. **764**: p. 156-166.
43. Richard, D., M. Ferrand, and G. Kearley, *Analysis and visualisation of neutron-scattering data*. Journal of Neutron Research, 1996. **4**(1-4): p. 33-39.

## **3 NOVEL INSIGHTS INTO STRUCTURAL VARIABILITY OF *IN-SITU PHOTO-* POLYMERISED DIMETHACRYLATE POLYMERS**

### **3.1 Introduction**

Photo-initiated resin polymers are of great biomedical importance, in orthopaedics and in particular in dentistry where they are used as a matrix to form resin based-composites (RBC) filling materials. The physiochemical properties of these materials are highly sensitive to photo-polymerisation variables and as a consequence clinical performance is not ideal. The effect that photo-polymerisation has on the polymer phase of RBCs has been extensively characterised through the use of FTIR (Fourier transform infra-red spectroscopy) to quantify real time monomer-polymer conversion from which many correlations with mechanical properties have been extrapolated [1-3]. However, the impact that polymerisation rate has on the resultant cross-linked structure is unknown. The present work explores for the first time the effect that polymerisation variables and ultimately the reaction rate have on the short range (<10 Å) polymer structure of common dimethacrylate resin systems.

The majority of dental RBCs are comprised of combinations of dimethacrylate resins and inorganic filler particles. Following application to the tooth surface the uncured RBC filling is 'demand-set' using light excitation of a photo-initiator species dispersed within the resin matrix to initiate free radical polymerisation, generating a solid three-dimensional cross-linked network [4, 5]. Contemporary RBCs typically achieve between 55-75% of monomer-polymer conversion of the starting reagents [6, 7]. A higher degree of monomer conversion (*DC*) has been shown to significantly influence resultant mechanical properties, conferring increased flexural strength, surface hardness [8], elastic modulus and wear resistance to an RBC. Increasing conversion however, is accompanied by a deleterious effect of polymerisation shrinkage [9]. This process is inherent in dimethacrylate materials as the conversion of carbon-carbon double bonds reduces intermolecular separation distances and condenses interstitial free

volume between monomers [10, 11]. Polymerisation shrinkage generates internal stresses [12] within the resin matrix, which can be transferred to the interface with the tooth structure and compromise the bond, leading to premature failure of the RBC [9].

Several studies have therefore proposed that the final properties of an RBC are determined predominantly by the maximum degree of conversion ( $DC_{max}$ ) which can be 'tuned' by manipulating the intensity of and exposure to the activating light source [13-15]. It has been argued that  $DC_{max}$  and the subsequent mechanical properties are influenced by the total photon delivery irrespective of how they are delivered, a concept known as exposure reciprocity [16, 17]. However, several studies have criticised these findings, citing a narrow range of reaction rates and resin viscosities as a limiting factor to the behaviour of these systems [13, 18]. RBCs are complex and a total energy/ $DC$  concept may not adequately describe their behaviour. The polymer phase of contemporary RBCs is typically composed of a viscous monomer and reactive low molecular weight diluent monomer(s). Monomer structure, viscosity and co-monomer concentration will all impact on the mobility and reactivity of the evolving network [19-23]. Similarly, photo-initiator chemistry can influence the polymerisation rate and  $DC_{max}$  with common initiators providing differences in quantum efficiency and absorption spectra [24-26]. The efficacy of the photo-initiator though, is also dependent on the emission spectra, intensity and exposure time of the activating light source and the better the overlap between the emission and absorption spectra, the greater the radical production efficiency [27]. These systems therefore are dependent on the interplay of many variables which cannot be separated from each other nor can be simply reduced to the sum of absorbed photons or  $DC_{max}$ .

Contrary to the total energy/ $DC_{max}$  concept numerous recent studies have demonstrated that different combinations of light intensity and exposure i.e. reaction rate, can significantly influence final material properties. It is widely reported that accelerating polymerisation using high intensity light activation can impact on the tensile strength, toughness, hardness and degree of polymerisation shrinkage and stress of these materials [3, 18, 28, 29]. Indeed a parabolic relationship between the reaction rate,  $DC$  and final mechanical properties [30] has been shown

to exist [31]. To date these differences in mechanical properties have been ascribed to cross-link density and its effect on network architecture. Faster reactions reduce the lifetime of radical species with respect to bimolecular termination [29], reducing the degree of cross-linkage which will lower the strength of the resultant RBC. Therefore, in cases where glass transition temperatures ( $T_g$ ) are similar, small differences in  $T_g$  may yield significant discrepancies in mechanical properties [17]. Conversely, a slower reaction and the delayed onset of gelation allows more time for emerging radicals to propagate and to cross-link. Further, a greater mobility by the extension of pre-gel stages of the reaction may allow the bulk of the resin matrix to relax and relieve stress by elastic flow. This notion has been incorporated into ‘soft-start’ light irradiation techniques to reduce polymerisation stress, whereby low intensity light is used to instigate polymerisation whilst higher intensities are used later in the reaction [32]. However, this condition appears to hold only at low  $DC$  and its ability to alleviate stress becomes negligible at higher  $DC$  [33].

Previous research has focussed on interpreting final mechanical properties from the  $DC$  of RBCs and indirect measures of cross-link density such as surface hardness. It is therefore surprising that despite much effort being made to alter monomer chemistry [34] to increase reactivity and  $DC_{max}$ , no consideration has been given as to what effect reaction rate and conversion have on the final polymer structure.

The concept that an identically composed and converted material can demonstrate different structures as a consequence of polymerisation rate arises from consideration of the reaction itself. Photo-curing at a high irradiance in contrast with low irradiance will drive the polymerisation reaction faster. At increased rates of monomer to polymer conversion and cross-linking, the emerging structure has less time to achieve its most energetically favourable form. In contrast slowing the reaction rate down may allow the propagating polymer chains to move relatively to find the most energetically efficient state. Accordingly, a difference in order (conformation) at short length-scales can exist and such differences can affect the mechanical properties of the material. The challenge in identifying such differences in order exists, because

the likely structural differences at relatively short ( $<10 \text{ \AA}$ ) and longer length scales are likely to be subtle.

Structural order in materials can be detected using light and particle scattering methods. Standard scattering measurements using laboratory X-ray sources fail to provide sufficient flux to discern such differences in these materials, especially when dynamic (*in-situ*) curing studies with short measurement times are conducted. Synchrotron light sources however, provide the necessary flux, energy range and flexible sample environment to allow order at intramolecular distances to be determined using X-ray scattering methods. For this study commercially available dental RBCs, were purposely not used, since resin compositions photo-initiator and inhibitor chemistry and filler morphology vary widely are often not fully specified by the manufacturer. The differences in formulation would make it difficult to systematically determine the impact of compositional variables on subtle structural changes within the resin matrix. Instead, experimental resin blends of clinically relevant monomers, consisting of a viscous monomer, a diluent and photo-initiator system were used to understand the effects that relative viscosity, reactivity and terminal conversion have on the resultant polymer structure.

This novel enquiry aims to characterise the evolution of the polymer structure during photopolymerisation in terms of order and correlation lengths as a function of polymerisation rate. As there is no previous enquiry in this area the null hypothesis that there is no relationship between polymerisation rate and structural conformation of the resultant RBC polymer network normalised to *DC* was tested.

## **3.2 Methods**

### **3.2.1 Preparation of Photo-Polymerisable Dimethacrylate Resin Blends**

Dimethacrylate monomers, bisphenol-A-glycidyl-methacrylate (Bis-GMA and triethyleneglycol-dimethacrylate (TEGDMA) (Sigma-Aldrich, Dorset, UK) were proportioned in 70/30, 60/40, 50/50 and 40/60 (Bis-GMA/TEGDMA) weight percentage (wt. %) ratios and combined to produce 10 g mixes. The viscosity of the blend increases with the proportion of Bis-GMA. The monomer blends were produced according to the resin formulation protocol described in section 2.2.3

### 3.2.2 Synchrotron X-ray Scattering Measurements

Synchrotron X-ray scattering experiments were carried out on the XMaS beamline (BM28) at the European Synchrotron Radiation Facility (ESRF, Grenoble, France). An incident X-ray energy of 15 keV was used corresponding to a wavelength ( $\lambda$ ) of 0.82 Å, with a beam size of 0.08 × 0.5 mm (horizontal × vertical) defined by vacuum tube slits. Measurements were carried out in air, at 23 ± 1 °C with light excluded other than the photo-curing light source.

For each resin blend, test specimens were prepared according to section 2.4.1. A 5 mm diameter light guide (Lumencor, Kent, UK) was fixed normal to and 10 mm distant from the centre of the resin surface and connected to a multichannel light source (Lumencor Aura Light engine, Lumencor, Kent, UK) to illuminate the sample. For the TPO initiated resins, the light engine was programmed to emit a peak emission spectrum at 405 nm, whilst for CQ systems a wavelength of 470 nm was employed. The wavelengths of light were chosen to match the maxima in the absorption spectra of the respective photo-initiators [35]. For each unique composition, samples of monomer blends were photo-polymerised at four different irradiances for each wavelength controlled by the power output of the light engine (5, 20, 60 and 100% power output) for a total of 300 s. Irradiances were calculated at increasing power outputs using a UV/visible spectrometer (MARC Light Collector, Dalhousie, USA) positioned normal to the tip of the light guide at separation distances of either 10 or 15 mm. The irradiance for each experimental set-up, for each light source and power setting and are reported in the results section.

2D scattering images were collected using a 2048×2048 pixel MAR CCD (MAR CCD 165, Rayonix, Norderstedt, Germany) camera, 570 mm from the sample to give a  $q$  range of 0.1 to 1.9 Å<sup>-1</sup>, where  $q=4\pi \sin\theta/\lambda$  (here  $\theta$  is equivalent to half the angle between the incident X-rays and the detector). A Helium filled flight tube was employed to minimise air scattering. Scattering images were collected with a 1 s count time and a 4 s readout time giving a 5 s

temporal resolution. Time resolved scattering measurements were conducted for each resin-blend by initially collecting data for 20 s prior to remote activation of the light engine. In addition to the time resolved photo-activated samples, X-ray measurements were acquired for the constituent monomers (Bis-GMA and TEGDMA) in isolation and containing photo-initiator to identify their contributions to the scattering signal of each blend. The contribution of the X-ray beam to the measurements was assessed by conducting observations for over 30 min for the uncured and polymerised samples in the absence of light (see appendix). To aid data analysis measurements were taken for direct beam, empty sample containers, Mylar windows, water and a silver behenate calibration standard to allow the scattering patterns to be corrected for background and normalisation effects. Transmitted beam was recorded throughout using a beam-stop mounted photodiode. Data were normalised to the incident monitor intensity and background corrected using the Fit2D software package (version 12.077, ESRF) [36]. Data were azimuthally integrated over  $360^\circ$  to produce a 1D output and were subsequently fitted with Gaussian [37] models to determine peak positions and relative order.

### 3.2.3 Ex-situ Fourier Transform Near Infrared Spectroscopy

Laboratory-based Fourier Transform Near Infrared Spectroscopy (FT-NIR) was used to determine the reaction rate and  $DC_{\max}$  for each resin blend. Details of the sample preparation, sample geometry, sample containment and data collection are covered in chapter two, section 2.5.2 and shown schematically in Figure 2.7. The degree of monomer to polymer conversion was calculated using equation (2.2).

### 3.2.4 Simultaneous X-ray Scattering and FT-NIR Measurements and Increased Time Resolution

To confirm the correlation of observations from synchrotron radiation (SR) X-ray scattering and separate laboratory FT-NIR experiments further simultaneous SR-scattering/FT-NIR measurements were performed on the I22 beamline (Diamond Light Source, Oxford, UK). An incident X-ray energy of 12 keV was used corresponding to a wavelength of  $1.033\text{\AA}$  with a beam size of  $0.32 \times 0.08$  mm (horizontal  $\times$  vertical). Identical sample geometries and sample holders to those used in previous experiments at BM28 were used with the exception of the replacement of Mylar windows with 25  $\mu\text{m}$  thick mica (Attwater Group, Lancashire, UK). Samples were mounted to impinge the X-ray beam at a  $40^\circ$  incline in the positive azimuthal direction. The light guide of the multi-channel Lumencor light engine was placed 15 mm distant from and perpendicular to the resin sample and fixed in place to illuminate only the sample that was directly in the path of the X-rays. 2D scattering patterns were collected every second (1 s readout) with a Pilatus (P3-2M) providing a  $q$  range of 0.1 to  $1.6\text{\AA}^{-1}$ . Additional measurements were made using a 400  $\mu\text{s}$  time resolution to confirm that a one second capture rate, used for all other scattering measurements, accurately characterised dynamic structural changes. *In-situ* real time FT-NIR was incorporated into the beamline set-up to obtain simultaneous (to the scattering data) measurements of monomer conversion throughout photo-polymerisation. Identical FTIR fibres to those used in previous measurements were mounted at a  $45^\circ$  incline relative to the

sample face and connected to a Nicolet IS50 spectrometer (Thermo Scientific, Warrington, UK). Real time NIR spectra (4000 to 10000  $\text{cm}^{-1}$ ) were collected in transmission mode (4 $\text{cm}^{-1}$  spectral resolution) for 300 s with an integration time of 0.3 s. The experimental set up for the simultaneous X-ray scattering and FTIR measurements is shown in Figure 3.1.

In addition to *in-situ* photo-polymerisation measurements and control/calibration measurements, scattering patterns were obtained for control molecules that possess similar structures to those under investigation (methacrylic acid, methyl methacrylate, ethylene glycol, tri-ethylene glycol, bisphenol A and bisphenol A dimethacrylate (Sigma-Aldrich, Dorset, UK)). The data were normalised and background corrected using the DAWN software package [38]. Data were radially averaged over 360° to produce a 1D output and were subsequently fitted with Gaussian models to obtain the peak centre and the full width at half maximum (FWHM). The peak position corresponds to the average bond length (correlation length) whilst the FWHM represents the distribution of correlation lengths that the peak denotes. Therefore, a narrower peak shape will correlate to less variability in the correlation length, which would be referred to as having greater short range order. The increase in relative order was calculated as the absolute percentage change in the FWHM with respect to the initial value. Increases in the correlation length and relative order were normalised to the final degree of conversion in order to allow comparisons between polymer samples with different degrees of conversion. Error bars for the change between the initial and final values of the correlation length and relative order were calculated by substituting peak fitting uncertainties, as obtained from the fitting software, into propagation of error equations [39]. Additionally, for measurements normalised to  $\text{DC}_{\text{max}}$ , the uncertainty in  $\text{DC}_{\text{max}}$  was obtained from the standard deviation of the co-added FT-NIR scans of the aliphatic =CH<sub>2</sub> IR absorption band signal.

Weighted least squares (WLS) fitting was used to determine the contribution of individual monomers and constituent monomers, approximating the structure of segments of the Bis-GMA and TEGDMA, to the total X-ray scattering pattern. Time resolved X-ray scattering patterns for Bis-GMA and TEGDMA were initially (WLS) fitted to Bis-GMA/TEGDMA resin blend

signals to ascertain their respective contributions at the beginning and end of polymerisation. This process was then repeated for each of the component monomers, for example methacrylic acid which represents the methacrylate functional group found in Bis-GMA and TEGDMA, to determine the location(s) of structural changes within Bis-GMA and TEGDMA.

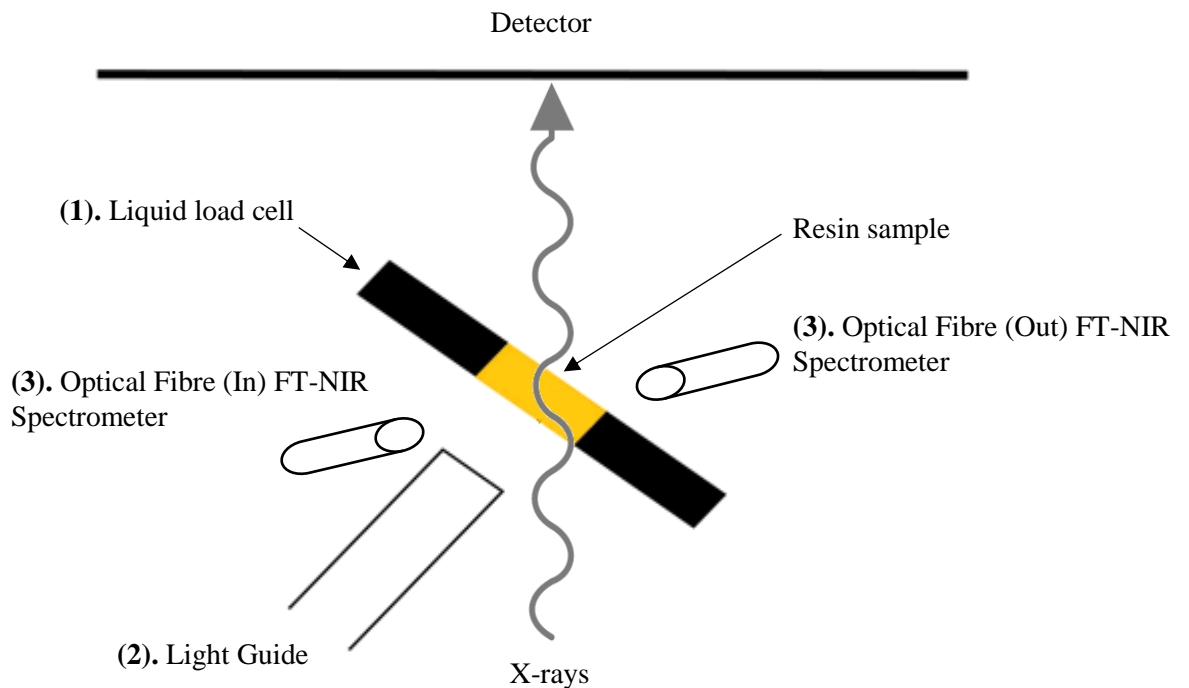
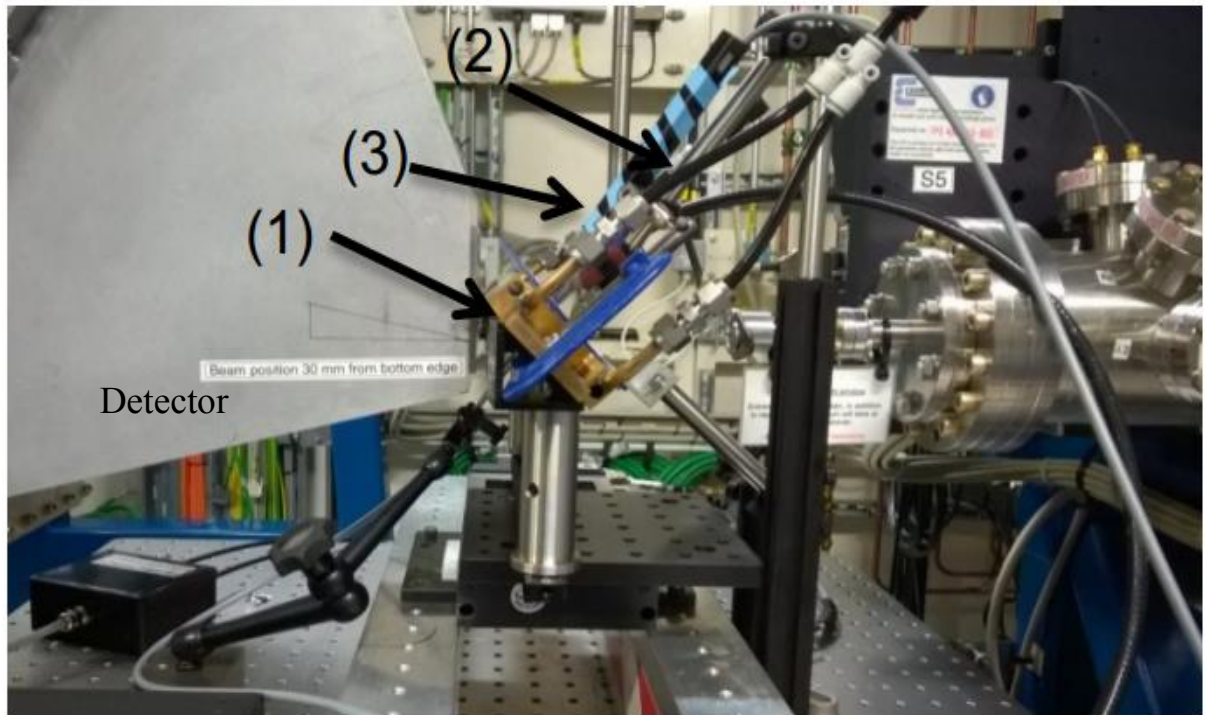


**Figure 3.1.** Real time SAXS measurements of dental resin composites polymerised in-situ on the I22 beam-line (1) liquid resins loaded in to a sample rack in the path of impinging X-rays, (2) A liquid light guide instigates photo-polymerisation by illuminating the resin sample with visible or UV light and (3) FT-NIR optical fibres are used to quantify real time monomer to polymer conversion.

### 3.3 Results

#### 3.3.1 De-convolving the Contributions of Monomeric Components to the Scattering Signal

Figure 3.2(a) shows the radially averaged X-ray scattering profile for a TPO initiated 60/40 wt% Bis-GMA/TEGDMA resin blend in its monomer form prior to photo-polymerisation (solid black line), and in the polymer state following 300 s of constant light application at an intensity of  $450 \text{ mW cm}^{-2}$  (dotted black line). A broad Gaussian feature is observed, typical of all these resin blends, with a peak initially located at  $q \sim 1.35 \text{ \AA}^{-1}$  corresponding to a length of  $4.65 \text{ \AA}$  in real space. This peak moved to lower values of  $q$ , approximately  $1.23 \text{ \AA}^{-1}$  ( $5.1 \text{ \AA}$ ) and incrementally narrowed throughout photo-polymerisation. The shift to lower  $q$  is indicative of an overall net length increase of the scattering centres that contribute to the broad peak feature, whilst the narrowing of the peak demonstrates an increase in the short range ( $<10 \text{ \AA}$ ) relative order.

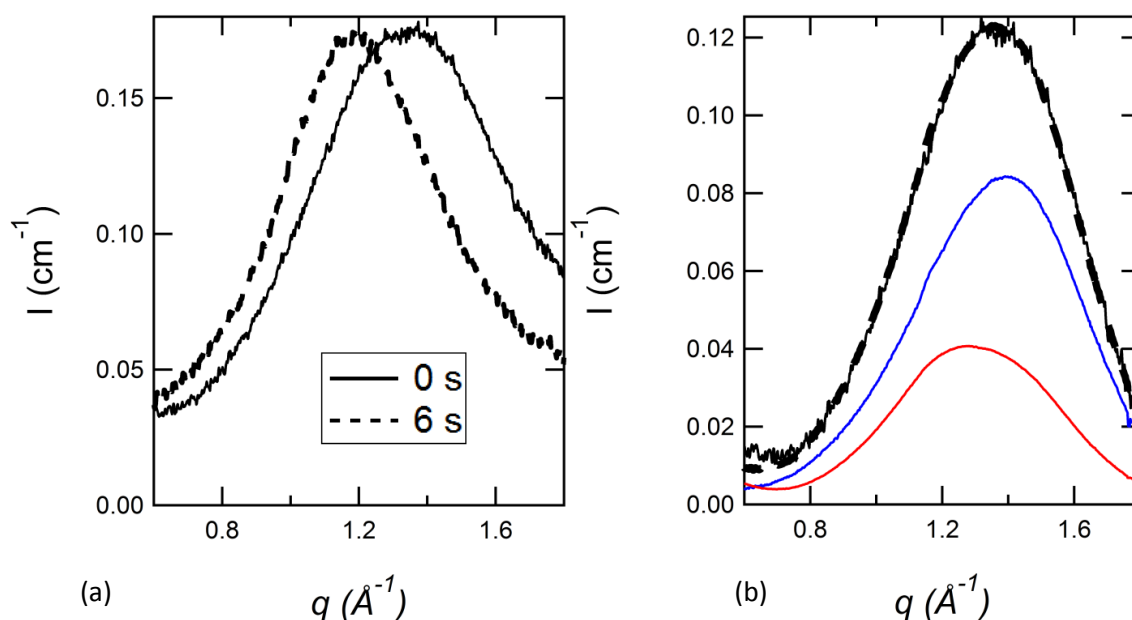
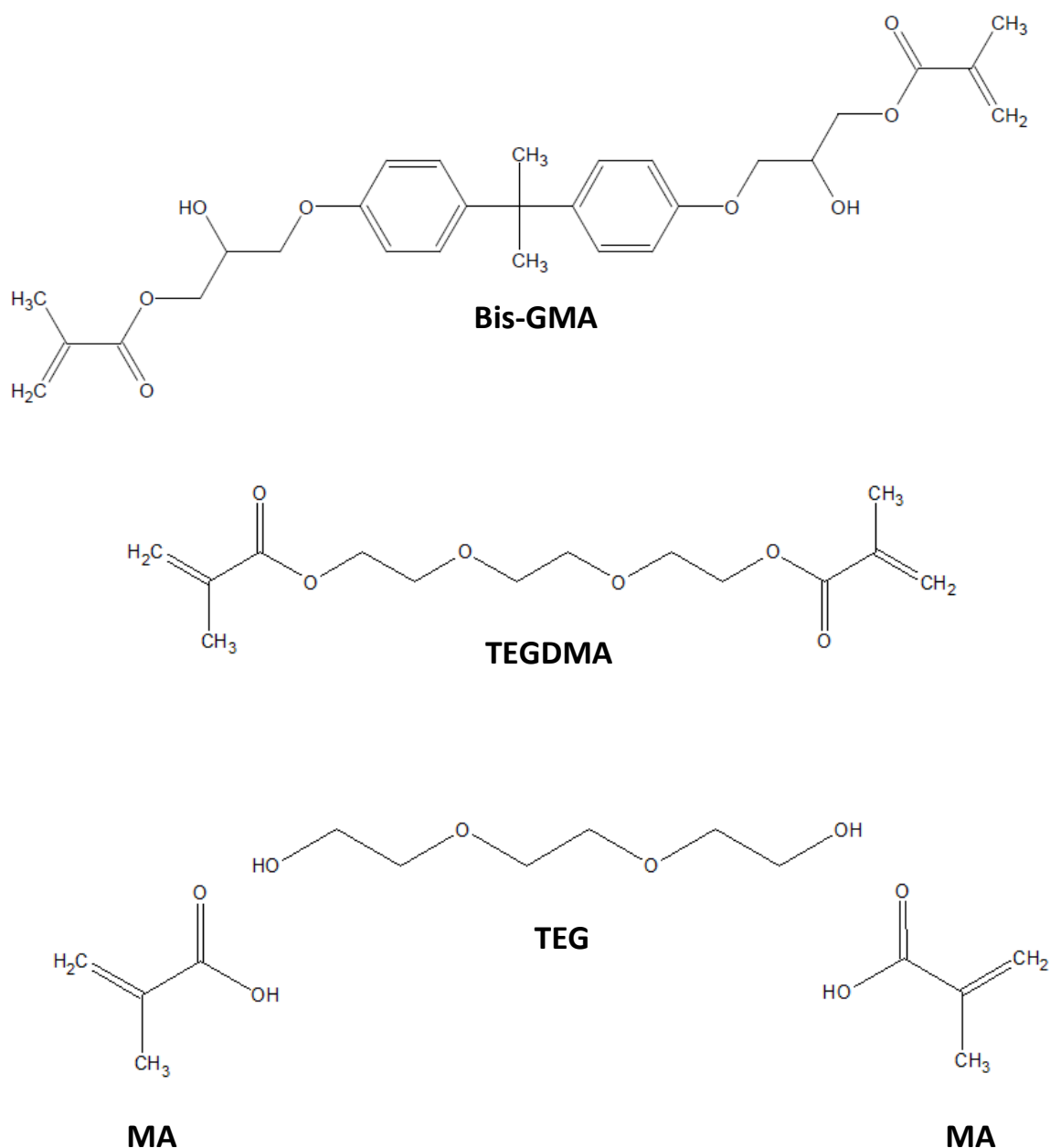


**Figure 3.2.** (a) X-ray scattering of a 60/40 Bis-GMA/TEGDMA resin blend initiated with TPO using constant light application at an intensity of  $450 \text{ mW cm}^{-2}$  for 300 s. Prior to polymerisation (bold black line), a broad Gaussian feature is centred at  $q \sim 1.35 \text{ \AA}^{-1}$  which narrows and moves to  $q \sim 1.23 \text{ \AA}^{-1}$  (broken black line). (b) Weighted least squares fitting (broken black line) of scattering data from the individual Bis-GMA (red) and TEGDMA (blue) monomers to the 60/40 wt% blend (solid black line) following baseline corrections. Bis-GMA and TEGDMA contribute 30 and 70 % to the signal respectively.

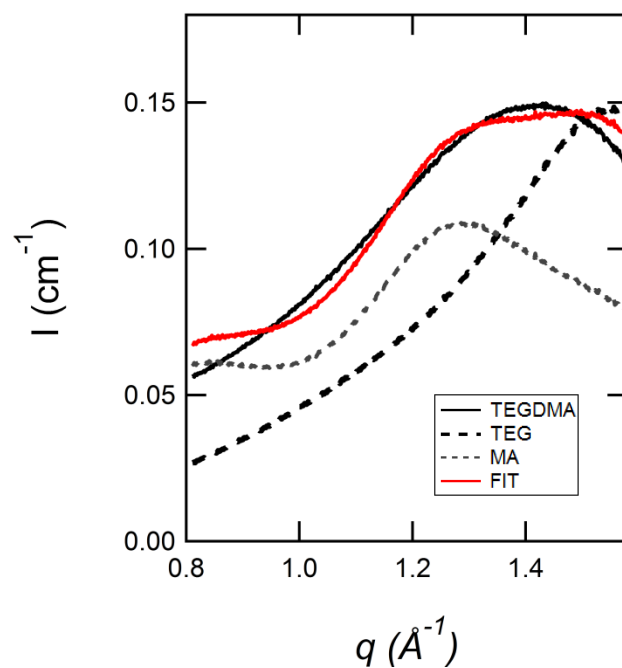
The  $q$  range of the broad peak feature is indicative of a structural feature equivalent to 3-4 atomic bond lengths. To identify the contribution of segments of individual monomers to the scattering pattern, signal simulations were undertaken for each resin blend. Figure 3.2(b) demonstrates the weighted least squares fitting (WLS) of Bis-GMA and TEGDMA X-ray scattering spectra, simulating the signal of the 60/40 wt% resin blend. WLS was performed to help identify the structural origin responsible for the peak shift with respect to each monomers contribution to the overall observed signal. It was identified that TEGDMA is the predominant contributor to the observed peak ( $q \sim 1.35 \text{ \AA}^{-1}$ ) and its shift, accounting for 70 % of the shift whilst only 30 % was attributed to Bis-GMA. This is critical as the monomers have identical end groups so the shift is indicative of structural changes in the monomer backbone. The contribution of each monomer to the signal varied with the composition of the resin blend.

Figure 3.3 shows the chemical structures of TEGDMAs' constituent monomers (methacrylic acid and triethylene glycol). Figure 3.4 shows the deconvolution of the TEGDMA X-ray scattering signal based upon the scattering data for the constituent monomers to approximate its chemical structure. WLS fitting reveals that ~68 % of the TEGDMA signal was attributed to methacrylic acid, representing the methacrylic functional end groups (34% per end group) (Figure 3.3). The remaining ~32 % of the TEGDMA signal contribution originated from the Triethylene glycol structure which approximates the section of the TEGDMA monomer terminated by the functional end groups. Furthermore, ~48 % of the 60/40 wt% Bis-GMA/TEGDMA (total) signal was attributed to the methacrylic acid (functional end group) originating from the TEGDMA monomer and ~22 % was weighted to the TEG component of the same monomer. Only ~30 % of the change in scattering following photo-polymerisation of the resin-blend was ascribed to Bis-GMA. The contribution of aromatic groups found in Bis-GMA to this change in the correlation length is considered negligible, based on numerous studies measuring the IR spectra of Bis-GMA based resins with no reports of significant changes in the aromatic absorption bands [4, 40, 41]. Any changes in the correlation length, originating from the Bis-GMA monomer, are therefore likely to be attributed to the linear

segment of the monomer incorporating the functional end groups. For a 60/40 wt% blend the non-aromatic segments of the Bis-GMA monomer contribute ~30% to the total molecular weight of the 60/40 wt% blend. This is equivalent to the contribution that Bis-GMA makes to the scattering signal for the Gaussian feature observed in Figure 3.2.



**Figure 3.3.** Chemical structures of Bis-GMA and TEGDMA monomers used to formulate each blend. Methacrylic acid (MA) and triethylene glycol (TEG) were used to simulate the chemical structure and dynamic behaviour of the TEGDMA monomer during polymerisation.

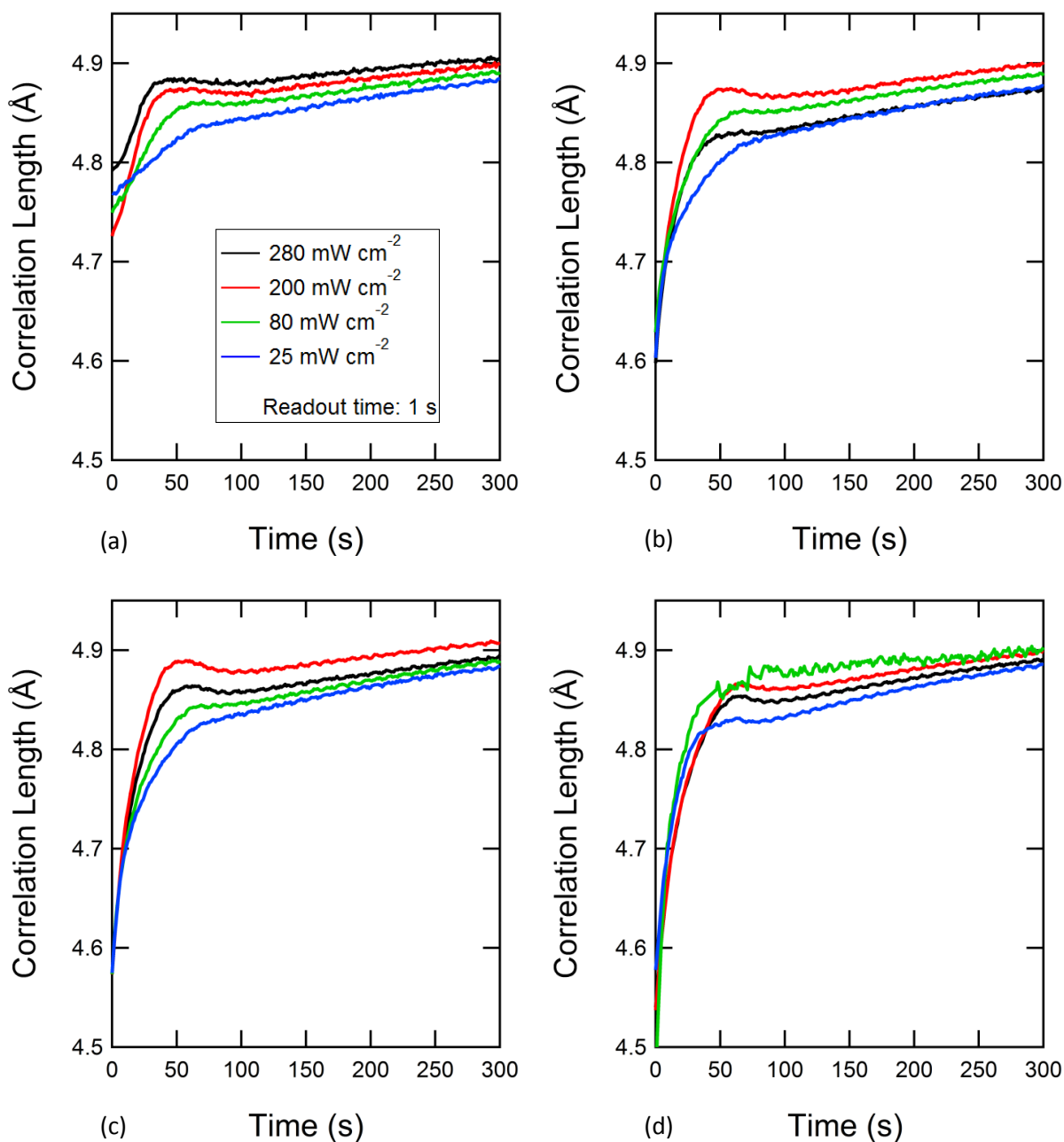


**Figure 3.4.** WLS fitting of methyl methacrylate (MA) and triethylene glycol (TEG) X-ray scattering spectra to that of TEGDMA. MA and TEG were used to approximate both the structure and X-ray scattering pattern of the TEGDMA monomer. Close to 70% of the shift and narrowing in scattering following polymerisation was attributed to MA with the remainder ascribed to TEG. The fit is not ideal at higher and lower  $q$  values, which may be due to the small  $q$  range which was limited by the sample environment. Additionally, it should be considered that MA and TEG monomers will have different mobility in comparison to the equivalent structures found in the TEGDMA monomer and will therefore show different correlation lengths.

### 3.3.2 Impact of Irradiance on Resultant Polymer Structure of CQ Initiated Resins

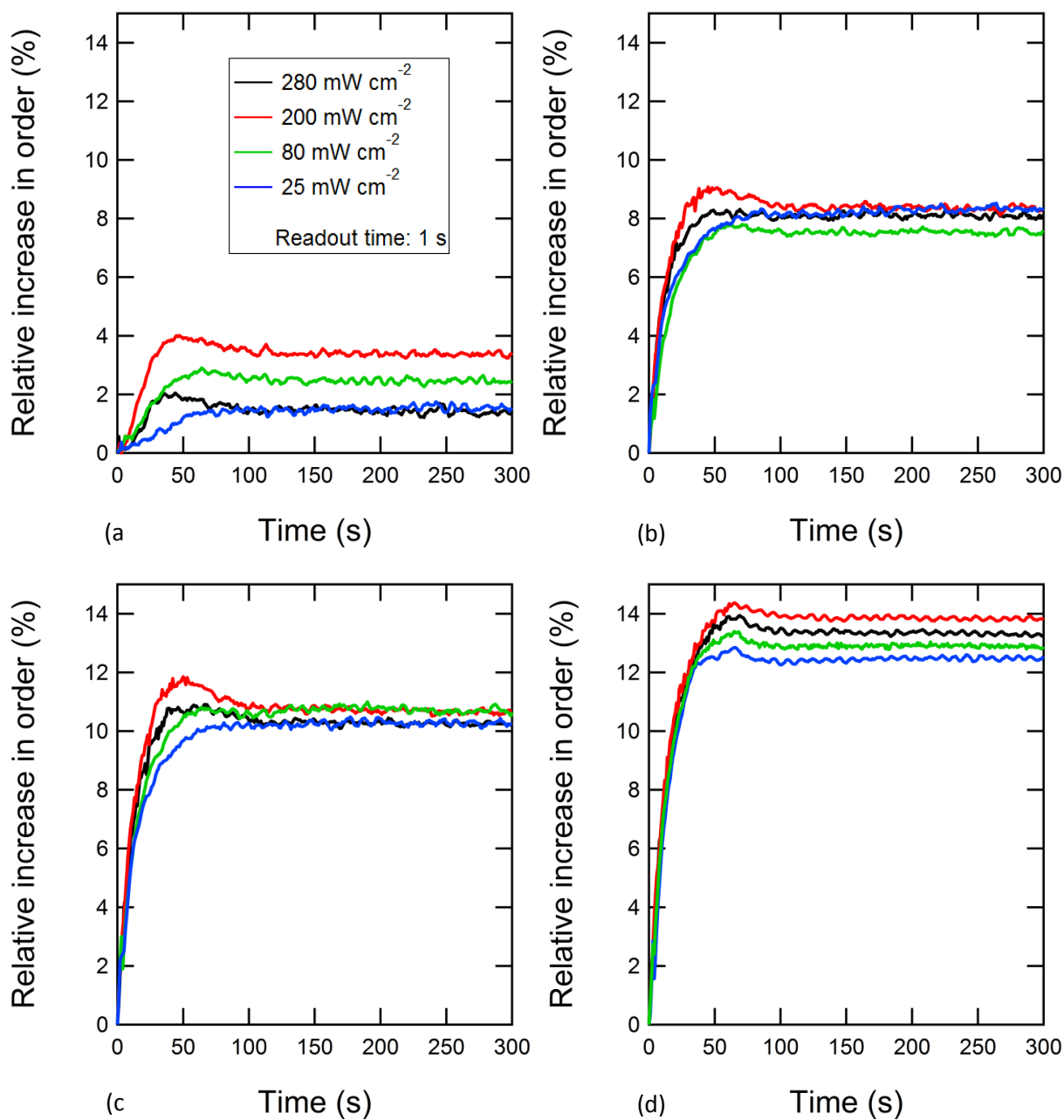
Figure 3.5 illustrates the evolution of the correlation length for resins photo-initiated with CQ as a function of time. The peak position of the broad Gaussian feature observed in Figure 3.2(a) is shown in real space at each time point (measured at every second) during light irradiation, and an increase in the correlation length is observed. All blends, regardless of their received irradiance, demonstrated a two stage increase in correlation length with respect to time. A relatively abrupt increase in the correlation length is followed by a gradual gain over time. The first stage is most pronounced in systems photo-polymerised using a high intensity of light correlating to a higher rate of polymerisation. It can be seen in Figure 3.5(c) (50/50 CQ) that resins photo-polymerised using the greatest intensity of light ( $280 \text{ mWcm}^{-2}$ ) complete this first stage within 45 s whilst for systems photo-polymerised with  $25 \text{ mWcm}^{-2}$  changes in correlation length continued for in excess of 60 s.

Figures 3.5(a-c) display that after a rapid increase in correlation length a small decrease (between 25 and 75 s) was subsequently observed for CQ initiated resins. This reduction was approximately 3% of the initial increase and was negligible or non-existent in the less viscous resins that contained a higher proportion of TEGDMA, and resins cured using a low light intensity (a slower reaction rate). Subsequently a gradual minor increase in the correlation length was observed for all conditions up to 300 s (end of measurement). The final (observed) correlation length remained smaller for resins polymerised slowly i.e. using the lowest irradiance.



**Figure 3.5.** Real time evolution of the correlation length observed in CQ initiated resins for (a) 70/30, (b) 60/40, (c) 50/50 and (d) 40/60 wt% blends (Bis-GMA/TEGDMA) during 300 s of photopolymerisation for a range of reaction rates. All resins display an increase in the correlation length which is larger and faster when a high rate of polymerisation is used. For particularly fast reactions, a subsequent relaxation period can be seen after the initial increase in length, although relaxation is negligible in more fluid blends.

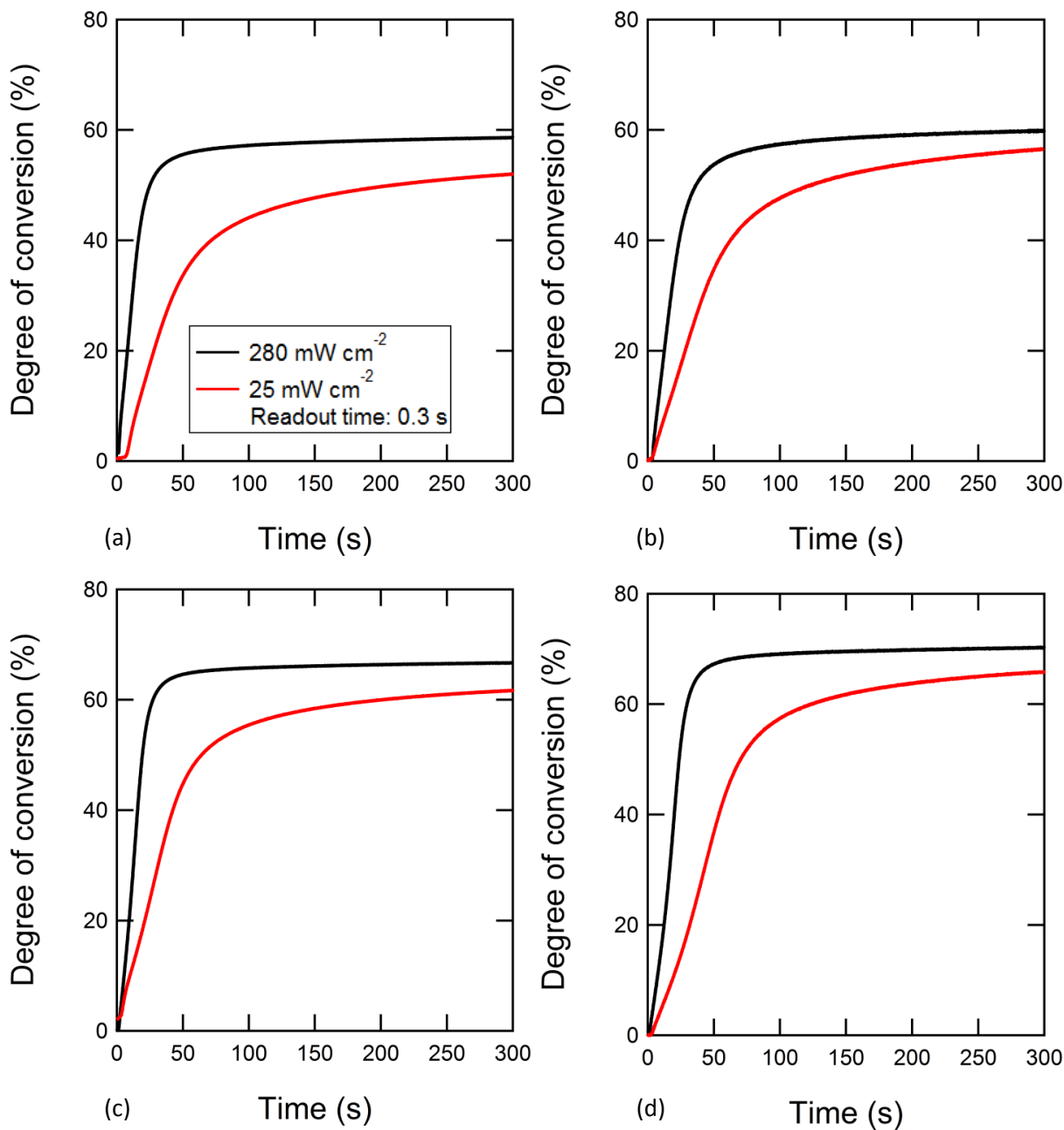
Figure 3.6 shows the increase in relative order which provides insight into the distribution of correlation lengths, for each blend as a function of time during photo-polymerisation. The change in relative order displays a two stage increase similar to that observed in the correlation length. An initial increase and maximum in relative order corresponds to a maximum increase in the correlation length for all blends at all photo-polymerisation irradiances – increases in correlation length and order are simultaneous. Increasing the irradiance and therefore the reaction rate conferred a larger gain in relative order in less time in contrast to the slower curing methods. At this point in the reaction differences in order between resins of the same blend, but cured at different irradiances vary by 2-4% (% of the maximum value). Resins photo-polymerised at high light intensities also demonstrated a small relaxation in order, typically ~10% of the initial increase, depending on the rate of the reaction. In particularly fluid blends, i.e. 40/60 wt% of Bis-GMA/TEGDMA, this relaxation was negligible. The relative order subsequently reaches a plateau (at least for the duration of the measurements) with differences between increasing irradiances varying by 1-2%. Resins containing a higher content of the smaller molecule TEGDMA displayed a greater increase in order, as well as in the correlation length, than in more viscous blends with a higher proportion of Bis-GMA.



**Figure 3.6.** The relative percentage increase in short range order during photo-polymerisation as a function of polymerisation rate for resin samples initiated with CQ for (a) 70/30, (b) 60/40, (c) 50/50 and (d) 40/60 wt% blends. Changes in order are similar and occur simultaneously to those observed in the correlation length for CQ initiated blends.

### 3.3.3 Polymerisation Kinetics of CQ Initiated Resins Blends

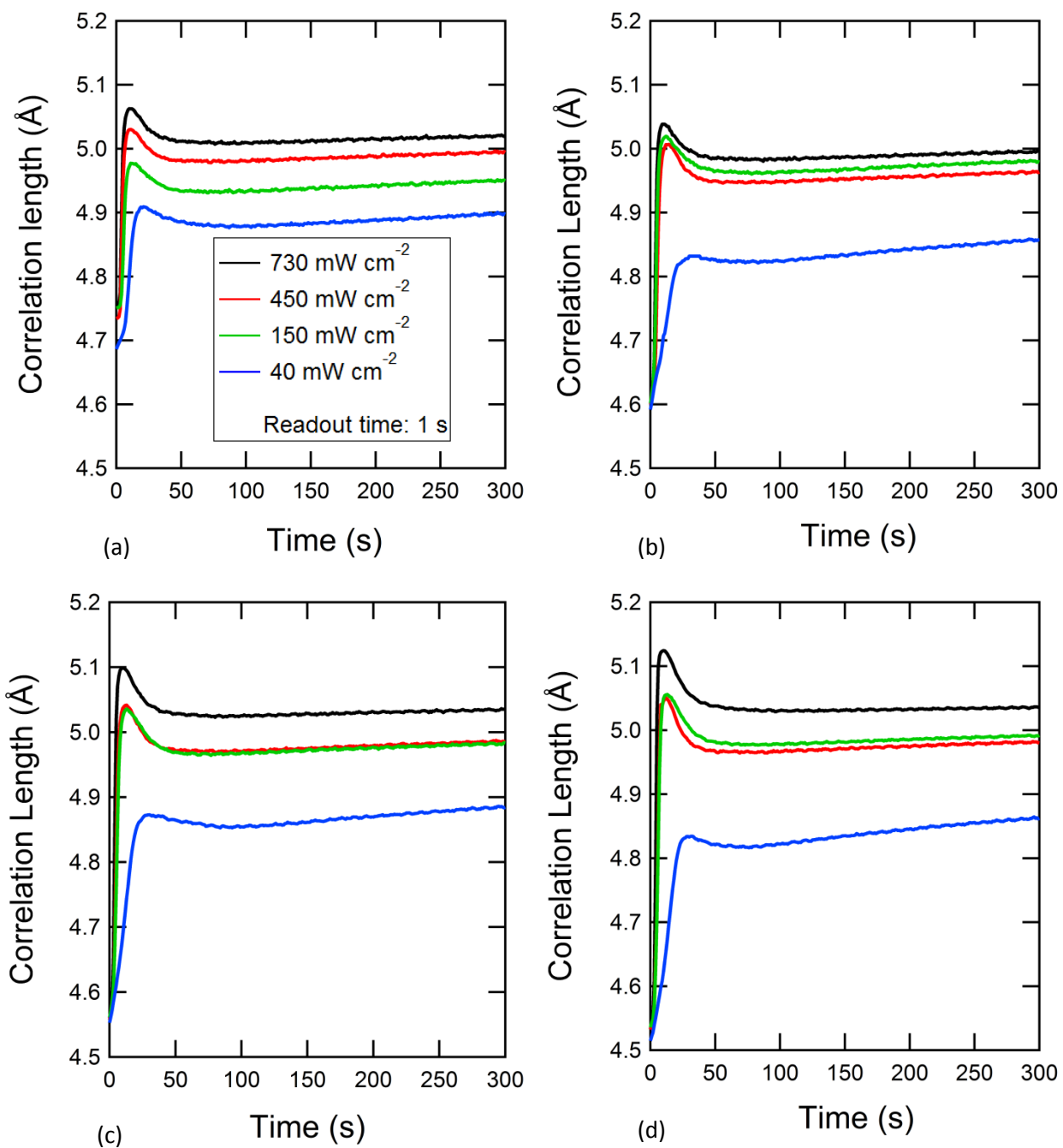
Figure 3.7(a-d) demonstrates the real time polymerisation of the methacrylate functional group for the CQ initiated resins as a function of time for the highest and lowest irradiance. Final conversion ( $DC_{max}$ ) and polymerisation rate ( $Rp$ ) are greater in resins polymerised at high light intensities for each blend ( $p < 0.05$ ) ( $n = 3$ ). Auto-acceleration occurs alongside the initial increases in the correlation length and order. However, the turning point in the polymerisation lagged behind the local maxima of the correlation length and order by 5-10 s depending on the polymerisation rate. Additional cure following auto-deceleration corresponded to gradual increases in the correlation length, albeit at a slower rate than at the start of the reaction, whilst no such behaviour was observed between additional cure and relative order. Instead it can be seen that despite ongoing curing, changes in short range order remain constant after the initial increase for the duration of the measurement (Figure 3.6).



**Figure 3.7.** Degree of conversion in real time during illumination of resin samples initiated with CQ for (a) 70/30, (b) 60/40, (c) 50/50 and (d) 40/60 wt% blends. Solid black lines correspond to samples irradiated with 280 mWcm<sup>-2</sup> of light whilst the red line indicates an energy output of 25 mWcm<sup>-2</sup>.

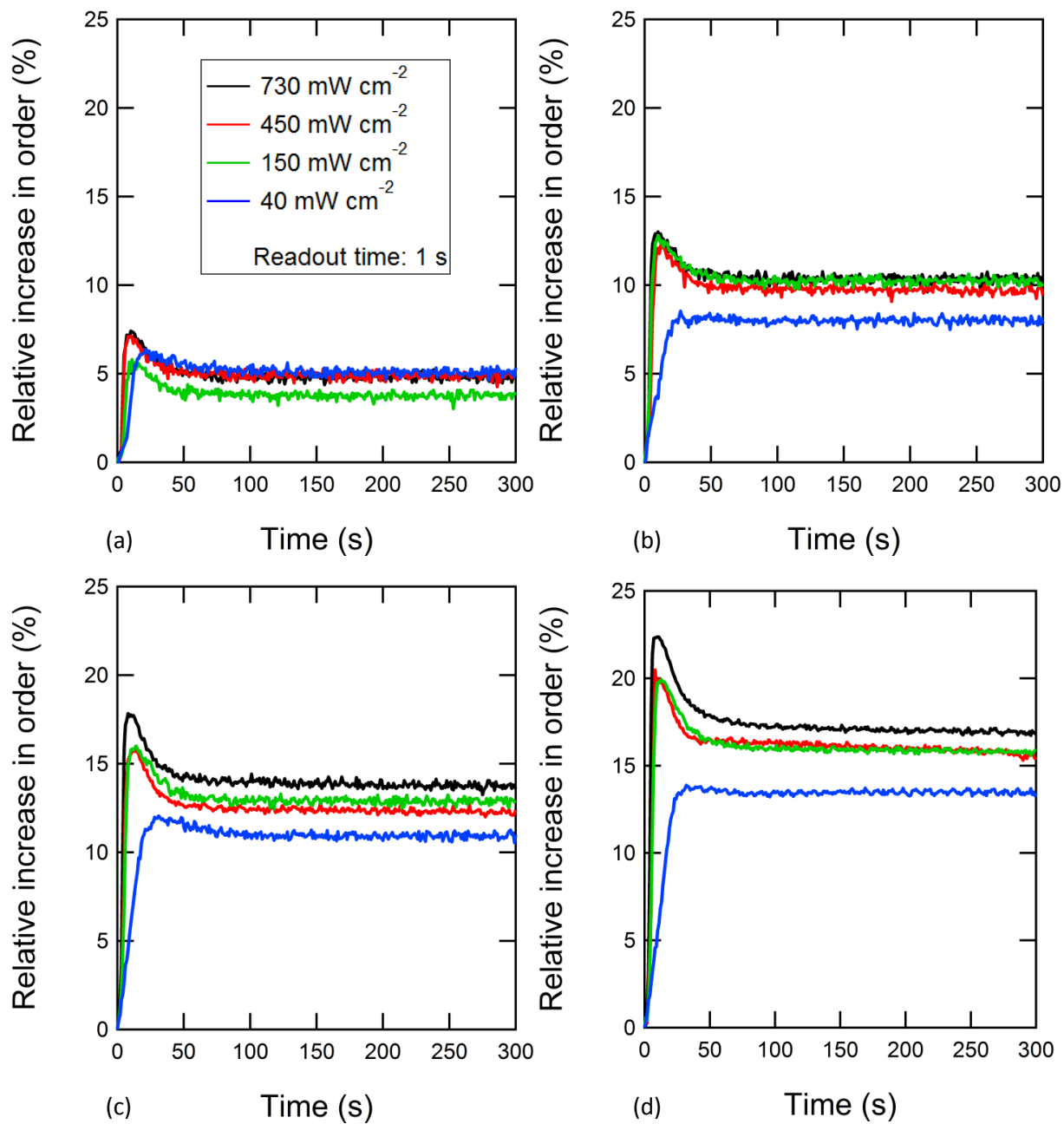
### **3.3.4 Impact of Irradiance on Resultant Polymer Structure of TPO Initiated Resins**

Figure 3.8 illustrates the correlation length for TPO initiated resins as a function of time for a range of viscosities, polymerised using different irradiances. All TPO initiated systems demonstrated three distinct changes in the evolution of the correlation length; a large initial increase, a brief reduction in length, followed by a small but progressive increase. The initial increase was approximately double that observed in CQ initiated systems for similar curing regimens and reached a local maxima within 8-10 s. Increasing the irradiance corresponded to a greater increase in the correlation length in a shorter period of time (Figure 3.8). This behaviour was well defined for viscous resins (70/30 wt % blends, Figure 3.8(a)), but not for more fluid mixes where similar increases in the correlation length were seen for identical resin blends polymerised at the different rates (Figure 3.8(c) and (d)). All TPO based resins displayed a subsequent decrease in the correlation length equal to approximately 5 % of the initial increase for systems photo-polymerised at the lowest light intensity and 15 % for all other irradiances. A small subsequent increase was observed in the correlation length for most blends following this transient reduction in length (Figure 3.8(a-c)). It can be seen in Figure 3.8 that this slow increase in the correlation length was larger when the system was polymerised at lower irradiances, whereas resins polymerised more rapidly showed little or no increase.



**Figure 3.8.** Time resolved changes in the correlation length as observed in TPO initiated resins for (a) 70/30, (b) 60/40, (c) 50/50 and (d) 40/60 wt% blends (Bis-GMA/TEGDMA) during 300s of photopolymerisation for a range of reaction rates. Initial increases in the correlation length upon illumination and subsequent relaxations are larger and more rapid for TPO initiated resins, corresponding to a faster polymerisation rate.

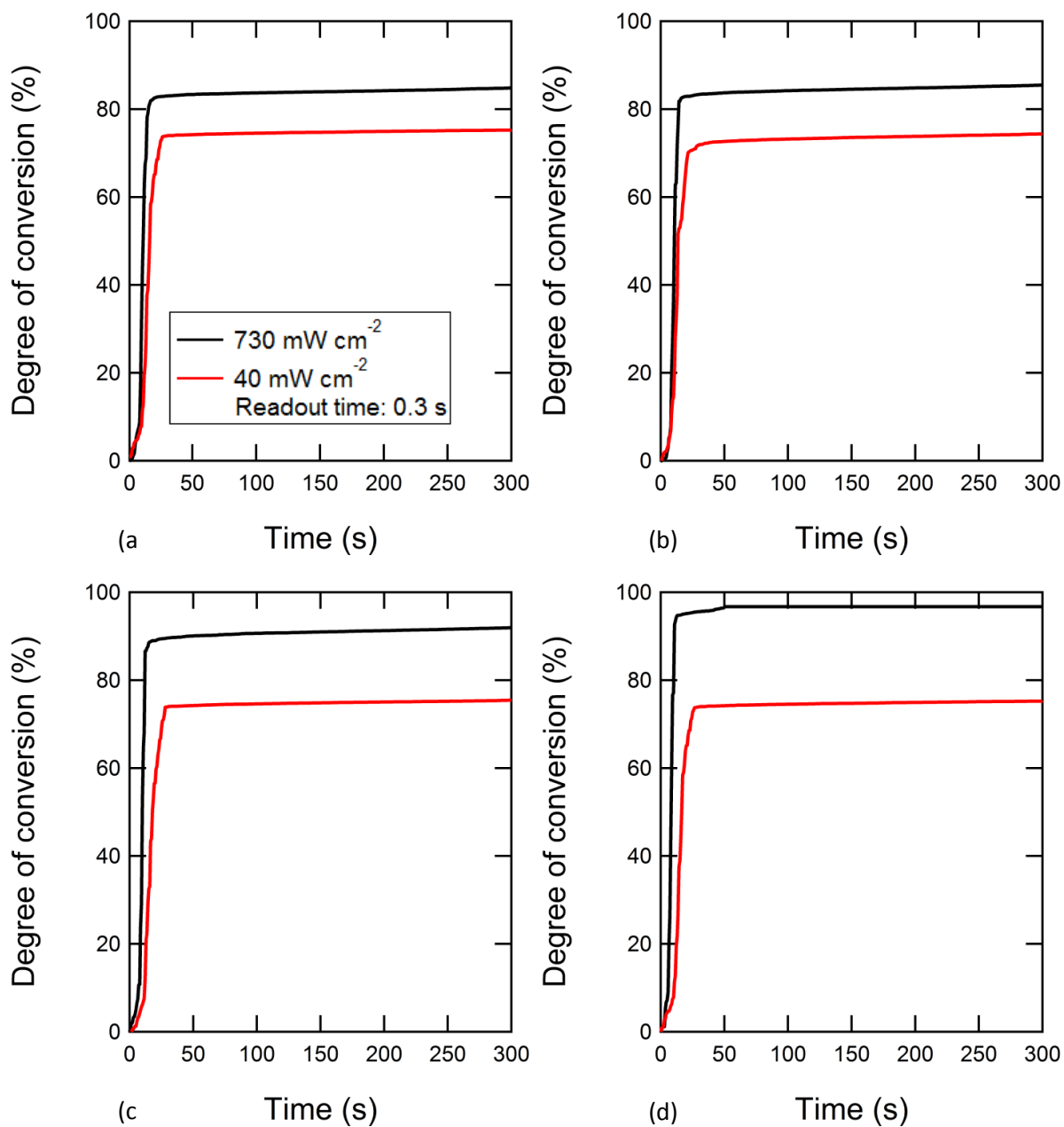
Figure 3.9 shows the increase in relative order for resins initiated with Lucirin TPO as a function of time. The changes in the relative order had similar characteristics to those seen in the correlation length demonstrating a large initial increase and a subsequent relaxation. All TPO based resins displayed a large increase in order which was dependent on irradiance (proportional to the rate of polymerization). The observed maxima in the relative order corresponded to the maximum in the correlation length i.e. changes in the correlation length and relative order occur simultaneously in TPO systems. Similarly, following an increase in order we observed a reduction in order (or relaxation), where approximately 5 to 15% (depending on the polymerisation rate) of the initial gain was lost. However, relative orders do not show a post relaxation increase as was observed in the correlation length, instead appearing to plateau. The final (measured) value of order was on average greater in resins containing a higher proportion of the TEGDMA monomer (Figure 3.9(d)). These less viscous systems also showed greater differences in the magnitude of the final relative order, for identical blends polymerised at different rates.



**Figure 3.9.** Changes in the relative order throughout photo-polymerisation for TPO initiated (a) 70/30, (b) 60/40, (c) 50/50 and (d) 40/60 wt% resin blends. Unlike CQ initiated resins, these systems demonstrate a large relaxation feature.

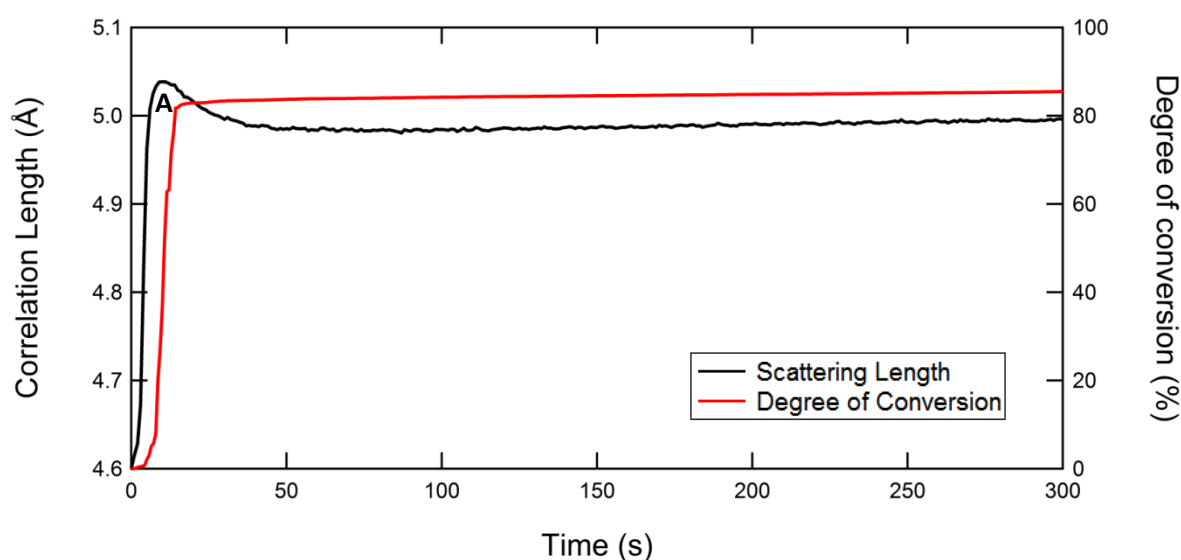
### 3.3.5 Polymerisation Kinetics of TPO Initiated Resin Blends

Figure 3.10 demonstrates conversion of the methacrylate functional group (collected simultaneously with the X-ray measurements) for the TPO initiated resins as a function of time for highest and lowest irradiances. In both cases, TPO systems showed more rapid periods of initiation and propagation in comparison with the CQ based resins, reaching auto-deceleration earlier. Resins initiated with a high light intensity displayed a final degree of conversion, typically 10 % greater when irradiated at low intensity. Post auto-deceleration polymerisation continued for all systems but was most prominent for cases of low irradiance photo-polymerisation. Less viscous resins containing a higher proportion of the TEGDMA monomer displayed greater final conversion and continued curing.



**Figure 3.10.** Real time degree of conversion during illumination of resin samples initiated with TPO for (a) 70/30, (b) 60/40, (c) 50/50 and (d) 40/60 wt% blends. Solid black lines correspond to samples irradiated with  $730 \text{ mWcm}^{-2}$  of light whilst the red line indicates an energy output of  $40 \text{ mWcm}^{-2}$ .

The relationship between functional end group conversion and structural changes in the polymer are outlined in Figure 3.11, where the data sets are overlaid. The auto-acceleration period corresponds to the large initial increase in the correlation length and relative orders i.e. as the polymer network grows, short range order and the length scales increase. When the system has reached 98% of the maximum monomer conversion (point A, Figure 3.11), short range order and the correlation length also reached a maximum. Post-cure appears to correspond to a continued increase in the correlation length. Greater post-cure in slowly polymerised resins corresponded to a larger gain in the correlation length following relaxation, whilst resins cured using high light intensities showed negligible post-auto-deceleration cure and changes in the correlation length.



**Figure 3.11.** Real time degree of conversion (red line) and scattering length (black line) for a 60/40 wt% blend initiated with TPO. Auto-acceleration in the resin bulk corresponds to a large initial increase in the correlation length. The point of auto-deceleration in the polymer network (the start of the plateau in the *DC* plot) coincides with the maximum increase in scattering length.

### 3.3.6 The Effect of Polymerisation Rate on the Resultant Polymer Structure

A range of polymerisation rates (determined by FT-NIR) for each resin blend were achieved by varying photo-initiator chemistry and light irradiance. In Figure 3.12 by correlating polymerisation rate with changes in X-ray scattering it was possible to relate the reaction rate to (short-range) structural evolution. As polymerisation rate increased there was a greater increase in the correlation length (extension) and relative short range order. Figures 3.12-3.14 demonstrate how systems initiated with Lucirin TPO (the last four data points on each plot) display polymerisation rates typically an order of magnitude greater than the CQ counterpart (the first four data points on each plot) for similar irradiances. Faster polymerisation rates conferred larger gains in the correlation length which were approximately twice those seen in CQ systems. At lower polymerisation rates ( $<5\% \text{ s}^{-1}$ ) the increase in the correlation length was observed to increase linearly with the polymerisation rate (Figure 3.12) however as the reaction rate increases the change in correlation length begins to plateau. Less viscous resins, with a greater content of TEGDMA, displayed a greater increase in the correlation length for equivalent polymerisation rates. A similar pattern of relationship was observed when changes in short range order were correlated with the polymerisation rate (Figure 3.13) albeit that the initial increases in relative order were much greater for the less viscous systems containing greater wt% of TEGDMA.

### 3.3.7 Normalisation of Scattering Data to the Degree of Monomer-Polymer Conversion

Direct correlations between X-ray data and the polymerisation rate are complicated by the relative differences in monomer-polymer conversion for each polymerising system. Normalising the increase in correlation length with respect to  $DC_{max}$  resulted in a similar pattern of behaviour to that observed in Figure 3.12. However, normalising order to  $DC_{max}$  and plotting as a function of polymerisation rate (Figure 3.14) demonstrated that at polymerisation rates greater than  $\sim 5\% \text{ s}^{-1}$  the change in order decreases with increasing reaction rate for all resin

blends. Relative order remained ranked by relative viscosity (defined by TEGDMA wt%) with blends composed primarily of the Bis-GMA monomer demonstrating greater disorder at all polymerisation rates.

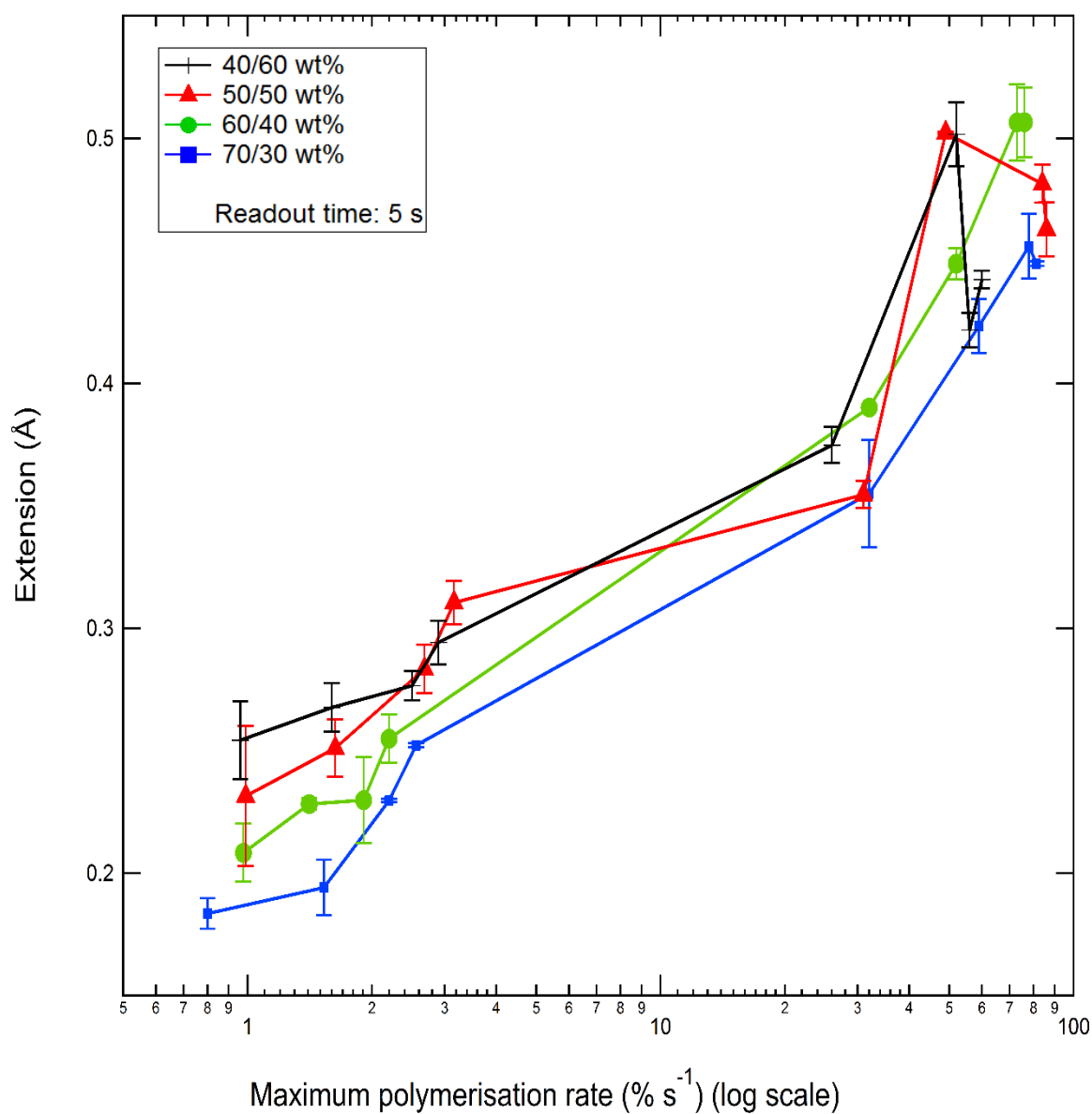


**Figure 3.12.** Maximum chain extension for each resin blend (viscosity) versus polymerisation rate (irradiance). CQ initiated resins are shown by the first four points, whilst the other data points refer to TPO initiated resins. Error bars represent uncertainty in the values as calculated by propagation of errors. Resins polymerised at higher rates display the greatest increase in the correlation length. Data was obtained from BM28 (ESRF).

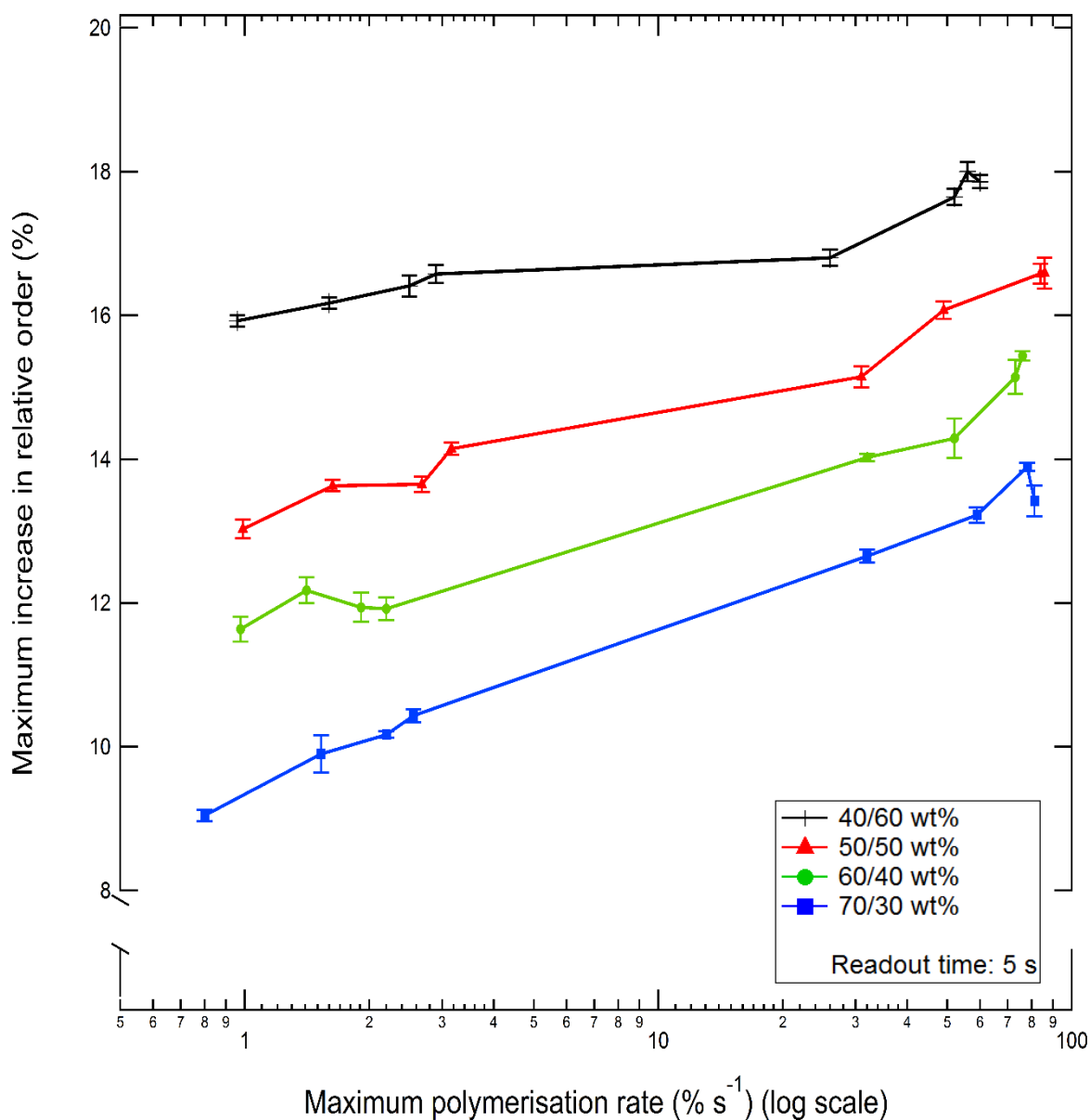


**Figure 3.13.** Maximum increase in order for each resin blend (viscosity) versus polymerisation rate (irradiance). CQ initiated resins are shown by the first four points, whilst the other data points refer to TPO initiated resins. Error bars represent uncertainty in the values as calculated by propagation of errors. Resins polymerised rapidly demonstrate the greatest increase in order, although this is likely an artefact of different conversion values, as a more converted system will inevitably be more ordered.

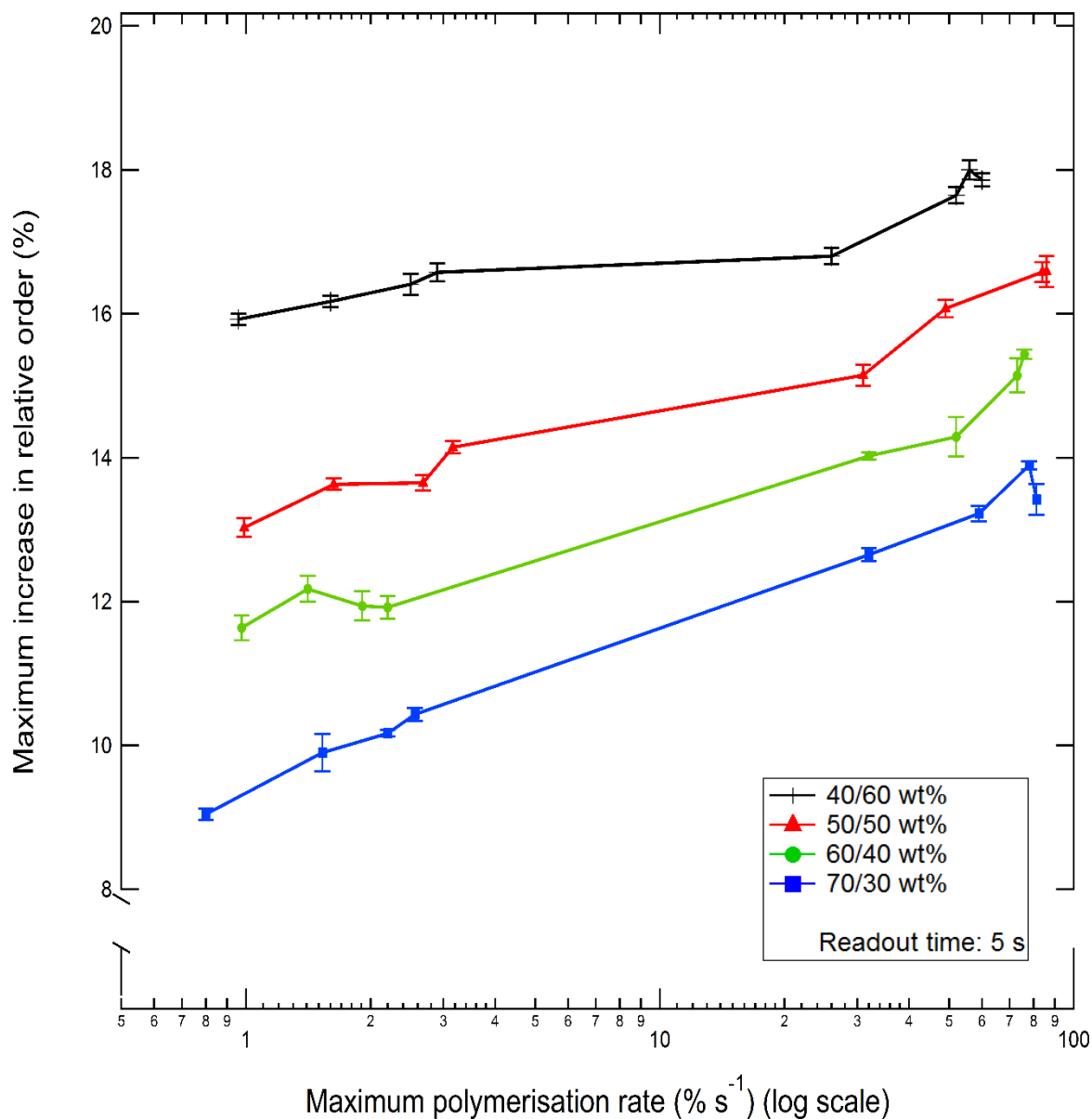


**Figure 3.14.** Normalised maximum increase in relative short range order for each resin blend (viscosity) versus polymerisation rate (irradiance). Data has been normalised to the degree of monomer conversion to determine chain extension and order per converted C=C bond. CQ initiated resins are shown by the first four points, whilst the other data points refer to TPO initiated resins. Error bars represent uncertainty in the values as calculated by propagation of errors. Systems polymerised at slower rates display the greatest increase in order for a given blend, whilst increasing viscosity decreases short range order.

## 3.4 Discussion

### 3.4.1 De-convolving the Contributions of Monomeric Components to the Scattering Signal

Photo-polymerisation induced an increase in the length of the principal X-ray scattering feature observed in measurements on the Bis-GMA/TEGDMA monomer blends (Figure 3.2). Previous laboratory based measurements (WAXS) have measured this broad peak feature but have failed to determine its origin or explain the subtle differences in the peak position between resin blends of varying viscosities [42] which have been resolved here. In this current study the correlation length increases from an initial value of  $\sim 4.45 \text{ \AA}$  to  $\sim 5.1 \text{ \AA}$  (Figures 3.5 and 3.8) depending on the resin formulation and the polymerisation rate. Weighted least squares fitting (WLS) of the scattering data for a 60/40 BisGMA/TEGDMA wt% blend, revealed that the majority of the length change originates from the TEGDMA monomer (Figure 3.2(b)) and specifically within the methacrylate functional end groups ( $\sim 48\%$  of the total signal). The remaining portion of this length change is ascribed to the middle section of the TEGDMA monomer terminated by the functional groups, which accounts for the remaining  $\sim 22\%$  of the total signal (Figure 3.3).

The mechanism behind the length increase can be determined by considering that during polymerisation the C=C double bond in the methacrylate functional group is converted to a single covalent bond with a carbon atom from a neighbouring monomer. Bond conversion confers a length increase equivalent to  $0.2 \text{ \AA}$  [the difference in bond length between a C=C bond ( $1.33 \text{ \AA}$ ) and a C-C bond ( $1.53 \text{ \AA}$ )] [43]. Figures 3.5, 3.8(d) and 3.12 show that for lower rates of polymerisation, less than  $2 \text{ \% s}^{-1}$ , the increases in the observed correlation length approximates the difference in length between double and single carbon-carbon bonds following polymerisation. This implies that at lower reaction rates the predominant form of length change arises from bond exchange. However, at greater reaction rates, in excess of  $50 \text{ \% s}^{-1}$ , the increase in the correlation length is more than double the bond exchange value (Figure

3.12). This additional increase in length, which cannot be accounted for through bond exchange, is therefore ascribed to chain segment extension. Fu et al (2015) [44] reported chain extension in methacrylate functionalised monomers which were photo-initiated with UV light. However, the location(s) of the chain extension were not elucidated in their study nor was any consideration given to the effect of reaction rate on the resultant monomer structure.

In the current study most of the extension occurs within the functional end groups, although a significant portion is predicted to come from extension of the backbone of the TEGDMA monomer (the TEG portion of the chain). This deduction is supported by the observed change in correlation length exceeding length increases afforded by bond exchange, and predictions for WLS fitting of the broad peak feature attributing ~22% (for a 60/40 BisGMA/TEGDMA wt% blend) of the scattering peak to the 'TEG' portion of the TEGDMA monomer unit (Figure 3.3). This suggests that chain segment extension occurs at sites distant from bond conversion. The Bis-GMA monomer also displays a smaller contribution to the total scattering signal (~30%) and subsequent  $q$  shift. Any extension arising from the Bis-GMA monomer is attributed solely to the non-aromatic portion of the monomer, including the functional end groups, given the rigidity of the aromatic rings at the centre of the monomer. No reports in the literature have indicated structural changes to the aromatic groups via vibrational spectroscopy methods [4, 40]. To summarise, structural changes within this system are attributed to the functional end groups for both monomers and the flexible backbone of the TEGDMA monomer.

### 3.4.2 Impact of Irradiance on the Resultant Polymer Structure

Systems polymerised relatively slowly, typically CQ initiated resins and some TPO systems polymerised at low light intensities, demonstrated a gradual increase in the correlation length up to a gain of approximately 0.2 Å (Figures 3.5 and 3.8). This is also accompanied by simultaneous increases in the short range order during polymerisation, both of which are synchronised with the real time degree of conversion (Figure 3.7). Hence, polymerisation of the system confers an increase in the correlation length (corresponding to segments within a monomeric unit) and short range order. In Figure 3.5, a gradual increase in correlation length is observed representing a gradual increase in the contribution of the longer correlation lengths (arising from increasing C=C to C-C conversion) to the average scattering signal, which is why this length scale increases with conversion. It can be seen that short range order also displays a similar initial increase which coincides with polymerisation (Figure 3.6) and is also attributed to bond conversion. It is known that polymerisation limits the range of monomer motion at the end groups which reduces the number of possible bond conformations [45]. Figures 3.5 and 3.7 show that the local maxima in the correlation length corresponds to plateauing of  $DC$ . Similar behaviour is seen in the correlation length where the increase steadily exceeds 0.2 Å (Figure 3.5) after a small reversal in extension feature which may represent a transition from chain growth induced length changes to true chain extension. Therefore, chain extension in slowly polymerised resins occurs after the majority of the cross-linked network has been formed whilst any additional modifications to order and free volume are ascribed to chain extension linearizing the monomer segment [46, 47].

At faster polymerisation rates (Figures 3.8-3.10) greater increases in the correlation length and order in a shorter period of time are observed. At higher rates (TPO, high irradiance) the increase in the correlation length is more than double of that than can be ascribed to bond-exchange (associated with chain growth) and is followed by a relatively large reduction in extension length, proportional to the initial length increase. This implies that rapid polymerisation and polymer growth generates stress within monomeric units, causing extension

of segments into a possibly more ‘linearized conformation’ (more so than for systems polymerised with lower reaction rates). Relaxation of these length scales may therefore represent a reorientation of bond geometry to lower the energy state of the system. This is supported by the reversal in extension seen in short range order measurements (Figure 3.9).

Figure 3.8 also shows that systems polymerised rapidly can demonstrate varying degrees of chain extension post-relaxation. This feature is most prominent in systems polymerised using lower light intensities, achieving lower conversion. In comparison, a system which has been polymerised rapidly and has reached a high terminal conversion displays negligible extension after the initial increase and subsequent reduction in correlation length. Any changes in correlation length after gelation must be attributable to either continued conversion (post-cure) or bond exchange. Post-cure (which is proportionally greater in lower *DC* systems, where free-volume in the polymer network is greater and radical diffusion is permissible) will be associated with polymerisation with less geometric freedom for the reacting monomer. This restriction of geometric freedom is likely to lead to bond and chain geometries that are longer than a comparative unconstrained state and leads to the net increase in correlation lengths seen at extended times for systems with initially lower *DC*.

At lower *DC* more free volume is likely to be available and diffusion limits do not fully restrict the movement of radical species. This allows for continued monomer-polymer conversion (Figure 3.10) which causes the monomer segment to incrementally extend. Resins polymerised rapidly with a greater terminal degree of conversion (> 90%) will demonstrate little free volume and will be vitrified. This limited mobility restricts further structural modifications such that an extended chain conformation is fixed into the polymer network.

To summarise, chain extension in rapidly polymerised resins occurs during the formation of the cross-linked network, unlike at slower reaction rates, with the resultant structures unable to undergo further modifications post auto-deceleration with respect to short range order due to mobility restrictions.

The contribution of polymerisation exotherm and potentially heat transferred by the instigating light source at early stages of the reaction to the magnitude of the observed extension and relaxation must also be considered. Shortall *et al* (2013) [48] demonstrated that a  $1013 \text{ mWcm}^{-2}$  light source (blue light centred at 450 nm) can cause a temperature increase of between 2-5 °C in commercial RBCs during polymerisation when positioned 7 mm from the RBC. Exothermic output particularly during auto-acceleration will drive a faster reaction and exacerbate thermal motions of the forming polymer. A greater reaction rate will ultimately generate a larger extension and relaxation in these systems. In this study thermal effects are however, expected to be reduced in comparison to Shortall *et al* due to the use of a less intense light source and a larger separation distance from the resin sample.

### 3.4.3 The Effect of Polymerisation Rate on the Resultant Polymer Structure

It can be seen from Figure 3.12 that as the polymerisation rate is increased there is a greater increase in the correlation length (extension) and relative short range order. At lower reaction rates (less than  $2\% \text{s}^{-1}$ ) the relationship between extension and rate is linear (Figure 3.12), however above this threshold the extension begins to plateau. This plateau in extension at higher reaction rates may represent either the maximum extension of the monomer segment i.e. an ideal conformation or alternatively the maximum length before vitrification restricts further extension. A similar pattern relationship is observed when changes in short range order were correlated with the polymerisation rate (Figure 3.13). Greater relative order in resins polymerised using a fast rate is likely an effect of differences in monomer-polymer conversion. A more polymerised system will inevitably display greater order due to the restriction of the thermal motions and chemical bond distributions.

Direct correlations between X-ray scattering data and the polymerisation rate are therefore complicated by the relative differences in monomer-polymer conversion for each polymerising system. Degree of conversion was quantified using both real time *ex-situ* laboratory based FT-NIR and *in-situ* measurements performed simultaneously to the acquisition of X-ray data with differences between the two measurements considered negligible. Normalising the increase in correlation length with respect to *DC* resulted in a similar pattern of observations to those seen in Figure 3.12. However, Figure 3.14 shows that normalised order decreases with increasing reaction rate. This implies that driving the reaction rate faster reduces the amount of time that the monomeric structure has to reorient and optimise its bond geometry during network growth. At slower polymerisation rates, more time is allowed to achieve a lower energy (a more ordered) conformation.

Volumetric shrinkage is known to be facilitated by the conversion of C=C bonds which reduces intermolecular distances and increases the molecular packing density. Data from this study also indicates that chain segment extension acts as a secondary mechanism for volumetric shrinkage,

whereby chain linearization increases the packing density, which has not been previously considered in these materials. Unlike  $DC_{max}$  this mechanism is highly sensitive to the reaction rate and may explain why several studies have reported greater volumetric shrinkage and shrinkage rates in similarly converted materials when polymerisation is accelerated [12, 28, 32, 49, 50]. The generation of macroscopic shrinkage associated with the reduction of free volume during the polymerisation of these materials must be considered when interpreting these results. When shrinkage is constrained, the result is the generation of residual stress which will likely impact on the observed correlation lengths within the polymer system. The geometry of the test specimens used in this study were largely unconstrained with a large aspect ratio between the disc surface and the sample holder, with a readily deformable mica window. Although shrinkage has not been measured in this study, residual shrinkage strains would manifest as increased correlation lengths that may relax over time. When polymerisation is accelerated through the use of TPO initiator and the highest irradiance a relaxation feature is observed. It is conceivable that this feature is a form of stress relief mechanism, such as bond exchange or breakage.

### 3.5 Conclusions

The evolving polymer structure of photo-activated dimethacrylate resins has been studied using time resolved X-ray scattering and *in-situ* FT-NIR as a function of reaction rate. Photopolymerisation induces structural changes in the monomeric units with regards to chain segment extension and relative order which to date is unreported. It appears that chain extension occurs predominantly in the methacrylate functional groups of the more flexible TEGDMA monomer, although extension is also thought to occur in the central portion. Faster polymerisation rates generate greater extension in a shorter period of time and as a consequence the developing structure has less time to orient to a lower energy (higher order) conformation. By polymerising the system rapidly, to the point of vitrification, any residual stresses generated by chain extension remain fixed into the polymer network. In comparison, slowly polymerised systems are capable of modifying the polymer structure after the majority of the network has formed likely due to a greater availability of free volume. This unique and novel experiment within the context of dental research has shown how operator-induced, environmental and compositional variables may impact on the structure of the polymer matrix components of dental RBCs and may ultimately explain the discrepancies in the predictive modelling of the mechanical behaviour of these materials using more conventional techniques.

### 3.6 References

1. Calheiros, F.C., et al., *Influence of radiant exposure on contraction stress, degree of conversion and mechanical properties of resin composites*. Dent Mater, 2006. **22**(9): p. 799-803.
2. Stansbury, J.W., *Dimethacrylate network formation and polymer property evolution as determined by the selection of monomers and curing conditions*. Dental Materials, 2012. **28**(1): p. 13-22.
3. Ogunyinka, A., et al., *Photoinitiation chemistry affects light transmission and degree of conversion of curing experimental dental resin composites*. Dent Mater, 2007. **23**(7): p. 807-13.
4. Stansbury, J.W. and S.H. Dickens, *Determination of double bond conversion in dental resins by near infrared spectroscopy*. Dental Materials, 2001. **17**(1): p. 71-79.
5. Dickens, S.H., et al., *Photopolymerization Kinetics of Methacrylate Dental Resins*. Macromolecules, 2003. **36**(16): p. 6043-6053.
6. Ruyter, I.E. and H. Oysaed, *Composites for use in posterior teeth: composition and conversion*. J Biomed Mater Res, 1987. **21**(1): p. 11-23.
7. Ferracane, J.L., *Current trends in dental composites*. Crit Rev Oral Biol Med, 1995. **6**(4): p. 302-18.
8. Lima, A.F., et al., *Influence of light source and extended time of curing on microhardness and degree of conversion of different regions of a nanofilled composite resin*. European Journal of Dentistry, 2012. **6**(2): p. 153-157.
9. Braga, R.R., R.Y. Ballester, and J.L. Ferracane, *Factors involved in the development of polymerization shrinkage stress in resin-composites: A systematic review*. Dental Materials, 2005. **21**(10): p. 962-970.

10. Venhoven, B.A.M., A.J. Degee, and C.L. Davidson, *POLYMERIZATION CONTRACTION AND CONVERSION OF LIGHT-CURING BISGMA-BASED METHACRYLATE RESINS*. *Biomaterials*, 1993. **14**(11): p. 871-875.
11. Patel, M.P., M. Braden, and K.W. Davy, *Polymerization shrinkage of methacrylate esters*. *Biomaterials*, 1987. **8**(1): p. 53-6.
12. Atai, M., D.C. Watts, and Z. Atai, *Shrinkage strain-rates of dental resin-monomer and composite systems*. *Biomaterials*, 2005. **26**(24): p. 5015-5020.
13. Feng, L. and B.I. Suh, *Exposure Reciprocity Law in Photopolymerization of Multi-Functional Acrylates and Methacrylates*. *Macromolecular Chemistry and Physics*, 2007. **208**(3): p. 295-306.
14. Emami, N. and K.J. Soderholm, *How light irradiance and curing time affect monomer conversion in light-cured resin composites*. *Eur J Oral Sci*, 2003. **111**(6): p. 536-42.
15. Halvorson, R.H., R.L. Erickson, and C.L. Davidson, *Energy dependent polymerization of resin-based composite*. *Dental Materials*. **18**(6): p. 463-469.
16. Sakaguchi, R.L. and J.L. Ferracane, *Effect of light power density on development of elastic modulus of a model light-activated composite during polymerization*. *J Esthet Restor Dent*, 2001. **13**(2): p. 121-30.
17. Lovell, L.G., et al., *The effect of cure rate on the mechanical properties of dental resins*. *Dental Materials*, 2001. **17**(6): p. 504-511.
18. Miyazaki, M., et al., *Effect of light exposure on fracture toughness and flexural strength of light-cured composites*. *Dent Mater*, 1996. **12**(6): p. 328-32.
19. Venhoven, B.A.M., A.J. deGee, and C.L. Davidson, *Light initiation of dental resins: Dynamics of the polymerization*. *Biomaterials*, 1996. **17**(24): p. 2313-2318.
20. Sideridou, I., V. Tserki, and G. Papanastasiou, *Effect of chemical structure on degree of conversion in light-cured dimethacrylate-based dental resins*. *Biomaterials*, 2002. **23**(8): p. 1819-1829.

21. Lovell, L.G., et al., *Effects of Composition and Reactivity on the Reaction Kinetics of Dimethacrylate/Dimethacrylate Copolymerizations*. *Macromolecules*, 1999. **32**(12): p. 3913-3921.
22. Amirouche-Korichi, A., M. Mouzali, and D.C. Watts, *Effects of monomer ratios and highly radiopaque fillers on degree of conversion and shrinkage-strain of dental resin composites*. *Dental Materials*, 2009. **25**(11): p. 1411-1418.
23. Van Landuyt, K.L., et al., *Systematic review of the chemical composition of contemporary dental adhesives*. *Biomaterials*, 2007. **28**(26): p. 3757-3785.
24. Nie, J., et al., *Effect of peroxides and hydroperoxides on the camphorquinone-initiated photopolymerization*. *Macromolecular Chemistry and Physics*, 1999. **200**(7): p. 1692-1701.
25. Monroe, B.M. and S.A. Weiner, *Mechanisms of photochemical reactions in solution. LVIII. Photoreduction of camphorquinone*. *Journal of the American Chemical Society*, 1969. **91**(2): p. 450-456.
26. Chen, Y.-C., J.L. Ferracane, and S.A. Prahl, *Quantum yield of conversion of the photoinitiator camphorquinone*. *Dental Materials*, 2007. **23**(6): p. 655-664.
27. Neumann, M.G., et al., *The initiating radical yields and the efficiency of polymerization for various dental photoinitiators excited by different light curing units*. *Dental Materials*, 2006. **22**(6): p. 576-584.
28. Asmussen, E. and A. Peutzfeldt, *Polymerization contraction of resin composite vs. energy and power density of light-cure*. *Eur J Oral Sci*, 2005. **113**(5): p. 417-21.
29. Feng, L., R. Carvalho, and B.I. Suh, *Insufficient cure under the condition of high irradiance and short irradiation time*. *Dent Mater*, 2009. **25**(3): p. 283-9.
30. Peutzfeldt, A. and E. Asmussen, *Resin composite properties and energy density of light cure*. *J Dent Res*, 2005. **84**(7): p. 659-62.
31. Dewaele, M., et al., *Influence of curing protocol on selected properties of light-curing polymers: degree of conversion, volume contraction, elastic modulus, and glass transition temperature*. *Dent Mater*, 2009. **25**(12): p. 1576-84.

32. Silikas, N., G. Eliades, and D.C. Watts, *Light intensity effects on resin-composite degree of conversion and shrinkage strain*. Dental Materials, 2000. **16**(4): p. 292-296.
33. Yap, A.U., M.S. Soh, and K.S. Siow, *Effectiveness of composite cure with pulse activation and soft-start polymerization*. Oper Dent, 2002. **27**(1): p. 44-9.
34. Cramer, N.B., J.W. Stansbury, and C.N. Bowman, *Recent Advances and Developments in Composite Dental Restorative Materials*. Journal of Dental Research, 2011. **90**(4): p. 402-416.
35. Stahl, F., et al., *Light-emitting diode (LED) polymerisation of dental composites: flexural properties and polymerisation potential*. Biomaterials, 2000. **21**(13): p. 1379-1385.
36. Hammersley, A.P., et al., *Two-dimensional detector software: From real detector to idealised image or two-theta scan*. High Pressure Research, 1996. **14**(4-6): p. 235-248.
37. Arnold, O., et al., *Mantid—Data analysis and visualization package for neutron scattering and SR experiments*. Nuclear Instruments and Methods in Physics Research Section A: Accelerators, Spectrometers, Detectors and Associated Equipment, 2014. **764**: p. 156-166.
38. Basham, M., et al., *Data Analysis WorkbeNch (DAWN)*. Journal of Synchrotron Radiation, 2015. **22**(3): p. 853-858.
39. Taylor, J.R., *An Introduction to Error Analysis: The Study of Uncertainties in Physical Measurements*. 1997: University Science Books.
40. Rueggeberg, F.A., D.T. Hashinger, and C.W. Fairhurst, *Calibration of FTIR conversion analysis of contemporary dental resin composites*. Dent Mater, 1990. **6**(4): p. 241-9.
41. Palin, W.M., et al., *Monomer conversion versus flexure strength of a novel dental composite*. J Dent, 2003. **31**(5): p. 341-51.
42. Fong, H., S.H. Dickens, and G.M. Flaim, *Evaluation of dental restorative composites containing polyhedral oligomeric silsesquioxane methacrylate*. Dent Mater, 2005. **21**(6): p. 520-9.
43. Cottrell, T.L., *The Strengths of Chemical Bonds*. 1958, London: Butterworths.

44. Fu, Q., et al., *Tertiary amine catalyzed photo-induced controlled radical polymerization of methacrylates*. *Polymer Chemistry*, 2015. **6**(30): p. 5362-5368.
45. Darvell, B.W., *Chapter 5 - Acrylic*, in *Materials Science for Dentistry (Ninth edition)*, B.W. Darvell, Editor. 2009, Woodhead Publishing. p. 108-127.
46. Watts, D.C., *Reaction kinetics and mechanics in photo-polymerised networks*. *Dental Materials*, 2005. **21**(1): p. 27-35.
47. Williams, G. and D.C. Watts, *Non-symmetrical dielectric relaxation behaviour arising from a simple empirical decay function*. *Transactions of the Faraday Society*, 1970. **66**(0): p. 80-85.
48. Shortall, A., et al., *Initial fracture resistance and curing temperature rise of ten contemporary resin-based composites with increasing radiant exposure*. *Journal of Dentistry*, 2013. **41**(5): p. 455-463.
49. Sakaguchi, R.L. and H.X. Berge, *Reduced light energy density decreases post-gel contraction while maintaining degree of conversion in composites*. *Journal of Dentistry*, 1998. **26**(8): p. 695-700.
50. Sakaguchi, R.L., W.H. Douglas, and M.C.R.B. Peters, *Curing light performance and polymerization of composite restorative materials*. *Journal of Dentistry*, 1992. **20**(3): p. 183-188.

## **4 RELATIVE ORDERS IN RBC POLYMER NETWORK STRUCTURE DEFINED BY NEUTRON SCATTERING**

### **4.1 Introduction**

It is widely reported that accelerating polymerisation in resin based composites using high intensity light activation can impact on the tensile strength, toughness, hardness and degree of polymerisation shrinkage [1-3] and stress [4-6] of these materials [7-10]. However, the mechanisms by which these differences in physico-mechanical properties are achieved are still widely debated and the current understanding of these materials appears to be incomplete. It is accepted that properties are dictated by the chemical structure [11], chain length and architecture of the polymer. Consequently, IR spectroscopy has been used to correlate the degree of conversion [12-15] and polymerisation rate to these structures. Glass transition measurements provide insight into the polymer architecture and free volume [16], and have been used to explain mechanical differences between similarly converted polymers in terms of cross-linkage density. Whilst this interpretation has been very useful it should be noted that although  $T_g$  shows a dependency on cross-linkage [17], it is directly related to segmental polymer motions [18], which are also constrained by increasing cross-linkage. During polymerisation the conformation of monomer and forming polymer segments will inevitably evolve as a function of conversion and polymerisation rate, yet this has been seldom studied in detail.

In chapter three time resolved studies of the polymer structure were obtained using a combination of synchrotron X-ray scattering and FTIR measurements to correlate the polymerisation rate with the polymer structure. A correlation length believed to have an intramonomeric origin increased during polymerisation and results demonstrated that driving polymerisation at faster rates generated a lower ordered polymer conformation which at extreme rates may store residual strain. The changes in the correlation length seen in chapter

three cannot be explained by chain growth alone and relatively large increases in the correlation length suggest that chain segment extension was a contributory factor. Weighted least squares fitting of X-ray scattering spectra from constituent monomers was used to approximate the structure of Bis-GMA and TEGDMA. These results showed that chain extension is likely and that a significant degree of extension occurs in the flexible backbone of the TEGDMA monomer, which can form cross-links. Chain segment extension is therefore either attributable to linearization effects, which is believed to happen more in constrained geometries and/or by real strain i.e. the cross-link is more linear in certain structures or indeed is under strain. The purpose of this chapter was to therefore address uncertainties in the polymer structure. To do so required in depth analysis of the structure of the TEGDMA monomer itself within the Bis-GMA/TEGDMA system.

X-ray scattering is a powerful technique for understanding the effects of polymerisation rate on the polymer structure (chapter three), which by extrapolation may be used to understand final physico-mechanical properties. A deficiency of X-ray scattering however, is that it is strictly limited to structural features with sufficient electron density [19-21]. Hydrogen atoms have a very small X-ray scattering cross-section [22, 23] and do not scatter X-rays efficiently. This is problematic as the TEGDMA monomer and particularly the functional groups where the monomer forms cross-links, are highly hydrogenated. Correlation lengths arising from cross-linking distances can therefore not be distinguished through X-ray scattering techniques.

Whilst X-rays are largely insensitive to correlation lengths at longer cross-link length scales in these systems, this can be circumvented by the use of a complimentary technique like neutron scattering [24]. Neutrons alone are unable to discern structures in highly hydrogenated materials such as dimethacrylate polymers used for dental restorations, due to the hydrogen atom possessing a large incoherent scattering cross section [25]. However, hydrogen atoms may be substituted for its isotope deuterium, which has a relatively large coherent neutron scattering cross section [25], thus scattering more efficiently. Selective exchange of hydrogen for deuterium can therefore be used to modify the neutron scattering cross-section [26] to allow for

specific structures and correlation lengths within a molecule (or monomer), which would not be detected by conventional scattering methods [27], to be highlighted whilst leaving the physical and chemical properties of the molecules largely intact.

It is possible by using a combination of small angle neutron scattering (SANS) methods and isotopic substitution [28] to understand additional structural changes in the resin post-polymerisation. This chapter seeks to address questions raised in chapter three regarding the effects of polymerisation rate on longer range order within the system relating specifically to whole monomeric units and cross-link distances.

## 4.2 Methods

Experimental resin blends were prepared by combining a partially deuterated monomer with a completely hydrogenated dimethacrylate monomer species. Hydrogen has a large incoherent neutron scattering cross section and scatters poorly. Deuterium, the heavier isotope of hydrogen, has a larger coherent neutron scattering cross section and scatters more efficiently making. Deuterium exchange was used in the hydrogenated portion of the methacrylate functional end groups, i.e. the methyl and methylene groups (Figure 4.1), to create a ‘molecular ruler’ to effectively measure the average end to end distance of the TEGDMA monomer prior to and post polymerisation. The procedure by which hydrogen was exchanged for deuterium is outlined in greater detail in section 2.2.2

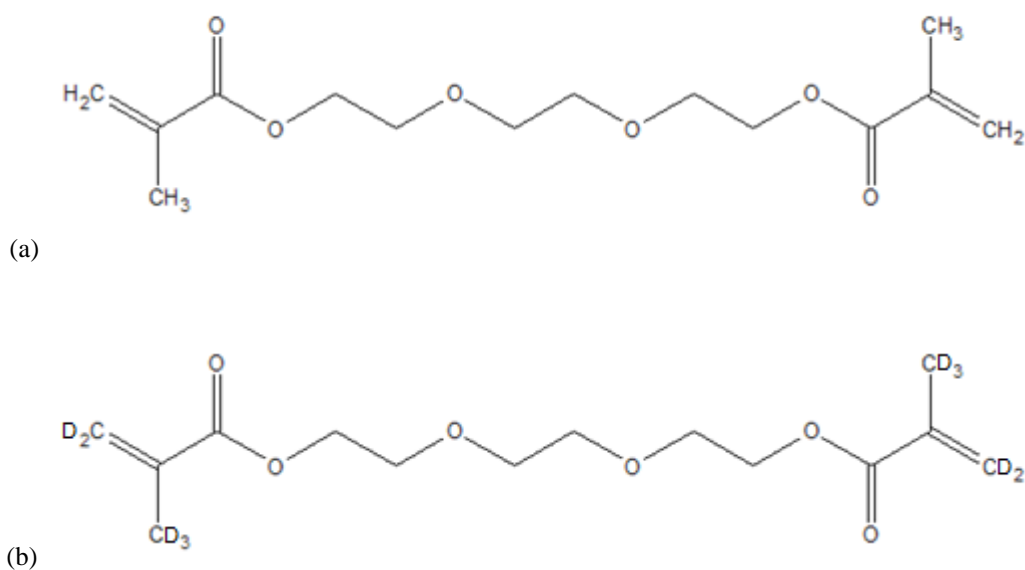


**Figure 4.1.** (a) Fully hydrogenated TEGDMA and (b) partially deuterated TEGDMA where the methyl and methylene groups have had hydrogen exchanged with deuterium.

#### 4.2.1 Preparation of Photo-Polymerisable Dimethacrylate Resin Blends

Bisphenol-A-glycidyl-methacrylate (Bis-GMA) (Sigma-Aldrich, Dorset, UK) and deuterated triethyleneglycol-dimethacrylate (d-TEGDMA) were proportioned in 60/40, 50/50 and 40/60 (Bis-GMA/d-TEGDMA) weight percentage (wt. %) ratios and combined to produce 1 g mixes. The viscosity of the blend increases with the proportion of Bis-GMA. The monomer blends were combined with a photo-initiator as either 0.2 wt% Camphorquinone (CQ) with 0.8 wt% of its tertiary amine N,N-dimethylaminoethyl-methacrylate (DMAEMA) or 1 wt% of the type 1 photo-initiator, Lucirin-TPO (Sigma-Aldrich, Dorset, UK), which does not require a co-initiator. As these partially deuterated monomer blends were produced in significantly smaller quantities than for hydrogenated counterparts it was not possible to homogenise blends using a mixing machine. The proportioned monomers and photo-initiators were instead manually stirred with a spatula for 60 minutes per blend at  $50 \pm 1$  °C in dark conditions until homogenous.

Test specimen discs were prepared by filling a circular impression in a polyvinylsiloxane mould (11 mm diameter and 1 mm in depth), and pressed flat with a microscope cover slide to prevent the formation of an oxygen inhibition layer. Samples were purposely manufactured to be no more than 1 mm in thickness to reduce the effects of absorption and incoherent and inelastic scattering which is significant in materials with a 1:1 ratio of hydrogen to deuterium [29]. Resins were photo-polymerised using an EMS Swiss master light curing unit (EMS OPTIDENT, electro medical systems, Nyon Switzerland) which was placed normal to and in contact with the cover slide. The curing unit had a spectral output range of 390 – 550 nm to provide significant overlap with the absorption peaks of the Camphorquinone (470 nm) and Lucirin TPO (381 nm) photo-initiators. For each unique composition, the resin was either photo-polymerised at a relatively high ( $3000 \text{ mW cm}^{-2}$  for 6 s) or low ( $300 \text{ mW cm}^{-2}$  for 60 s) light intensity to introduce extreme rates of polymerisation whilst ensuring matched total energy doses. The resultant specimens were stored in dark conditions in sealed containers at  $4 \pm 1$  °C

prior to further use. Resin disc samples and their respective photo-polymerisation regimes are summarised in Table 2.5 in Materials and Methods.

## 4.2.2 Neutron Scattering

### 4.2.2.1 LOQ

Preliminary small angle neutron scattering (SANS) measurements were carried out on the LOQ [30] small-angle diffractometer at the ISIS Pulsed Neutron Source (STFC Rutherford Appleton Laboratory, Didcot, U.K.). The beam line is a time of flight instrument (TOF) and utilises a white beam with a wavelength range of 2.2 – 10 Å to provide a final  $q$  range [31] of 0.006 – 1.4 Å<sup>-1</sup>, where  $q=4\pi \sin\theta/\lambda$ , with a 8 mm (diameter) beam size [31]. Scattering data were collected simultaneously across the whole  $q$  range by a combination of low and high angle bank 2D area detectors (Ordela, <sup>3</sup>He – CF<sub>4</sub>, Oak Ridge National Laboratory, Tennessee, USA) covering  $q$  ranges of 0.006 – 0.24 Å<sup>-1</sup> and 0.15 – 1.4 Å<sup>-1</sup> respectively [31]. Resin disc samples were wrapped in Aluminium foil to prevent further photo-activated polymerisation and were mounted on a Cadmium sample rack and measured for 1 h. In addition to pre-polymerised samples, constituent monomers (Bis-GMA and d-TEGDMA) in isolation as well as in combination with each other in 60/40 and 40/60 wt% ratios, were placed inside 1 mm path length quartz cuvettes (quartz suprasil, Helma analytics, Essex, UK) and measured for 1 h to identify their contributions to the scattering signal and to establish initial values for correlation lengths of interest. To aid data analysis measurements were taken for the direct beam, empty sample containers (Aluminium foil and quartz cuvettes) and sample transmission. Data was converted to scattering cross section using the Loq plug in for the MantidPlot software package [32] and placed on an absolute scale (cm<sup>-1</sup>) using the scattering from a solid blend of hydrogenous and pre - deuterated polystyrene sample.

#### 4.2.2.2 SANS2D

Small angle neutron scattering (SANS) measurements were performed on the SANS2D [33] instrument at the ISIS pulsed neutron source (Rutherford Appleton Laboratories, Oxford, UK). Resin disc-shaped test specimens were sealed within Aluminium foil and mounted on a Cadmium sample rack to absorb neutrons. SANS2D is a time of flight (TOF) instrument which uses a wavelength range of 1-12 Å to provide a  $q$  range of  $0.004 - 2 \text{ \AA}^{-1}$ , where  $q = 4\pi/\lambda \sin\theta$ . An 8 mm (diameter) beam size was used to collect SANS data in a transmission mode geometry using a 2D area detector (Ordela,  $^3\text{He} - \text{CF}_4$ , Oak Ridge National Laboratory, Tennessee, USA) [34]. Acquisition times per sample were approximately 1 hour and additional measurements were also taken on hydrogenated sample counterparts to serve as controls. Further measurements were taken for the direct beam, empty sample rack, sample transmission, Aluminium foil and a Vanadium calibration standard to correct for background and transmission effects and to normalise the data to absolute scattering units respectively. Data was reduced to 1D in absolute scattering units using the SANS2D plugin for the Mantidplot [32] software package.

#### 4.2.2.3 D16

Neutron diffraction experiments were performed on the small-momentum transfer cold neutron two circle diffractometer D16 [35] at the Institut Laue-Langevin (ILL, Grenoble, France). The instrument was operated with a neutron beam energy of 2.6 keV corresponding to a wavelength of 4.75 Å and  $\Delta\lambda/\lambda = 0.01$ , with a beam size of 5 by 5 mm (horizontal  $\times$  vertical) [35, 36]. Resin disc samples were wrapped in Aluminium foil to prevent further photo-activated polymerisation, whilst liquid monomer blends were contained in 1 mm path length quartz cuvettes (Helma Analytics, Essex, UK) and mounted on a cadmium sample rack. The intensity of the diffracted beam was recorded at a sample to detector distance of 500 mm by the

millimetre-resolution large-area neutron detector (MILAND)  $^3\text{He}$  position-sensitive detector [37], which consists of  $320 \times 320$  (xy) channels with a resolution of  $1 \times 1 \text{ mm}^2$ . Three detector bank positions were used to capture structural features over a total  $q$  range of  $0.01 - 2.0 \text{ \AA}^{-1}$ . Each detector bank position had a measurement time of 15 min, giving a total collection time of 45 min per sample. Intensities on the detector surface were corrected for solid angle and pixel efficiency and normalized to the flat incoherent signal of a 1 mm water cell following subtraction of the empty sample cell background. A photo-diode mounted on to the beam stop was used to measure the sample transmission for corresponding data corrections. Scattering data was converted to absolute units using measurements from a Boron Carbide standard. All data reduction was performed using the ILL in-house LAMP (Large Array Manipulation Program) software package [38].

#### 4.2.2.4 Synchrotron X-ray Scattering Measurements

In chapter three structural changes were only observed *in-situ* using X-ray scattering for 360 s during photo-polymerisation giving no insight into possible structural evolution that may occur during post-cure. Deuterated test samples were photo-polymerised several weeks before the SANS experiment and will have undergone some degree of post cure [39-43] in the time between. A gap in the data therefore exists, describing how the structure is modified throughout post-cure. Additional SAXS measurements were conducted over a time scale of three hours to characterise structural changes during post-cure. The duration of the measurement was restricted to three hours per sample due to the time constraints imposed by using a synchrotron source.

Synchrotron X-ray scattering experiments were carried out on the XMaS beamline (BM28) [44-46] at the European Synchrotron Radiation Facility (ESRF, Grenoble, France). An incident X-ray energy of 15 keV was used corresponding to a wavelength ( $\lambda$ ) of 0.82 Å, with a beam size of 0.08 × 0.5 mm (horizontal × vertical) defined by vacuum tube slits. Measurements were carried out in air, at 23 ± 1 °C with light excluded other than the photo-curing light source.

Test specimens were prepared by filling a 0.9 mm thick stainless steel ring with a 10 mm internal diameter with 60/40 (Bis-GMA/TEGDMA) wt % hydrogenated resin blends initiated with either TPO or CQ as the photo-initiator (Section 2.4.1), which was sealed on both faces by 25 µm thick Mylar film (RS, Northants, UK). The resin filled rings were housed within a brass block annulus (Daresbury Laboratory, Warrington, UK) and mounted at 30° normal to the path of the incident X-rays, 300 mm from the X-ray source. A 5 mm diameter light guide (Lumencor, Kent, UK) was fixed normal to and 10 mm distant from the centre of the resin surface and connected to a multichannel light source (Lumencor Aura Light engine, Lumencor, Kent, UK) to illuminate the sample.

For the TPO initiated resins, the light engine was programmed to emit a peak emission spectrum at 405 nm, whilst for CQ systems a wavelength of 470 nm was employed. The wavelengths of light were chosen to match the maxima in the absorption spectra of the respective photo-initiators [47]. Camphorquinone initiated resins were either photo-polymerised at a relatively high ( $634 \text{ mW cm}^{-2}$  for 30 s) or low ( $53 \text{ mW cm}^{-2}$  for 360 s) light intensity to introduce extreme rates of polymerisation whilst ensuring matched total energy doses. Resins utilising TPO were photo-polymerised at a light intensity of  $1640 \text{ mW cm}^{-2}$  for 30 s to understand how the polymer structure evolved at longer time scales when polymerised at an extremely fast rate.

2D scattering images were collected using a  $2048 \times 2048$  pixel MAR CCD (MAR CCD 165, Rayonix, Norderstedt, Germany) camera, 570 mm from the sample to give a  $q$  range of 0.1 to  $1.9 \text{ \AA}^{-1}$ , where  $q=4\pi \sin\theta/\lambda$  (here  $\theta$  is equivalent to half the angle between the incident X-rays and the detector). A Helium filled flight tube was employed to minimise air scattering. Scattering images were collected with a 1 s count time and a 4 s readout time giving a 5 s temporal resolution. Time resolved scattering measurements were conducted for each resin-blend by initially collecting data for 20 s prior to remote activation of the light engine. In addition to the time resolved photo-activated samples, X-ray measurements were acquired for the constituent monomers (Bis-GMA and TEGDMA) in isolation and containing photo-initiator to identify their contributions to the scattering signal of each blend. The contribution of the X-ray beam to the measurements was assessed by conducting observations for over 30 min for the uncured and polymerised samples in the absence of light. To aid data analysis measurements were taken for direct beam, empty sample containers, Mylar windows, water and a silver behenate calibration standard to allow the scattering patterns to be corrected for background and normalisation effects. Transmitted beam was recorded throughout using a beam-stop mounted photodiode. Data were normalised to the incident monitor intensity and background corrected using the Fit2D software package (version 12.077, ESRF) [48]. Data were azimuthally

integrated over  $360^\circ$  to produce a 1D output and were subsequently fitted with Gaussian [32] models to determine peak positions and relative order.

### 4.2.3 Density Measurements

The densities of the deuterated resin disc samples were determined via helium gas pycnometry (Quantachrome ULTRAPYC 1200e, Hartley Whitney, England). The device was calibrated using a stainless steel sphere with a known volume and weight (volume = 2.145 cm<sup>3</sup>, weight = 16.383 g). Individual resin discs were measured inside a micro cell chamber (internal diameter = 15 mm, volume = 4.25 cm<sup>3</sup>) to a resolution of  $1 \times 10^{-4}$  g cm<sup>-3</sup>. Each individual density value was the average of five internal automated measurements, a process repeated five times per disc to calculate an average density for a specific blend and polymerisation regime. Due to the limited number of deuterated resin disc specimens, density measurements were repeated with hydrogenated counterparts to ascertain differences in density between blends and polymerisation regimes and to improve statistics. Similarly, the density was measured five times per disc (with each measurement consisting of five automated internal measurements) for three disc specimens and these values were used to calculate an average density for a specific blend and polymerisation regime. Uncertainties in the density for each composition are reported as the standard deviation of all measurements.

### 4.2.4 Data Analysis

SANS patterns were integrated over respective detector banks and merged to produce a 1D output of  $q$  versus scattering intensity ( $I(q)$ ) using the MantidPlot [32] package for data obtained at ISIS and the LAMP package [38] for data generated at the ILL. Due to a low signal to noise ratio data was smoothed with a six point Savitzky-Golay polynomial to aid peak fitting. Scattering peaks were fitted with Gaussian models to determine the peak position and full width at half maximum (FWHM) using the MantidPlot software package [32] (version 3.0.0, 2013). The peak position corresponds to the average bond length (correlation length), whilst the FWHM gives insight into the distribution of chemical bond lengths and angles termed as order. Correlation lengths and order were compared between identically composed resin samples photo-polymerised at relatively slow and fast rates.

## 4.3 Results

### 4.3.1 Scattering Features Pre and Post Photo-Polymerisation

Figure 4.2 shows the radially averaged neutron scattering profile for a 60/40 wt % (Bis-GMA/d-TEGDMA) resin blend utilising a CQ photo-initiator system, prior to photo-polymerisation, in the liquid-monomeric form (solid line) after being stored in dark conditions and in the polymer state (broken line) following photo-polymerisation with a light source intensity of 3000 mW cm<sup>-2</sup> for 6 s. It can be seen in the monomer form that three scattering features exist; a low  $q$  feature is found at  $q \sim 0.22 \text{ \AA}^{-1}$  corresponding to a correlation length of approximately 28.5 Å. Additionally, a broad but well defined scattering peak is located at  $q \sim 0.6 \text{ \AA}^{-1}$  (~10.5 Å) and a poorly defined feature is seen between 1.35 – 1.4 Å<sup>-1</sup> (4.48 - 4.65 Å).

Post photo-polymerisation it can be seen that four scattering features are now present. The low  $q$  peak (a) displays a small shift to lower  $q$  (0.22 to 0.2 Å<sup>-1</sup>) equivalent to a length increase of approximately 3 Å. This scattering feature also shows a change in intensity and shape which may suggest that this peak is an artefact of scattering at low  $q$  due to a high background measurement and will not be discussed in detail. The peaks initially located at (b)  $q \sim 0.6 \text{ \AA}^{-1}$  and (c)  $q \sim 1.15 \text{ \AA}^{-1}$  has shifted to significantly lower  $q$  and has become narrower. These changes are indicative of an increase in the measured correlation length and a decrease in the associated short range order. A new scattering peak (d) is identified at  $q \sim 1.35 \text{ \AA}^{-1}$ , whilst the high  $q$  broad scattering peak moves to slightly higher  $q$ , corresponding to a decrease in this possible correlation length.

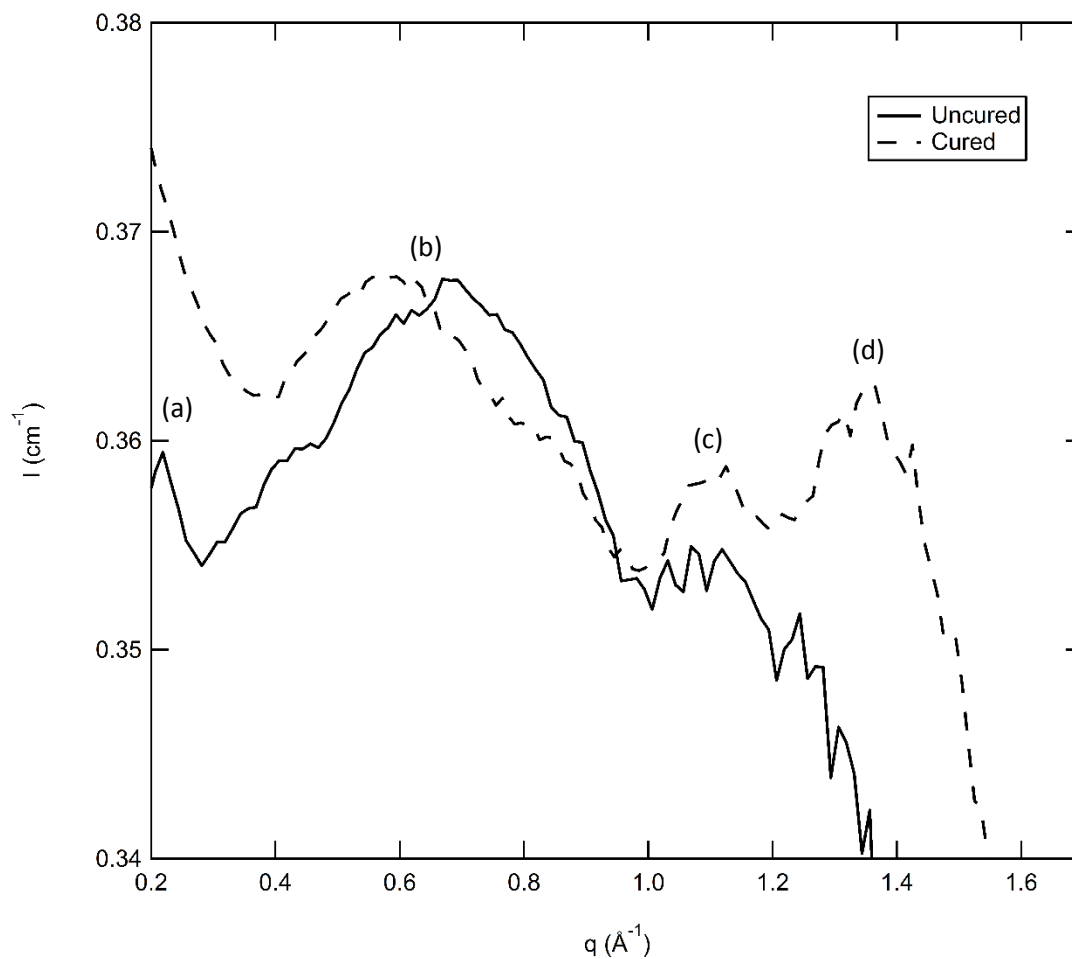


**Figure 4.2.** Small angle neutron scattering spectra of a 40/60 wt % (Bis-GMA/d-TEGDMA) blend initiated with CQ, prior to photo-polymerisation (solid line) and after photo-polymerisation (broken line). Three prominent scattering features are located at  $q \sim 0.6$ ,  $1.15$  and  $1.4 \text{ \AA}^{-1}$ . The feature at  $\sim 0.2$  may not represent a true structural feature and may instead be a low  $q$  artefact.

### 4.3.2 Contributions to the Neutron Scattering Spectra

Figure 4.3 shows the SANS spectra for the constituent monomers (liquid form) d-TEGDMA and hydrogenated Bis-GMA. It can be seen that d-TEGDMA displays two broad scattering peaks located at  $q \sim 0.4 \text{ \AA}^{-1}$  ( $\sim 1.57 \text{ \AA}$ ) and  $q \sim 1.33 \text{ \AA}^{-1}$  ( $\sim 4.72 \text{ \AA}$ ). Hydrogenated Bis-GMA is featureless within the region up to  $q \sim 1 \text{ \AA}^{-1}$ , but displays a scattering peak at  $\sim 1.18 \text{ \AA}^{-1}$  ( $\sim 5.32 \text{ \AA}$ ). This scattering peak is located at a similar length scale to scattering peak (c) (Figure 4.2), albeit at slightly higher values of  $q$ . Figure 4.4 displays the SANS spectra of a 60/40 Bis-GMA/TEGDMA blend with CQ as the initiator. This completely hydrogenated resin blend shows only one scattering peak at  $q \sim 1.2 \text{ \AA}^{-1}$ , but the region up to  $q \sim 1 \text{ \AA}^{-1}$  displays no scattering features. In comparison the SANS spectra of the same blend, but with d-TEGDMA substituted for TEGDMA shows two broad scattering peaks at  $q \sim 0.6$  and  $q \sim 1.2 \text{ \AA}^{-1}$ . It should be noted that there is a difference between the correlation length ( $q \sim 0.6 \text{ \AA}^{-1}$ ) of the neat d-TEGDMA liquid and the Bis-GMA/d-TEGDMA liquid blend. For the neat d-TEGDMA the scattering feature corresponds to a correlation length of approximately  $15 \text{ \AA}$ , which is close to the ideal chain length for this monomer ( $\sim 19 \text{ \AA}$ ). Whilst in the blend the correlation length is significantly shorter at  $\sim 10.5 \text{ \AA}$ . This peak is also quite broad in both monomer and polymer form, which represents some considerable variation in the conformation of the d-TEGDMA.

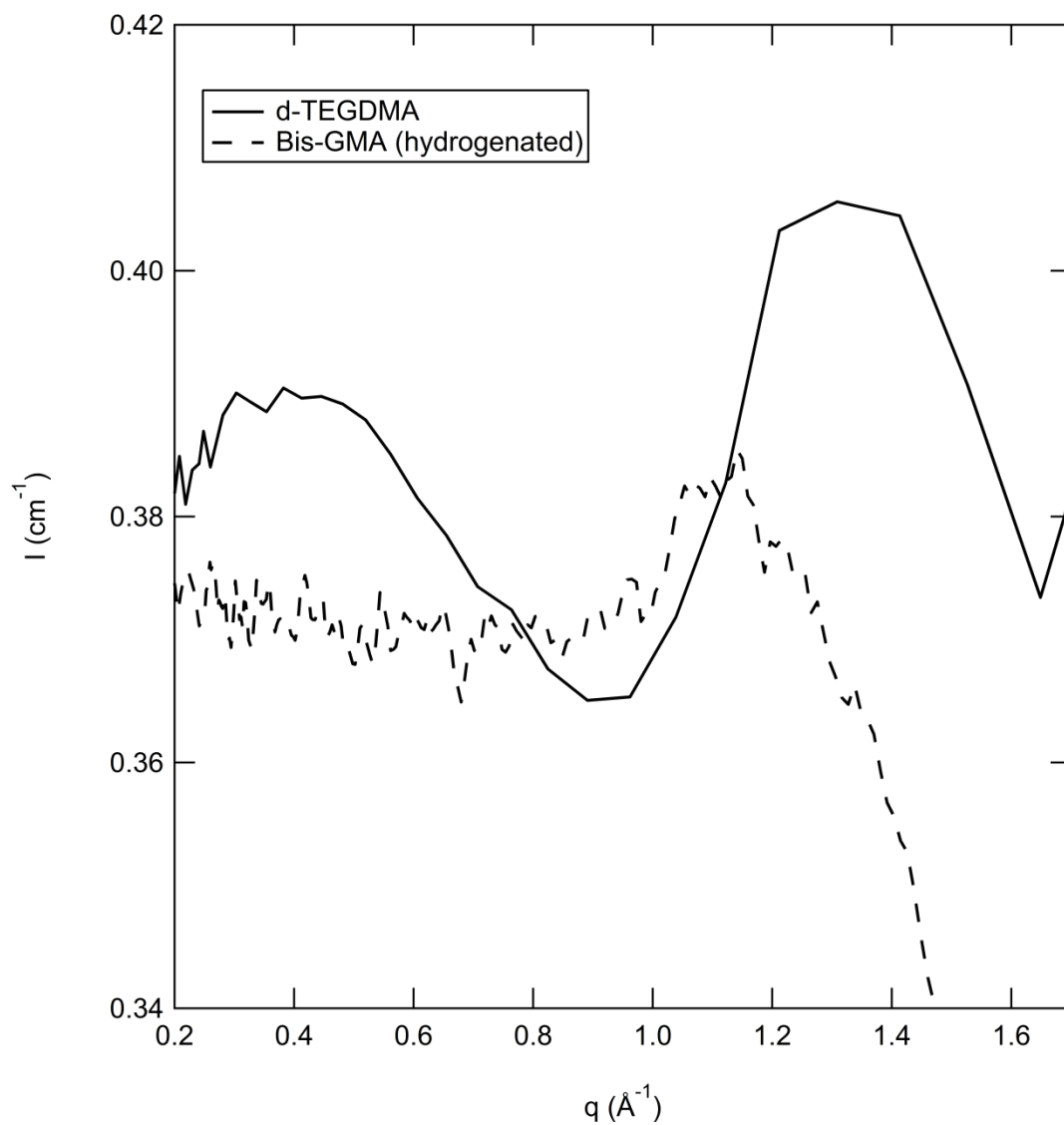


**Figure 4.3.** SANS spectra of liquid monomers d-TEGDMA (solid black line) and hydrogenated Bis-GMA (broken black line).

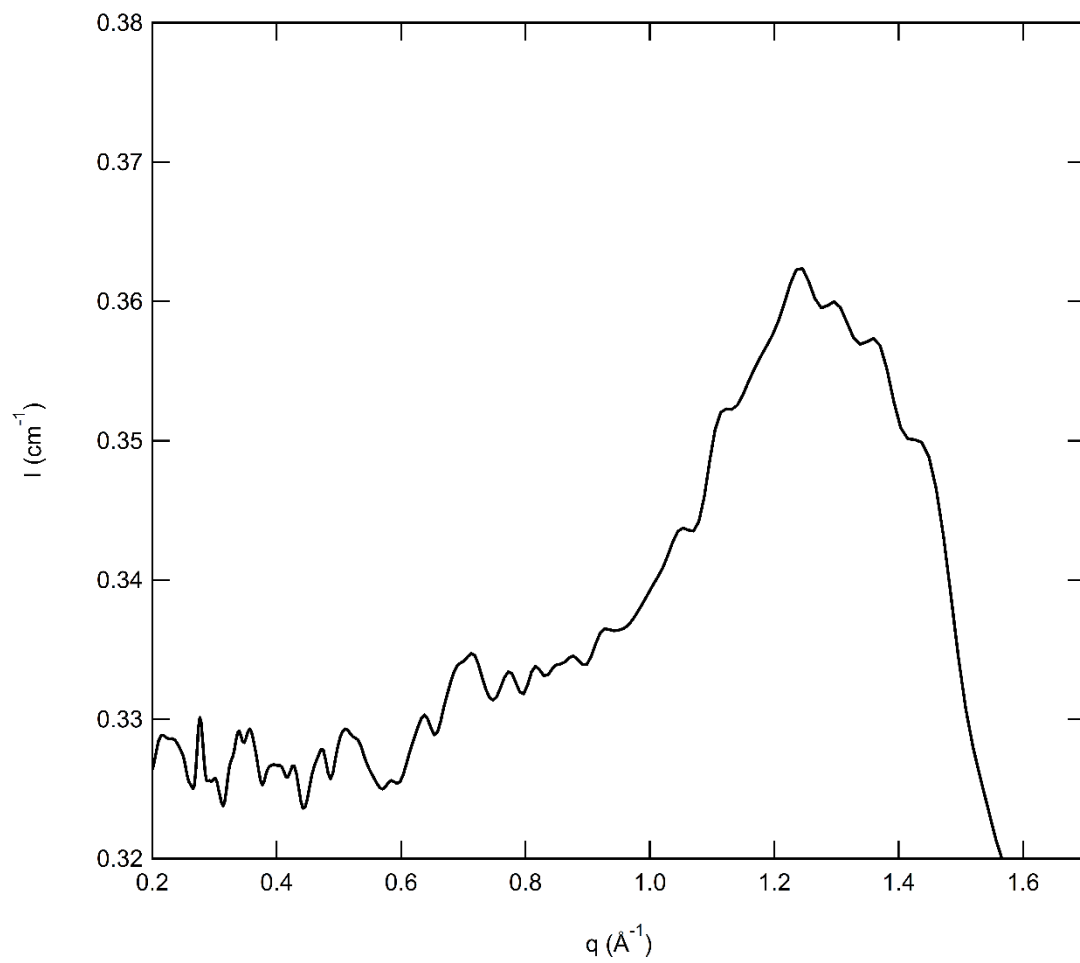


**Figure 4.4.** SANS spectra of a completely hydrogenated 60/40 wt% (Bis-GMA/TEGDMA) sample with a CQ initiator system.

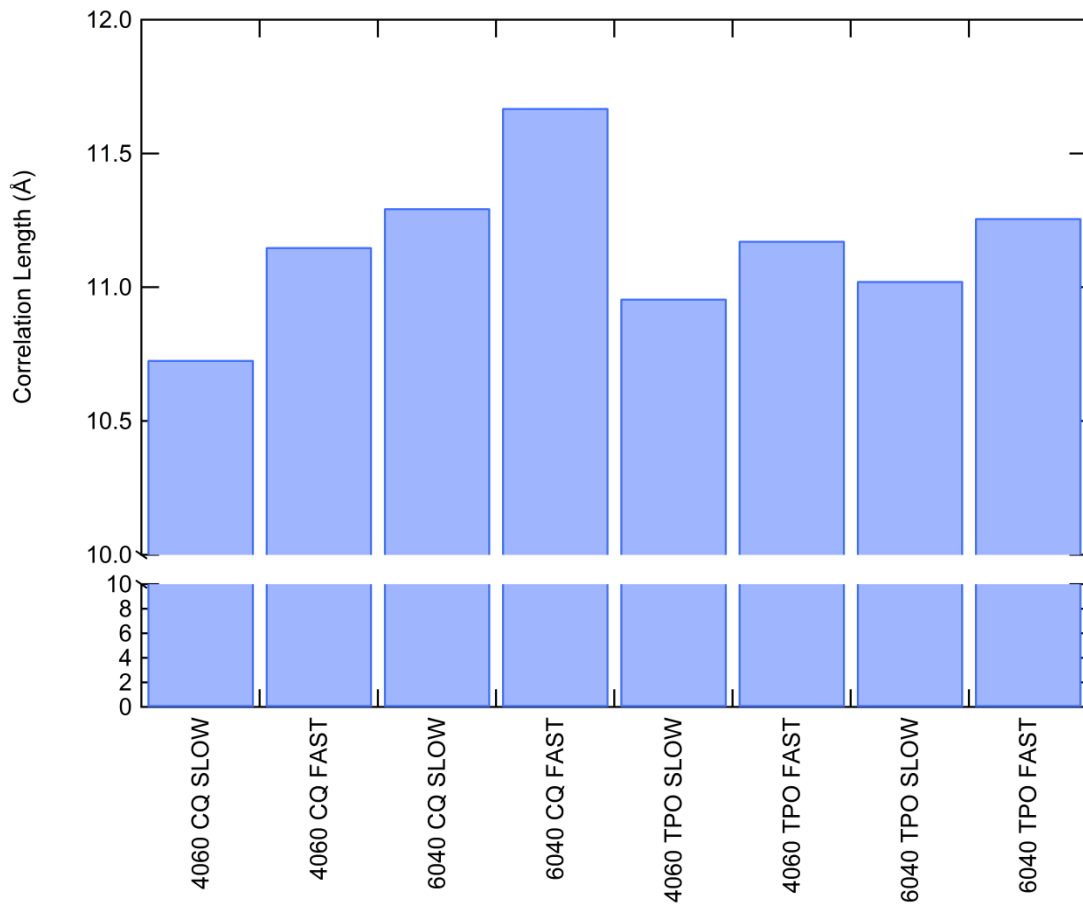
### 4.3.3 The Effect of Relative Differences in Polymerisation Rate on the Final Polymer Structure

#### 4.3.3.1 Scattering Feature (b)

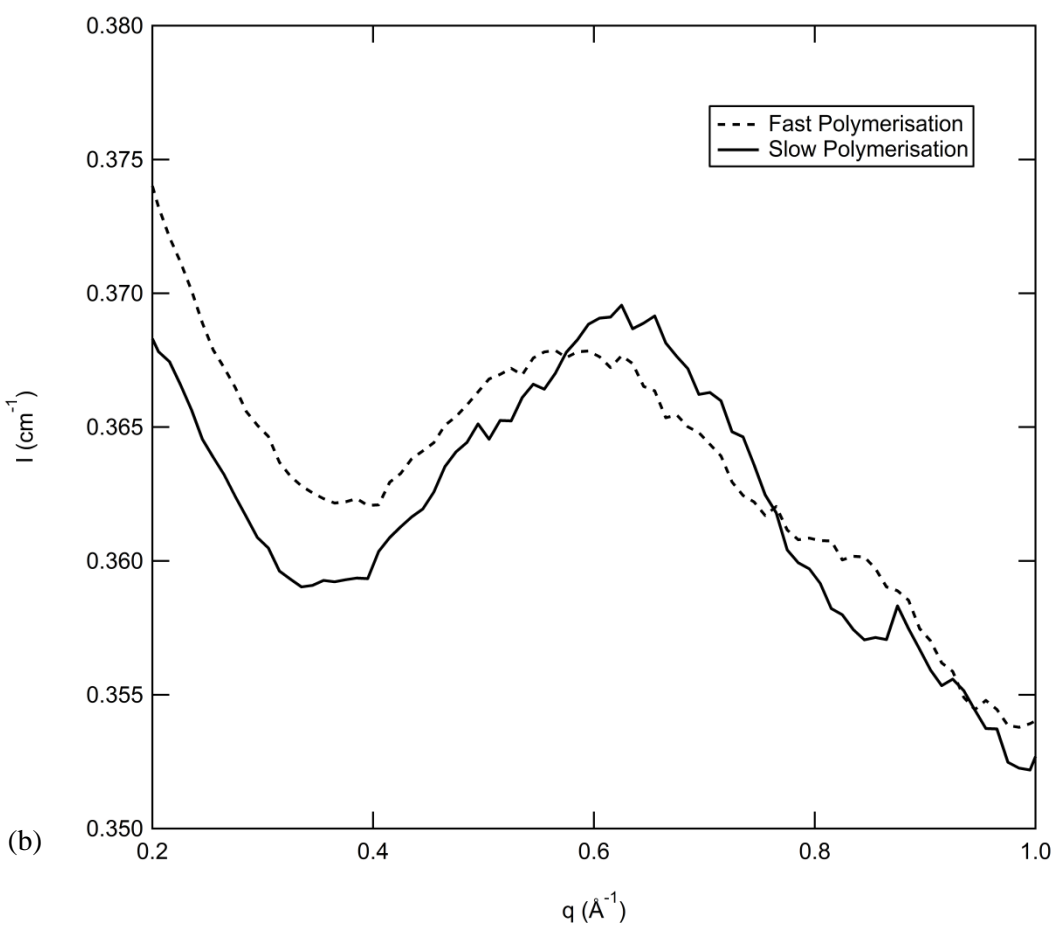
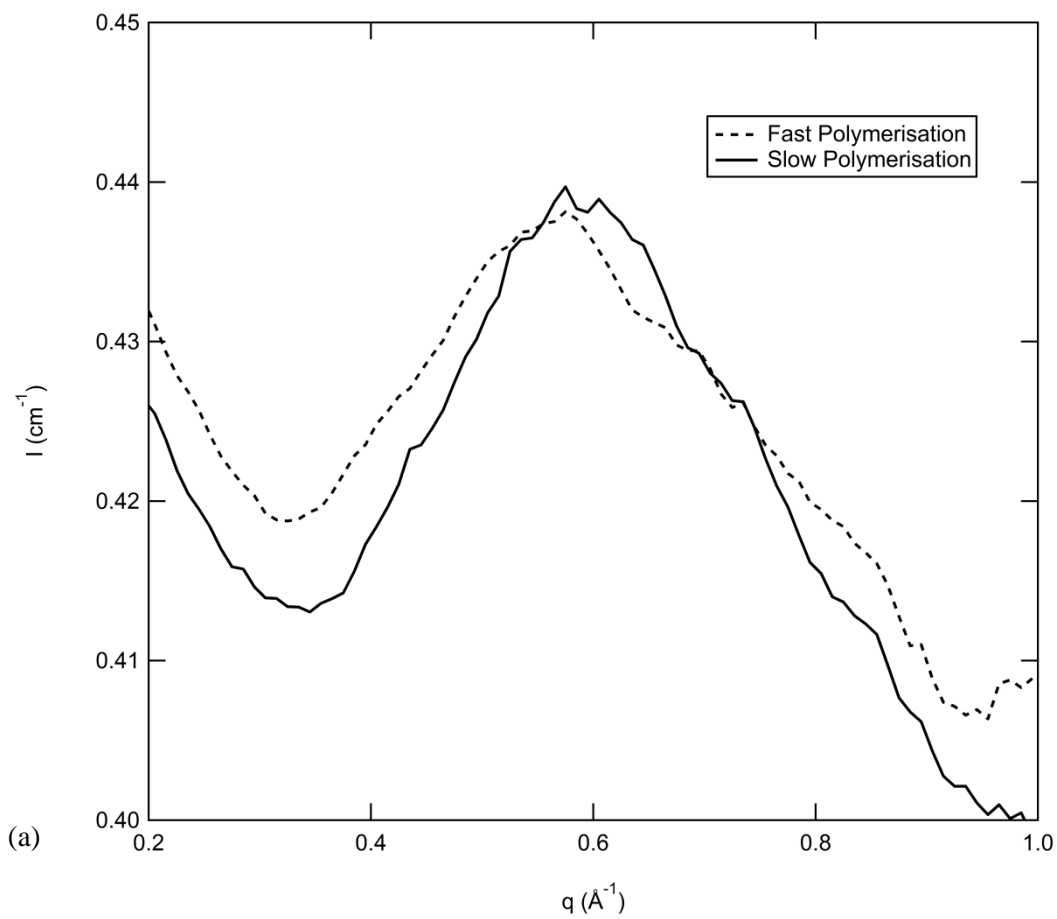
In this study photo-initiator chemistry and the irradiance protocol was used to generate relative differences in the polymerisation rate (characterised using FT-NIR in chapter three). Figure 4.5 illustrates the position of the  $q \sim 0.6 \text{ \AA}^{-1}$  scattering peak post photo-polymerisation, for each resin blend at each photo-polymerisation regimen. Here the final correlation lengths are shown in real space. It can be seen for all blends, regardless of photo-initiator chemistry, that accelerating polymerisation through the use of a higher light intensity confers a greater increase in the correlation length, as also shown in Figure 4.5 and 4.6. The use of the more reactive TPO photo-initiator also yields a greater increase in the correlation length under the same irradiation protocols. TPO initiated resins polymerised at relatively high ( $3000 \text{ mWcm}^{-2}$ ) and low ( $300 \text{ mWcm}^{-2}$ ) light intensities demonstrate larger final correlation lengths by  $\sim 0.1$  and  $\sim 0.23 \text{ \AA}$  respectively in comparison to CQ based resins of identical monomer formulation. Differences in the final correlation length between the high and low light irradiance density regimes, for a specific blend, are typically twice as large in CQ initiated resins ( $\sim 0.44 \text{ \AA}$ ) than TPO based systems ( $\sim 0.2 \text{ \AA}$ ). Altering the relative resin viscosity (the ratio of Bis-GMA to TEGDMA) appears to have little effect on the correlation length, with only relatively small differences present between the more fluid (40/60 wt%) and viscous (60/40 wt%) blends for identical irradiation protocols. This is likely due to greater cross-linking by TEGDMA monomers in comparison to Bis-GMA. This has been suggested indirectly through elution studies of Bis-GMA/TEGDMA resins which showed leaching of Bis-GMA [49-51].

Figure 4.7 shows the full width half maximum (FWHM) of the  $q \sim 0.6 \text{ \AA}^{-1}$  correlation peak for all resin disc-shaped samples. The FWHM provides insight into the distributions of chain conformations i.e. bond lengths and angles within the d-TEGDMA monomer, for relatively fast and slow polymerisation rates. It can be seen that for a fixed resin composition and photo-

initiator chemistry that resins polymerised at faster rates through the use of a higher light intensity, but shorter exposure time, demonstrate a larger FWHM indicative of lower short range order. However for each irradiance, the difference in the FWHM between resin blends utilising different photo-initiator chemistry or different viscosities are very small.



**Figure 4.5.** Correlation lengths, corresponding to the scattering peak initially located at  $q \sim 0.6 \text{ \AA}^{-1}$ , post photo-polymerisation for the respective resin blend test specimens.



**Figure 4.6.** SANS spectra of 60/40 wt % (Bis-GMA/d-TEGDMA) blends utilising either (a) CQ or (b) TPO photo-initiator. Resin samples polymerised at high irradiance densities are referred to as the fast regimen (broken black line) whilst low irradiance density curing protocols are termed slow regimens (solid black line).

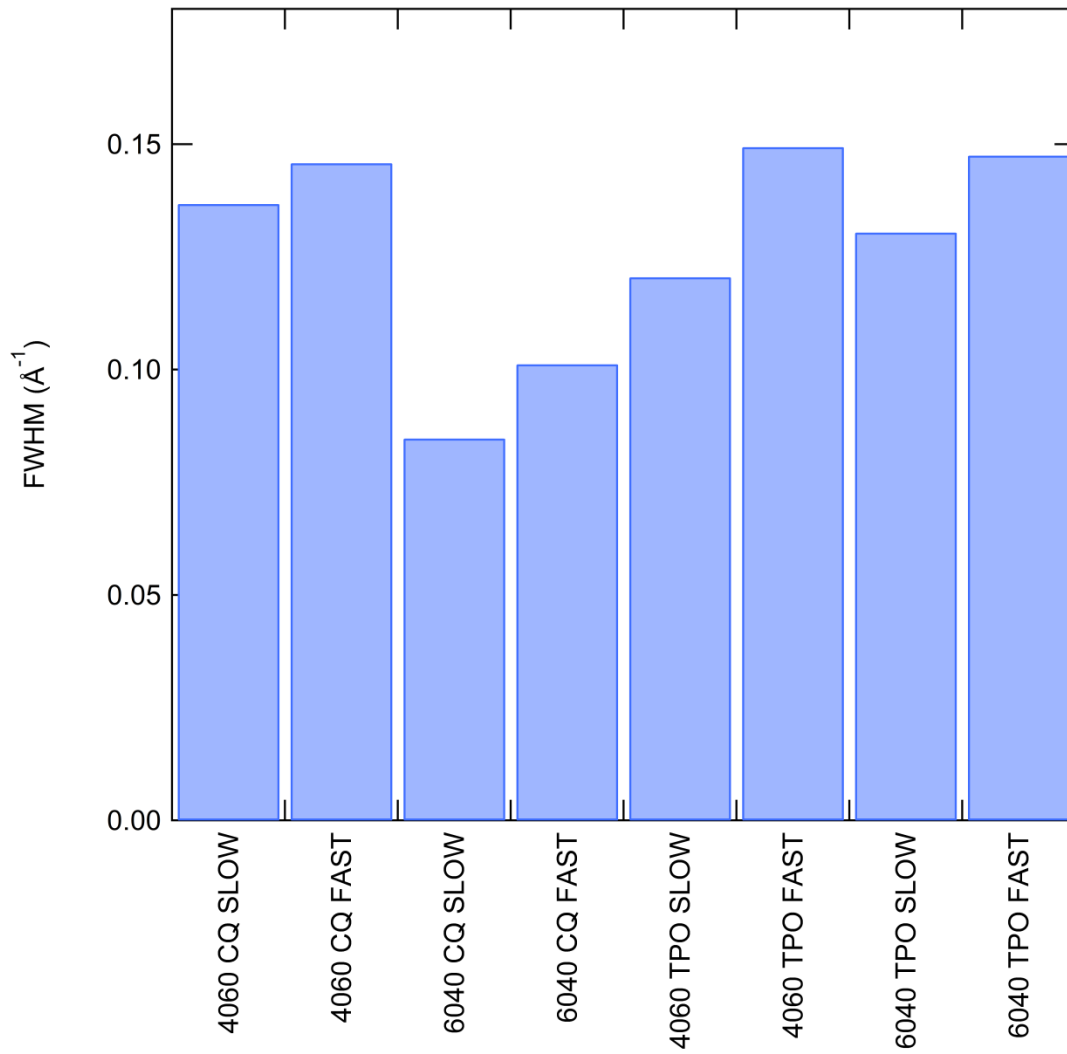


**Figure 4.7.** Full width at half maximum (FWHM) for the scattering peak located at  $q \sim 0.6 \text{ \AA}^{-1}$ , post photo-polymerisation for the respective resin blend specimens.

### 4.3.3.2 Scattering feature (c)

Figure 4.8 shows the final correlation length for scattering feature (c), for each resin blend and irradiance protocol, post photo-polymerisation. It can be seen that for all blends that accelerating photo-polymerisation through the use of high light intensity conferred a greater increase in the correlation length. Differences in correlation lengths between high and low light intensity irradiance protocols were  $\sim 0.05 \text{ \AA}$  for both photo-initiator methods. Resins using TPO initiator showed greater final correlation lengths at equivalent irradiance protocols in comparison to CQ based systems. Typically, for a given blend the correlation length was approximately  $0.17 \text{ \AA}$  larger in a TPO based resin. Correlation lengths are not shown for all samples as the signal to noise ratio for this peak was not always high enough to perform a reliable and accurate fit.

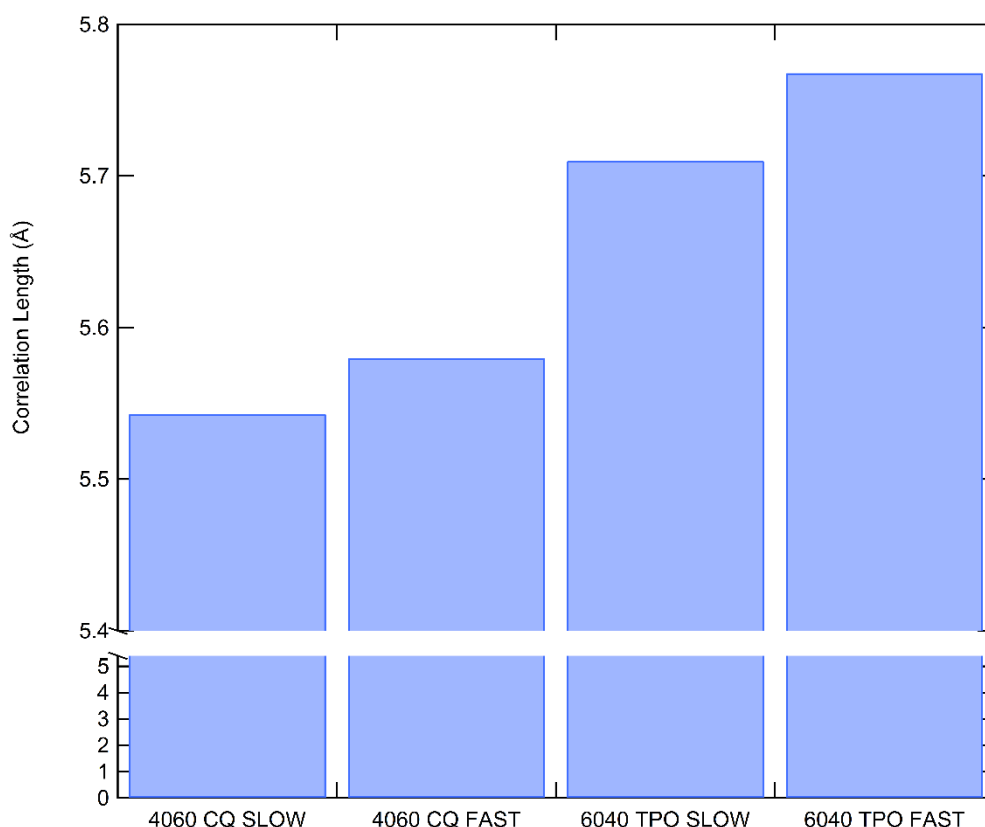


**Figure 4.8.** Final correlation lengths for peak (c) ( $q \sim 1.15 \text{ \AA}^{-1}$ ), for each resin formulation and irradiance protocol.

#### 4.3.3.3 Scattering Feature (d)

Figure 4.9 illustrates the final position, in real space, of the higher  $q$  peak ( $\sim 1.4 \text{ \AA}^{-1}$ ) seen in Figure 4.2 for all resin blends and irradiance protocols post photo-polymerisation. All blends display a shift to higher  $q$  and it can be seen that accelerating polymerisation through the use of the more reactive photo-initiator species TPO, confers a smaller final correlation length in comparison to identically composed resins initiated with CQ under the same illumination protocols. Similarly, sub sets of assumed polymerisation rates for each photo-initiator chemistry, introduced by different light intensities, show that for TPO based systems a relatively large difference exists between the high and low light intensity illumination regimes equivalent to approximately  $0.15 \text{ \AA}$ . However, in CQ based systems differences in the correlation lengths between relatively fast and slow polymerisation rates are negligible. The data also shows no clear relationship between the relative viscosity (Bis-GMA/TEGDMA ratio) of the system and correlation length. For CQ initiated resins the more fluid blend (40/60 wt%) displays a larger correlation length in comparison to the relatively viscous (60/40 wt%) counterpart, whilst the opposite is true for TPO based systems, although differences in the latter system are smaller.

#### 4.3.3.4 Density Measurements

Figure 4.10 summarises the average densities for hydrogenated counterparts of the deuterated resin specimens used for SANS. Hydrogenated versions were used instead of deuterated samples as duplicates could be easily and inexpensively made to improve statistics. Resins initiated with TPO typically display greater densities in comparison to CQ based systems. This is likely due to differences in terminal monomer to polymer conversion. It can be seen that for CQ initiated resins, samples polymerised with lower light intensities display greater densities. However, TPO initiated resins show negligible differences with regards to irradiance protocol.

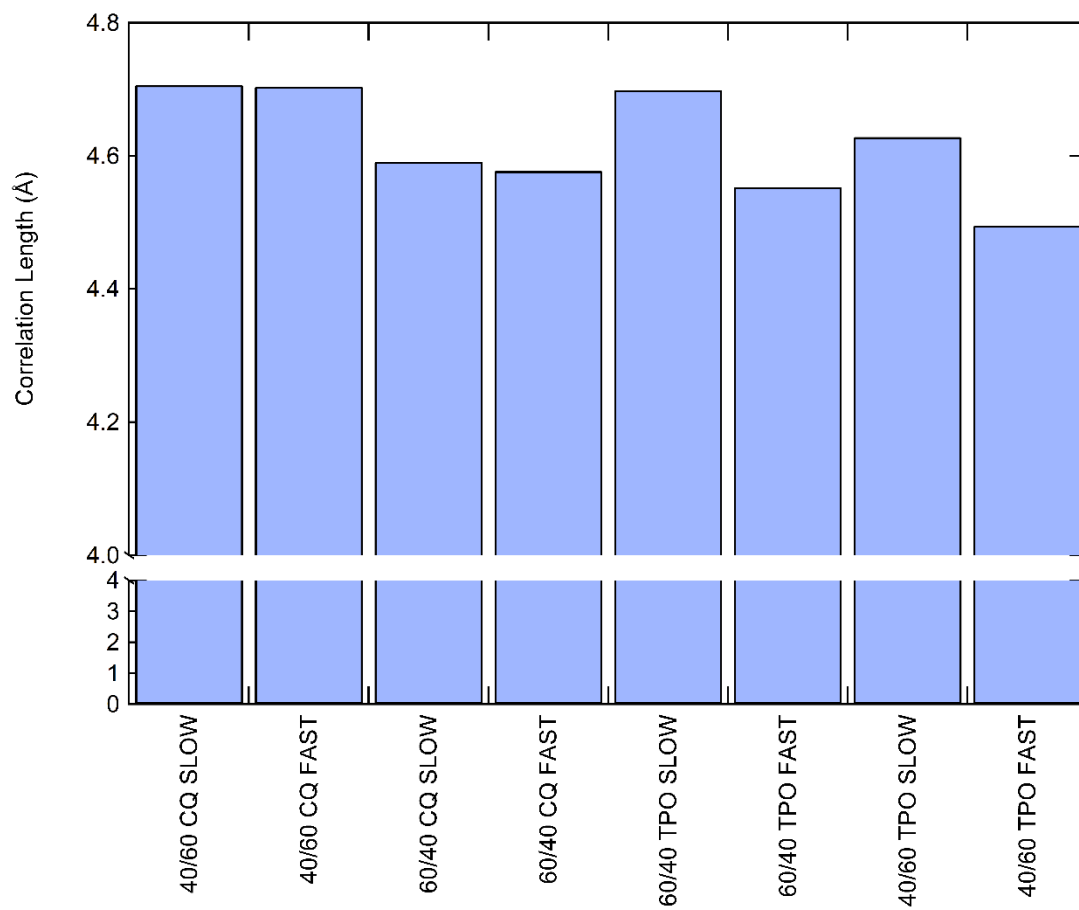


**Figure 4.9.** Final correlation lengths (peak (d),  $q \sim 1.4 \text{ \AA}^{-1}$ ) for the each resin specimen post-polymerisation

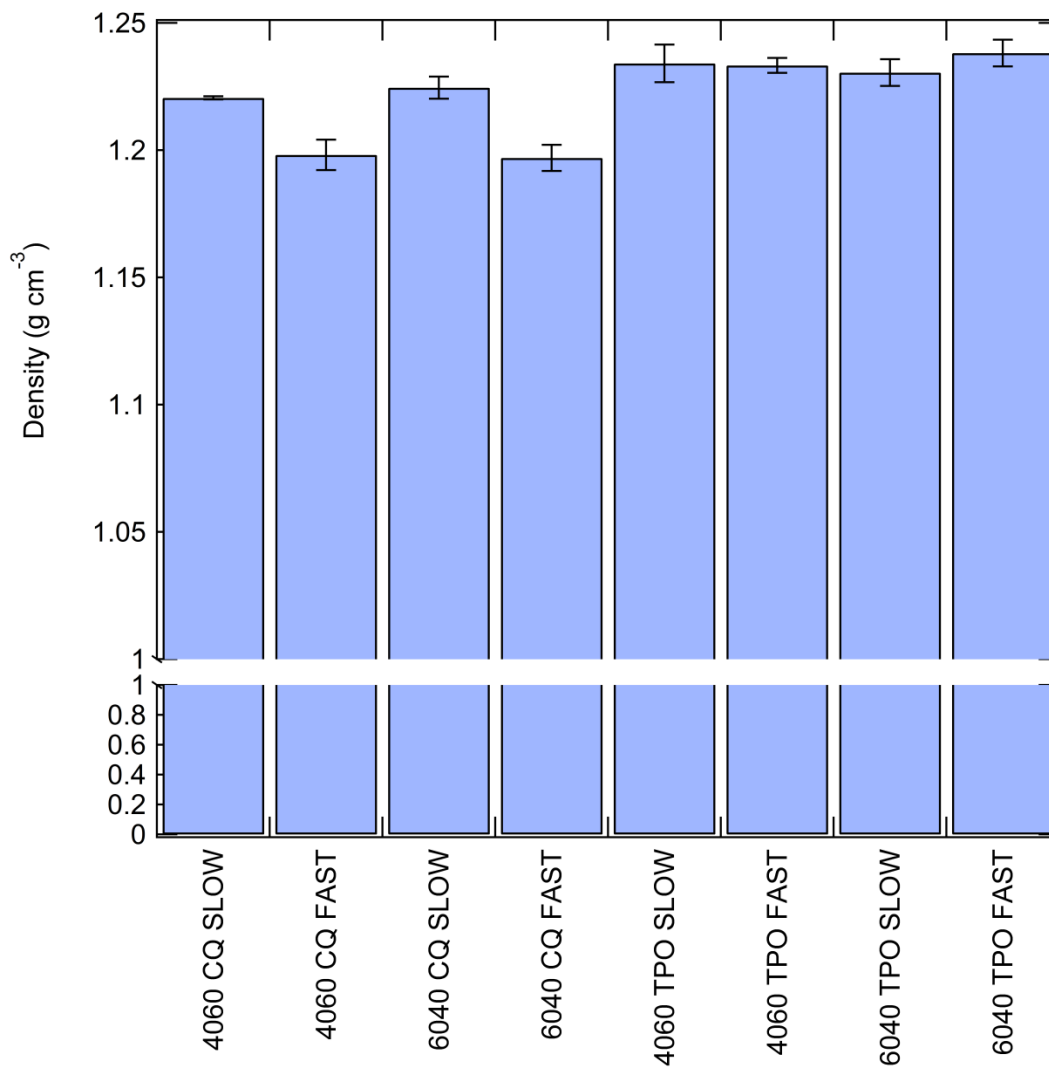


**Figure 4.10.** Density measurements of hydrogenated counterparts to deuterated resin blends used for SANS. Hydrogenated versions were used as each sample formulation could be reproduced several times to gain better statistics, unlike for deuterated samples. Error bars represent the standard deviation for three repeat measurements per sample.

#### 4.3.4 Time Resolved X-ray Scattering Measurements

In this chapter, the use of SANS techniques allows only for static measurements of the resin samples post-polymerisation. Insufficient flux, in comparison with synchrotron X-ray sources makes it practically impossible to time resolve subtle structural changes, particularly in highly hydrogenated and amorphous polymer samples such as those used in this experiment. Although SAXS techniques were previously used to observe correlation lengths, describing polymer segment motions (chapter three), given the correlation lengths observed using SANS it is very likely that the two are related and that additional X-ray results may provide further insight. In chapter three structural changes were only observed *in-situ* using SAXS for 360 s giving no insight into further structural evolution that may occur during post-cure. Deuterated test samples were photo-polymerised several weeks before the SANS experiment and will have undergone some degree of post cure in the time between. A gap in the data therefore exists, describing how the structure is modified throughout post-cure. Figure 4.11 illustrates the changes in the correlation length and relative order for 60/40 wt% blends (Bis-GMA/TEGDMA) utilising either CQ or TPO photo-initiator, when polymerised at different light intensities but matched total irradiances (see methods), over a period of three hours following light exposure. Time resolved correlation lengths and order were obtained via X-ray scattering and correspond to the peak position and full width at half maximum respectively from the scattering peak described in chapter three.

Resins initiated with CQ display typical changes in the correlation length and order when polymerised at relatively fast and slow rates (relative high and low irradiances) during the initial 300 s. When irradiated with lower intensities of light, the correlation length shows a two stage increase whereby a relatively abrupt increase in the correlation length is followed by a gradual gain over time, as described in chapter three. Similarly when polymerisation is accelerated using a higher irradiance, the characteristic reduction in extension feature outlined in detail in chapter three is observed before the transition into the third stage of gradual increase. At this point in time ( $t=300$  s) the total increase in the correlation length is greater for the CQ resin

blend which has been polymerised at the faster rate. Similarly, gains in relative order increase faster for the high irradiance scenario and achieve greater order at  $t = 300$  s (Figure 4.11 b)). After 300 s when neither CQ sample is being illuminated, both resins demonstrate an incremental increase in the correlation length and relative order, however the relative rate of increase for both these parameters is greatest for the more slowly polymerised system during the first hour of post-cure. Between  $t = 7200$  (2 h) to  $t = 10800$  s (3 h) the rate of increase of the correlation length ( $\sim 0.01$  Å/hour) and order for both CQ resins is now very similar. After three h of post-cure the correlation length for the slower polymerised CQ resin has slightly overtaken its faster counterpart, although this is not true for increases in relative order. However the differences between both parameters for each resin composition are almost negligible. It can be seen that for the first 30 s of illumination, TPO initiated resins demonstrate a characteristic large initial increase and relaxation in the correlation length relative orders as described in chapter three. Despite additional time for post-cure, the system shows no development in either correlation length or increase in relative order, as illustrated by a plateau in both data sets. During post-cure the increase in relative order for both CQ resins approaches that of TPO based systems with near negligible differences, however this was not mirrored in the correlation lengths which appear to begin to plateau  $\sim 0.1$  Å short of those seen in TPO initiated resins

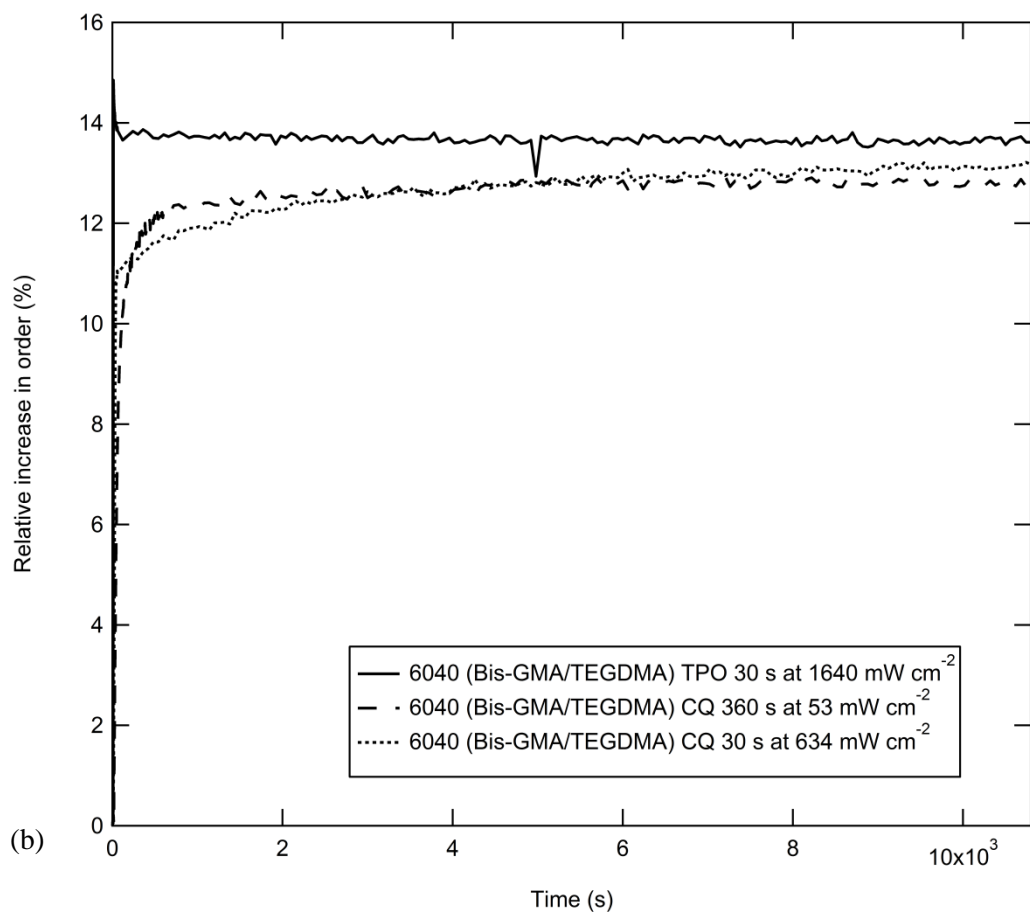
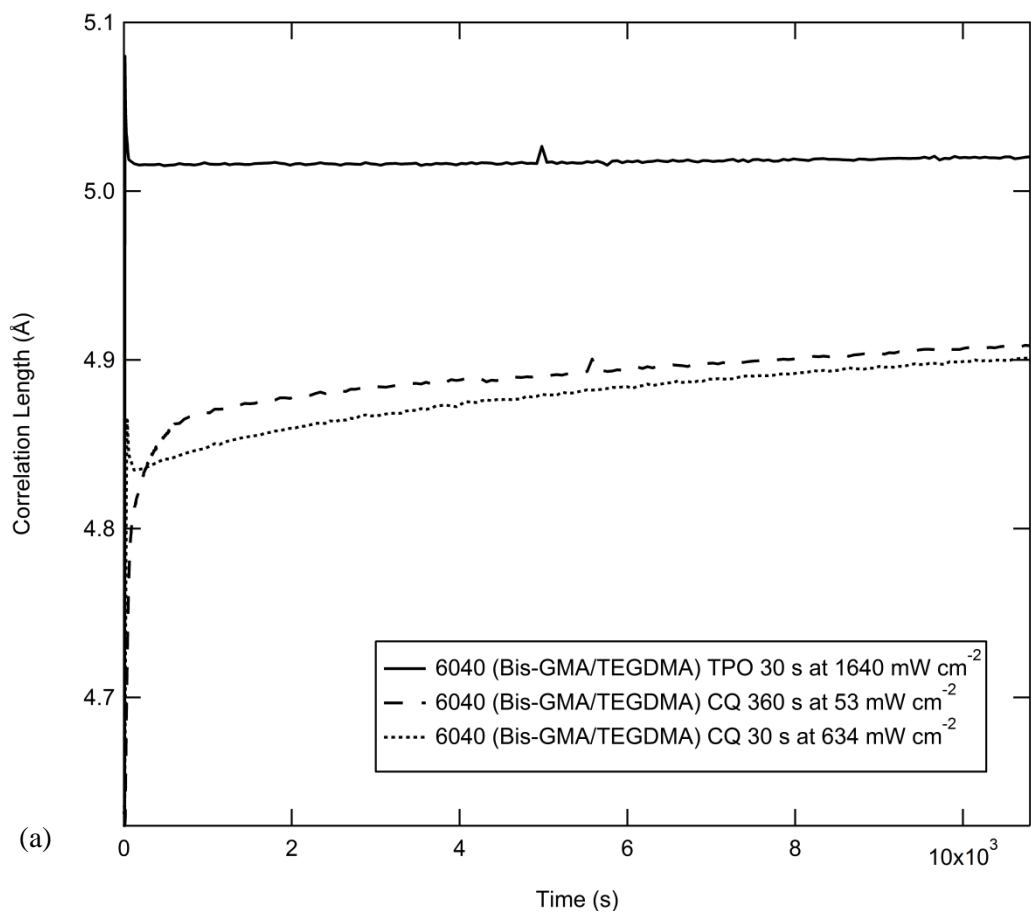


**Figure 4.11.** Real time evolution of the (a) correlation length and (b) relative increase in order for 60/40 wt% (Bis-GMA/TEGDMA) blends. Resins photo-initiated with CQ at high (dotted line) and low (broken line) light irradiance densities are shown in addition to a TPO initiated resin polymerised at a relatively high light irradiance density (solid line)

## 4.4 Discussion

### 4.4.1 Scattering Peak Origins

#### 4.4.1.1 Scattering Feature (a)

The scattering feature observed at  $q \sim 0.22 \text{ \AA}^{-1}$  corresponds to a correlation length of approximately  $28.5 \text{ \AA}$ . It is conceivable that this feature corresponds to a cross-link repeat distance. However, this feature is also present in the SANS spectra for the liquid monomer blend where no cross-links would be expected to exist. It is therefore likely that this feature is an artefact from scattering at low  $q$ .

#### 4.4.1.2 Scattering Feature (b)

Photo-polymerisation generated an increase in the correlation length corresponding to the broad scattering peak located at approximately  $0.6 \text{ \AA}^{-1}$  (Figures 4.2, 4.5 and 4.6). The correlation length increases from a real space value of  $\sim 10.5 \text{ \AA}$  up to approximately  $11.7 \text{ \AA}$  depending on the resin composition (which indirectly reflects on the relative resin viscosity), photo-initiator chemistry and light intensity. Partially deuterated TEGDMA were prepared to enhance scattering length densities and to provide contrast in the hydrogenated parts of the methacrylate moieties. Selected exchange of hydrogen for deuterium increases the scattering length of the functional groups, artificially creating a correlation length that would not be visible to neutrons for a hydrogenated counterpart. The origin of the  $q \sim 0.6 \text{ \AA}^{-1}$  peak is therefore ascribed to the end to end distance of the d-TEGDMA monomer. This artificially induced correlation length is observed in the SANS spectra for the liquid (monomer) d-TEGDMA. The scattering peak located at  $\sim 0.4 \text{ \AA}^{-1}$  corresponds to a real space correlation length of approximately  $15 \text{ \AA}$ , which is very similar to the ideal chain length of the d-TEGDMA monomer ( $\sim 20 \text{ \AA}$ ) to which it is believed to represent. Furthermore, this feature is not observed in either of the pure TEGDMA or Bis-GMA resins, nor hydrogenated resin blends which lack the necessary coherent scattering

lengths. Deuterated blends display a broad scattering peak within the region of  $0.1 - 0.8 \text{ \AA}^{-1}$ , although this peak is at higher  $q$  (shorter correlation length in real space) than seen in the pure d-TEGDMA monomer. This peak is believed to originate from the d-TEGDMA end to end distance despite the difference in the correlation length, as it is not seen in the hydrogenated blends and is the only plausible structural feature at this length scale given prior knowledge of sample deuteration. The decrease in the correlation length in the Bis-GMA/d-TEGDMA blend relative to d-TEGDMA is attributed to a difference in interaction potentials [52] between neighbouring d-TEGDMA monomers and d-TEGDMA and Bis-GMA. Bis-GMA contains an aromatic core with steric effects as well as additional hydrogen bonding arising from hydroxyl/carbonyl groups, which will modify interactions between the two monomer species. It must also be acknowledged that partial deuteration of the methacrylate moieties of TEGDMA will increase the molecular weight of the monomer relative to its hydrogenated counterpart. This will inevitably alter the diffusion properties of the monomer however, given that the percentage change in molecular weight is  $\sim 1.5 \%$ , differences in diffusion and hence polymerisation rates between the hydrogenated and deuterated monomers is considered to be negligible.

To summarise, the end to end length of d-TEGDMA therefore seems the most plausible correlation length within this structural regimen. It should be noted that additional contributions will arise from neighbouring pendent d-TEGDMA monomers (furthest end of pendent to nearest bound end of other TEGDMA) and trapped unreacted monomers, which will likely broaden the scattering peak. Given that the maximum increase in the correlation length was  $\sim 1.2 \text{ \AA}$  (Figure 4.5) and the most that bond conversion can contribute to this is  $\sim 0.4$  when the monomer is fully cross-linked, the mechanism for a length increase along a whole monomeric unit is attributed predominantly to chain extension.

#### 4.4.1.3 Scattering Feature (c)

The peak located at  $q \sim 1.15 \text{ \AA}^{-1}$  in the Bis-GMA/d-TEGDMA blend appears to correspond to the scattering peak observed in the SANS spectra of the liquid Bis-GMA monomer as no other scattering feature is observed in this spectra or that of d-TEGDMA. Figure 4.8 shows that the final position of this scattering peak, in Bis-GMA/d-TEGDMA blends, varies with the assumed polymerisation rate. The position of this peak is found at lower  $q$  for higher light irradiance protocols i.e. faster polymerisation confers a greater increase in this correlation length. This implies that, much like in chapter three, that this peak corresponds to a correlation length within the Bis-GMA monomer particularly when considering the magnitude of the correlation length and associated increase in length, which cannot both be ascribed to inter-monomer separation distances. In chapter SAXS it was shown that chain extension occurs in the non-aromatic portion of the Bis-GMA monomer. The correlation length seen in Figures 4.2 and 4.8 approximates the non-aromatic portion of Bis-GMA i.e. the structure between the aromatic ring and the methylene group where cross-links form. To summarise, this peak likely represents the non-aromatic segment of Bis-GMA which may be undergoing segment extension that is sensitive to the polymerisation rate.

#### 4.4.1.4 Scattering Feature (d)

Following photo-polymerisation, the high  $q$  feature initially located at  $\sim 1.4 \text{ \AA}^{-1}$  moved to higher  $q$ , indicative of a decrease in the respective correlation length. This scattering peak is located at a similar region in  $q$  to the one observed in the X-ray scattering data. However, as this correlation length does not increase post-polymerisation, this implies that this structural feature is not related to chain extension within segments of the polymer. It is conceivable that this scattering peak corresponds to the separation distance between neighbouring monomers in the liquid state, and polymer chains in the solid state i.e. correlation lengths arising from the

deuterated functional groups of neighbouring monomers. Several studies have investigated the origin of this peak in polymer systems and it is believed to arise from Van der Waals separation distances [53, 54] in the monomer form, which becomes smaller as the polymer chains pack closer together the result of polymerisation. This is further supported by the decrease in the correlation length which shows some correlation to an increase in density.

#### **4.4.2 Impact of Irradiance on the Resultant Polymer Structure**

It can be seen from Figures 4.5 and 4.7 that accelerating the rate of photo-polymerisation typically confers greater chain extension along the length of the d-TEGDMA monomer and reduced short range order relative to slower polymerisation regimes. In this study, photo-initiator chemistry and the intensity and exposure to the impinging light source was used to introduce relative differences in the polymerisation rate. The light intensity had the greatest effect on introducing differences in the final correlation length and relative order of the d-TEGDMA monomer. It can be seen in Figure 4.5 that the difference in the final correlation length is larger between identically composed resins polymerised at different light intensities, but which have the same initiator chemistry, in comparison with resins polymerised at the same light intensity but with different (less/more reactive) initiators. This is somewhat counterintuitive as TPO is a more efficient photo-initiator than CQ and achieves a greater terminal conversion and maximum polymerisation rate [7]. Furthermore, previous X-ray scattering results presented in chapter three indicate that, at least for the initial 360 s during photo-polymerisation, significantly greater chain extension is generated in TPO initiated system regardless of the impinging light intensity. Similarly, TPO initiated resins displayed greater short range order (non-normalised data), although this is a consequence of greater conversion reducing thermal motions of monomers/polymers.

However, in this study X-ray scattering measurements identical to those presented in chapter three were extended over a three hour period (instead of 360 s) to observe structural changes in the polymer during the post cure phase for high and low light intensity regimes with matched total irradiances. It can be seen in Figure 4.11(a) that during the initial 360 s structural changes with regards to chain extension and order are typical of those described in chapter three. Hence, rapid polymerisation generates the greatest intra-monomeric chain extension and increase in order, which are accompanied by a relaxation (reduction in extension) feature. Slow polymerisation confers gradual, but smaller increases in chain extension and order. In Figure 4.11, it can be seen that after the initial light exposure both the relatively fast and slow CQ initiated systems continue to extend. However, the rate of chain extension during the post-cure phase is actually greater for the system photo-polymerised at a slower polymerisation rate, particularly during the first hour of post cure. At two hours of post-cure, chain extension for the fast and slow curing regimes is almost equivalent. Additionally, the initial increase in relative order follows a similar pattern with differences in the two polymerisation regimes effectively negligible after three hours of post cure. Additional X-ray scattering measurements were taken of a TPO system, illuminated with the greatest achievable light intensity to understand how the polymer structure evolved at longer times scales when polymerised at an extremely fast rate. This system displays the greatest and most rapid initial increase in both chain extension and relative short range order during the initial period of illumination and demonstrates a large relaxation feature. Yet, during the post cure phase no additional modification to either chain extension or short range order is observed. In comparison, if the CQ resins were to continue to extend at the rate observed in Figure 4.11(a) then they would achieve an equivalent chain extension within an additional ~ 16 hours of post cure (19-20 hours in total). It is therefore not unreasonable to conclude that continual and incremental modification of the structure during post-cure has produced the similar values in the final correlation lengths obtained via neutron scattering for resin systems polymerised using identical irradiance regimes but with different photo-initiator chemistry. However, given that there is a greater similarity in the correlation lengths of systems exposed to the same light intensity regimes rather than the photo-initiator

chemistry suggests that the initial and rapid production of free radicals provides a force which adds additional extension to the monomer to that which may be intrinsically achieved, as a consequence of monomer conversion, at slower rates. Also, that we observed similar final correlation lengths despite using photo-initiators which produce vastly different polymerisation rates suggests that there is a threshold polymerisation rate which will result in no greater additional chain extension.

It can be seen in Figure 4.7, that accelerating polymerisation, typically for higher light intensity polymerisation regimes, conferred greater FWHM for a given scattering peak, indicative of reduced short range order with respect to slower polymerised systems. Differences in the FWHM of the  $q \sim 0.6 \text{ \AA}^{-1}$  peak would typically suggest that the structure of the cross-link is more or less ordered as a function of the polymerisation rate, but this may also be related to the density and distribution of the cross-links within the polymer. Simulations by Sarkar *et al* [55] suggested that rapid photo-polymerisation of Bis-GMA/TEGDMA systems, achieved through exposure to high intensity light, results in a heterogeneous ‘patchy’ distribution of cross-links throughout the system, whilst at slower rates cross-links are more evenly distributed. A greater FWHM (reduced order), which is predominantly affected by light intensity may allude to this distribution. Extension is likely to be greatest in d-TEGDMA monomers which are cross-linked, so regions of high cross-link density are also likely to have cross-links in an extended conformation.

This interpretation may better explain mechanical differences in resins which have been polymerised at different rates but to a similar terminal degree of conversion. Fast polymerisation creates more extended cross-links, fixed into this conformation, which are therefore less able to deform to relieve stress. If this is coupled with heterogeneity in the cross link density then we have regions of high cross link density, with reduced potential to deform, neighbouring a less densely cross-linked and extended matrix. This may imply that stress relief would occur at the interface of these regions

## 4.5 Conclusions

The final polymer structure of photo-activated dimethacrylate resins has been studied, using small angle neutron scattering in combination with isotopic substitution and longer term X-ray scattering measurements, as a function of reaction rate. Neutron scattering demonstrates that the polymerisation rate not only affects the density and distribution of cross-links as previously reported in the literature, but also influences the final conformation of the whole cross-link unit with respect to chain extension and short range order. Accelerating polymerisation confers greater chain extension and reduced short range order relative to slower rates. The intensity of the irradiating light source had the greatest effect on chain extension and relative order suggesting that, despite the use of photo-initiators which generate significantly different polymerisation rates, a threshold polymerisation rate limits the final chain extension and changes in order. Long term X-ray scattering measurements show that although resins polymerised at slower rates may exhibit reduced chain extension, the polymer structure is continually modified during post cure, which is not the case for faster polymerisation. However this post cure behaviour is not quite sufficient to achieve a similar final cross-link structure as for faster rates.

## 4.6 References

1. Feilzer, A.J., et al., *Influence of light intensity on polymerization shrinkage and integrity of restoration-cavity interface*. European Journal of Oral Sciences, 1995. **103**(5): p. 322-326.
2. Unterbrink, G.L. and R. Muessner, *Influence of light intensity on two restorative systems*. Journal of Dentistry, 1995. **23**(3): p. 183-189.
3. Uno, S. and E. Asmussen, *Marginal adaptation of a restorative resin polymerized at reduced rate*. European Journal of Oral Sciences, 1991. **99**(5): p. 440-444.
4. Emami, N., K.-J.M. Söderholm, and L.A. Berglund, *Effect of light power density variations on bulk curing properties of dental composites*. Journal of Dentistry, 2003. **31**(3): p. 189-196.
5. Lim, B.S., et al., *Reduction of polymerization contraction stress for dental composites by two-step light-activation*. Dental Materials, 2002. **18**(6): p. 436-444.
6. Mehl, A., R. Hickel, and K.-H. Kunzelmann, *Physical properties and gap formation of light-cured composites with and without 'softstart-polymerization'*. Vol. 25. 1997. 321-30.
7. Ogunyinka, A., et al., *Photoinitiation chemistry affects light transmission and degree of conversion of curing experimental dental resin composites*. Dent Mater, 2007. **23**(7): p. 807-13.
8. Miyazaki, M., et al., *Effect of light exposure on fracture toughness and flexural strength of light-cured composites*. Dent Mater, 1996. **12**(6): p. 328-32.
9. Asmussen, E. and A. Peutzfeldt, *Polymerization contraction of resin composite vs. energy and power density of light-cure*. Eur J Oral Sci, 2005. **113**(5): p. 417-21.
10. Feng, L., R. Carvalho, and B.I. Suh, *Insufficient cure under the condition of high irradiance and short irradiation time*. Dent Mater, 2009. **25**(3): p. 283-9.

11. Sideridou, I., V. Tserki, and G. Papanastasiou, *Effect of chemical structure on degree of conversion in light-cured dimethacrylate-based dental resins*. *Biomaterials*, 2002. **23**(8): p. 1819-1829.
12. Al-Zain, A.O., et al., *Degree of conversion and cross-link density within a resin-matrix composite*. *Journal of Biomedical Materials Research Part B: Applied Biomaterials*: p. n/a-n/a.
13. Ferracane, J.L. and E.H. Greener, *The effect of resin formulation on the degree of conversion and mechanical properties of dental restorative resins*. *Journal of Biomedical Materials Research*, 1986. **20**(1): p. 121-131.
14. Schneider, L.F.J., et al., *Influence of photoinitiator type on the rate of polymerization, degree of conversion, hardness and yellowing of dental resin composites*. *Dental Materials*, 2008. **24**(9): p. 1169-1177.
15. Chung, K.H. and E.H. Greener, *Correlation between degree of conversion, filler concentration and mechanical properties of posterior composite resins*. *Journal of Oral Rehabilitation*, 1990. **17**(5): p. 487-494.
16. Kannurpatti, A.R., J.W. Anseth, and C.N. Bowman, *A study of the evolution of mechanical properties and structural heterogeneity of polymer networks formed by photopolymerizations of multifunctional (meth)acrylates*. *Polymer*, 1998. **39**(12): p. 2507-2513.
17. Nielsen, L.E., *Cross-Linking—Effect on Physical Properties of Polymers*. *Journal of Macromolecular Science, Part C*, 1969. **3**(1): p. 69-103.
18. *Dielectric Spectroscopy of Polymeric Materials: Fundamentals and Applications* Edited by James P. Runt (Pennsylvania State University) and John J. Fitzgerald (General Electric Company). *American Chemical Society: Washington, DC, 1997. xvi + 461 pp. \$124.95. ISBN 08412-3335-7*. *Journal of the American Chemical Society*, 1997. **119**(49): p. 12029-12029.

19. Feigin, L.A., D.I. Svergun, and G.W. Taylor, *Principles of the Theory of X-Ray and Neutron Scattering*, in *Structure Analysis by Small-Angle X-Ray and Neutron Scattering*, G.W. Taylor, Editor. 1987, Springer US: Boston, MA. p. 3-24.
20. Schmidtman, M., et al., *Determining hydrogen positions in crystal engineered organic molecular complexes by joint neutron powder and single crystal X-ray diffraction*. CrystEngComm, 2014. **16**(7): p. 1232-1236.
21. Müller, P., et al., *Crystal Structure Refinement: A Crystallographer's Guide to SHELXL*. International Union of Crystallography Texts on Crystallography. 2006, Oxford: Oxford University Press. 232.
22. Stewart, R.F., E.R. Davidson, and W.T. Simpson, *Coherent X-Ray Scattering for the Hydrogen Atom in the Hydrogen Molecule*. The Journal of Chemical Physics, 1965. **42**(9): p. 3175-3187.
23. Iijima, T. and R.A. Bonham, *X-ray scattering factor of a hydrogen atom in a hydrogen molecule*. Acta Crystallographica, 1963. **16**(10): p. 1061-1062.
24. Woińska, M., et al., *Hydrogen atoms can be located accurately and precisely by x-ray crystallography*. Science Advances, 2016. **2**(5): p. e1600192.
25. Sears, V.F., *Neutron scattering lengths and cross sections*. Neutron News, 1992. **3**(3): p. 26-37.
26. Sivia, D.S., *Elementary Scattering Theory: For X-ray and Neutron Users*. 2011: OUP Oxford.
27. *Neutron scattering in biology, chemistry and physics - Neutron diffraction, isotopic substitution and the structure of aqueous solutions*. Philosophical Transactions of the Royal Society of London. B, Biological Sciences, 1980. **290**(1043): p. 553-566.
28. Hamilton, M.A., et al., *A neutron diffraction and isotopic substitution measurement of the structure of liquid Cu<sub>2</sub>Se*. Journal of Physics: Condensed Matter, 2000. **12**(46): p. 9525.
29. *Sans2d technical information [cited 2017 June 6]; Available from: <https://www.isis.stfc.ac.uk/Pages/Sans2d-technical-information.aspx>*.

30. *Loq* [cited 2017 August 2]; Available from: <https://www.isis.stfc.ac.uk/Pages/loq.aspx>.
31. *Loq Technical Information*. [cited 2017 August 1]; Available from: <https://www.isis.stfc.ac.uk/Pages/Loq-technical-information.aspx>.
32. Arnold, O., et al., *Mantid—Data analysis and visualization package for neutron scattering and SR experiments*. Nuclear Instruments and Methods in Physics Research Section A: Accelerators, Spectrometers, Detectors and Associated Equipment, 2014. **764**: p. 156-166.
33. Heenan, R., et al., *SANS2D at the ISIS Second Target Station*. 2006.
34. Duxbury, D., et al., *Performance characteristics of the new detector array for the SANS2d instrument on the ISIS spallation neutron source*. Journal of Instrumentation, 2014. **9**(12): p. C12051.
35. *D16 - Small momentum transfer diffractometer*. [cited 2017 July 8]; Available from: <https://www.ill.eu/instruments-support/instruments-groups/instruments/d16/description/instrument-layout/>.
36. Cristiglio, V., et al., *D16 is back to business: more neutrons, more space, more fun*. Neutron News, 2015. **26**(3): p. 22-24.
37. *D16 - Small momentum transfer diffractometer - Characteristics*. [cited 2017 August 9]; Available from: <https://www.ill.eu/en/instruments-support/instruments-groups/instruments/d16/characteristics/>.
38. Richard, D., M. Ferrand, and G. Kearley, *Analysis and visualisation of neutron-scattering data*. Journal of Neutron Research, 1996. **4**(1-4): p. 33-39.
39. Lovell, L.G., et al., *Understanding the kinetics and network formation of dimethacrylate dental resins*. Polymers for Advanced Technologies, 2001. **12**(6): p. 335-345.
40. Peutzfeldt, A. and E. Asmussen, *The effect of postcuring on quantity of remaining double bonds, mechanical properties, and in vitro wear of two resin composites*. Journal of Dentistry, 2000. **28**(6): p. 447-452.

41. Wu, W. and B.M. Fanconi, *Post-curing of dental restorative resin*. Polymer Engineering & Science, 1983. **23**(13): p. 704-707.
42. Pilo, R. and H.S. Cardash, *Post-irradiation polymerization of different anterior and posterior visible light-activated resin composites*. Dental Materials, 1992. **8**(5): p. 299-304.
43. Miettinen, V.M., K.K. Narva, and P.K. Vallittu, *Water sorption, solubility and effect of post-curing of glass fibre reinforced polymers*. Biomaterials, 1999. **20**(13): p. 1187-1194.
44. Brown, S.D., et al., *The XMaS beamline at ESRF: instrumental developments and high-resolution diffraction studies*. Journal of Synchrotron Radiation, 2001. **8**(6): p. 1172-1181.
45. Thompson, P., et al., *New Developments at the XMaS Beamline For Magnetic and High Resolution Diffraction*. Vol. 705. 2004.
46. Thompson, P., et al., *Optimizing the XMaS Beamline for Low energy Operations to Maximize Benefits from the ESRF Upgrade Program*. Vol. 1234. 2010. 407-410.
47. Stahl, F., et al., *Light-emitting diode (LED) polymerisation of dental composites: flexural properties and polymerisation potential*. Biomaterials, 2000. **21**(13): p. 1379-1385.
48. Hammersley, A.P., et al., *Two-dimensional detector software: From real detector to idealised image or two-theta scan*. High Pressure Research, 1996. **14**(4-6): p. 235-248.
49. Pulgar, R., et al., *Determination of Bisphenol A and Related Aromatic Compounds Released from Bis-GMA-Based Composites and Sealants by High Performance Liquid Chromatography*. Vol. 108. 2000. 21-7.
50. Inoue, K. and I. Hayashi, *Residual monomer (Bis-GMA) of composite resins*. Journal of Oral Rehabilitation, 1982. **9**(6): p. 493-497.
51. Goldberg, M., *In vitro and in vivo studies on the toxicity of dental resin components: a review*. Clinical Oral Investigations, 2008. **12**(1): p. 1-8.

52. Van Krevelen, D.W., *CHAPTER 1 - POLYMER PROPERTIES*, in *Properties of Polymers (Third, completely revised edition)*. 1997, Elsevier: Amsterdam. p. 3-5.
53. Miller, R.L., R.F. Boyer, and J. Heijboer, *X-ray scattering from amorphous acrylate and methacrylate polymers: Evidence of local order*. *Journal of Polymer Science: Polymer Physics Edition*, 1984. **22**(12): p. 2021-2041.
54. Wind, M., et al., *Structure of amorphous poly-(ethylmethacrylate): A wide-angle x-ray scattering study*. *The Journal of Chemical Physics*, 2005. **122**(1): p. 014906.
55. Sarkar, S., et al., *Quantifying the sensitivity of the network structure and properties from simultaneous measurements during photopolymerization*. *Soft Matter*, 2017. **13**(21): p. 3975-3983.

## **5 MODIFICATION OF POLYMER STRUCTURE THROUGH THERMAL LOADING: A PRELIMINARY STUDY**

### **5.1 Introduction**

The main body of this thesis has focused on characterising and understanding the polymer conformation of a dental resin matrix as a function of the polymerisation rate and matrix viscosity. However, in clinical practice an RBC filling will, following photo-polymerisation, be subject to external perturbations, both physical and chemical that are likely to alter the resin structure. *In-vivo*, a dental RBC filling will typically be exposed to an average temperature of 37 °C when no additional thermal load is applied [1]. Eating, drinking and breathing will induce thermal fluctuations in the intra-oral environment which have been shown using thermocouples to range from 4 °C to 60 °C [2, 3] and will be (partially) transferred to the RBC material. The RBC's location within the mouth and its morphology will dictate local as well as differential temperatures within the prosthetic. The thermal response of the polymer will be influenced by the chemical structure [4] of the constituent monomers that form the resin matrix, photo-initiator chemistry, polymer network architecture and the degree of monomer to polymer conversion [5]. To date, characterisation methods have focussed on understanding the response of RBCs to thermal perturbations using methods such as measuring dimensional changes, mechanical tests [6] and glass transition temperatures [5, 7], from which assumptions are extrapolated about the polymer structure. In chapter three, synchrotron X-ray scattering was shown to be a useful tool for determining the polymer structure under dynamic conditions. The aim of the work presented in this chapter is to therefore form a preliminary investigation into how temperature modifies different polymer conformations, generated at different polymerisation rates, using synchrotron X-ray scattering.

## 5.2 Methods

### 5.2.1 Preparation of Photo-Polymerisable Dimethacrylate Resin Blends

Dimethacrylate monomers, bisphenol-A-glycidyl-methacrylate (Bis-GMA and triethyleneglycol-dimethacrylate (TEGDMA) were proportioned in 70/30, 60/40, 50/50 and 40/60 (Bis-GMA/TEGDMA) weight percentage (wt. %) ratios and combined to produce 10 g mixes. Liquid resin blends were prepared as described in section 2.2.3.

Test specimen discs were prepared by filling a circular impression in a polyvinylsiloxane mould (11 mm diameter and 1 mm in depth), and pressed flat with a microscope cover slide to prevent the formation of an oxygen inhibition layer. Resins were photo-polymerised using an EMS Swiss master light curing unit (EMS OPTIDENT, electro medical systems, Nyon Switzerland) which was placed normal to and in contact with the cover slide. The curing unit had a spectral output range of 390 – 550 nm to provide significant overlap with the absorption peaks of the Camphorquinone (470 nm) and Lucirin TPO (381 nm) photo-initiators. For each unique composition, the resin was either photo-polymerised at a relatively high ( $3000 \text{ mW cm}^{-2}$  for 6 s) or low ( $300 \text{ mW cm}^{-2}$  for 60 s) light intensity to introduce extreme rates of polymerisation whilst ensuring matched total energy doses. Samples polymerised at high and low irradiances are referred to a ‘fast’ and ‘slow’ samples respectively in this chapter. Samples were produced two weeks prior to the experiment to minimise post-cure effects. The resultant specimens were stored in dark conditions in sealed containers at  $4 \pm 1 \text{ }^\circ\text{C}$  prior to further use.

### 5.2.2 Synchrotron X-ray Scattering Measurements

Synchrotron X-ray scattering experiments were performed on the I16 [8] beamline at the Diamond Light Source (Oxford, UK). An incident X-ray energy of 12 keV was used corresponding to a wavelength ( $\lambda$ ) of 1.033 Å, with a beam size of 30 (vertical)  $\times$  200 (horizontal) microns defined by vacuum tube slits. Measurements were carried out in air, at 23  $\pm$  1 °C with light excluded to reduce further post cure.

A bespoke heating module was used to increase the temperature of resin disc test specimens as shown in Figure 5.1. The module consisted of an aluminium plate (25  $\times$  25 mm area) with a 6 mm (diameter) circular aperture, to allow for the transmission of X-rays, fixed in contact perpendicular to a kinematic heating platform. The temperature of the heating platform was remotely controlled via a cryogenic temperature modulator (model 3.8, Lake Shore cryotonics, Elliot Scientific Ltd, Hertfordshire, UK). Resin discs were held in good contact with the aluminium plate by a second plate which screwed into the first. The temperature of test specimens was increased through heat transfer from the kinematic stage to the aluminium plate and finally to the resin disc. The temperature as set by the external controller could not be used to verify the sample temperature due to differences in thermal conductivity. Instead three thermocouples were placed in contact with the kinematic stage, aluminium plates and the resin disc to measure the temperature of each component. The heating module and housed sample was oriented with the annulus of the aluminium plate normal to the path of the impinging X-rays. A compressed air blower valve with a 5 mm diameter was positioned 20 mm from the sample face offset at an angle of 30 ° from the path of the impinging X-rays to cool the test specimens after thermal loading. The temperature of the compressed air was 20 °C  $\pm$  1 °C to avoid cooling the sample below the initial and ambient temperature.

Resin disc test specimens were heated at a relatively slow rate of 5 °C per minute, in order to obtain a uniform heat distribution within the specimen, from a starting temperature of 20 °C to 160 °C ( $\pm$ 1 °C). This thermal range was selected to understand the polymer structure within the

context of intra-oral temperatures and above  $T_g$ . X-ray scattering measurements were taken at each 5 °C increment to characterise structural changes as a function of temperature. X-ray scattering data was collected using a 2D area detector (Pilatus 100K ) with a  $487 \times 195$  pixel format (pixel size =  $172 \times 172 \mu\text{m}^2$ ) fixed on to a two theta detector arm. The detector was placed 470 mm behind the sample and collected scattering data at angles of  $2\theta = 7, 13$  and  $22$  to cover a  $q$  range of  $0.2$  to  $1.8 \text{ \AA}^{-1}$  where  $q = 4\pi\sin\theta/\lambda$  for each 5 °C temperature increment. Scattering data were collected with a 1 s count time and a 2.7 ms readout time. Transmitted beam was also recorded at each angle/temperature increment using a photodiode to correct for changes to the sample density and thickness.

The contribution of the X-ray beam to the measurements i.e. beam damage was assessed by conducting observations for over 30 min for the pre-polymerised samples at ambient temperature. Additional measurements were also conducted on the liquid monomer (Bis-GMA/TEGDMA) blends, housed within liquid cells, to establish a baseline for the initial correlation length and order parameter. To aid data analysis measurements were taken for direct beam, empty sample containers, and a silver behenate calibration standard to allow the scattering patterns to be corrected for background and normalisation effects. Data were normalised to the incident monitor intensity and background corrected. Data were azimuthally integrated over  $360^\circ$  to produce a 1D output and were subsequently fitted with Gaussian models to determine peak positions and relative order using the Dawn software package (version 2.6.0) [9].

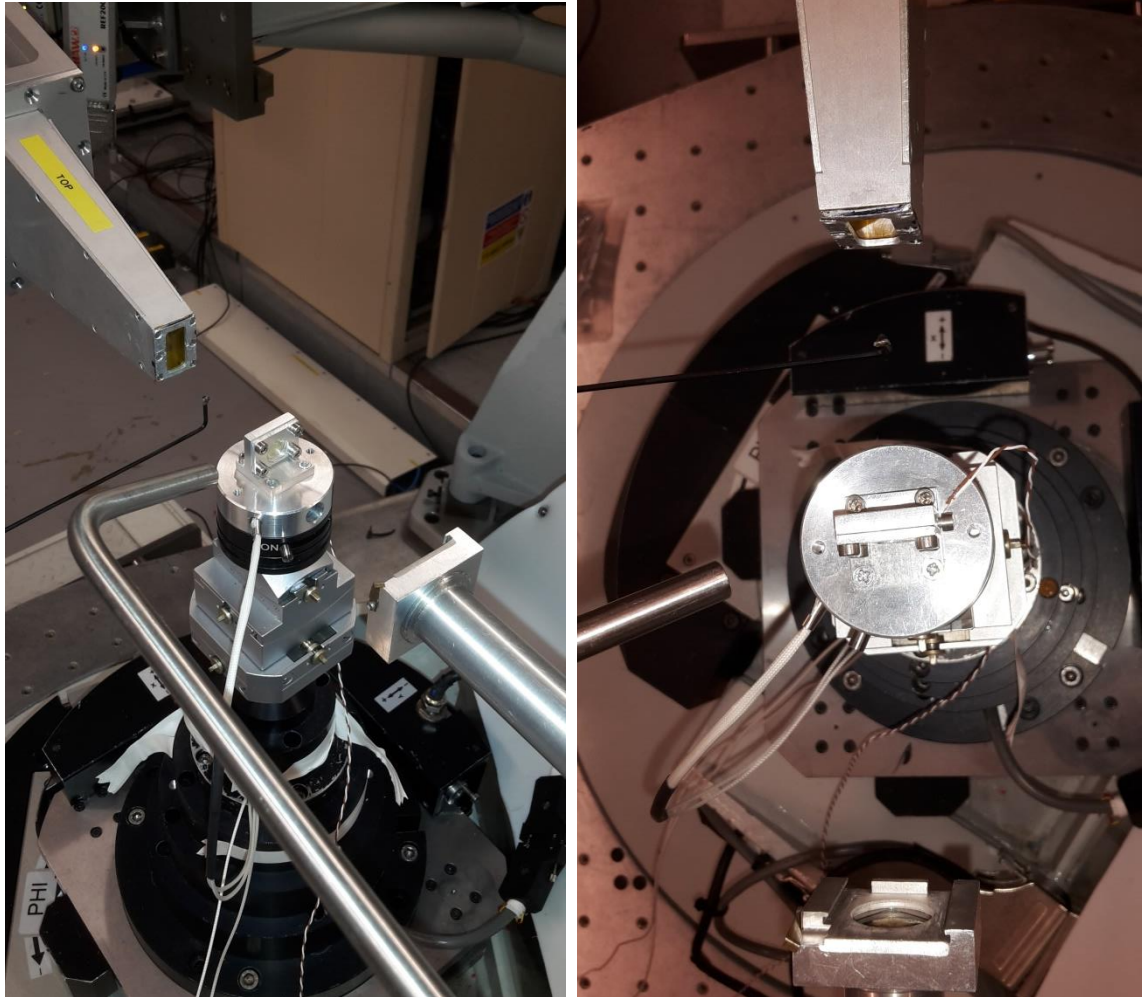


**Figure 5.1.** (left) Two Aluminium plates, mounted onto a heated kinematic stage, heats a resin disc test specimen held between the plates. X-rays impinge normal to the sample face and scatter into a Pilatus 100 K detector mounted onto a  $2\theta$  detector arm. (right) Top down view of the experimental set-up. The pipe to the left of the image blows cold air ( $20\text{ }^{\circ}\text{C} \pm 1\text{ }^{\circ}\text{C}$ ) to cool the stage after heating.

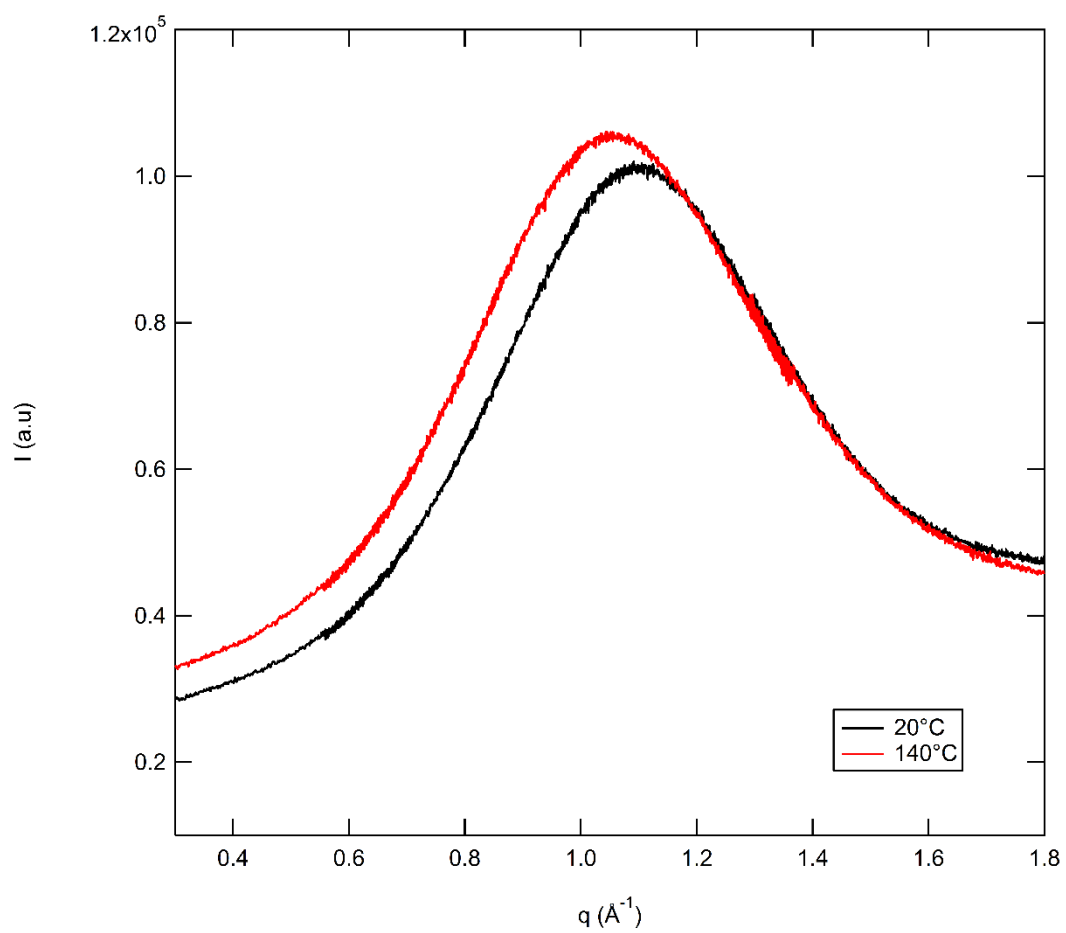
## 5.3 Results

### 5.3.1 The Effect of Temperature on Correlation Length

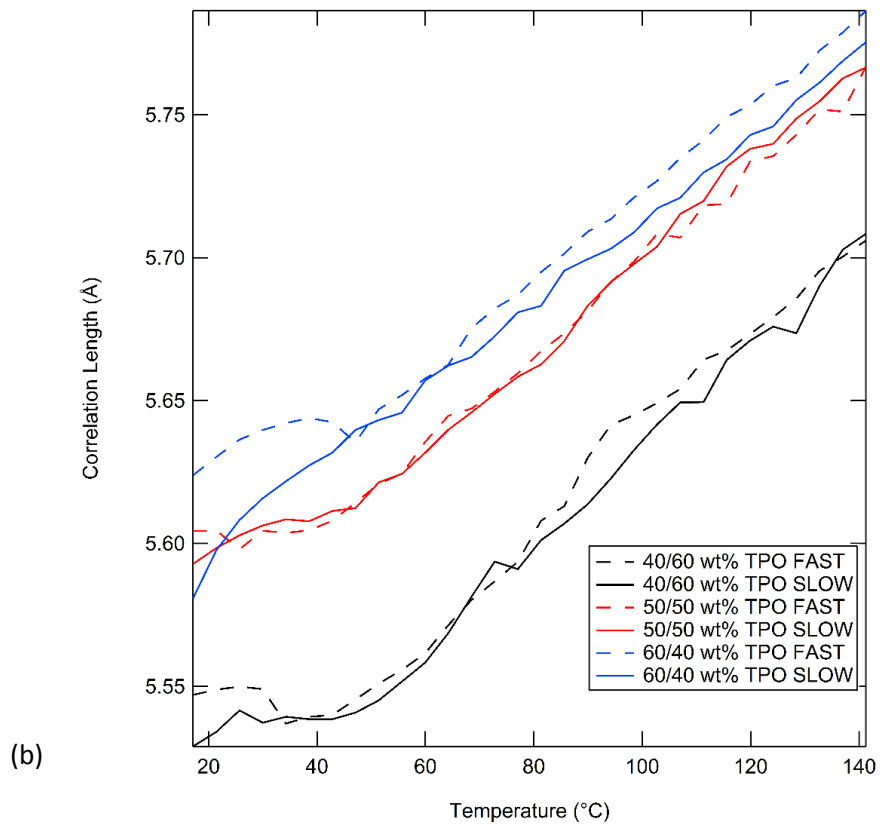
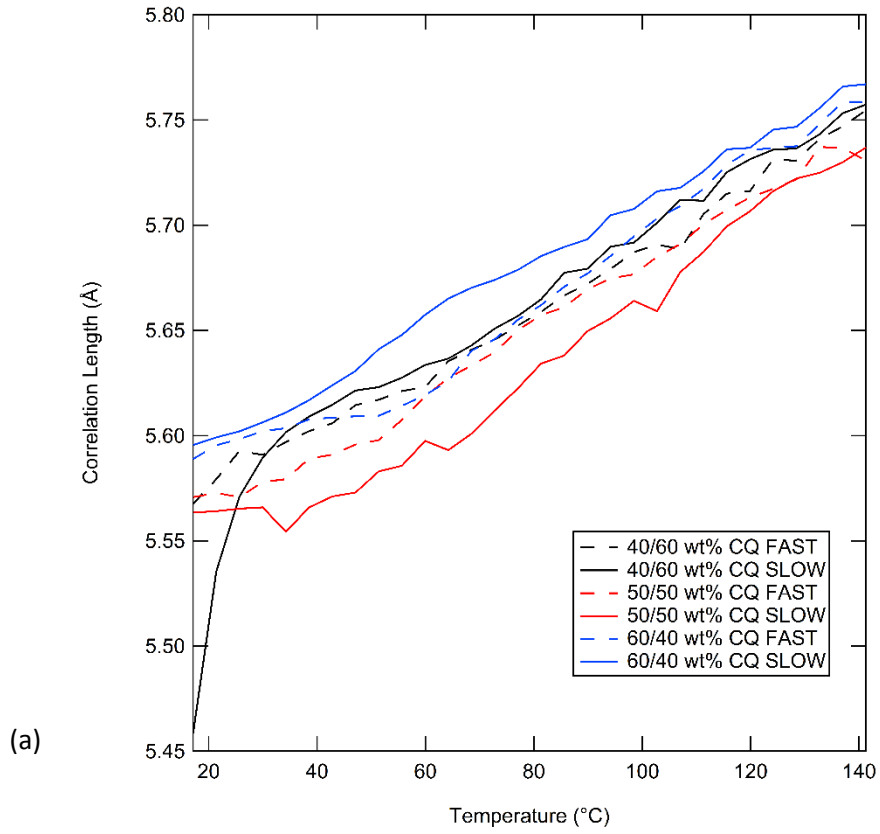
Figure 5.2 shows an X-ray scattering peak, for a 40/60 wt % (Bis-GMA/TEGDMA) resin disc sample initiated with TPO, located at  $q \sim 1.14 \text{ \AA}^{-1}$ , corresponding to a correlation length in real space of approximately  $5.55 \text{ \AA}$ . It can be seen that when the resin disc specimen is incrementally heated to higher temperatures the scattering peak shifts to lower  $q$ , which is indicative of an increase in the correlation length. Additionally, the width of the peak varies as a function of temperature indicating temperature dependent changes in short range order.

Figure 5.3 illustrates the changes in the correlation length for resin test specimens as a function of temperature. Here the correlation length at each temperature increment corresponds to the peak position of the scattering peak in Figure 5.2 at the respective temperature step. It can be seen that all resin samples demonstrate an increase in the correlation length as temperature is increased. The correlation length increases linearly with respect to temperature and the rate of increase is approximately  $0.0013 \text{ \AA K}^{-1}$  for all test specimens, regardless of differences in system viscosity (ratio of Bis-GMA/TEGDMA), photo-initiator chemistry or irradiance protocol. Similarly the total increase in this correlation length i.e. between the highest and lowest temperature values is  $\sim 0.175 \text{ \AA}$  ( $CQ = 0.175 \pm 0.00886 \text{ \AA}$  TPO =  $0.1758 \pm 0.0122 \text{ \AA}$ ) for all samples.

Samples using TPO photo-initiator demonstrated larger initial and final values of the correlation length for each blend and irradiance protocol in comparison to CQ based counterparts. Differences in correlation lengths are consistent with the findings presented in chapter three. However, differences in correlation length between identically composed samples photopolymerised at different irradiance are negligible. It can also be seen that for TPO initiated systems, the magnitude of the correlation length is ranked according to differences in relative viscosity, with more viscous blends demonstrating the greatest correlation length at all temperatures. No such ranking was observed in CQ initiated resins.



**Figure 5.2.** X-ray scattering of a 40/60 wt % (Bis-GMA/TEGDMA) resin disc sample initiated with TPO. At  $20^\circ\text{C}$  the scattering peak (black line) is located at approximately  $1.14 \text{ \AA}^{-1}$ , but moves to lower  $q$  (red line), indicative of an increase in the correlation length.



**Figure 5.3.** Correlation length as a function of temperature for (a) CQ and (b) TPO initiated RBCs.

### 5.3.2 The Effect of Temperature on Short Range Order

Figure 5.4 shows the relative changes in order as a function of temperature for resin samples. Here, values of order correspond to the change in the FWHM of the scattering peak shown in Figure 5.2, relative to the initial FWHM value for each temperature increment. A narrowing of the scattering peak therefore represents an increase in relative order, whilst a broadening of this peak relates to reduced order. An initial increase in order, up to ~ 2%, is observed between 20 – 60 °C, typically reaching a peak value at ~ 55 °C. As the temperature is increased further, gains in order in the system tend to zero at approximately 120 °C i.e. the value of the FWHM is almost equivalent to the initial value. As the system is heated to a maximum temperature of ~ 160 °C, order is seen to increase almost linearly back to a value of ~ 2%. Systems initiated with TPO demonstrate slightly larger increases in order at both ~ 60 and 160 °C in comparison to CQ RBCS. Differences in order as a function of irradiance protocol and relative viscosities (ratio of Bis-GMA/TEGDMA) are negligible.

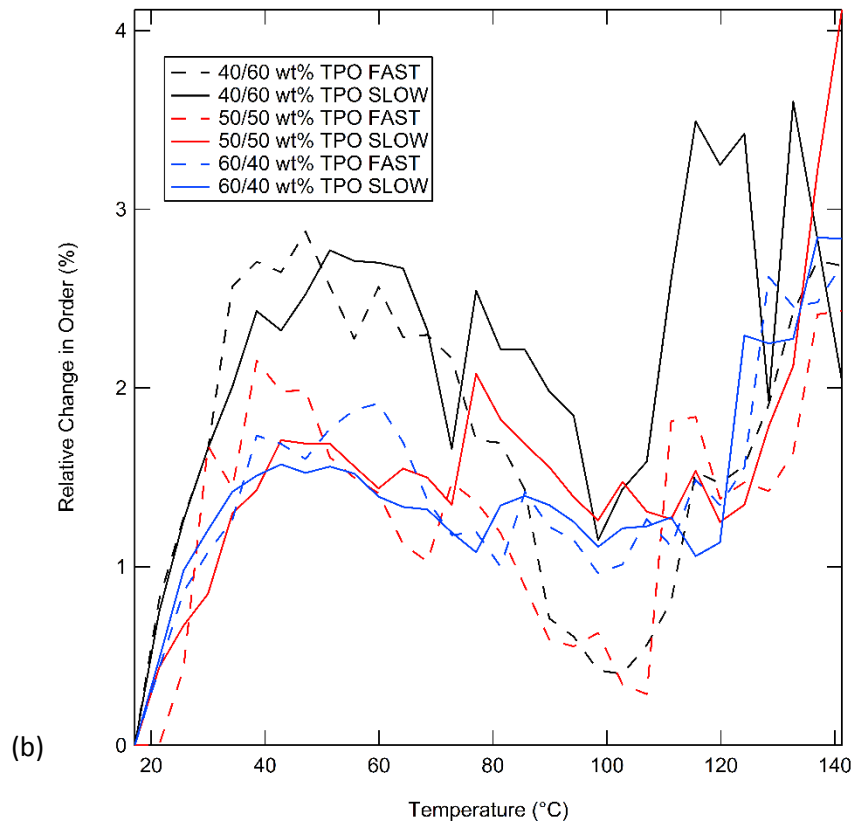
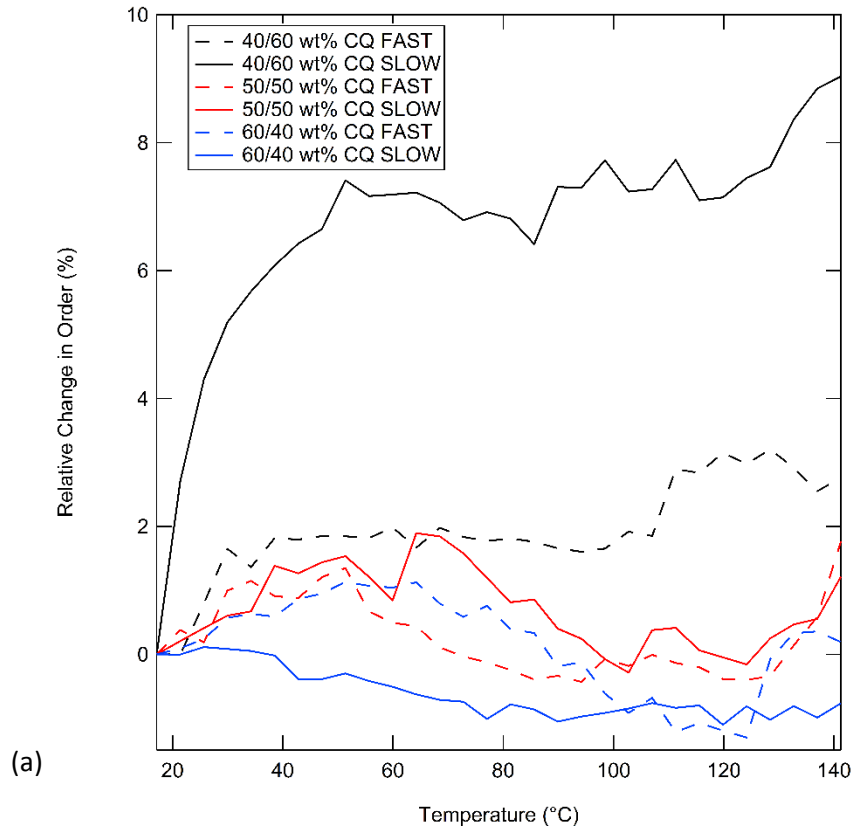


**Figure 5.4.** Relative changes in order as a function of temperature for (a) CQ and (b) TPO initiated RBCs.

## 5.4 Discussion

It was shown that the scattering peak at  $q \sim 1.14 \text{ \AA}^{-1}$  (Figure 5.2) shifted to lower  $q$  as the polymer was placed under thermal load, indicative of an increase in the correlation length. In chapter three it was demonstrated that this scattering peak corresponds to polymer segments, specifically the methacrylic functional groups of the Bis-GMA and TEGDMA monomer and the TEGDMA backbone, which display the ability to extend. This increase in the correlation length is therefore ascribed to chain extension within the aforementioned polymer structures, induced by the applied thermal load. It is known that RBCs demonstrate volumetric expansion when heated, an effect attributed to increased polymer chain mobility which increases the effective volume of the polymer and generates a relative increase in free volume. It is therefore likely that increased polymer mobility in the system is driving chain extension.

It can be seen from Figure 5.3 that the total amount of chain extension and the rate of chain extension with respect to temperature is very consistent for all samples, regardless of composition, photo-initiator chemistry or irradiance protocol. However, initial offsets in the correlation lengths assumed to be generated from different polymerisation rates are preserved. It is suggested that this is due to all the chemical bonds possessing similar rotational freedom to each other, despite differences in the conformation of the polymer segment i.e. the basic mechanism for chain extension is identical for all atoms and chemical bonds. Therefore, as the same amount of energy is put into the system, all of the bonds even if they are constituent in different polymer segment conformations, individually will rotate in the same way as a function of their energy causing the polymer segments to extend at similar rates and magnitude. Volumetric expansion of similar polymers may be expected to be linear given that the coefficient of thermal expansion is likely to hold in the observed temperature range. Any non-linear behaviour should likely be ascribed to additional events e.g. bond degradation or further conversion associated with loss of radical entrapment.

It can be seen for the 40/60 wt% CQ (SLOW) sample that upon thermal loading, increases in the correlation length and relative order are significantly greater in comparison to other resin blends and irradiance protocols (Figures 5.3(a) and 5.4(a)). This is likely the effect of the results being based on a sample number of  $n = 1$ . Relatively large increases in the correlation length and order are therefore attributed to insufficient cure. Consequently, as the polymer is heated increases in system mobility drive additional polymerisation, corresponding to an increase in the correlation length and order. Future experiments will ideally perform repeat X-ray scattering measurements per unique sample formulation/production procedure i.e.  $n = 3$ , whilst FTIR could also be used to quantify consistent degree of conversion per formulation protocol, to account for under or over cured test specimens.

It must be acknowledged that heating the polymer will increase the mobility of previously trapped free radical species and generate relative increases in free volume, allowing the radicals to propagate through the system and continue polymerisation. Additional polymerisation will confer an increase in the observed correlation length. This is not necessarily attributed to true chain extension but will represent a gradual increase in the contribution of longer correlation lengths (arising from increasing C=C to C-C conversion) to the average scattering signal.

In Figure 5.4, changes in relative order showed undulating behaviour with respect to temperature. As the RBCs were heated up to  $\sim 50$  °C relative orders in the system increased for all samples by approximately 2 %. It is known that during polymerisation unreacted radical species will become trapped in the polymer network and that heating an RBC during post-cure can drive additional polymerisation. This is likely the cause of the small increase in order as increased polymerisation will restrict the geometric freedom of the polymer chains. In this study, increases in chain extension and order attributed to either conversion effects or thermal loading cannot be separated as the two variables are related. Although there is likely an opposing effect which reduces order due to increased Brownian motion of polymer segments due to the energy put into the system. A maxima in relative order is observed at  $\sim 55$  °C, which decreases to near zero as the temperature reaches 120 °C. Dewaele *et al* [10] and

Sideridou *et al* [4] reported that the glass transition temperature of resins formulated from Bis-GMA and TEGDMA ranged between 40-55 °C depending on composition and irradiance protocol. This peak in order and the following decrease may represent the transition through  $T_g$ , as increasing temperature confers greater mobility and geometrical freedom to polymer segments reducing order in the system. Within the temperature range of 120 – 160 °C relative order increases back up to ~ 2%. Given that this temperature range also corresponds to larger amounts of chain extension (Figure 5.3), it is conceivable that thermal expansion of the polymer network is great enough to constrain polymer segments into a more linearized conformation, thereby increasing order.

A deficiency of this study is that changes in the polymer structure have only been observed as the temperature increases. It is unknown how the structure evolves as the polymer cools and whether structural differences that were induced by different polymerisation rates will remain as the polymer segments relax at lower temperatures.

## 5.5 Conclusions

In this study X-ray scattering has been used to understand how different polymer structures of dimethacrylate resins, generated through different rates of photo-polymerisation, are modified by thermal loading. It was shown that thermal loading of RBCs confers chain extension in the polymer segments described in chapter three which increases proportional to the sample temperature. Changes in the relative short range order were observed but its relationship with respect to temperature is more complex than chain extension and appears to be sensitive to second order phase transitions i.e. glass transition. The rate and total magnitude of chain extension is independent of the photo-polymerisation variables that were implemented to cure the RBCs. However, the initial and final structures still maintain differences in chain extension as a function of irradiance protocol. Further study is required to elucidate the relationship between these microscopic structural changes, post-cure and macroscopic volumetric changes.

## 5.6 References

1. Gale, M.S. and B.W. Darvell, *Thermal cycling procedures for laboratory testing of dental restorations*. J Dent, 1999. **27**(2): p. 89-99.
2. Minami, H., et al., *Effects of thermal cycling on surface texture of restorative composite materials*. Dent Mater J, 2007. **26**(3): p. 316-22.
3. Drummond, J.L., *Degradation, fatigue and failure of resin dental composite materials*. Journal of dental research, 2008. **87**(8): p. 710-719.
4. Sideridou, I., V. Tserki, and G. Papanastasiou, *Effect of chemical structure on degree of conversion in light-cured dimethacrylate-based dental resins*. Biomaterials, 2002. **23**(8): p. 1819-1829.
5. Ferracane, J.L. and E.H. Greener, *The effect of resin formulation on the degree of conversion and mechanical properties of dental restorative resins*. Journal of Biomedical Materials Research, 1986. **20**(1): p. 121-131.
6. Lovell, L.G., et al., *The effect of cure rate on the mechanical properties of dental resins*. Dent Mater, 2001. **17**(6): p. 504-11.
7. Sideridou, I., D.S. Achilias, and E. Kyrikou, *Thermal expansion characteristics of light-cured dental resins and resin composites*. Biomaterials, 2004. **25**(15): p. 3087-3097.
8. Collins, S.P., et al., *Diamond Beamline I16 (Materials & Magnetism)*. AIP Conference Proceedings, 2010. **1234**(1): p. 303-306.
9. Basham, M., et al., *Data Analysis WorkbeNch (DAWN)*. Journal of Synchrotron Radiation, 2015. **22**(3): p. 853-858.
10. Dewaele, M., et al., *Influence of curing protocol on selected properties of light-curing polymers: degree of conversion, volume contraction, elastic modulus, and glass transition temperature*. Dent Mater, 2009. **25**(12): p. 1576-84.

## **6 INTER-PARTICULATE SPATIAL VARIABILITY IN DEGREE OF POLYMERISATION OF DIMETHACRYATE DENTAL RBC FILLING MATERIALS**

### **6.1 Introduction**

Contemporary RBCs typically achieve between 55 – 75 % monomer to polymer conversion under clinical setting parameters [1, 2]. The degree of conversion (DC) of RBCs is routinely quantified using Fourier transform infra-red (FTIR) spectroscopy and is often used to discriminate between materials and photo-polymerisation regimens [3-6]. During the setting process, neighbouring polymer chains cross-link with each other and the material develops a greater elastic modulus and becomes stiffer. RBCs with greater conversion often demonstrate superior strength, surface hardness, flexural and elastic modulus [7, 8], whilst limiting the amount of residual unreacted monomer that may leach from the composite [9].

These materials are not homogenous by definition and differential conversion in unfilled resins has been demonstrated for increasing sample thicknesses of a few millimetres indirectly using surface (Knoop and Vickers) hardness measurements [10] and directly by applying bulk spectroscopic measurements on serially sectioned specimens of photo-polymerised dimethacrylate resin [11]. Filler particles, usually silica or zirconia, are combined with the unfilled bulk resin matrix to improve composite strength, toughness and wear resistance [2, 12-14]. The inclusion of filler has also been shown to reduce the generation of shrinkage stresses associated with volumetric shrinkage on curing, at the expense of increased DC. However, quantifying DC using FTIR spectroscopy is complicated by the presence of filler particles which introduce additional refractive indexes, light scattering and extinction coefficients to the system which differ to that of the dynamic properties of the resin matrix [15]. Monte Carlo simulations based on radiative transfer models have been applied to these systems to approximate light irradiance as a function of depth and have used this to extrapolate DC and hardness [16, 17]. Simulation results correspond well to experimental data, demonstrating reduced light transmission, DC and hardness at increasing RBC thickness relative to unfilled

RBCs and is therefore a good first term approximation for understanding how filler particles modify the DC profile. Unfortunately, current numerical solutions have not been extended to consider regional lateral variation in conversion at inter-particulate length scales, whilst experimental efforts have been hindered by technological limitations.

FTIR remains the most promising technique to inform the relationship between polymerisation variables and monomer to polymer conversion, and for bulk measurements two approaches exist. Mid-IR was originally used to quantify DC by comparing aliphatic absorption bands in the monomer and polymer states, but this technique is limited to samples with a thickness less than 30  $\mu\text{m}$  [6] and offers no insight into the reaction rate. More recently Near-IR techniques have been developed to allow for time resolved reaction kinetics to be observed in samples several millimetres in thickness [3, 18]. The key limitations of these studies are the lack of lateral resolution required to study regional monomer to polymer conversion in systems where the organic polymer matrix contains an inorganic filler fraction. Conventional Fourier-transform infrared (FTIR) micro spectroscopic systems are limited by a trade-off between spatial resolution, acquisition time, signal-to-noise ratio (SNR) and sample coverage, whilst even advanced synchrotron sources remain diffraction limited to spatial resolutions of 5 – 10  $\mu\text{m}$  [19]. Inevitably, monomer to polymer conversion is averaged over length scales much larger than the size of a filler particle. Localised variation in the photo-polymerisation of the interstitial resin matrix is yet to be elucidated but is essential for understanding structural variation in these materials.

In this study it is shown how focal plane array (FPA) technology coupled with a novel synchrotron source allows for sampling below the diffraction limit of conventional FTIR microscopes, to provide insight into inter-particulate heterogeneity of monomer to polymer conversion and residual stress states as a function of polymerisation variables.

## 6.2 Methods

### 6.2.1 Preparation of Experimental Resin Based Composites (RBCs)

Experimental RBC materials were prepared by combining monodispersed filler particles with dimethacrylate monomers proportioned to provide differences in matrix viscosity and containing different photo-initiator chemistries to modify photo-polymerisation kinetics. The dimethacrylate monomers, Bisphenol-A-glycidyl-dimethacrylate (Bis-GMA and Triethyleneglycol-dimethacrylate (TEGDMA) (Sigma-Aldrich, Dorset, UK) were proportioned in 70/30 and 60/40 (Bis-GMA/TEGDMA) weight percentage (wt%) ratios and combined to produce 10 g mixes. The monomer blends were combined with a photo-initiator as either 0.2 wt% Camphorquinone (CQ) with 0.8 wt% of its tertiary amine N,N-dimethylaminoethyl-methacrylate (DMAEMA) or 1 wt% Lucirin-TPO (Sigma-Aldrich, Dorset, UK). The proportioned monomers and photo-initiators were homogenised in a glass beaker using a magnetic stirrer at  $50 \pm 1$  °C for 30 mins in dark conditions. Non-silanized, 8 µm (diameter) silica microspheres (Cospheric, Santa Barbara, CA, refractive index = 1.54) were added to the resin blends in either 50/50 or 40/60 wt% ratios and mixed to form composites, using a high speed mixing machine (SpeedMixer™ DAC 150.1 FVZ-K, Synergy Devices Limited, Buckinghamshire, UK) for 5 minutes at 1000 rpm. The compositions for the filled resin blends are summarised in table 6.1.

**Table 6.1.** Weight percentage (wt%) mixing ratios of Bis-GMA and TEGDMA monomers used to formulate each resin blend. Each mixing ratio was combined with a photo-initiator as either 0.2 wt% Camphorquinone (CQ) with 0.8 wt% of its tertiary amine N,N-dimethylaminoethyl-methacrylate (DMAEMA) or 1 wt% Lucirin-TPO photo-initiator. Silica filler particles were added in high (HF) (40/60) and low (50/50) loadings.

| Bis-GMA | TEGDMA | Photo-initiator | Resin/filler (wt%) | Sample Code  |
|---------|--------|-----------------|--------------------|--------------|
| 70      | 30     | CQ              | 50/50              | 70/30 CQ     |
| 70      | 30     | TPO             | 50/50              | 70/30 TPO    |
| 60      | 40     | CQ              | 50/50              | 60/40 CQ     |
| 60      | 40     | TPO             | 50/50              | 60/40 TPO    |
| 60      | 40     | CQ              | 40/60              | 60/40 CQ HF  |
| 60      | 40     | TPO             | 40/60              | 60/40 TPO HF |

For each composition, 0.1mL of RBC was applied to the surface of a calcium fluoride (CaF<sub>2</sub>) disc (30 mm × 1mm (diameter × thickness), UV grade polished window, Crystan, Dorset,UK), and pressed with a microscope cover slide to an approximate thickness of 100 µm. Composites were photo-polymerised using an EMS Swiss master light curing unit (EMS OPTIDENT, electro medical systems, Nyon Switzerland) which was placed normal to and in contact with the cover slide, illuminating the composite for 60s at an intensity of 300 mWcm<sup>-2</sup> over a spectral range of 390-550 nm. SiC paper (P4000 roughness, Agar Scientific, Stansted, Essex, UK) was used to polish polymerised composites to a thin layer, approximately 10 µm thick with only a single layer of particles, suitable for mid infra-red measurements. The resultant resins were stored in dark conditions in sealed containers at 4 ± 1 °C prior to further use.

### **6.2.2 Synchrotron Fourier Transform Mid-Infra-Red Spectroscopy Mapping**

High resolution Fourier transform mid-infra-red (FT-MIR) images were taken of each RBC formulation using the IRENI (**I**nfra**R**ed **E**nvironmental **I**maging) beamline (Figure 6.1) (Synchrotron Radiation Centre, University of Wisconsin-Madison, Wisconsin, USA) [20]. Radiation from the synchrotron storage ring was extracted via a bending magnet into 320 mrad (horizontal) by 25 mrad (vertical) swathes. Each swathe resembles a fan of radiation consisting of twelve beams of synchrotron light which were collimated and combined side by side into a 3 × 4 matrix using an array of toroidal mirrors. The beam matrix illuminates a 60 × 40 µm<sup>2</sup> region on an MCT (Mercury Cadmium Telluride) focal plane array (FPA, Santa Barbara) detector, housed within a Hyperion 3000 IR microscope (Bruker Optics) coupled with a Bruker 70FTIR spectrometer. Transmission measurements were performed using a 74 x magnification objective (Ealing, Thermo-scientific) with a numerical aperture (NA) of 0.65. This optical configuration coupled with spatial oversampling allowed for diffraction limited imaging (spatially) over a spectral Mid-IR range of 850 – 4000 cm<sup>-1</sup>, corresponding to an effective pixel size geometry of 0.54 µm × 0.54 µm. Spectra were collected with a 2 cm<sup>-1</sup> resolution using 128 co-added spectral scans per pixel.

The FPA detector was equipped with a programmable mapping stage, enabling mosaic IR imaging. FT-MIR maps of the RBCs were collected in tile mosaics, with a single tile equivalent to an illuminated area of  $35\ \mu\text{m} \times 35\ \mu\text{m}$  ( $64 \times 64$  pixels). Larger maps were constructed from the combination of several tiles, up to a maximum of eight, recorded sequentially. A single tile collected a total of 4096 individual FT-MIR spectra (the sum of 128 scans per pixel recorded simultaneously), with a measurement time of approximately five minutes per tile. Maps were collected from the outer edge to the centre of each RBC/CaF disc in 1 mm increments using the commercial Bruker OPUS software package (version 6.5, Bruker Optics) in maps consisting of 4, 6 or 8 tiles. For each map, a visible image was collected over the same area in order to locate the centre of each filler particle for analysis. Measurements were carried out in a nitrogen filled atmosphere at  $23 \pm 1\ ^\circ\text{C}$  within a sealed Plexiglas container.



**Figure 6.1.** (a) Schematic of the IRENI beamline (Synchrotron Radiation Centre, Wisconsin, U.S.A), where M1 – M4 are mirror sets (adapted from Nasse *et al* 2011). (b) Long-exposure photograph showing the combination of the 12 individual beams to form a  $3 \times 4$  matrix. (c) A visible-light photograph of a 60/40 wt% TPO initiated composite, where each map panel measures  $32 \times 32 \mu\text{m}$ .

## 6.2.3 Data Analysis

### 6.2.3.1 Degree of Conversion

The degree of monomer to polymer conversion (DC) for each pixel in a given map was calculated from the ratio of the area of the aliphatic absorption peak ( $1637\text{ cm}^{-1}$ ) in the monomer and polymer states. Aliphatic absorption peaks were normalised to the aromatic stretching band ( $1609\text{ cm}^{-1}$ ) to correct for variations in sample thickness.

$$DC = \left(1 - \frac{C=C_{aliphatic}^p/C=C_{aromatic}^p}{C=C_{aliphatic}^m/C=C_{aromatic}^m}\right) \cdot 100 \quad (6.1)$$

where  $C=C_{aliphatic}$  and  $C=C_{aromatic}$  refer to the peak area of the  $1637\text{ cm}^{-1}$  and  $1609\text{ cm}^{-1}$  absorption bands respectively in the monomer ( $m$ ) and polymer ( $p$ ) forms. FT-MIR maps were analysed using IRyidys ([www.iryidys.com](http://www.iryidys.com)), an in-house program generated at the SRC which runs on the commercial software package IGOR PRO (version 6.3.5.5, [www.wavemetrics.com](http://www.wavemetrics.com)). Each map was integrated over the C=C aromatic ( $1609\text{ cm}^{-1}$ ) and aliphatic ( $1637\text{ cm}^{-1}$ ) absorption bands respectively (following baseline corrections for each peak) to produce an image for each vibration. The degree of monomer to polymer conversion was determined using equation 1 for each given pixel. Laboratory based FT-MIR was used to obtain baseline spectra of the composite prior to photo-polymerisation. Bulk measurements of the uncured composite were collected using a Nicolet 6700 spectrometer (Thermo Scientific, Warrington, UK). Spectra were collected in ATR mode using a white light source and an InGaAs detector over a spectral range of  $800\text{ to }4000\text{ cm}^{-1}$  with a  $2\text{ cm}^{-1}$  spectral resolution. An in-house script, written in MATLAB © (version R2012b, Mathworks ©) was used to locate the centre of each filler particle (obtained from the visual images) and radially average the DC, over a radius of  $\sim 5\mu\text{m}$  at  $0.54\mu\text{m}$  increments, for all particles in a map. Conversion was also measured at inter-particulate distances, by obtaining conversion values at the midpoint between neighbouring particles (centre to centre distance) for all particles within a map.

### 6.2.3.3 Measurements of Residual Stress

Residual strain was visualised indirectly from positional fluctuations of the aromatic  $1609\text{ cm}^{-1}$  absorption band, corresponding to the aromatic C=C stretching frequency originating from the benzene rings at the centre of the Bis-GMA monomer. The aromatic group is ideally located to quantify bond strain and has a distinct chemical signature in the mid-IR region. To quantify residual bond strain stored within the polymer structure, full IR spectra were extracted from each pixel in a map. Following an initial rubber band baseline correction to the spectra [21], the aromatic peak was fitted with a Gaussian model to determine peak positional fluctuation with respect to location from a filler particle. Principal component analysis (PCA), as described by Ryu and Noda (2010) [22], was used to rule out positional fluctuations in the  $1609\text{ cm}^{-1}$  absorption band due to the combined effect of relative intensity changes in neighbouring bands and transmission artefacts which may artificially shift an absorption peak [22]. PCA calculation was performed using *prcomp* from the R statistical library in the R programming language (R version 3.1.3 2015). Data was mean centred prior to PCA calculations, but was not scaled to the standard deviation to preserve the amplitude information of the spectral intensities. 2D maps of aromatic peak position, corresponding to the original pixels that the spectra were extracted from, were constructed to visualise inter-particulate variation. Radial and inter-particulate profiles were calculated in the same way as for DC. Correlations between DC and aromatic strain were obtained by calculating Pearson product-moment correlation coefficient. All calculations were performed using R programming (version 3.1.3, 2015, R Foundation).

### 6.3 Results

Figure 6.2a shows a visible image of a 60/40 (Bis-GMA/TEGDMA) wt% resin matrix composite initiated with TPO, containing a 50 wt% filler loading of highly mono-disperse particles (shown as circles in 2D). The degree of monomer to polymer conversion over the same 2D area is shown in Figure 6.2b. Pseudo colour coding is used to highlight areas of relatively high (red) and low (blue) conversion corresponding to the resin matrix immediately surrounding and between filler particles. Spatial variation of residual strain within the RBC was determined semi-quantitatively by measuring changes in the wavenumber position of the aromatic absorption peak ( $1609\text{ cm}^{-1}$ ), for each pixel and its corresponding mid-IR spectra to produce maps of wavenumber for every RBC (Figure 6.2b and d). Lower and higher wavenumbers were coloured red and blue respectively to illustrate higher and lower states of residual strain (Figure 6.2c). Colour maps were produced for each RBC for every unique resin matrix, initiator and filler load composition. Values vary for each RBC composition, so maps were independently scaled to best visualise the respective distributions with respect to the position of filler particles.

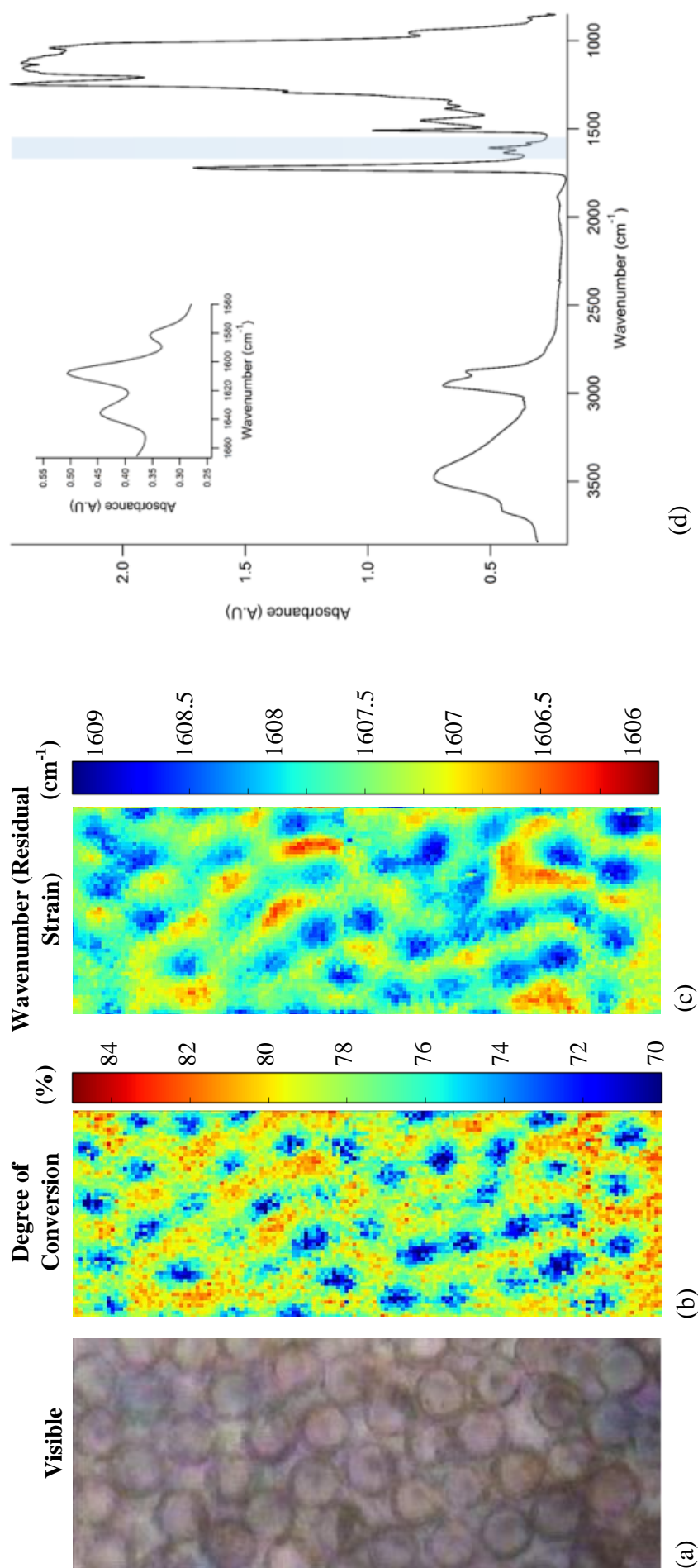


**Figure 6.2.** (a) Visible image of a TPO initiated RBC composed of a 60/40 wt % (Bis-GMA/TEGDMA) resin matrix containing 50 wt% of monodisperse 8  $\mu\text{m}$  silica particles. (b) A map of monomer to polymer conversion over the identical area shown in (a). Areas coloured blue and red correspond to regions of relatively low and high conversion respectively. (c) A pseudo-coloured map of the aromatic ( $1609\text{ cm}^{-1}$ ) absorption band wavenumber position over the same area, where lower wavenumbers correspond to larger residual strain within the polymer (red regions). (d) (main) Raw Mid-IR spectra of a TPO initiated composite composed of a 60/40 wt % (Bis-GMA/TEGDMA) resin matrix containing 50 wt % of monodisperse 8  $\mu\text{m}$  silica particles. The spectra was collected over  $850 - 4000\text{ cm}^{-1}$ , with a  $2\text{ cm}^{-1}$  resolution. (inset) Aromatic ( $1609\text{ cm}^{-1}$ ) and aliphatic ( $1637\text{ cm}^{-1}$ ) absorption bands which were used to calculate the degree of monomer to polymer conversion and relative residual strain for each pixel within a map.

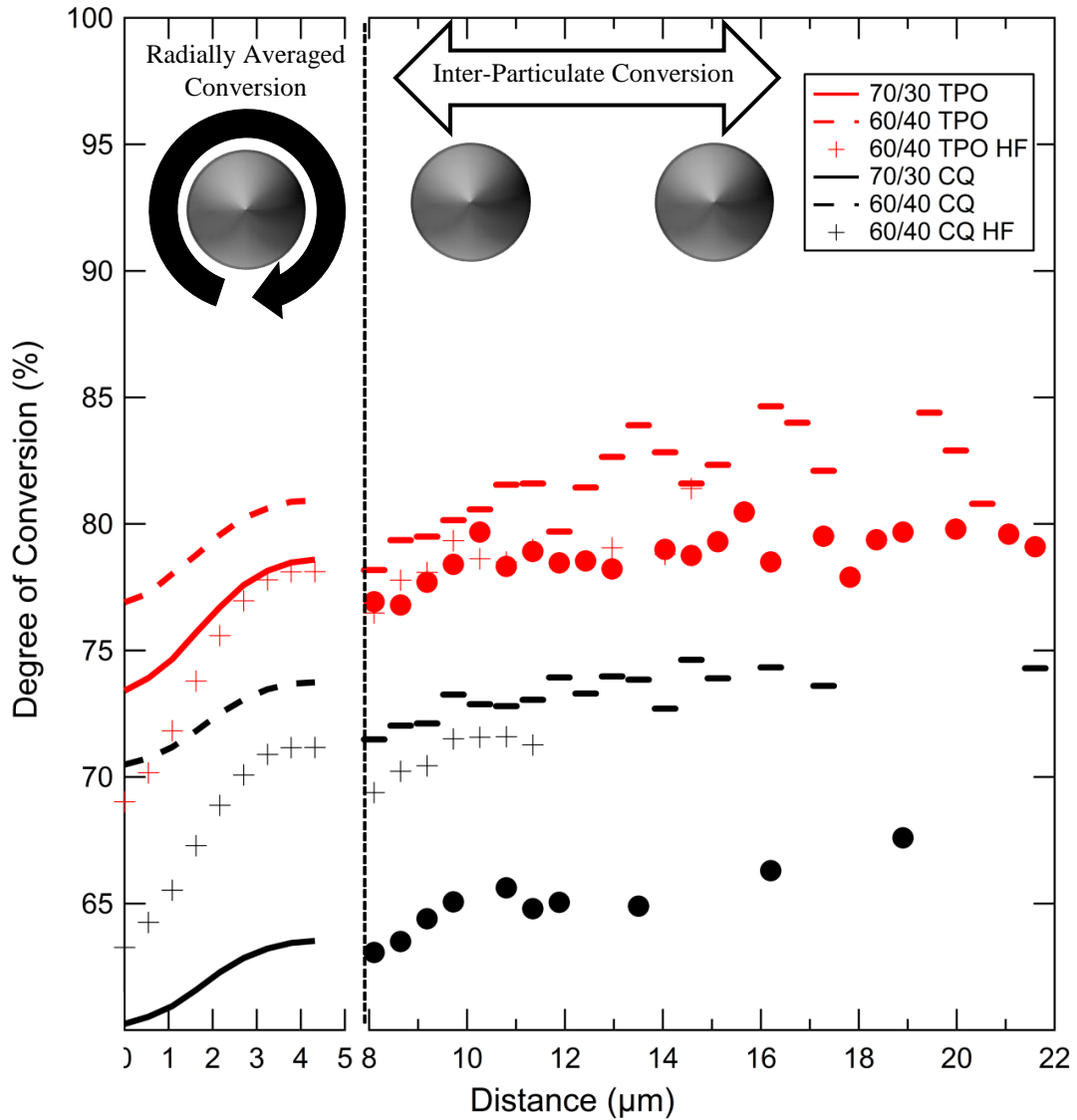
### 6.3.1 Micro-scale Spatial Variation in Polymerisation

Figure 6.2b illustrates how the degree of conversion within the resin matrix varies as a function of distance from a filler particle for all RBC compositions. Radial averages of monomer to polymer conversion integrated over the 2D face of all filler particles for each specific RBC are displayed to the left of the broken line in Figure 6.3. It can be seen that for all RBCs the degree of conversion is lowest at the 2D particle centre and increases, in a Gaussian form, towards the particle edge approaching the bulk of the resin matrix. Composites polymerised at relatively fast rates with the more reactive photo-initiator, Lucirin TPO, demonstrate greater conversion for identical compositions in comparison to CQ based systems polymerised at slower rates. For the 70/30 and 60/40 wt% blends, DC is 15 and 7 % greater respectively when the system is polymerised with TPO for both filler loading fractions.

The percentage point increase in conversion from the centre to the edge of a filler particle is consistent at ~ 5% for all 50/50 wt% filler loading RBCs, regardless of viscosity or photo-initiation chemistry. The radial profile for composites with a higher loading fraction is similar to the 50/50 wt%, with respect to the Gaussian shape. However, DC is significantly lower at the 2D particle centre which is reflected by a 13 % point increase from centre to edge.

Inter-particulate conversion for all RBCs, where DC was measured at the midpoint between the centre points of two neighbouring particles for a range of separation distances, is shown to the right of the broken line in Figure 6.3. A larger separation distance between local filler particles corresponds to increased conversion in the resin matrix. Offsets in inter-particulate DC between identical blends but polymerised with different photo-initiator species are consistent with their corresponding radial profiles, with TPO initiated resins showing almost 15% and 10 % greater DC between filler particles for 70/30 and 60/40 wt% blends respectively. The degree of conversion shows a larger correlation with separation distance in CQ initiated systems and is ranked by viscosity. The 70/30 and 60/40 wt% of CQ resins show correlation values between DC and particle separation of  $r=0.86$  and  $r= 0.75$  respectively. In comparison, corresponding

TPO based RBCs show correlation values of  $r=0.57$  and  $r=0.68$ . Conversion increases up to ~80% in TPO RBCs before plateauing when particles are separated by 15  $\mu\text{m}$ , whilst in CQ RBCs conversion continues to increase with particle separation distance.



**Figure 6.3.** Degree of conversion is shown as a function of distance from a filler particle centre. Radially averaged conversion (over all particles, centre to edge) is shown to the left of the dashed line, whilst conversion at the midpoint between particle centres is shown to the right.

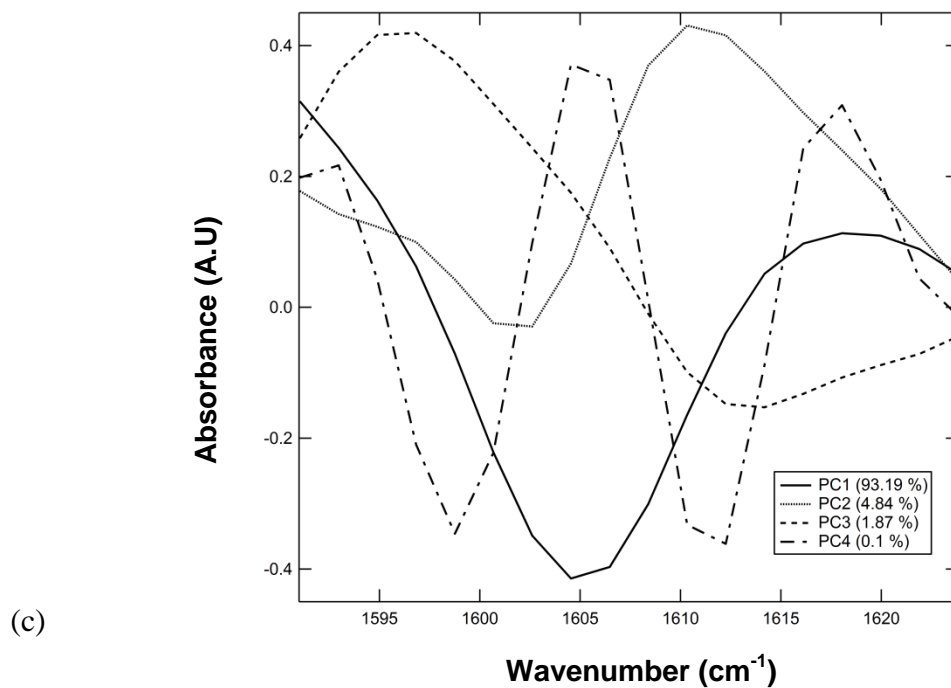
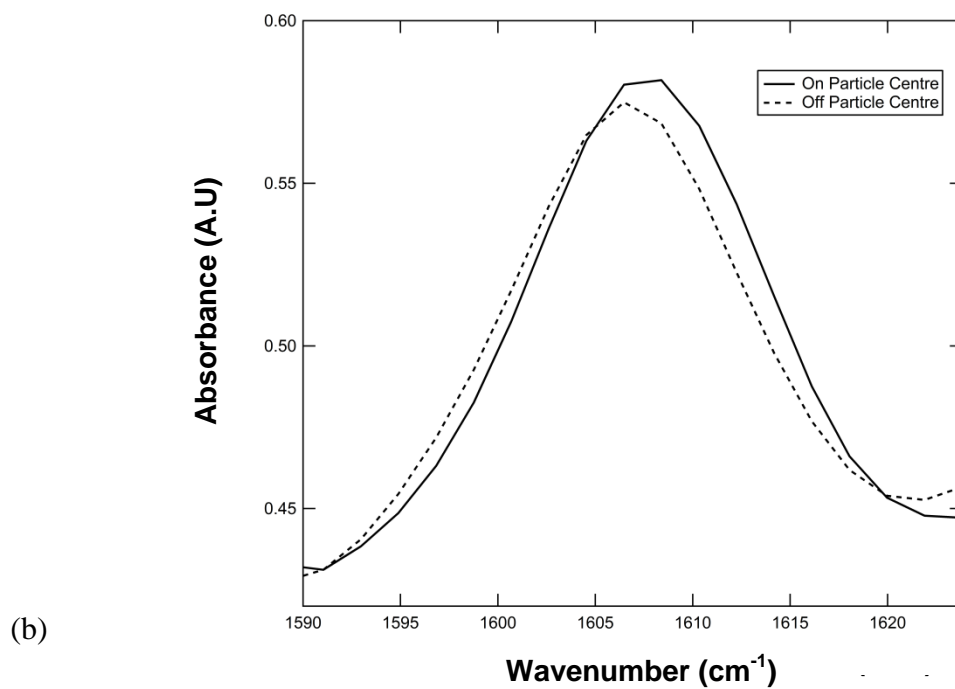
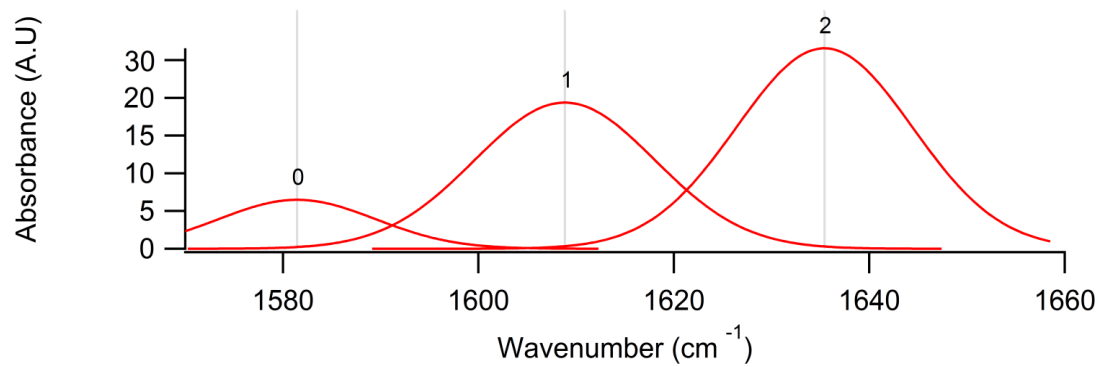
### 6.3.2 Residual Strain

Figure 6.2(c) displays the spatial variability in the wavenumber peak of the aromatic absorption band originating from the Benzene groups at the centre of the Bis-GMA monomer. Prior to plotting maps of the aromatic wavenumber and performing quantitative analysis it was necessary to determine the origin of these wavenumber changes. Strain in chemical bonds has been shown to correspond to a decrease in the observed wavenumber for a specific absorption band [23]. However, wavenumber shifts may be artificially induced by relative intensity changes in neighbouring and overlapping absorption bands and transmission artefacts. For example, regions of higher conversion correspond to a comparatively reduced aliphatic peak intensity and therefore lower overlap between the two absorption bands, altering the magnitude of apparent peak shifts. In this study the principal components analysis (PCA) technique as described by Ryu *et al* (2010) [22] was adopted when treating spectral data to discern peak shifts ascribed to overlapping peaks and visualise spatial variation in strain.

Spectra have been windowed to show the aromatic ( $1609\text{ cm}^{-1}$ ) and aliphatic ( $1637\text{ cm}^{-1}$ ) absorption bands. Each absorption peak has been de-convolved as seen in Figure 6.4a, with each band displaying degree of overlap with its neighbour. Overlapping peaks and differences in relative intensity changes across samples makes it difficult to compare the origins of peak shifts for composites with differences in terminal conversion. For example, a TPO initiated RBC will show greater conversion towards the centre of a filler particle in comparison to a CQ RBC of the same formulation. Higher conversion corresponds to a comparatively reduced aliphatic peak intensity and therefore lower overlap between the two absorption bands, altering the magnitude of apparent peak shifts.

Principal components analysis (PCA) was applied to the spectral data to obtain the loading vectors (Figure 6.4(c)) to determine the origin of the peak shift, from spectra taken from a line transect over a filler particle (Figure 4(b)). The number of loading vectors for a peak shift attributed to relative intensity changes is equal to the number of sampled peaks, as the resultant

shift will be a linear combination of the weighted contribution of each peak. A peak shift due to physical changes to the chemical structure is a non-linear effect and the number of loading vectors will exceed the number of overlapping peaks. It can be seen that the peak shift in Figure 4(b) requires four principle components to describe all variance and is identified as a true peak shift.



**Figure 6.4.** (a) Deconvolution of the aromatic ( $1609\text{ cm}^{-1}$ ) and aliphatic ( $1637\text{ cm}^{-1}$ ) absorption bands. (b) The aromatic absorption band taken as a line transect from the centre of a particle into the resin matrix. (c) Loading vectors of the aromatic peak over the aforementioned line transect.

All composites display higher aromatic wavenumbers (lower residual strain) at the 2D particle centre, as seen in Figure 6.5. Radial averages are displayed to the left of the broken line whilst inter-particulate changes are shown to the right. Radial averages for all RBC compositions show that Bis-GMA with higher aromatic wavenumbers are found at the 2D particle 'centre'. Wavenumber values at the centre are typically  $\sim 1609 \text{ cm}^{-1}$  with small variations between blends. This value is very similar to the wavenumber of the aromatic absorption band in the unperturbed Bis-GMA (liquid) monomer form. The aromatic wavenumber decreases towards the edge of the filler particle. Decreases in wavenumber are greatest for TPO initiated RBCs and are approximately three times larger than observed in CQ based systems of the same blend. Additional differences in the wavenumber shift exist between different blends with the same photo-initiator chemistry, with the resin matrix containing a higher proportion of the diluent TEGDMA showing a larger wavenumber decrease, although differences between RBCs with different filler loading fractions are negligible. For all RBC compositions, the decrease in wavenumber correlates strongly with increasing degree of conversion, with correlation coefficients of  $r \sim -0.99$ . The relationship between conversion and wavenumber shift is linear near the particle edge, although this is not true closer to the particle centre, as shown by the inflection point in Figure 6.6. In this region a similar increment in conversion corresponds to a smaller shift in the wavenumber.

To the right of the dotted line in Figure 6.5, it can be seen that differences in wavenumber shift with respect to photo-initiator chemistry and blend viscosity are maintained at inter-particulate distances. However, strong correlations between wavenumber shift and the degree of conversion are no longer ubiquitous, as seen in CQ RBCs which plateau at approximately  $1608.25 \text{ cm}^{-1}$ , which corresponds to a low correlation value of  $r \sim -0.22$ . In comparison, the aromatic wavenumber for TPO RBCs decreases to  $\sim 1606.5 \text{ cm}^{-1}$  at larger particle separation distances and correlates more with increasing conversion ( $r = -0.80$ ).

Direct comparison of wavenumber shift between similar RBCs photo-polymerised with different initiator chemistries are complicated by differences in monomer to polymer

conversion for each polymerising system. Normalising the wavenumber shift to the degree of conversion for each data point (Figure 6.7) shows a similar relationship as the radial averages in Figure 6.5, but demonstrates that TPO initiated RBCs display a greater shift per converted monomer.

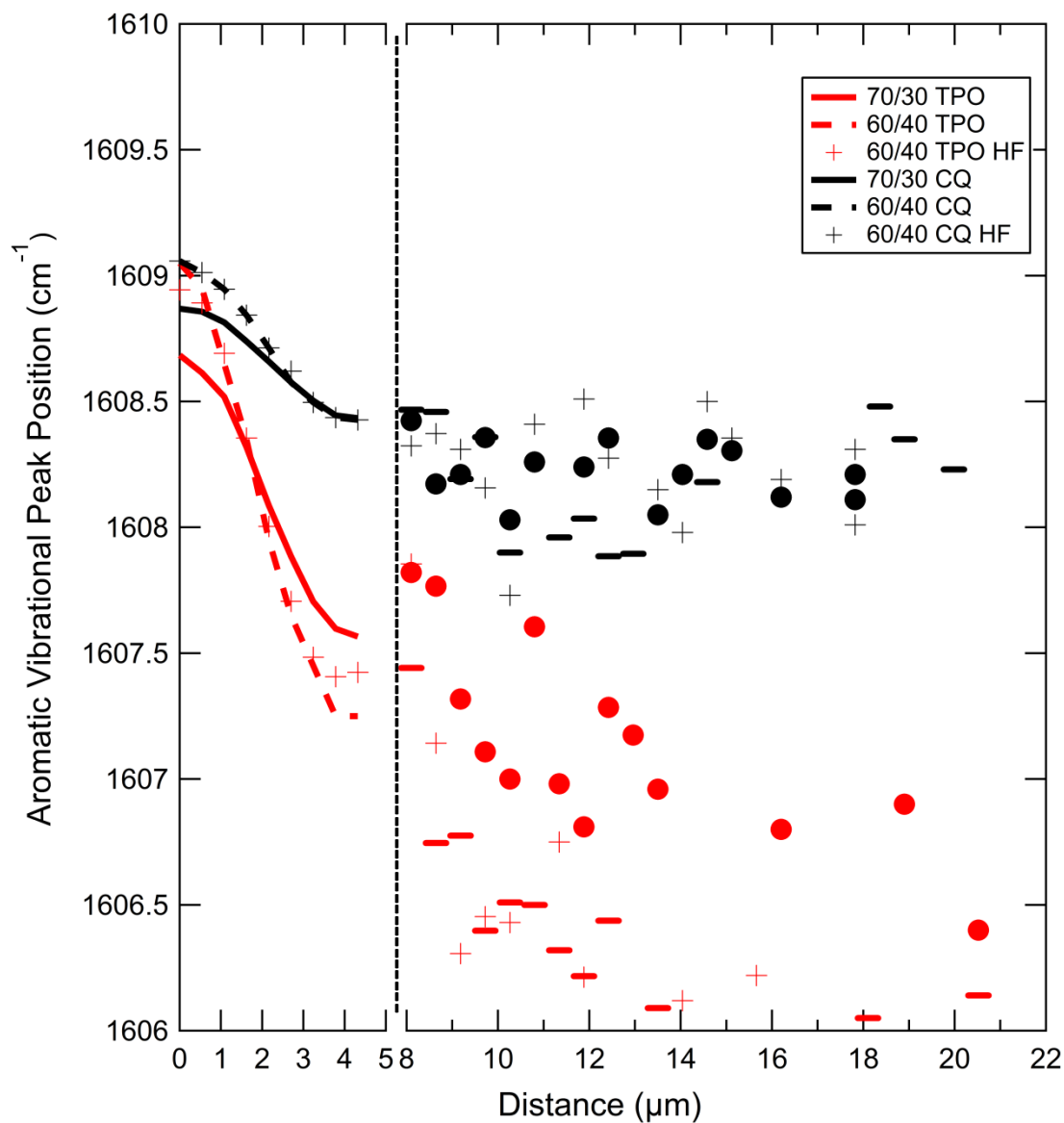


**Figure 6.5.** The aromatic wavenumber for the aromatic group at the centre of the Bis-GMA monomer is shown as a function of distance from a filler particle centre. Radially averaged wavenumber (over all particles, centre to edge) is shown to the left of the dashed line, whilst the wavenumber value at the midpoint between particle centres is shown to the right. (**inset**) The chemical structure of the Bis-GMA monomer - ring strain was detected in the aromatic core.

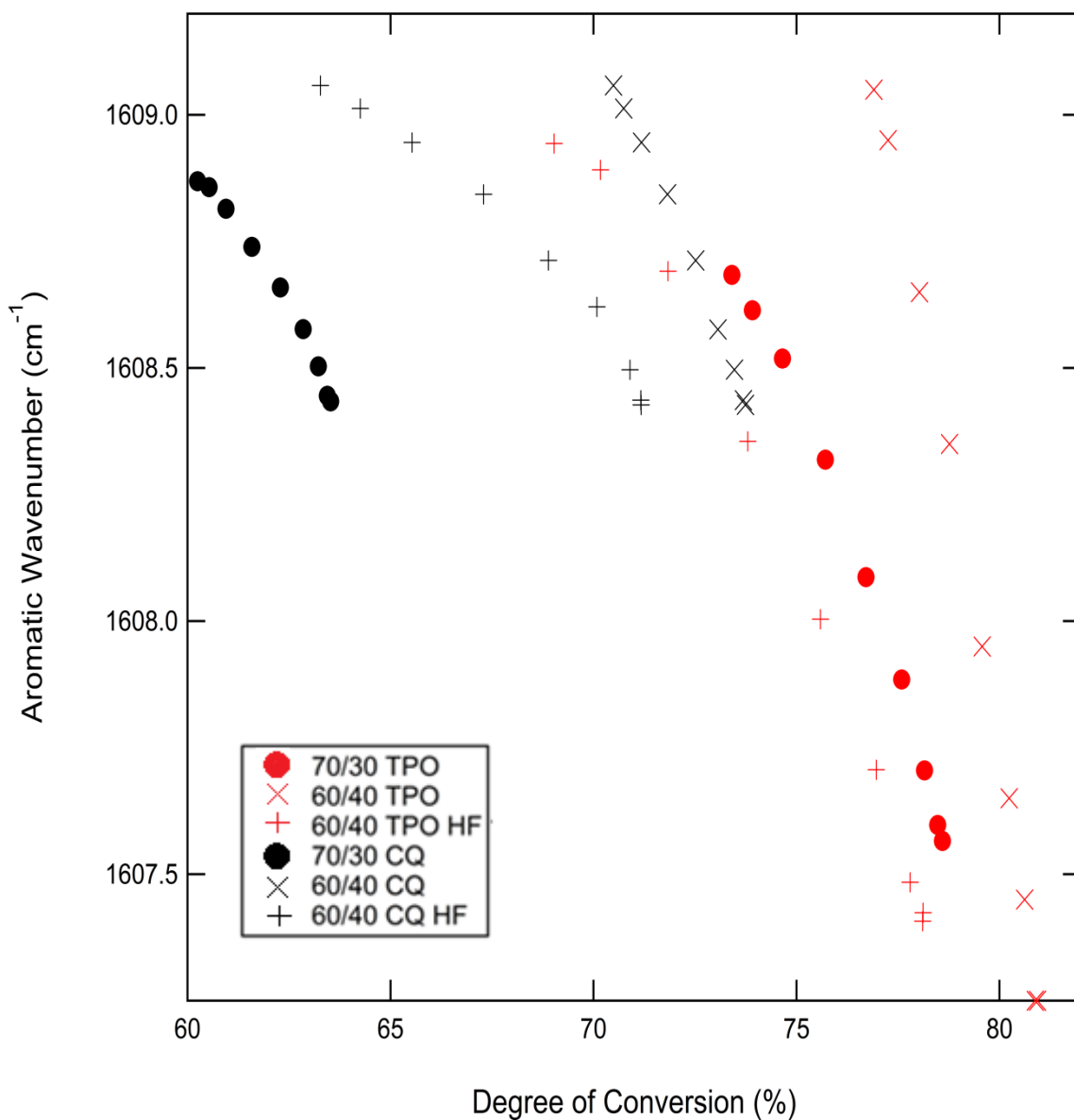


**Figure 6.6.** The radially averaged decrease in the aromatic wavenumber as a function of monomer to polymer conversion. Each plotting point represents a distance increment of 0.54  $\mu\text{m}$  from the centre of the filler particle, the first point to the left, to the edge of the particle. Here data are replotted with different symbols to previous figures to clarify the number and location of points.

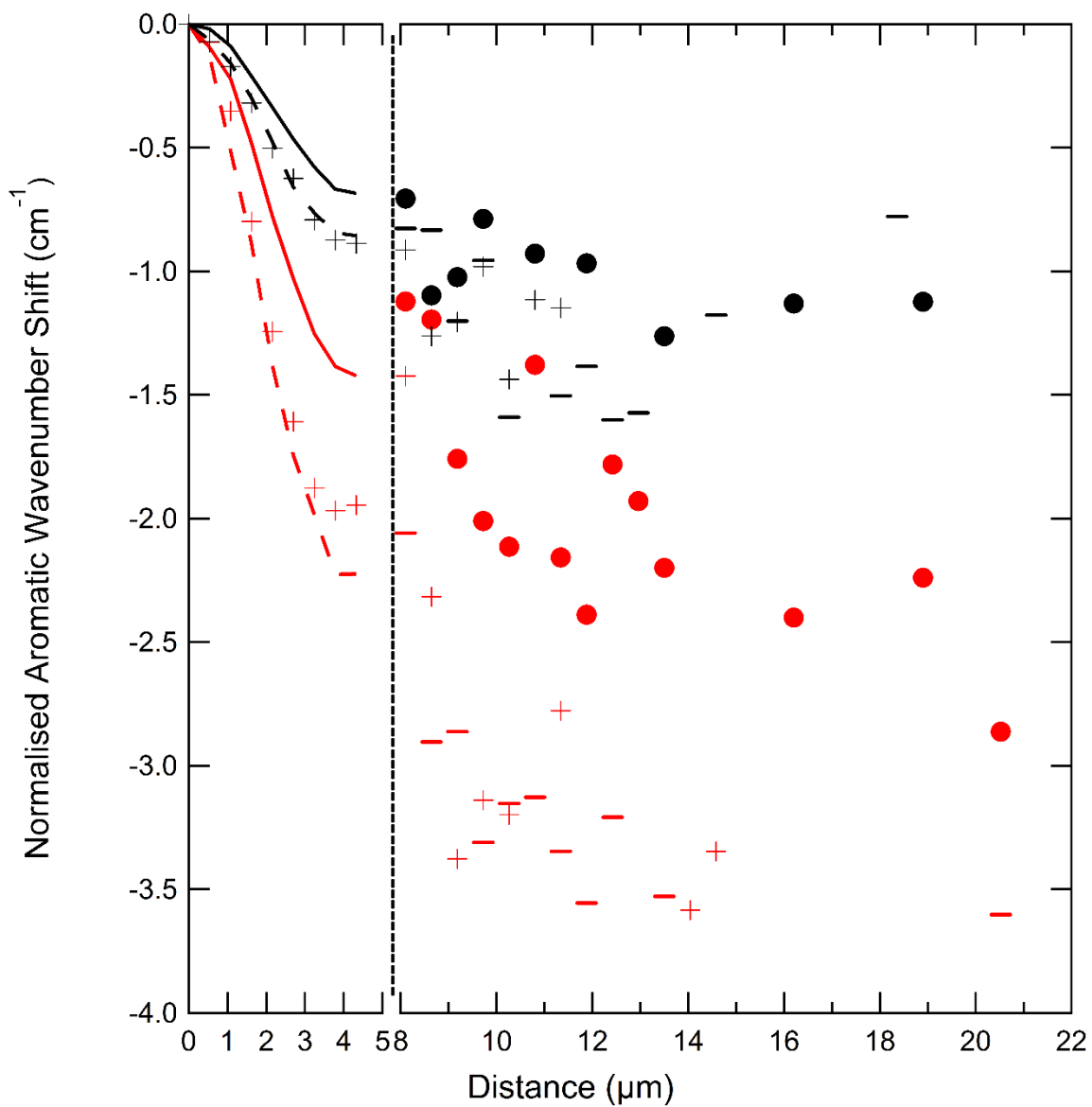


**Figure 6.7.** The decrease in the aromatic wavenumber (an increase in residual strain), normalised to the degree of conversion at each distance increment. The generation of residual strain within the RBC is ranked by the relative differences in polymerisation rate.

## 6.4 Discussion

### 6.4.1 Understanding Conversion and Strain Profiles around Filler

Figures 6.2b and c illustrate how the introduction of silica filler particles into a dimethacrylate polymer matrix induced spatial heterogeneity with respect to monomer to polymer conversion and residual strains, in comparison to an unfilled test specimen. Several previous laboratory based FTIR studies have quantified DC in RBCs [6, 24-26], but to date have only been able to provide measurements of the bulk material, with diffraction limited instrumentation effectively averaging values of conversion arising from resin coating/wetting filler particles and the inter-particulate resin matrix. Consequently, subtle differences in the microscale structure of composites at inter-particulate length scales had not been identified, but have been resolved in this study for the first time.

Local minima in conversion are observed at the 2D centre of each filler particle (Figures 6.2 and 6.3) which increases towards the particle edge and into the inter-particulate resin matrix, whilst the aromatic wavenumber displays an inverse relationship with respect to conversion (Figure 6.5). Several studies have demonstrated that a shift to lower wavenumbers for an absorption band is indicative of chemical bond strain [23]. However, wavenumber shifts may be artificially induced by relative intensity changes in overlapping neighbouring peaks i.e. the aliphatic band which overlaps the aromatic absorption. In this study, a PCA technique described by Ryu *et al* (2010) [22] was used to discern between false and true peak shifts. The number of principal components required to describe the total variance in the spectral data, for a false peak, is equivalent to the number of overlapped peaks. It can be seen in Figure 6.4 that four principal components are needed to describe the variance for the aromatic peak shift from the 2D centre to the particle edge. The peak shift is therefore a non-linear effect indicative of possible residual ring strain stored in the Bis-GMA aromatic core.

It can be seen from the radially averaged plots (Figures 6.3 and 6.5) that conversion and residual strain (inversely proportional to wavenumber) display a Gaussian increase from the 2D

centre to the particle edge for all RBC formulations. This increase is not attributed to variation in conversion due to limited depth of cure, which has been shown to exhibit similar differences in conversion for these materials when the sample thickness exceeds 1 mm. Given that the samples were 8-10  $\mu\text{m}$  thick, the effects of linear attenuation on conversion are considered to be negligible. The most likely explanation for this relationship is the presence of a lower converted boundary layer [27, 28] storing less residual bond strain, encapsulating each filler particle, relative to the inter-particulate resin matrix. As each filler particle is viewed in 2D, the measured values of conversion and strain in a pixel are weighted sums of the values arising from the boundary layer and the inter-particulate resin matrix. At the 2D 'centre', there is little free resin matrix and the boundary layer contributes most to the signal. Similarly, towards the particle edge the inter-particulate resin matrix makes an increasing contribution and so conversion and strain increase. The formation of this boundary layer is attributed to reduced monomer mobility around the silica particle [29, 30], due to drag along the particle surface mediated by surface porosity and hydrogen bonding interactions (between the monomers and silica). Lower monomer mobility will restrict the diffusion of propagating radical species during polymerisation, reducing conversion in these regions relative to the bulk matrix.

The physico-mechanical and optical properties of RBCs have been shown to vary as a function of conversion and are often reported as a binary system, combining the properties of the resin bulk and that of the filler. However, a boundary layer with lower conversion will produce an additional region which will mismatch with the inter-particulate matrix with respect to elastic modulus, glass transition temperature [31], tensile and compressive strength, refractive index, thermal expansion, polymerisation shrinkage and polymerisation induced stresses [15, 32-37]. The generation and relaxation of internal shrinkage stresses in these materials are often considered in terms of viscous flow of the bulk during polymerisation, varying as a function of terminal conversion and polymerisation rate [38]. It is accepted that for dimethacrylate based polymers, immediate shrinkage strain is the result of Van der Waals inter-molecular spacing being exchanged for that of carbon-carbon bonds as the polymer forms. However, there is little

information in the literature elucidating how polymerisation impacts on the final conformation of the polymer at intra-molecular length scales. It can be seen in Figure 6.6 that aromatic strain varies almost linearly with conversion over the 2D face of a filler particle. Even though the aromatic core of Bis-GMA is the stiffest component of the molecule, it is discrete with respect to polymerisation and cross-linking reactions. Other bonds in the monomer will be subject to strain before strains in the aromatic groups are detectable [39, 40], but as the IR absorption peak corresponding to this structure is very well defined, subtle differences in the peak position can be elucidated. Greater average aromatic strain will therefore be measured for a more converted and cross-linked region of the polymer. The relationship between DC and aromatic strain over a particle is not entirely linear however (Figure 6.6), with an inflection point observed near to the 2D particle centre for all RBCs where the aromatic wavenumber is similar to that measured in the liquid monomer form. This may represent several effects; reduced cross-linkage in the boundary layer, detachment of the polymer from the particle surface as a form of stress relief [41] or the result of insufficient monomer mobility to generate aromatic stress. However, this may also be an artefact from sampling very little of the boundary layer.

#### 6.4.2 Understanding Conversion and Strain Profiles Between Particles

The right hand side of Figure 6.3 shows two distinct features of conversion at inter-particulate length scales. A slight decrease in DC, relative to conversion at the edge of the radially averaged profile, is observed when particles are in contact or are minimally separated, but gradually increases at larger separations. The difference in values of conversion at small separations is attributed to the radial average being taken over a range of particle packing densities, with some of these particles being effectively isolated. In comparison, DC values taken at short separation distances correspond to higher packing densities where impinging light has been attenuated by previous layers of silica particles. Additionally, at short separation distances two boundary layers from separate particles may contribute to the measured value of DC within a pixel that lies between particles, lowering the average value of DC in that pixel. The actual value of DC at the midpoint between closely neighbouring particles, without the contribution of boundary layers which are not in contact with each other, cannot be determined due to insufficient spatial resolution.

The gradual increase in conversion at larger separation distances may be explained by considering differences in particle packing density and relative pressure in the resin matrix in the pre-gel and gel states. When the packing density is high, light that reaches the surrounding resin matrix will have been attenuated via interactions with silica microspheres e.g. absorption, scattering and refraction, reducing the number of photons that can activate photo-initiator molecules. Decreasing particle packing density reduces attenuation arising from filler particles, leaving interactions primarily with the resin matrix and scattering and extinction by photo-initiator molecules. Similarly, increasing particle separation will also reduce relative pressures in the resin matrix and allowing for greater mobility of propagating radical species and monomers to achieve higher terminal conversion.

### 6.4.3 The Effect of Relative Rate on DC and Aromatic strain

In this study photo-initiator chemistry and the fluidity of the resin matrix, controlled by increasing the proportion of the diluent monomer TEGDMA, was used to introduce a range of polymerisation rates. Composites initiated with TPO achieved greater DC for radial and inter-particulate profiles for a given blend. Within each photo-initiator system conversion was greatest for composites with the more fluid resin matrix. This is consistent with the literature which has shown that TPO is a more efficient photo-initiator than CQ and achieves greater terminal conversion and maximum polymerisation rate, typically by an order of magnitude for the latter. Similarly, a more fluid resin matrix confers greater mobility for propagating radical species during polymerisation [35, 42-44].

It can be seen in Figure 6.5 that RBCs photo-polymerised at faster rates, through the use of the more reactive TPO initiator and a more fluid resin matrix, demonstrate greater aromatic bond strain through a greater shift to lower wavenumbers. Furthermore, it is observed that at inter-particulate distances strain continues to increase when the RBC was polymerised at relatively fast rates (TPO) but plateaus for more slowly cured systems (CQ). Making correlations however, between residual strain and relative polymerisation rate are complicated by differences in monomer to polymer to conversion for each RBC. A more converted polymer will generate greater internal stresses in comparison to a lower converted material that has been polymerised at the same rate. Normalising the decrease in the aromatic wavenumber with respect to  $DC_i$  (where  $DC_i$  represents the measured value of conversion at the  $i^{th}$  increment of particle separation) and plotting against distance demonstrated that the generation of aromatic strain (residual strain within the polymer structure) is ranked by relative polymerisation rates i.e. by photo-initiator chemistry with sub-sets of viscosity (Figure 6.7). A faster polymerisation rate and polymer growth may therefore exert a larger force on the polymer chains and cross-links, causing it to extend more so than composites polymerised at relatively lower rates, storing chemical bond strain presumably within the whole monomeric unit and not just in the aromatic core.

Composites with a 60/40 wt% loading of filler display similar radial and inter-particulate profiles, with respect to conversion and aromatic strain, in comparison to lower filled counterparts. As the filler particles are very uniform, individual filler particles will produce the same patterns in conversion as a function of packing density, which will control light attenuation and relative monomer mobility. However, as larger particle separation distances do not exist in higher filler load conditions, the composite cannot achieve greater conversion. Therefore the average value of conversion for a high filled composite is relatively lower, which is consistent with reported bulk measurements. A small discrepancy in DC between composites with the lower and higher loadings of filler can be seen at the 2D particle centre in the radial plot. This is likely a sampling effect, with the radial profile for the 60/40 wt% filler loading composites being calculated over a narrower distribution of particle packing densities in comparison to lower loadings.

It must be acknowledged that spherical particles of this size are known to induce possible wavenumber shifts due to Mie scattering [45, 46] during FTIR measurement. For a given composition of RBC, the resin matrix formulation and filler particles are identical with the only difference arising from photo-initiator chemistry. The filler particles are highly monodisperse and measurements have been made on more than 200 particles (with radial averages taken over only close packed particles to reduce further possible wavenumber shifts) for each individual composition. Therefore, Mie scattering contributions to any wavenumber shift taken over radial averages should be quite consistent for each RBC map. This is true when comparing maps taken at different regions from the same sample i.e. maps from the edge and the centre of the composite. Taking in to account a shift in the aromatic wavenumber due to scattering effects, any significant differences in the wavenumber shift between CQ and TPO initiated RBCs are therefore ascribed to the polymerisation rate.

## 6.5 Conclusions

The micro-structure of experimental dental composites has been studied for the first time with sub-micron spatial resolution synchrotron FTIR mapping at inter-particulate length scales. The presence of filler particles in a resin matrix has been shown to introduce inter-particulate spatial heterogeneity with regards to both monomer to polymer conversion and residual bond strain, which is unreported in any RBC system to date. Heterogeneity close to the particle is believed to originate from a lower converted and reduced residual strain boundary layer which surrounds each particle. At inter-particulate length scales, increases in conversion and strain are proportional to particle separation which is attributed to reduced attenuation of impinging light and greater mobility within the resin matrix. Greater conversion, achieved through photo-initiator chemistry, resin matrix composition or increased filler particle separation, confers greater total bond strain in the cross-linking monomer. However, the generation of residual bond strain appears to be far more sensitive to the polymerisation rate. Variations in bond strain suggest different final polymeric conformations, likely the result of chain motions modified by the polymerisation rate, which may provide insight as to how similarly converted materials polymerised at different rates can demonstrate discrepancies in polymerisation shrinkage and stress development of these materials.

These results are applicable to a wide range of polymer composite materials, demonstrating how resin composition, filler morphology and cure rate impact on the final micro-structure of the material. This information bridges a fundamental gap in the understanding of composite systems, providing a valuable link between material composition and bulk properties.

## 6.6 References

1. Ruyter, I.E. and H. Oysaed, *Composites for use in posterior teeth: composition and conversion*. J Biomed Mater Res, 1987. **21**(1): p. 11-23.
2. Ferracane, J.L., *Current trends in dental composites*. Crit Rev Oral Biol Med, 1995. **6**(4): p. 302-18.
3. Stansbury, J.W. and S.H. Dickens, *Determination of double bond conversion in dental resins by near infrared spectroscopy*. Dental Materials, 2001. **17**(1): p. 71-79.
4. Cherfi, A., G. Fevotte, and C. Novat, *Robust on-line measurement of conversion and molecular weight using NIR spectroscopy during solution polymerization*. Journal of Applied Polymer Science, 2002. **85**(12): p. 2510-2520.
5. Ferracane, J.L. and E.H. Greener, *Fourier transform infrared analysis of degree of polymerization in unfilled resins--methods comparison*. J Dent Res, 1984. **63**(8): p. 1093-5.
6. Stansbury, J.W., et al., *Conversion-dependent shrinkage stress and strain in dental resins and composites*. Dental Materials, 2005. **21**(1): p. 56-67.
7. Palin, W.M., et al., *Monomer conversion versus flexure strength of a novel dental composite*. J Dent, 2003. **31**(5): p. 341-51.
8. Lovell, L.G., et al., *The effect of light intensity on double bond conversion and flexural strength of a model, unfilled dental resin*. Dental Materials, 2003. **19**(6): p. 458-465.
9. Sideridou, I.D. and D.S. Achilias, *Elution study of unreacted Bis-GMA, TEGDMA, UDMA, and Bis-EMA from light-cured dental resins and resin composites using HPLC*. Journal of Biomedical Materials Research Part B: Applied Biomaterials, 2005. **74B**(1): p. 617-626.
10. Price, R.B., et al., *Effect of light source and specimen thickness on the surface hardness of resin composite*. Am J Dent, 2002. **15**(1): p. 47-53.
11. Leprince, J.G., et al., *New insight into the "depth of cure" of dimethacrylate-based dental composites*. Dent Mater, 2012. **28**(5): p. 512-20.

12. Lim, B.-S., et al., *Effect of filler fraction and filler surface treatment on wear of microfilled composites*. Dental Materials, 2002. **18**(1): p. 1-11.
13. Turssi, C.P., J.L. Ferracane, and K. Vogel, *Filler features and their effects on wear and degree of conversion of particulate dental resin composites*. Biomaterials, 2005. **26**(24): p. 4932-4937.
14. Ferracane, J.L., *Resin composite--state of the art*. Dent Mater, 2011. **27**(1): p. 29-38.
15. Howard, B., et al., *Relationships between Conversion, Temperature and Optical Properties during Composite Photopolymerization*. Acta biomaterialia, 2010. **6**(6): p. 2053-2059.
16. Chen, Y.-C., J.L. Ferracane, and S.A. Pahl. *A dynamic Monte Carlo model for predicting radiant exposure distribution in dental composites: model development and verifications*. 2005.
17. Chen, Y.C., J.L. Ferracane, and S.A. Pahl, *A pilot study of a simple photon migration model for predicting depth of cure in dental composite*. Dent Mater, 2005. **21**(11): p. 1075-86.
18. Lovell, L.G., et al., *The effect of cure rate on the mechanical properties of dental resins*. Dental Materials, 2001. **17**(6): p. 504-511.
19. Susini, J., et al., *Technical Report: The FTIR Spectro-Microscopy End-Station at the ESRF-ID21 Beamline*. Synchrotron Radiation News, 2007. **20**(5): p. 13-16.
20. Nasse, M.J., et al., *High-resolution Fourier-transform infrared chemical imaging with multiple synchrotron beams*. Nat Meth, 2011. **8**(5): p. 413-416.
21. Beleites, C. and V. Sergo, *hyperSpec: a package to handle hyperspectral data sets in R*. 2016.
22. Ryu, S.R., I. Noda, and Y.M. Jung, *What is the origin of positional fluctuation of spectral features: true frequency shift or relative intensity changes of two overlapped bands?* Appl Spectrosc, 2010. **64**(9): p. 1017-21.
23. Salmén, L. and E. Bergström, *Cellulose structural arrangement in relation to spectral changes in tensile loading FTIR*. Cellulose, 2009. **16**(6): p. 975.

24. Ilie, N., R. Hickel, and D.C. Watts, *Spatial and cure-time distribution of dynamic-mechanical properties of a dimethacrylate nano-composite*. Dent Mater, 2009. **25**(3): p. 411-8.
25. Randolph, L.D., et al., *Photopolymerization of highly filled dimethacrylate-based composites using Type I or Type II photoinitiators and varying co-monomer ratios*. Dental Materials, 2016. **32**(2): p. 136-148.
26. Halvorson, R.H., R.L. Erickson, and C.L. Davidson, *The effect of filler and silane content on conversion of resin-based composite*. Dent Mater, 2003. **19**(4): p. 327-33.
27. Berriot, J., et al., *Filler–elastomer interaction in model filled rubbers, a 1H NMR study*. Journal of Non-Crystalline Solids, 2002. **307**(Supplement C): p. 719-724.
28. Beun, S., et al., *Rheological properties of experimental Bis-GMA/TEGDMA flowable resin composites with various macrofiller/microfiller ratio*. Dental Materials, 2009. **25**(2): p. 198-205.
29. Hadis, M., et al., *High irradiance curing and anomalies of exposure reciprocity law in resin-based materials*. J Dent, 2011. **39**(8): p. 549-57.
30. Harton, S.E., et al., *Immobilized Polymer Layers on Spherical Nanoparticles*. Macromolecules, 2010. **43**(7): p. 3415-3421.
31. Berriot, J., et al., *Evidence for the Shift of the Glass Transition near the Particles in Silica-Filled Elastomers*. Macromolecules, 2002. **35**(26): p. 9756-9762.
32. Cramer, N.B., J.W. Stansbury, and C.N. Bowman, *Recent Advances and Developments in Composite Dental Restorative Materials*. Journal of Dental Research, 2011. **90**(4): p. 402-416.
33. Fujita, K., et al., *Effect of base monomer's refractive index on curing depth and polymerization conversion of photo-cured resin composites*. Dent Mater J, 2005. **24**(3): p. 403-8.
34. Lovell, L.G., et al., *The effect of light intensity on double bond conversion and flexural strength of a model, unfilled dental resin*. Dent Mater, 2003. **19**(6): p. 458-65.

35. Kim, S. and J. Jang, *The measurement of degree of conversion for BIS-GMA/silica composites by FT-IR spectroscopy*. Polymer Testing, 1996. **15**(6): p. 559-571.
36. Venhoven, B.A.M., A.J. deGee, and C.L. Davidson, *Light initiation of dental resins: Dynamics of the polymerization*. Biomaterials, 1996. **17**(24): p. 2313-2318.
37. Dewaele, M., et al., *Volume contraction in photocured dental resins: the shrinkage-conversion relationship revisited*. Dent Mater, 2006. **22**(4): p. 359-65.
38. Braga, R.R. and J.L. Ferracane, *Contraction stress related to degree of conversion and reaction kinetics*. J Dent Res, 2002. **81**(2): p. 114-8.
39. Watts, D.C., *Reaction kinetics and mechanics in photo-polymerised networks*. Dental Materials, 2005. **21**(1): p. 27-35.
40. Kloosterboer, J.G. and G.F.C.M. Lijten, *Photopolymers exhibiting a large difference between glass transition and curing temperatures*. Polymer, 1990. **31**(1): p. 95-101.
41. Condon, J.R. and J.L. Ferracane, *Reduction of composite contraction stress through non-bonded microfiller particles*. Dental Materials, 1998. **14**(4): p. 256-260.
42. Sideridou, I., V. Tserki, and G. Papanastasiou, *Effect of chemical structure on degree of conversion in light-cured dimethacrylate-based dental resins*. Biomaterials, 2002. **23**(8): p. 1819-1829.
43. Ferracane, J.L. and E.H. Greener, *The effect of resin formulation on the degree of conversion and mechanical properties of dental restorative resins*. Journal of Biomedical Materials Research, 1986. **20**(1): p. 121-131.
44. Lovell, L.G., et al., *Effects of Composition and Reactivity on the Reaction Kinetics of Dimethacrylate/Dimethacrylate Copolymerizations*. Macromolecules, 1999. **32**(12): p. 3913-3921.
45. Miljkovic, M., B. Bird, and M. Diem, *Line shape distortion effects in infrared spectroscopy*. Analyst, 2012. **137**(17): p. 3954-3964.
46. Hirschmugl, C.J. and K.M. Gough, *Fourier Transform Infrared Spectrochemical Imaging: Review of Design and Applications with a Focal Plane Array and Multiple Beam Synchrotron Radiation Source*. Applied Spectroscopy, 2012. **66**(5): p. 475-491.



## **7 INTRA-CORONAL STRESS TRANSFER THROUGH ENAMEL FOLLOWING RBC PHOTO-POLYMERISATION**

### **7.1 Introduction**

Whilst it has been demonstrated that most dental resin based composite (RBC) materials exhibit a volumetric shrinkage associated with polymerisation leading to the generation of shrinkage stresses, it is still debated as to whether these stresses affect restoration longevity. The stresses generated during photo-polymerisation of dental RBCs have been directly measured in *in-vitro* experiments and have identified that the magnitude and development of shrinkage stresses are dependent on factors including; RBC composition/resin chemistry [1, 2], photo-polymerisation variables [3-5] and the terminal degree of monomer to polymer conversion [6-8]. It has been proposed that both the magnitude of the shrinkage stress, and the kinetics of its development, are important factors in determining whether shrinkage stresses have an unfavourable impact on the remaining tooth tissue or the adhesive interface between the RBC and enamel and dentine. Stress transfer to the adhered tooth complex has been directly demonstrated using cuspal deflection methods and indirectly indicated through micro-leakage measurements [9-14] which are proposed to reflect interfacial debonding that has occurred as a stress relief mechanism [15-18]. Shrinkage stresses arise because the volumetric free shrinkage of the polymer matrix of RBCs that occurs during polymerisation is constrained by the geometrical confines of the substrate to which it is adhered [19-21]. It is accepted that the magnitude of stress generated is influenced by the monomer composition [1, 5, 22, 23], the polymerisation rate [24-28], the stiffness of the polymerised cross-linked matrix and the nature of the external constraints [29-34], which can also be considered as the compliance of the system [35, 36]. Of these factors, the effects of resin-matrix monomer composition, polymerisation kinetics and subsequent mechanical properties of the polymer composite including its adhesion to the tooth substrate have arguably been disproportionately studied, when compared with understanding the stress transfer to the tooth and stress relief within the tooth-restoration complex.

The tooth is a structure comprised of a highly mineralised (94-96 wt% hydroxyapatite [37, 38]) thin surface layer of enamel which is supported by a relatively compliant, less mineralised dentine substrate [39]. At the interface, adhesion between enamel and dentine is manifested by a hierarchically scalloped topology and a relatively protein rich organic matrix [40-43]. Enamel and dentine and their interface are subjected to extreme cyclic mechanical and thermal stresses however, show remarkable resistance to mechanical failure [44, 45]. Notably enamel has no cellular mediated capacity for repair but it is proposed that its hierarchical structure provides an inherent ability for stress relief conferring a damage tolerance that enables it to survive for the lifespan of the host [46, 47]. Enamel structure is comprised of nanoscale hydroxyapatite crystallite plates which are specifically orientated to form microscale 'keyhole shaped' prisms [38, 39, 48, 49], that are separated from each other by protein rich interfaces [50-52]. Both hydroxyapatite crystallites and enamel prisms have distinct orientations that are a function of their location [53-55]. As a bulk material, enamel is anisotropic with respect to its elastic modulus [56], exhibits a high fracture toughness [57] and has been shown to exhibit time dependent deformation as a response to applied stress. Using nano-indentation methods it has been shown that the creep behaviour of enamel was more similar to metallic materials than to its hydroxyapatite constituent [38]. These responses were attributed to the organic protein content between hydroxyapatite crystals which permitted both inelastic deformation and subsequent partial recovery of the deformation [58, 59].

The capacity for stress relief within the enamel structure may go some way to explaining the inconsistency in data generated from the cuspal deflection method [27, 28, 60-63] using natural teeth. Cuspal deflection tests typically require a large mesio-occlusal-distal (MOD) cavity to be prepared in a tooth and the distance between the points of maximum convexity of the facial and lingual surfaces are recorded dynamically during RBC placement and photo-polymerisation [32-34, 36, 64]. The magnitude of the decrease in inter-cuspal distance is used as a surrogate outcome of the net shrinkage stress generated and distributed within the RBC-tooth complex. Such measurements cannot discriminate the vector and location of stress generation and indeed

any stress relief that occurs, either with the tooth, the RBC or the interface between materials. A number of cuspal deflection studies have failed to show differences between variables which were strongly assumed to generate different magnitudes of shrinkage stress [62, 63].

The aim of this study was for the first time to empirically measure stresses within the enamel that had been induced by the polymerisation of dental RBCs. Using two-dimensional synchrotron X-ray diffraction (2D-SXRD) it is possible to measure lattice strain by observing the changes in lattice parameters of the crystalline phase (hydroxyapatite). The specific objective was to quantify spatially the distribution of strain generated in the hydroxyapatite lattice of human dental enamel. Photo-polymerisation of a single RBC material was induced using two different irradiances to generate differences in the kinetics of shrinkage stress generation [7, 65].

## 7.2 Materials and Methods

### 7.2.1 Sample Preparation

Unrestored human maxillary first premolars of similar size and morphology, previously extracted for orthodontic purposes, were selected from a biorepository (UK ethical approval, NRES-14/EM/2811, University of Birmingham, UK). Teeth were inspected using light microscopy and included if they were caries free, exhibited no enamel cracks or other defects and had buccal palatal widths of  $8.5 \pm 0.1$  mm measured with a digital micrometer. MOD cavities were cut using an air turbine with a pattern 541 diamond bur (MDT technologies, Israel) under copious water irrigation according to the protocol first described by Fleming *et al* [12]. Briefly, the proximal boxes were prepared to extend vertically to 1 mm above the cemento enamel junction (CEJ) with a width of two thirds of the buccal palatal width (BPW). The occlusal isthmus dimensions were standardised with a 3.5 mm depth relative to the palatal cusp and a width of half the BPW.

To provide a standardised thickness of facial enamel for micro-focussed X-ray diffraction measurements, the buccal enamel surface of each tooth was further machined using an air turbine with a 541 pattern diamond bur under water irrigation. Using an operating microscope, the enamel was machined at the point of maximum convexity to create a vertical ‘fin’ of 0.5 mm depth and 100  $\mu\text{m}$  thickness (measured using a digital micrometer). Tooth samples were prepared and restored by Professor Owen Addison, University of Alberta, Canada. Teeth were stored in moist conditions at  $4 \pm 1^\circ\text{C}$  prior to further use.

### 7.2.2 Synchrotron X-ray Diffraction Mapping

Synchrotron X-ray diffraction (SXRD) measurements were carried out on the B16 beamline [66] at the Diamond Light Source (Oxford Harwell Campus, Didcot, UK). An incident X-ray energy of 20 keV was used, equivalent to a wavelength ( $\lambda$ ) of 0.6212 Å, with a beam size of 100  $\mu\text{m}$   $\times$  100  $\mu\text{m}$  defined using collimation slits. Samples were mounted normal to the

impinging X-rays in transmission geometry onto a travelling x-y sample stage to allow measurements in two orthogonal directions perpendicular to the X-ray beam. A single SXRD measurement had an exposure time of 180 s and was collected using a 2D area detector (Image Star 9000, Photonic Science Ltd. UK) [67] with a  $3056 \times 3056$  pixel resolution ( $31 \times 31 \mu\text{m}$  optical pixel size) [67], placed 155 mm behind the sample to give a  $2\theta$  range of  $5\text{-}25^\circ$ . Instrument parameters including the X-ray wavelength and experimental geometry were accurately determined by calibrating using lanthanum hexaboride ( $\text{LaB}_6$ ) (Sigma Aldrich, Dorset, UK) standard samples.

Due to the precision required for repeat measurements of the identical areas of enamel before and after photo-polymerisation, the MOD cavities were bulk-filled with RBC in dark conditions. A commercial composite resin (Z100™ MP Universal Composite, 3M ESPE, MN, USA) based on bisphenol-A-glycidyl-methacrylate (Bis-GMA) and triethyleneglycol-dimethacrylate (TEGDMA) monomers and utilising a camphorquinone / tertiary amine photo-initiator system, was used. The RBC was shielded from light with aluminium foil prior to the tooth being mounted rigidly on an x-y stage. SXRD measurements were taken from the top to the bottom of each tooth fin in successive tracks, starting closest to the cavity wall with up to four tracks used to spatially characterise crystallographic changes. The vertical step size between SXRD measurements along the same track was 0.2 mm, whilst adjacent tracks were separated horizontally by 0.1 mm. Due to the time constrictions of using a synchrotron source only two of the six tooth specimens were mapped over a larger area consisting of four tracks (Figure 7.1a), whilst the remaining samples were mapped with a single track (Figure 7.1b). Larger area maps were sacrificed to gain repeat measurements for statistical analysis. All measurements were conducted in dark conditions at  $23 \pm 1^\circ\text{C}$ .

Following initial mapping of the unstrained tooth specimen, the aluminium shielding was removed and any minor slumping of the RBC material at the mesial and distal boxes was corrected using gentle manual adjustments. Two light curing units (LCUs) providing relative high and low light intensities were used for photo-polymerisation to induce relatively fast and

slower rates of polymerisation, respectively. To provide a relatively high irradiance, the RBC was illuminated using an LED LCU (Elipar S10, 3M ESPE, MN, USA) with an intensity of  $1200 \text{ mWcm}^{-2}$  over a spectral emission range of 430 - 480 nm. To produce a lower irradiance, a quartz tungsten halogen LCU (Optilux 501, Kerr dental, CA, USA) with an intensity of  $480 \text{ mWcm}^{-2}$  over a spectral emission range of 400 - 505 nm was used. An 11 mm light guide was used for both LCUs. For both LCUs the RBC was illuminated for 60 s from the occlusal surface at a distance of 2 mm followed by a 20 s exposure each on the mesial and distal aspects from 0 mm.

Following a standardised time of 30 min after polymerisation, to allow for post-cure effects, SXRD measurements were repeated across the same track positions under identical conditions as previously described. The process of initial map measurement, resin application/polymerisation and re-mapping was repeated three times per photo-polymerisation regimen on separate (unstrained) tooth specimens generating measurements for a total of 6 teeth with three teeth per curing protocol. Repeat measurements allowed for the spatial verification of relative changes in the crystallographic structure and statistical analysis for relevant lattice parameters for each curing regimen.

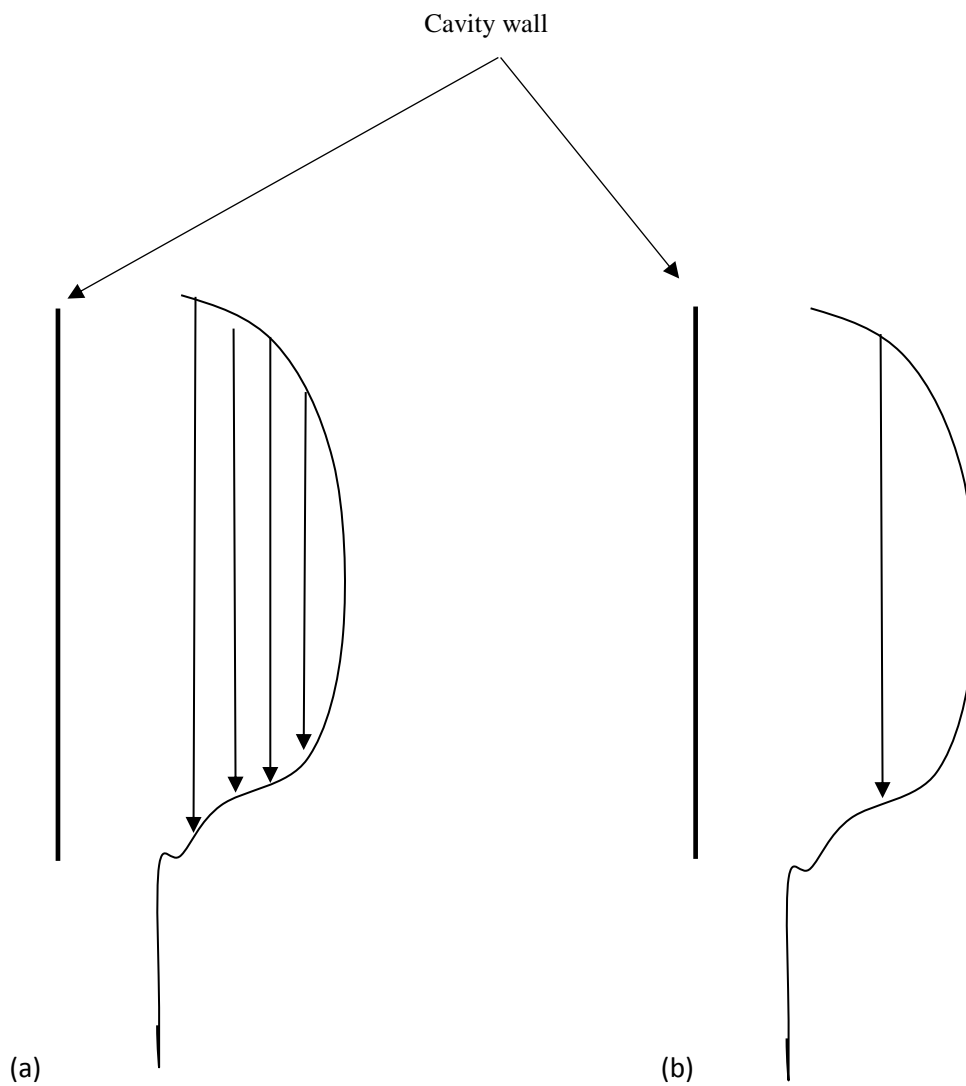


**Figure 7.1.** (a) Schematic of a tooth fin section showing the regions mapped by successive SXR line scan measurements. (b) A single line scan measurement used to acquire sufficient statistics for each polymerisation regime. The solid black line represents the boundary of the cavity wall.

### 7.2.3 Data Processing and Analysis

Two-dimensional diffraction images were processed using the ESRF software package Fit2D (version 12.077, ESRF) [68]. Diffraction patterns were azimuthally integrated to produce 1D spectra of intensity ( $I$ ) versus the scattering angle ( $2\theta$ ). The Bragg peaks corresponding to the (002) ( $\sim 10^\circ$ ) and (300) ( $\sim 13^\circ$ ) reflections were fitted with pseudo-Voigt peak shapes to obtain the peak position and the full width at half maximum (FWHM) to quantify possible changes to the crystal structure from the lattice parameters. The (002) and (300) planes were used to measure relative changes in the lattice parameters as they are normal to the  $c$  and  $a$  axis of the hydroxyapatite unit cell respectively. Peak positions were used to determine the inter-planar spacing ( $d$ ), where  $d = \lambda/2\sin\theta$ , from which lattice parameters were calculated. A hexagonal unit cell was assumed for hydroxyapatite, where the relationship between the  $d$  spacing and Miller indices for a given Bragg peak and lattice parameters are given as;

$$\frac{1}{d^2} = \frac{4}{3} \left( \frac{h^2 + hk + k^2}{a^2} \right) + \frac{l^2}{c^2} \quad (7.1)$$

where  $h, k$  and  $l$  refer to the Miller indices for a particular Bragg peak whilst  $a$  and  $c$  represent the relevant lattice parameters. Substituting the (002) and (300) indices into equation (7.1) gives the individual  $c$  and  $a$  lattice parameters respectively as a function of  $d$ .

$$c = 2d \quad (7.2)$$

$$a = \sqrt{12}d \quad (7.3)$$

Therefore, any crystallographic strain generated in the tooth associated with RBC photopolymerisation was calculated by precisely measuring changes in the  $c$  and  $a$  lattice parameters before and after photo-curing. Lattice strain ( $\zeta$ ) was calculated for every SXRD measurement

point along each track to produce strain maps, where the lattice strain was given as the percentage change in the lattice parameters, as shown in equation (7.4)

$$\xi = \left( \frac{P_{after} - P_{before}}{P_{before}} \right) \times 100 \quad (7.4).$$

Here  $P_{before}$  and  $P_{after}$  refer to the value of a given lattice parameter as measured at each point before and after the polymerisation of the resin composite. Values for strain were averaged over whole maps to ascertain statistically significant differences in strain between the two photopolymerisation regimes. A paired t-test was used to test for statistical significance at  $\alpha=0.001$ . All calculations were performed using R programming (version 3.1.3, 2015, R Foundation).

Texture parameters, including the direction and magnitude of the preferred orientation were obtained by integrating the intensity around the Debye ring of the (002) Bragg reflection over  $360^\circ$  and plotted against the azimuthal angle. Preferred orientation was determined as this reflection is perpendicular to the  $c$  axis of the hydroxyapatite unit cell. Peaks were fitted with a Gaussian shape to calculate the deviation angle  $\varphi$  of the crystallite axis with respect to the vertical axis and to also obtain the full width at half maximum (FWHM).

## 7.3 Results

### 7.3.1 XRD and Orientation

Figure 7.2 shows synchrotron X-ray diffraction (SXR) results for tooth specimens represented by 2D diffraction patterns collected on an area detector (Figure 7.2a and 7.2b) and an azimuthally integrated plot showing characteristic diffraction peaks typical of hydroxyapatite. The main indices ( $h k l$ ) used for the study of crystallographic strain were the (002) and (300) reflection planes/diffraction rings which are annotated in in Figure 7.2c. It can be seen in Figure 7.2a that the intensity of the (002) Debye ring varies as a function of the azimuthal angle, where  $0^\circ$  is defined as east on the detector face and increments positively in an anti-clockwise direction, which is indicative of texture and preferred orientation effects within the hydroxyapatite phase of the tooth (enamel). The strongest texture was found in the (002) diffraction ring. Figure 7.2a is annotated with a line at the zero degree position, to indicate the direction of preferred for hydroxyapatite crystals as shown by the maximum of the intensity variation of the diffraction ring. In comparison, Figure 7.2b shows a complete (002) diffraction ring, demonstrating little or negligible texture and no discernible direction of preferred orientation. The 1D diffraction spectra for a single measurement is shown in Figure 7.1c. The peaks located at  $\sim 10^\circ$  and  $\sim 13^\circ$  correspond to the (002) and (300) reflections respectively. Similarly, the relatively large intensity of the (002) illustrates the effects of texture on the diffraction pattern.

Hydroxyapatite that is present in teeth has been shown to exist in the form of polycrystalline hexagonal nanorods which grow in length parallel to the direction of the  $c$  axis [53] of the crystallographic unit cell. The direction of growth of these nanorods in the enamel of the tooth fin area can therefore be determined from the (002) diffraction ring. It can be seen from the 2D diffraction images that the intensity of the (002) reflection is greatest approximately perpendicular to the cavity wall, i.e. the  $c$  axis is oriented in this direction (Figure 7.3a, red markers). Assuming a hexagonal unit cell the  $a=b$  axis will therefore run perpendicular to the  $c$

axis and parallel to the cavity wall. However, azimuthal integration of the (002) partial diffraction ring yields an unexpected bimodal distribution (Figure 3b) for each intensity arc, with high and low peaks, in relation to the cavity wall, located at  $\sim 210$  and  $170^\circ$  respectively. This distribution of crystallite orientation was present in all tooth samples prior to polymerisation and remains unaltered by the photo-polymerisation of an RBC. The direction of orientation for each distribution is obtained by the deconvolution of the peaks with a pseudo-Voigt profile, whilst the integrated peak intensity gives the proportion of crystallites and or enamel prisms belonging to each distribution. Typically, 75-90% of the crystallites (75–90 % of the total integrated peak intensities) display a preferred orientation, along the crystallographic c axis, at a low angle ( $\sim 170^\circ$ ) direction almost normal to the cavity wall, however this varies spatially within each sample. Additionally, the high angle orientation distribution tends to display a significantly narrower FWHM in comparison to the low angle peak. This indicates greater relative texture in a given direction i.e. there is less variation in the orientation of the sampled crystallites. The spatial distribution of the direction for preferred orientation is described in section 7.3.3 alongside the additional results for crystallographic strain for the purpose of clarity.

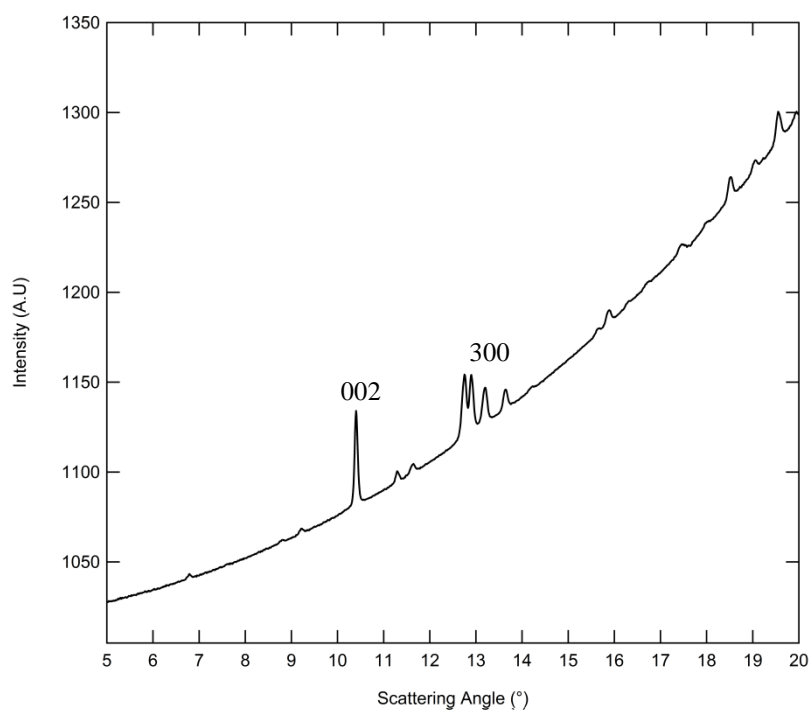
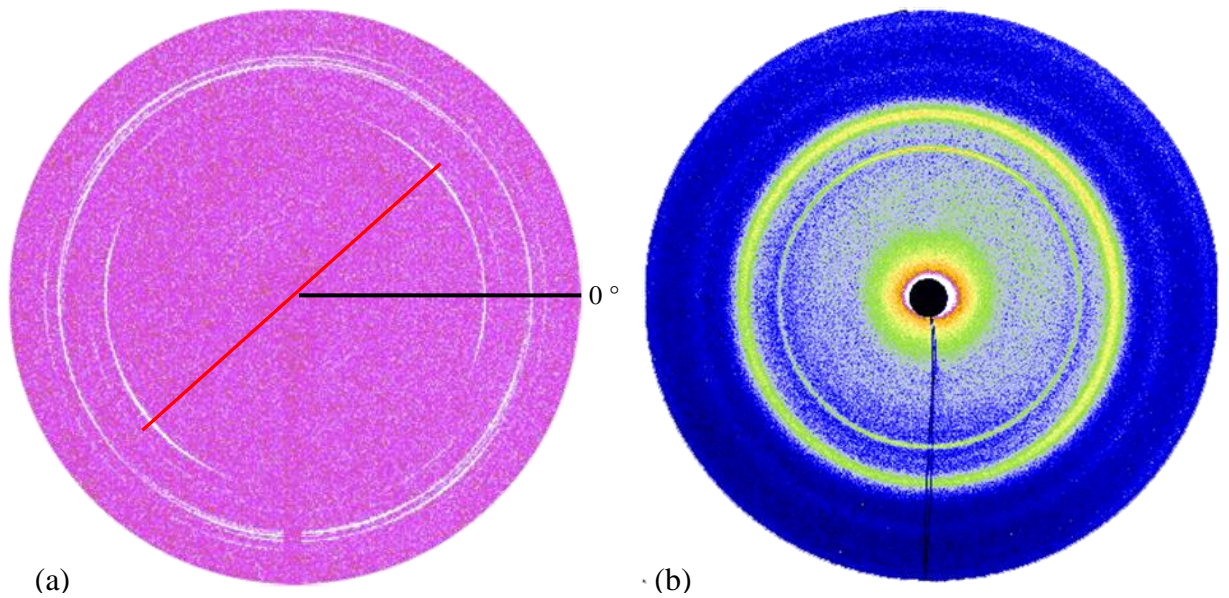
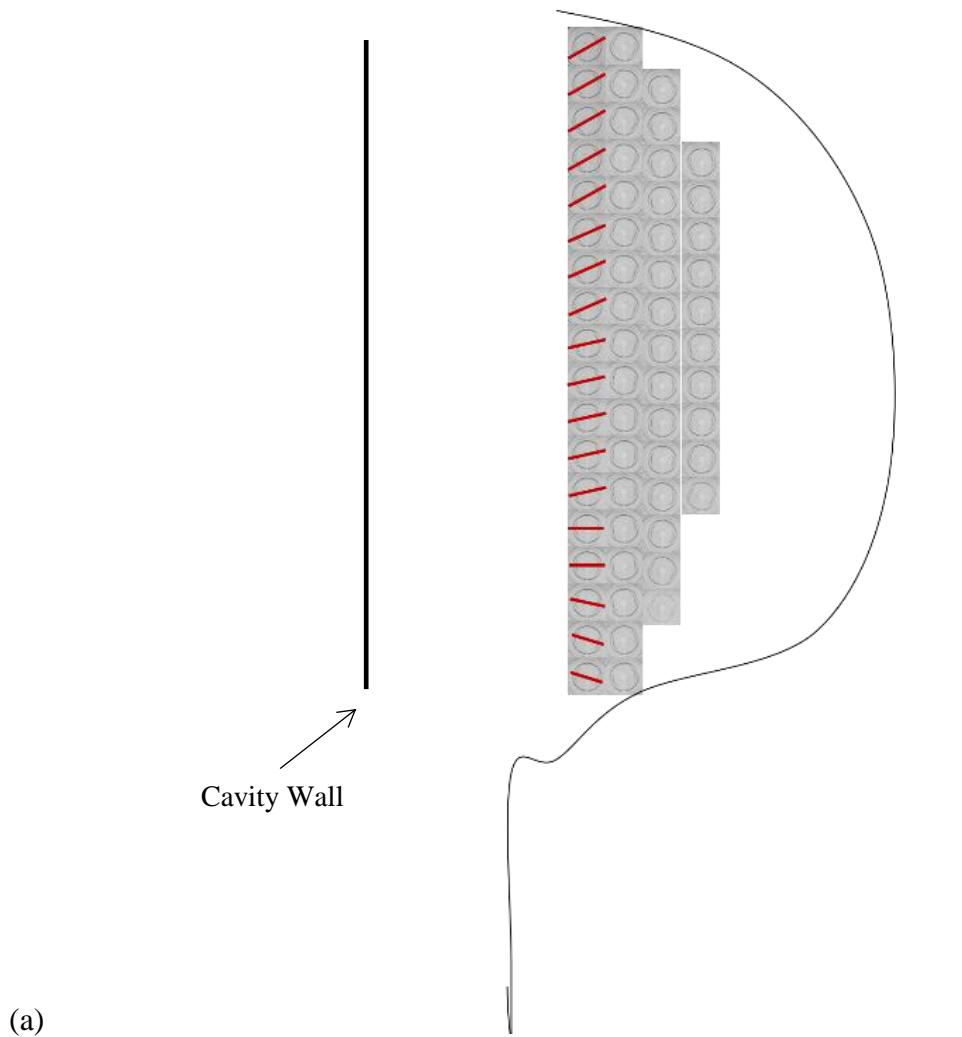
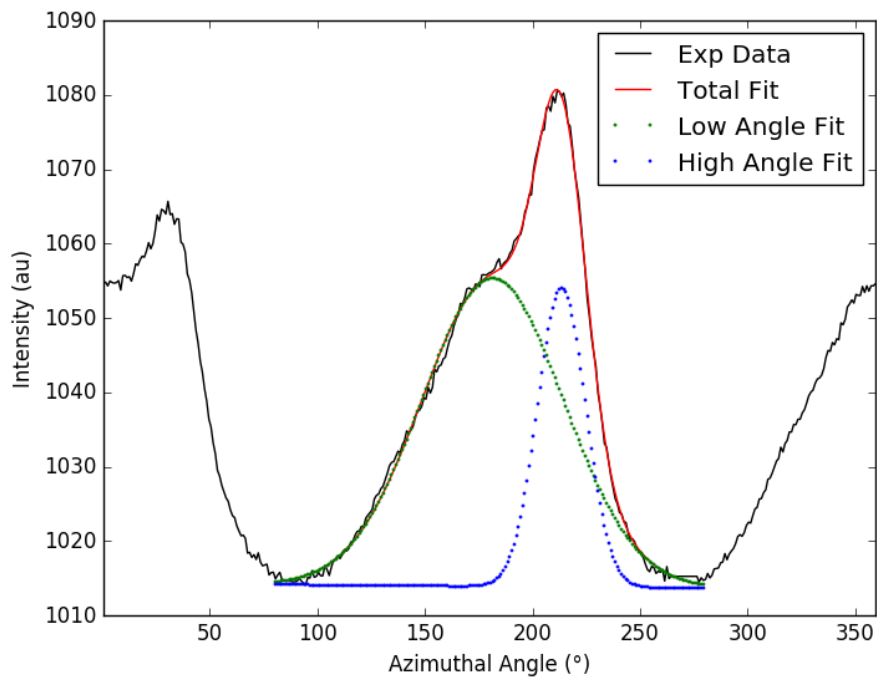


**Figure 7.2.** (a) Variation in intensity of the (002) diffraction ring is indicative of texture, whilst (b) a complete ring demonstrates little or no texture. Preferred orientation is defined from  $0^\circ$  which points east on the detector face, increasing azimuthally in the counter-clockwise direction. (c) A 1-D diffraction spectra with the (002) and (300) reflections corresponding to peaks located at  $\sim 10^\circ$  and  $\sim 14^\circ$  respectively.



(a)



(b)

**Figure 7.3.** (a) A composite image showing individual 2-D diffraction spectra, for each measurement along a track, superimposed on to a schematic of a tooth fin. Bisection of the (002) diffraction ring through points of greatest intensity yields the approximate direction of preferred orientation, which is shown as a red line. (b) Azimuthal integration of the (002) diffraction ring shows that two directions of crystallite/prismatic orientation exist within the tooth enamel.

## 7.3.2 Crystallographic Strain

### 7.3.2.1 c Axis Strain

Figure 7.4 illustrates the typical spatial distribution of the  $c$  lattice parameter calculated using equation (7.2), depicted as pseudo-colour maps, over the scanned region of a given tooth ‘fin’ before and after the application of RBC for relatively fast and slow polymerisation rates. Prior to RBC application the unstrained tooth samples have average  $c$  lattice parameters of  $6.9120 \pm 0.0110 \text{ \AA}$  and  $6.8546 \pm 0.0091 \text{ \AA}$  for the test specimens subjected to high and low irradiances, respectively. Variation of the  $c$  lattice parameter is relatively small at shorter length scales of  $\sim 0.6 \text{ mm}$  however, the spatial distribution of  $c$  axis lengths is quite different for each tooth with respect to location relative to the cavity wall. For the enamel subjected to high irradiance, the magnitude of  $c$  was greater closer to the cavity wall, but decreases towards the taper of the measurement ‘fin’. For the slow polymerisation tooth specimen, a gradient exists in the  $c$  axis from the top to the bottom of the ‘fin’ section.

Figures 7.4b and 7.4e display maps of the  $c$  lattice parameter after the application and polymerisation of the RBC to the cavity for each polymerisation regime. The spatial distribution for the  $c$  lattice parameter in comparison with the unstrained case for both curing protocols appears similar, however the  $c$  axis length shows a clear change which is present in both maps. Figures 7.4c and 7.4f show the average percentage change in the  $c$  lattice parameter or crystallographic strain within the unit cell per measurement following polymerisation. It can be seen that when the composite is polymerised using the highest irradiance that strain in the  $c$  lattice axis is approximately 2-5 times greater in comparison to the ‘slower curing’ regimen. This was consistent with corresponding tracks in other tooth samples, for repeat measurements of each condition (Table 7.1). It must be acknowledged however, that strain measured for the slow polymerisation protocol is practically negligible, having an average value close to zero (Figure 7.5) whilst spatial variations in strain fall within the standard deviation of the measurements (Table 7.1). Regarding the spatial distribution of strain, it is reasonably homogenous at length scales of  $\sim 0.5 \text{ mm}$ , although a gradient exists between the top and bottom

of the tooth fin for both conditions. Strain is typically greater towards the bottom of the fin, parallel to the bottom of the cavity (the closed end of the cavity) and decreases towards the top (the open end of the cavity) for both polymerisation conditions (Figure 7.4c and 7.4f). Strain at the bottom of the fin is approximately 40 % and 30 % greater in comparison to the top, for the slow and fast polymerisation regimes respectively.

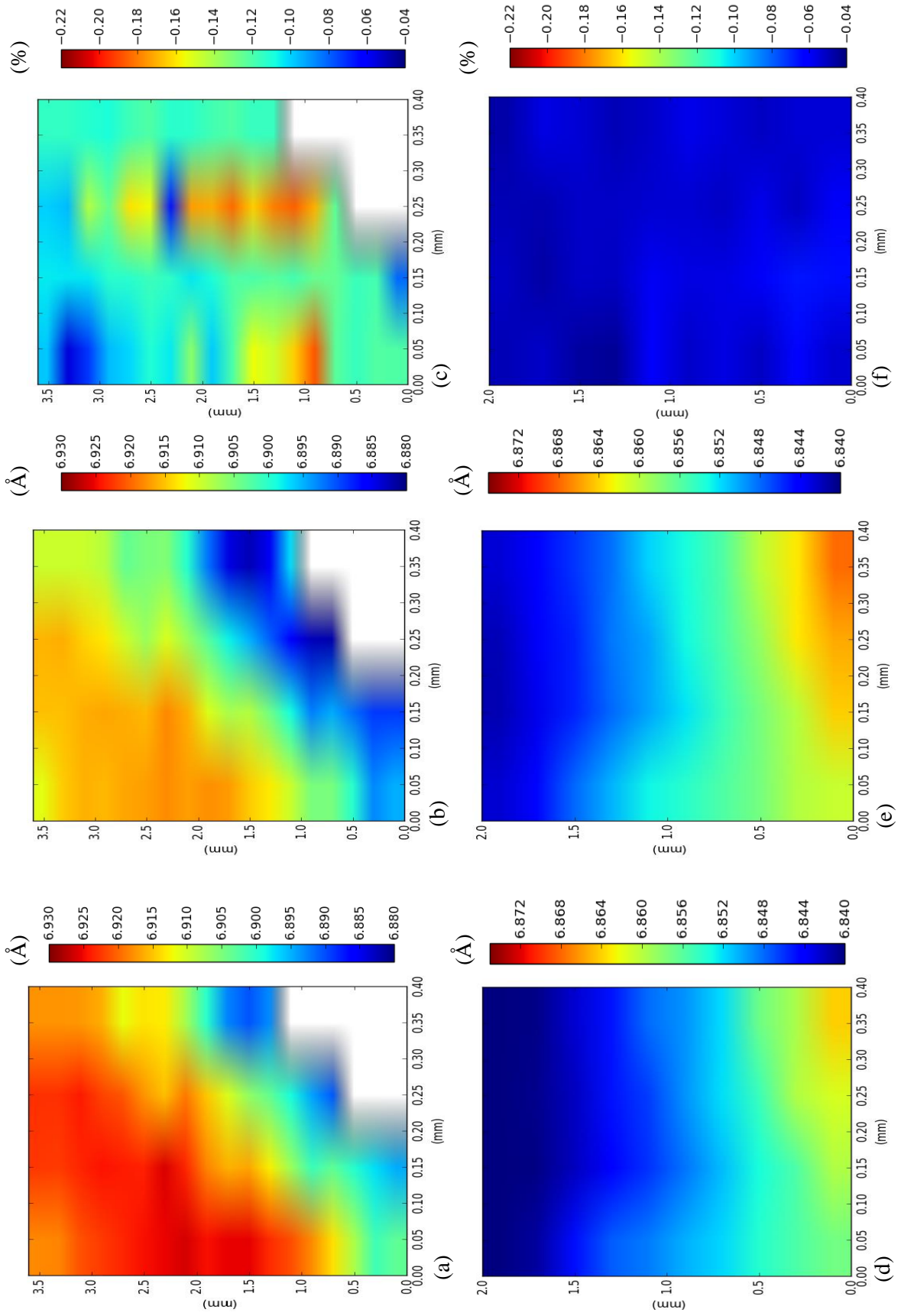


**Figure 7.4.** Contour maps for the  $c$ -lattice parameter for LED and QTH curing. (a) LED before (b) LED after (c) LED % strain; (d) QTH before (e) QTH after (f) QTH % strain. The cavity wall is located to the left of each map.

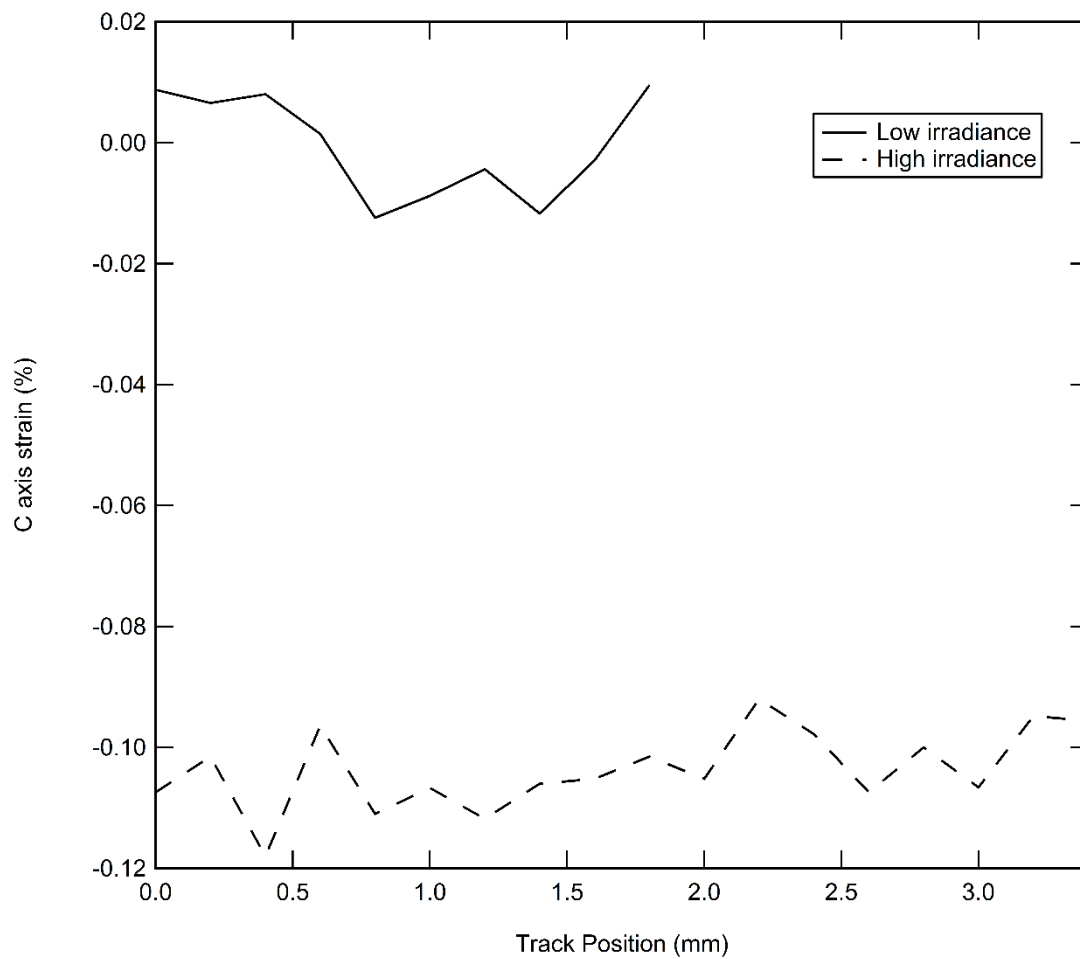


**Figure 7.5.** The percentage change in the *c* axis length, following the application of an RBC, is shown as a function of the measurement position along (here the top of the track position starts at 0 mm) the respective track for fast (broken line) or slow (solid line) polymerisation regimes.

### 7.3.2.2 a Axis strain

Figure 7.6 displays changes in the *a* lattice parameter, for the same specimens as shown in Figure 7.4, before and after polymerisation of the composite for relatively fast and slow curing regimes. The distribution of the *a* lattice parameter lengths in the unstrained enamel are very similar to that observed for the *c* axis with a gradient existing from left to right and top to bottom for the fast and slow curing regimes respectively. In the unstrained tooth ‘fins’ the average value of the *a* lattice parameter is  $9.1398 \pm 0.0036$  Å (high irradiance) and  $9.0755 \pm 0.0062$  Å (low irradiance). The distribution remains similar following the application of the RBC as seen in Figures 6b and 6e, but has decreased over the fin. Average lattice parameter values following polymerisation were  $9.1301 \pm 0.0034$  Å for the fast regime and  $9.0757 \pm 0.0063$  Å for slower curing. It can be seen in Figure 6c and 6f that faster polymerisation rates confer greater strain in the *a* lattice parameter. The average strains are given as -0.1063 % and -0.00186 % for the fast and slow maps respectively, which is consistent with repeat measurements (Table 1). A comparison of the mean strains for each polymerisation regime (Table 1) demonstrates a statistically significant difference in strain as a function of relative differences in reaction rate ( $p < 0.01$ ). The distribution of strain in the *a* axis appears to be more random in comparison with the *c* axis strains and accelerating polymerisation of the RBC seems to exacerbate this heterogeneity (Figure 7.6 c and f).

**Table 7.1.** Strains in the *c* and *a* axis for high and low irradiance curing protocols. Here the standard deviation is quoted with the value of strain.

|   | <i>c</i> axis strain (%) | <i>a</i> axis strain (%) |
|---|--------------------------|--------------------------|
| <b>High Irradiance (LED light source)</b>           | $-0.12 \pm 0.03$         | $-0.104 \pm 0.005$       |
| <b>Low Irradiance (Quartz halogen light source)</b> | $-0.053 \pm 0.006$       | $0.002 \pm 0.006$        |

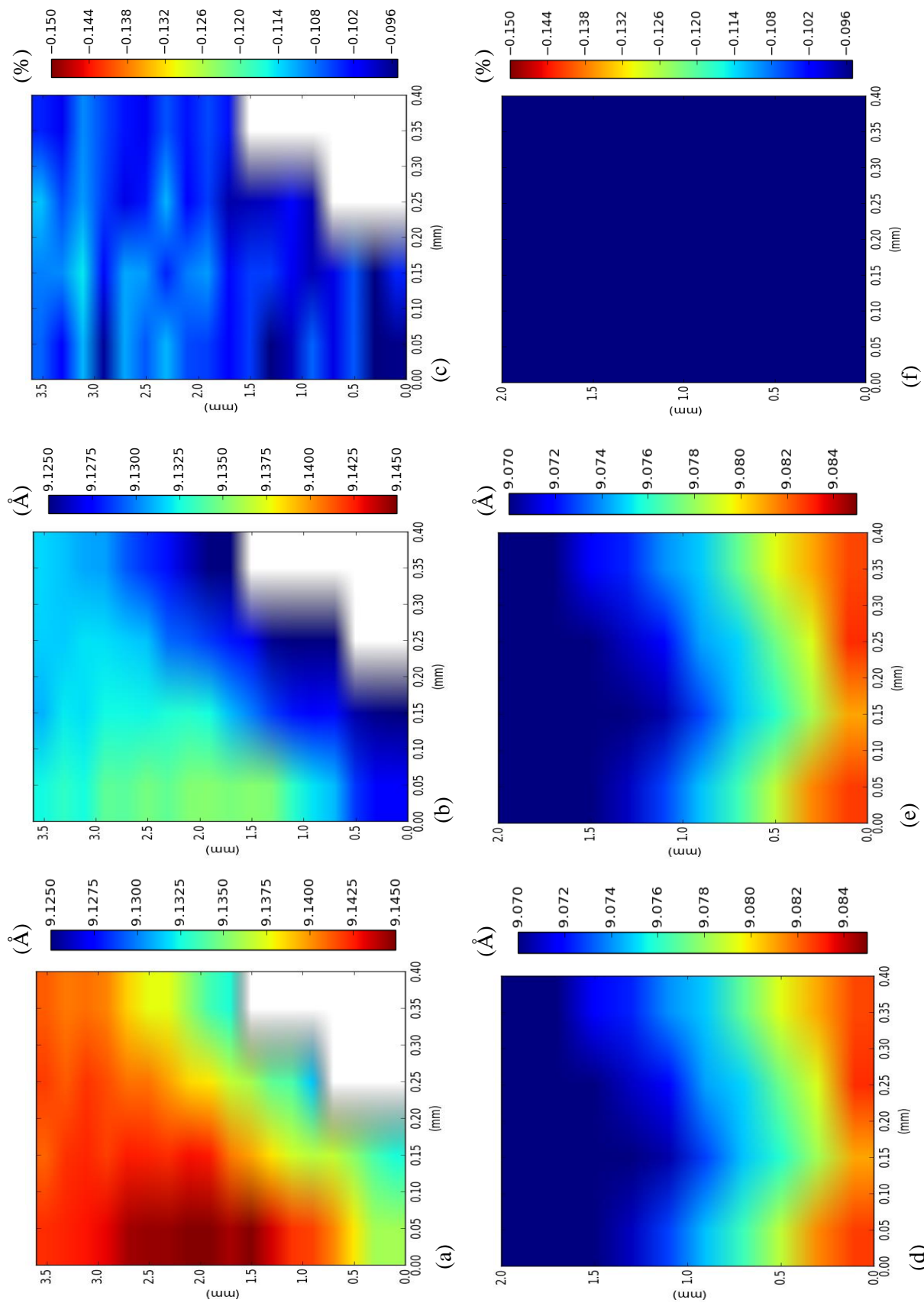


**Figure 7.6.** Contour maps for the  $a$ -lattice parameter for LED and QH curing; **(a)** LED before **(b)** LED after **(c)** LED % strain; **(d)** QH before **(e)** QH after **(f)** QH % strain. The cavity wall is located to the left of each map.

### 7.3.3 Impact of Crystallite Orientation on Resultant Strain

#### 7.3.3.1 *c* Axis Orientation

Azimuthal integration of the (002) diffraction ring revealed a bimodal distribution with respect to crystallite orientation (Figure 3b) with preferred directions about 170 and 210 ° in the azimuthal plane. This analysis was performed on the SXR images prior to and post polymerisation to ascertain any effects that RBC polymerisation had on crystallite orientation.

Figure 7.7 shows the change in the azimuthal angle for the low (blue) and high (red) crystallite orientations post-polymerisation. The average change in angular orientation following composite adhesion are 0.036 and 0.1° for the low and high azimuth orientations respectively, with rare outliers of  $\Delta\theta = 4.5^\circ$ . Changes in orientation appear to show no significant correlation with strain in the *c* axis along individual measurement tracks, with Pearson correlation coefficients of  $r = 0.210$  and  $r = -0.038$  for the low and high crystallite orientations. Figure 8 illustrates the spatial relationship between the bimodal orientation of the hydroxyapatite crystallites obtained from the azimuthal integration of the (002) diffraction ring with respect to the *c* axis strain distribution in the tooth fin. The peak positions obtained from the azimuthal integration represent the direction of the high and low orientations are plotted as red and blue bars respectively. The direction parallel to the long axis of these bars corresponds to the angular orientation of the *c* lattice parameter (obtained from the intensity variations in the (002) diffraction ring) where 0 ° is defined as pointing east on a clock-face with the angular increment increasing counter-clockwise. A horizontal bar therefore corresponds to directions of 0 and 180° (due to symmetry) whilst a vertical bar represents 90 and 270°. The length of the bar indicates the proportion of crystallites belonging to each directional distribution. Bar lengths are scaled to the integrated intensity of the respective peak and normalised to unity by the total integrated intensity. Orientation bars are superimposed on top of the strain pseudo-colour map and the aspect ratio of the image has been altered for clarity (Figure 7.8a).

It can be seen that regions of high strain in the *c* axis correspond to a relatively high proportion of hydroxyapatite crystallites/enamel prisms in the low angle (170°, perpendicular to the cavity

wall) distribution. At the top of the ‘fin’ where the strain is lowest ( $\sim -0.0968\%$ ), approximately 75% of the hydroxyapatite crystallites belong to the low angle distribution whilst the remaining 15% belong to the high angle distribution ( $\sim 210^\circ$ ). In comparison, at the bottom of the ‘fin’  $\sim 90\%$  of the crystallites are found in the low angle distribution which corresponds to the greatest magnitude of strain ( $\sim -0.22\%$ ). This correlation is better visualised via a vertical line transect taken through the first column of data in this map and plotted with the *c* axis strain as a function of track position (from top to bottom of the tooth ‘fin’), with the percentage of crystallites found in the low angle distribution plotted on the second y axis (Figure 7.8b). Figure 7.8b demonstrates that *c* axis strain increases with the percentage of crystallites oriented about the horizontal, showing a strong correlation of  $r = 0.85$ .

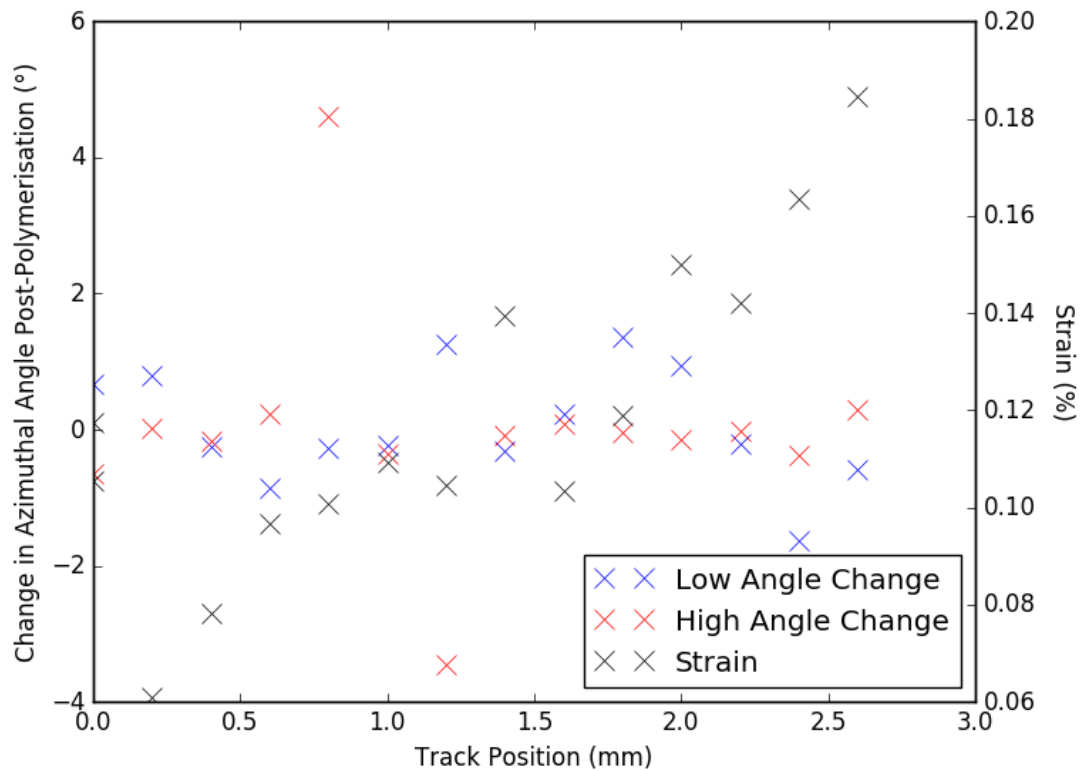


**Figure 7.7.** Changes in crystallite orientation angle post polymerisation for high irradiance curing, for the low (black solid line) and high (black broken line) angle directions, plotted as a function of track position with strain in the *c* lattice overlaid (red line). Track position is defined as 0 mm equal to the top of the tooth fin track and 2.4 mm representing the bottom of the fin.

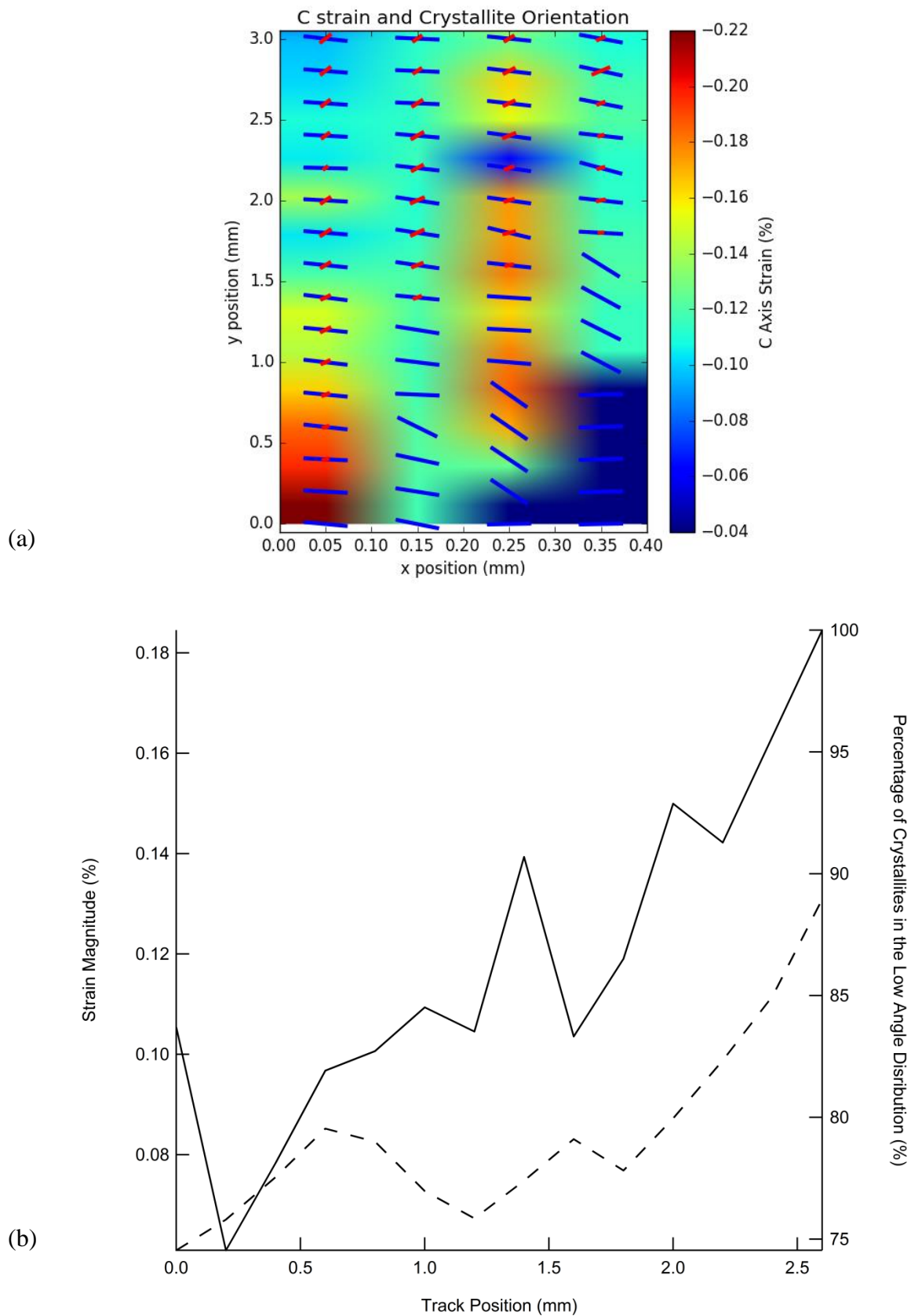
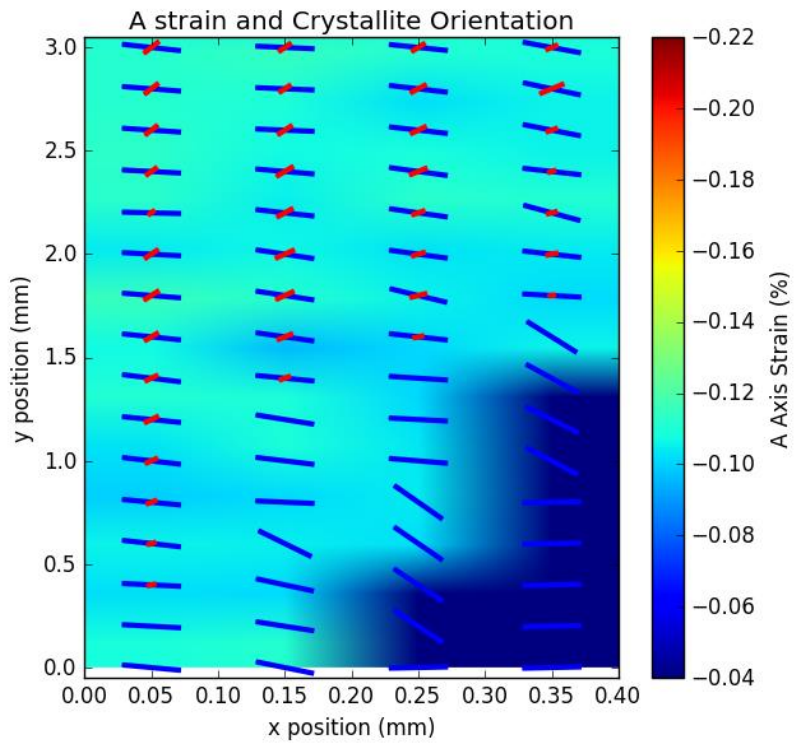


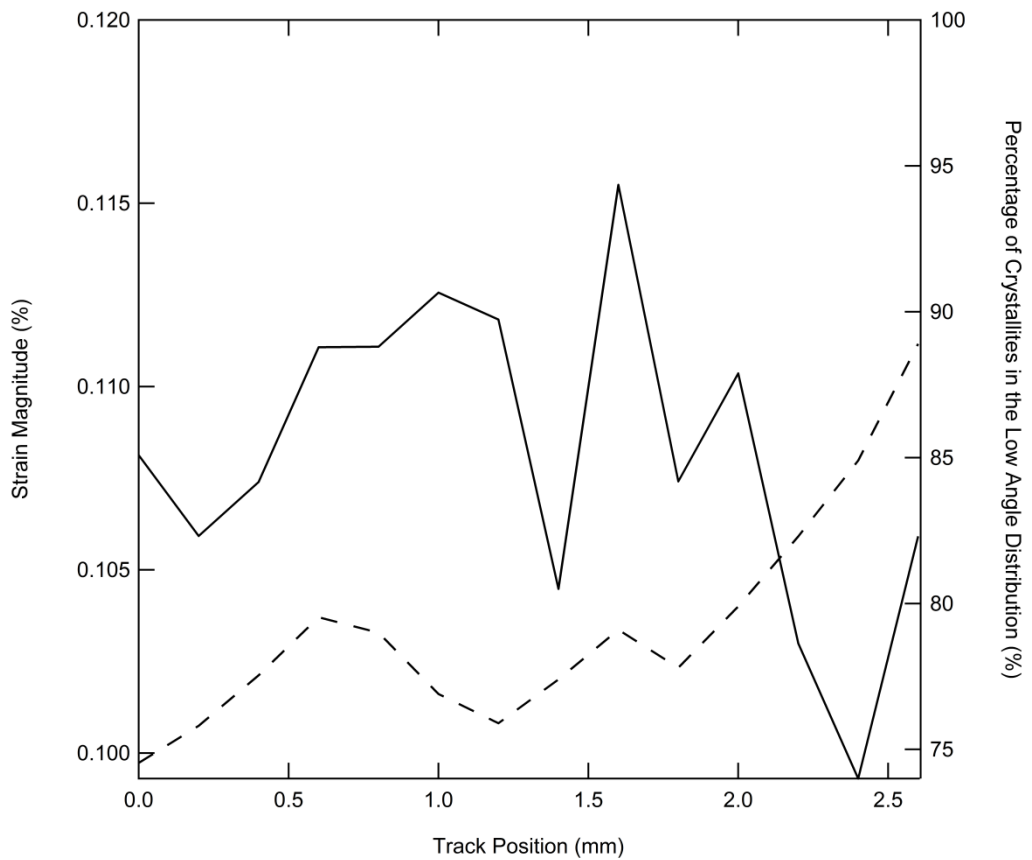
**Figure 7.8.** (a) Relative proportions of two crystallite orientations, red and blue bars, overlaid on to strain data. The aspect ratio has been altered, blurring the image, to allow for visualisation of orientation bars (b) Crystallographic strain in the *c* axis plotted against the percentage of crystallites in the low angle distribution as a function of track position. Data is taken from the first track of the tooth specimen subjected to the fast polymerisation regime.

### 7.3.3.2 a Axis orientation

Figure 7.9 illustrates the spatial relationship between the bimodal orientation of the hydroxyapatite crystallites obtained from the azimuthal integration of the (002) diffraction ring and the  $a=b$  axis strain distribution in the tooth fin. Strain in the  $a$  axis does not show a clear spatial relationship with the orientation distribution. In several regions of the map relatively low strain in the  $a$  axis correlates to a high proportion of crystallites belonging to the low angle population, however this relationship is not ubiquitous. Similarly, a vertical line transect through the first column of strain data and the respective percentage of crystallites found in the low angle population overlaid demonstrates a relatively weak Pearson correlation of  $r = 0.43$ . This is consistent with results from additional line transects taken through repeat track measurements on different tooth samples. Corresponding orientation maps are not shown for the low light intensity photo-polymerisation regime as the strains generated are almost negligible and are therefore difficult to correlate to orientation data in a meaningful way.



(a)



(b)

**Figure 7.9.** (a) Relative proportions of two crystallite orientations, red and blue bars, overlaid on to strain data. The aspect ratio has been altered, blurring the image, to allow for orientation bars. (b) Crystallographic strain in the  $a$  axis plotted against the proportion of crystallites in a predominantly horizontal orientation as a function of track position. Data is taken from the first track of the tooth specimen subjected to the fast polymerisation regime.

## 7.4 Discussion

### 7.4.1 Crystallographic Strain and Relief Mechanisms

Figures 7.4 and 7.6 illustrate that adhesion of an RBC within a tooth cavity induced strain within the hydroxyapatite nano-crystals that are the lowest hierarchal structural level of tooth enamel. Strain is due to stress transfer within the tooth structure as a consequence of shrinkage stresses generated by volumetric shrinkage of a constrained RBC material. Negative values of strain were reported in this study. It is suggested that as the cusp deflects towards the centre of the cavity it flexes (acting as a cantilever beam). The outer surface is put into a state of tension whilst the inner surface of the cusp is placed into compression. As the dentine is relatively thin and its elastic modulus is very low compared with the enamel the neutral axis of bending, i.e. where strain is zero will lie within the enamel layer itself. The nature of the preparation for the measurement zone is that measurements were not made close to the outer surface and it appears that the X-rays are positioned inwards and are located in an area that is in compression during flexure.

Previous laboratory based measurements utilising cuspal deflection and micro-leakage techniques have to date only been able to correlate photo-polymerisation variables to the combined behaviour of all hierarchal levels of tooth enamel and dentine. The results of this study show that the deformation of the unit cell within HAP nano-crystals is one mechanism by which strain relief may occur, however other methods are known to exist and are likely acting simultaneously. Belchte *et al* showed that within the first hierarchal level, the protein matrix that binds HAP crystallites will demonstrate shear behaviour prior to strain [69, 70] being exhibited in the crystallite itself. Similarly, at the second structural level it was found that when loads were applied parallel to the *c* axis of the enamel prisms that the stress strain relationship was dictated predominantly by soft protein constituent, whilst at perpendicular loading stress strain behaviour is governed by the crystal structure of the apatite. Additionally, Hon He *et al* reported that enamel has a stress-strain response similar to a metallic alloy and that backcreep [38] is observed after a load is removed. It is therefore likely that the crystallographic strain

observed in this study is not an absolute representation of the total strain generated by the shrinkage of the adhered composite with a portion of this relieved by the protein matrix.

#### **7.4.2 The Effect of Relative Polymerisation Rate on Crystallographic Strain**

In this study the irradiance of the impinging light source was used to introduce a range of polymerisation rates. Polymerisation rate was not measured in this study, but studies have shown that the polymerisation rate is proportional to the intensity of the impinging light. Additionally, FTIR measurements of conversion in Bis-GMA/TEGDMA based resins presented in this thesis (chapter three) has demonstrated the dependence of polymerisation rate on the light intensity. It can be seen in Figures 7.4 and 7.6 (both c and e) that when the RBC is photo-polymerised at the fastest rate, using the high intensity light source, that the hydroxyapatite crystallites demonstrate on average approximately 300 and 120 % times greater strain in the directions of the *c* and *a* crystallographic axis respectively in comparison with the low light intensity regime. First order differences in crystallographic strain for different light intensities are ascribed to the behaviour of the polymer phase of the RBC as a function of reaction rate. Faster polymerisation advances the onset of gelation [65], a stage in which the mobility of the forming polymer decreases. Reduced mobility may inhibit elastic flow of the bulk resin matrix allowing greater internal stresses to build which will transfer to the composite-enamel interface. However, the effect of polymerisation rate does not explain the discrepancy in strain ratios between fast and slow polymerisation rates for the respective crystallographic axis. It is likely that this arises due to the orientation of the enamel prisms, themselves composed of many stacked HAP crystallites relative to the cavity wall and contracting composite (Figure 7.3a). The crystallographic *c* axis of the HAP crystallite is known to point in the direction of the long axis of the enamel prism. In this case, the prism and therefore *c* axis are normal to the cavity wall and parallel to the applied stress from the shrinking composite. With macroscopic bending of the cusp towards the cavity, flexural stresses will be generated along the *c* axis. Conversely, the *a=b* parameter is perpendicular to the applied stress and is not orientated in the direction of

the stress. It must also be noted that although the low irradiance polymerisation regime shows negligible amounts of strain, this does not necessarily mean that no stress has been transferred to the crystalline structure, but relief mechanisms may have reduced this effect.

### 7.4.3 Spatial Distribution of Strain and Orientation

Figures 7.4 and 7.6 demonstrate how crystallographic strain is spatially distributed in the tooth fin section for each photo-polymerisation regime. Strain for the low light regime was close to being negligible; therefore the discussion and explanation of the spatial variation in strain will predominantly focus on the high light intensity illumination. Strain in the  $c$  axis was typically greatest towards the bottom of the fin and decreased gradually towards the top, although there are small regions which do not follow this trend. This effect is attributed to the geometry of the mesio-occlusal-distal cavity following sample preparation. The remaining cusp acts as a cantilever beam when placed under load. Consequently, the cusp bends around a fixed point, producing maximum stress within the tooth at the bottom of the cavity. This explanation however, cannot be extended to adequately describe the strain distribution in the  $a$  axis which demonstrates regions of greater strain typically located at the top of the cavity (Figure 7.6 c), although the magnitude of this strain is negligible.

Figure 7.3b Shows that two directions of crystallite/enamel prism orientation exist, distributed about  $170$  and  $210^\circ$  in the azimuthal plane. Typically, 75 - 90 % of the crystallites (75 – 90 % of the total integrated peak intensities, Figure 3b) display a preferred orientation about the low angle ( $170^\circ$ ) direction, which is almost normal to the cavity wall, although this varies spatially within each sample as seen in Figures 7.8 and 7.9. The low angle distribution is attributed to the HAP crystallites that comprise enamel prisms. This is based firstly on its relatively large contribution to the total signal but also on the width of the peak. Hydroxyapatite crystals are not perfectly aligned parallel with neighbouring crystals or to the long axis of the enamel prism but seem to entangle with each other [39] displaying a wide range of orientations. Additionally, Al-Jawad *et al* [54] showed that the crystallographic  $c$  axis is typically oriented normal to the outer tooth surface which is in good agreement with an orientation angle of  $\sim 170^\circ$ . There are likely

several factors contributing to the origin of the high angle distribution which may be determined by considering the sample preparation and enamel structure. Samples were inspected using light microscopy and used on the basis that they were caries free, exhibited no enamel cracks or other defects before being cut and polished. Yilmaz *et al* suggested that polishing can introduce micro-cracks into enamel and this may have some role in altering local prismatic and crystallographic orientation. However, cracks typically propagate through enamel via the inter-prismatic protein matrix boundary [42] before causing cracks in the enamel prisms themselves and would therefore unlikely cause an orientation change of up to  $40^\circ$  on a large enough scale to create a second orientation distribution. Furthermore, if the origin of this second orientation distribution was attributed to micro-cracks, then it would be expected that an applied load i.e. stress from a contracting RBC, would provide modification. Figure 7.7 shows that the azimuthal angle for both high and low angle distributions remained largely unaltered following photopolymerisation. This suggests that whilst the presence of micro-cracks may play a role in altering local crystallite/prism orientation this role is likely minimal. Alternatively, it is known that enamel prisms do not run continuously from the dental enamel junction to the outer enamel surface. Instead the inner section of enamel displays undulating prisms which may locally bend, twist and change their position [71], forming less common bands of decussating prisms. The presence of another orientation distribution (high angle) with a significantly different direction of preferred orientation and a lower contribution to the total diffraction signal suggests that this corresponds to decussated enamel prisms.

Figures 7.8 and 7.9 illustrate the azimuthal orientation of crystallites/prisms along the  $c$  axis belonging to either the high (red) or low (blue) angle direction (shown as bars) and the proportion of crystallites, as percentage of the total number of crystallites, orientated in the respective direction represented by the length of the coloured bar. Regions of greater strain in the  $c$  axis correspond to a relatively high proportion of crystallites/prisms ( $\sim 90\%$  of all crystallites/prisms) being oriented in in the  $170^\circ$  azimuthal direction. Conversely, lower  $c$  strain was found to correlate to fewer crystallites/prisms oriented about  $170^\circ$  (typically  $\sim 75\%$ ). Therefore, in regions of higher  $c$  axis strain the average direction of crystallite orientation along

the  $c$  axis is approximately horizontal; being perpendicular to the cavity wall and parallel to the direction of contraction in the RBC. Whereas in regions of lower strain the average orientation of the  $c$  axis deviates from this horizontal geometry and is at a diagonal (in 2D) to the cavity wall, due to an increased proportion of crystallites/prisms in the high angle distribution. This suggests that the orientation of the  $c$  axis relative to the bending moment of the cusp will determine the magnitude of strain that is observed. If it is assumed that a normal orientation of the  $c$  axis relative to the cavity produces a maximum in strain, then if fewer crystals are oriented in this direction less strain would be detected. Additionally, regions where there is more  $c$  axis alignment may be associated with greater macroscopic strain however, these two effects cannot be dissociated.

This argument is extended to the  $a$  axis to explain the strain distribution in this direction. Within the unit cell, the  $a$  axis is always perpendicular to the  $c$  axis, so when the  $c$  axis is normal to the cavity wall the  $a$  axis is parallel. In regions of the greatest  $a$  axis strain a higher percentage of crystallites/prisms are found in the high angle distribution. This corresponds to the  $a$  axis orientation becoming on average less parallel to the cavity wall and more perpendicular i.e. tilted towards the cavity wall along its axis. This geometry allows for this axis to be strained more easily along the axis in response to the stress of the contracting composite. The relationship between the respective crystallite/prism orientations and strain however, is not consistent throughout the mapped enamel area (Figure 7.9 a) and shows relatively low correlation in comparison to that seen in the  $c$  axis (Figures 7.8 b and 7.9 b). This may be due to an additional rotation of the crystallite/prism about the  $a$  axis i.e. so that the  $c$  axis tilts into and out of the plane of the page when viewed in 2D. This would result in the  $a$  axis being diagonal to the cavity wall in three dimensions rather than two, producing more complex strain behaviour. This could not be detected using conventional 2D SXRD and would therefore require a 3D approach.

There are some limitations to the experimental set-up in this study with respect to the light curing units used and the relationship between strain and DC. Two different LCUs were used

to achieve relatively high and low light intensities. The LCUs have different emission spectra which will affect the production rate of radicals in addition to the light intensity of the respective LCU. Ideally these differences would be accounted for by normalising strain to DC. Unfortunately, the sample geometry and positioning did not allow for conversion measurements. We therefore accept uncertainties introduced by this, however due to the large difference in intensities between the two photo-polymerisation regimes and the associated differences in polymerisation rate we believe that overall trends in strain are statistically significant and may therefore be determined as a function of relative differences in polymerisation rate.

## 7.5 Conclusions

The spatial distribution of strain in human enamel post composite restoration has been studied *ex vivo* using high resolution synchrotron X-ray diffraction mapping, as a function of relative differences in the polymerisation rate. The average strain in the enamel phase varies as a function of light curing intensity i.e. the rate of photo-polymerisation which is in agreement with previous cuspal deflection methods. However, strain in enamel is not uniformly distributed and varies spatially, demonstrating different magnitudes of strain in different lattice planes as a function of crystallite orientation and location relative to the cavity wall. The *c* axis typically displays greater strain in comparison to the *a* axis, which is attributed to the approximately perpendicular and parallel orientations relative to the cavity wall. When an axis is perpendicular to the cavity wall it is parallel to the force exerted on the enamel by the contacting composite, allowing more efficient transfer of strain along the axis. Interestingly, two directions of crystallite/enamel prism orientation exist with the less common distribution ascribed to decussated enamel prisms. The majority of crystallites/prisms are in an orientation where the crystallographic *c* axis is normal to the cavity wall, but a small proportion believed to be decussated prisms, are tilted towards a more parallel orientation. In regions of enamel where this titled proportion of prisms increases, strain in the *c* and *a* axis generally decrease and increase respectively depending on how parallel to the stress of the shrinking composite they are. Therefore, strain was mediated by subtle variations in the proportions of these two crystallite/prisms orientations which dictate the spatial variation of strain. This experiment has shown how the microstructure of enamel at the lower structural hierarchies can strongly influence the spatial distribution of strain in response to the adhesion of a photo-polymerised composite, which is not simply a function of polymerisation variables. These findings give further insights which may explain the discrepancy between polymerisation variables, shrinkage stresses and the manifestation of enamel strain reported via conventional laboratory based techniques, providing a more complete understanding as to how composite adhesion and strain in the enamel may impact on restoration longevity.

## 7.6 References

1. Braga, R.R. and J.L. Ferracane, *Alternatives in polymerization contraction stress management*. Crit Rev Oral Biol Med, 2004. **15**(3): p. 176-84.
2. Amirouche-Korichi, A., M. Mouzali, and D.C. Watts, *Effects of monomer ratios and highly radiopaque fillers on degree of conversion and shrinkage-strain of dental resin composites*. Dental Materials, 2009. **25**(11): p. 1411-1418.
3. Watts, D.C. and A.A. Hindi, *Intrinsic 'soft-start' polymerisation shrinkage-kinetics in an acrylate-based resin-composite*. Dental Materials, 1999. **15**(1): p. 39-45.
4. Hofmann, N., B. Hugo, and B. Klaiber, *Effect of irradiation type (LED or QTH) on photo-activated composite shrinkage strain kinetics, temperature rise, and hardness*. European Journal of Oral Sciences, 2002. **110**(6): p. 471-479.
5. Palin, W.M., et al., *In vitro cuspal deflection and microleakage of maxillary premolars restored with novel low-shrink dental composites*. Dental Materials, 2005. **21**(4): p. 324-335.
6. Darvell, B.W., *Chapter 5 - Acrylic*, in *Materials Science for Dentistry (Ninth edition)*, B.W. Darvell, Editor. 2009, Woodhead Publishing. p. 108-127.
7. Silikas, N., G. Eliades, and D.C. Watts, *Light intensity effects on resin-composite degree of conversion and shrinkage strain*. Dental Materials, 2000. **16**(4): p. 292-296.
8. Stansbury, J.W., et al., *Conversion-dependent shrinkage stress and strain in dental resins and composites*. Dent Mater, 2005. **21**(1): p. 56-67.
9. Cara, R.R., et al., *Cuspal deflection and microleakage in premolar teeth restored with resin-based composites with and without an intermediary flowable layer*. Journal of Dentistry, 2007. **35**(6): p. 482-489.
10. Moorthy, A., et al., *Cuspal deflection and microleakage in premolar teeth restored with bulk-fill flowable resin-based composite base materials*. Journal of Dentistry, 2012. **40**(6): p. 500-505.

11. Taha, N.A., J.E.A. Palamara, and H.H. Messer, *Cuspal deflection, strain and microleakage of endodontically treated premolar teeth restored with direct resin composites*. Journal of Dentistry, 2009. **37**(9): p. 724-730.
12. Abbas, G., et al., *Cuspal movement and microleakage in premolar teeth restored with a packable composite cured in bulk or in increments*. Journal of Dentistry, 2003. **31**(6): p. 437-444.
13. Fleming, G.J.P., et al., *Cuspal movement and microleakage in premolar teeth restored with resin-based filling materials cured using a 'soft-start' polymerisation protocol*. Dental Materials, 2007. **23**(5): p. 637-643.
14. Martin, N., N.M. Jedynekiewicz, and D.F. Williams, *Cuspal deflection during polymerisation of composite lutes of ceramic inlays I Work presented at the IADR/CED Conference in Madrid, September 1997 and submitted as a component of a Ph.D. thesis by N. Martin. I*. Journal of Dentistry, 1999. **27**(1): p. 29-36.
15. Alomari, Q., J. W Reinhardt, and D. B Boyer, *Effect on cusp deflection and gap formation in composite restorations*. Vol. 26. 2001. 406-11.
16. Li, H., et al., *Non-destructive examination of interfacial debonding using acoustic emission*. Dental Materials, 2011. **27**(10): p. 964-971.
17. Dauvillier, B.S., M.P. Aarnts, and A.J. Feilzer, *Developments in Shrinkage Control of Adhesive Restoratives*. Journal of Esthetic and Restorative Dentistry, 2000. **12**(6): p. 291-299.
18. Brunthaler, A., et al., *Longevity of direct resin composite restorations in posterior teeth: a review*. Clinical Oral Investigations, 2003. **7**(2): p. 63-70.
19. Davidson, C.L., A.J.D. Gee, and A. Feilzer, *The Competition between the Composite-Dentin Bond Strength and the Polymerization Contraction Stress*. Journal of Dental Research, 1984. **63**(12): p. 1396-1399.
20. Davidson, C.L. and A.J. Feilzer, *Polymerization shrinkage and polymerization shrinkage stress in polymer-based restoratives*. Journal of Dentistry, 1997. **25**(6): p. 435-440.

21. Soh, M.S., A.U.J. Yap, and A. Sellinger, *Physicomechanical evaluation of low-shrinkage dental nanocomposites based on silsesquioxane cores*. European Journal of Oral Sciences, 2007. **115**(3): p. 230-238.
22. Condon, J.R. and J.L. Ferracane, *ASSESSING THE EFFECT OF COMPOSITE FORMULATION ON POLYMERIZATION STRESS*. The Journal of the American Dental Association, 2000. **131**(4): p. 497-503.
23. Feilzer, A.J. and B.S. Dauvillier, *Effect of TEGDMA/BisGMA Ratio on Stress Development and Viscoelastic Properties of Experimental Two-paste Composites*. Journal of Dental Research, 2003. **82**(10): p. 824-828.
24. Davidson, C.L. and A.J. de Gee, *Light-curing units, polymerization, and clinical implications*. J Adhes Dent, 2000. **2**(3): p. 167-73.
25. Uno, S. and E. Asmussen, *Marginal adaptation of a restorative resin polymerized at reduced rate*. European Journal of Oral Sciences, 1991. **99**(5): p. 440-444.
26. Mehl, A., R. Hickel, and K.H. Kunzelmann, *Physical properties and gap formation of light-cured composites with and without 'softstart-polymerization'*. Journal of Dentistry, 1997. **25**(3): p. 321-330.
27. Hofmann, N., et al., *The influence of plasma arc vs. halogen standard or soft-start irradiation on polymerization shrinkage kinetics of polymer matrix composites*. Journal of Dentistry, 2003. **31**(6): p. 383-393.
28. Sakaguchi, R.L. and H.X. Berge, *Reduced light energy density decreases post-gel contraction while maintaining degree of conversion in composites*. Journal of Dentistry, 1998. **26**(8): p. 695-700.
29. Feilzer, A.J., A.J.D. Gee, and C.L. Davidson, *Setting Stress in Composite Resin in Relation to Configuration of the Restoration*. Journal of Dental Research, 1987. **66**(11): p. 1636-1639.
30. Feilzer, A.J., A.J.D. Gee, and C.L. Davidson, *Increased Wall-to-Wall Curing Contraction in Thin Bonded Resin Layers*. Journal of Dental Research, 1989. **68**(1): p. 48-50.

31. Lee, M.-R., et al., *Influence of cavity dimension and restoration methods on the cusp deflection of premolars in composite restoration*. Dental Materials, 2007. **23**(3): p. 288-295.
32. Segura, A. and K.J. Donly, *In vitro posterior composite polymerization recovery following hygroscopic expansion*. Journal of Oral Rehabilitation, 1993. **20**(5): p. 495-499.
33. Meredith, N. and D.J. Setchell, *In vitro measurement of cuspal strain and displacement in composite restored teeth*. Journal of Dentistry, 1997. **25**(3): p. 331-337.
34. Pearson, G. and S.M. Hegarty, *Cusp movement in molar teeth using dentine adhesives and composite filling materials*. Vol. 8. 1987. 473-6.
35. Suliman, A.A., D.B. Boyer, and R.S. Lakes, *Interferometric Measurements of Cusp Deformation of Teeth Restored with Composites*. Journal of Dental Research, 1993. **72**(11): p. 1532-1536.
36. Alomari, Q.D., J.W. Reinhardt, and D.B. Boyer, *Effect of liners on cusp deflection and gap formation in composite restorations*. Oper Dent, 2001. **26**(4): p. 406-11.
37. Gwinnett, A.J., *Structure and composition of enamel*. Oper Dent, 1992. **Suppl 5**: p. 10-7.
38. He, L.H. and M.V. Swain, *Enamel—A “metallic-like” deformable biocomposite*. Journal of Dentistry, 2007. **35**(5): p. 431-437.
39. Yilmaz, E.D., G.A. Schneider, and M.V. Swain, *Influence of structural hierarchy on the fracture behaviour of tooth enamel*. Philosophical Transactions of the Royal Society A: Mathematical, Physical and Engineering Sciences, 2015. **373**(2038).
40. Eastoe, J.E., *Organic Matrix of Tooth Enamel*. Nature, 1960. **187**(4735): p. 411-412.
41. Hu, C.-C., et al., *Sheathlin: Cloning, cDNA/Polypeptide Sequences, and Immunolocalization of Porcine Enamel Sheath Proteins*. Journal of Dental Research, 1997. **76**(2): p. 648-657.

42. He, L.H. and M.V. Swain, *Understanding the mechanical behaviour of human enamel from its structural and compositional characteristics*. Journal of the Mechanical Behavior of Biomedical Materials, 2008. **1**(1): p. 18-29.
43. Termine, J.D., D.A. Torchia, and K.M. Conn, *Enamel matrix: structural proteins*. J Dent Res, 1979. **58**(Spec Issue B): p. 773-81.
44. Waltimo, A. and M. Könönen, *Maximal bite force and its association with signs and symptoms of craniomandibular disorders in young Finnish non-patients*. Acta Odontologica Scandinavica, 1995. **53**(4): p. 254-258.
45. Hayasaki, H., et al., *Occlusal contact area of mandibular teeth during lateral excursion*. Int J Prosthodont, 2004. **17**(1): p. 72-6.
46. Xu, H.H.K., et al., *Indentation Damage and Mechanical Properties of Human Enamel and Dentin*. Journal of Dental Research, 1998. **77**(3): p. 472-480.
47. Baldassarri, M., H.C. Margolis, and E. Beniash, *Compositional Determinants of Mechanical Properties of Enamel*. Journal of Dental Research, 2008. **87**(7): p. 645-649.
48. D., S., *Beitrag zur Geschichte der Zähne*. Beiträge zur Zergliederungskunst, 1800. **1**: p. 1-7.
49. Osborn, J.W., *The nature of the Hunter-Schreger bands in enamel*. Archives of Oral Biology, 1965. **10**(6): p. 929-IN30.
50. Paine, M.L. and M.L. Snead, *Protein Interactions During Assembly of the Enamel Organic Extracellular Matrix*. Journal of Bone and Mineral Research, 1997. **12**(2): p. 221-227.
51. Bartlett, J.D., et al., *Protein-Protein Interactions of the Developing Enamel Matrix*, in *Current Topics in Developmental Biology*. 2006, Academic Press. p. 57-115.
52. Deutsch, D., et al., *Enamel Matrix Proteins and Ameloblast Biology*. Connective Tissue Research, 1995. **32**(1-4): p. 97-107.
53. Simmons, L.M., et al., *Distribution of enamel crystallite orientation through an entire tooth crown studied using synchrotron X-ray diffraction*. Eur J Oral Sci, 2011. **119** Suppl 1: p. 19-24.

54. Al-Jawad, M., et al., *2D mapping of texture and lattice parameters of dental enamel*. Vol. 28. 2007. 2908-14.
55. Al-Jawad, M., et al., *Three Dimensional Mapping of Texture in Dental Enamel*. Vol. 361-363. 2008. 877-880.
56. Spears, I.R., *A three-dimensional finite element model of prismatic enamel: a re-appraisal of the data on the Young's modulus of enamel*. J Dent Res, 1997. **76**(10): p. 1690-7.
57. White, S.N., et al., *Biological organization of hydroxyapatite crystallites into a fibrous continuum toughens and controls anisotropy in human enamel*. J Dent Res, 2001. **80**(1): p. 321-6.
58. Xie, Z., M.V. Swain, and M.J. Hoffman, *Structural integrity of enamel: experimental and modeling*. J Dent Res, 2009. **88**(6): p. 529-33.
59. He, L.H. and M.V. Swain, *Nanoindentation creep behavior of human enamel*. J Biomed Mater Res A, 2009. **91**(2): p. 352-9.
60. Uno, S. and E. Asmussen, *Marginal adaptation of a restorative resin polymerized at reduced rate*. Scand J Dent Res, 1991. **99**(5): p. 440-4.
61. Mehl, A., R. Hickel, and K.-H. Kunzelmann, *Physical properties and gap formation of light-cured composites with and without 'softstart-polymerization'*. Vol. 25. 1997. 321-30.
62. Sahafi, A., A. Peutzfeldt, and E. Asmussen, *Soft-start polymerization and marginal gap formation in vitro*. Am J Dent, 2001. **14**(3): p. 145-7.
63. Miyazaki, M., et al., *Effect of light exposure on fracture toughness and flexural strength of light-cured composites*. Dent Mater, 1996. **12**(6): p. 328-32.
64. Jantarat, J., et al., *Comparison of methods for measuring cuspal deformation in teeth*. Journal of Dentistry, 2001. **29**(1): p. 75-82.
65. Braga, R.R., R.Y. Ballester, and J.L. Ferracane, *Factors involved in the development of polymerization shrinkage stress in resin-composites: a systematic review*. Dent Mater, 2005. **21**(10): p. 962-70.

66. Sawhney, K.J.S., et al., *A Test Beamline on Diamond Light Source*. AIP Conference Proceedings, 2010. **1234**(1): p. 387-390.
67. *B16 Facility and Equipment Availability*. 2017 [cited 2017 June 29]; Available from: <http://www.diamond.ac.uk/Beamlines/Materials/B16/status.html>.
68. Hammersley, A.P., et al., *Two-dimensional detector software: From real detector to idealised image or two-theta scan*. High Pressure Research, 1996. **14**(4-6): p. 235-248.
69. Bechtle, S., et al., *Mixed-mode stress intensity factors for kink cracks with finite kink length loaded in tension and bending: application to dentin and enamel*. J Mech Behav Biomed Mater, 2010. **3**(4): p. 303-12.
70. Bechtle, S., et al., *The fracture behaviour of dental enamel*. Biomaterials, 2010. **31**(2): p. 375-84.
71. Radlanski, R.J., et al., *Outline and arrangement of enamel rods in human deciduous and permanent enamel. 3D-reconstructions obtained from CLSM and SEM images based on serial ground sections*. Eur J Oral Sci, 2001. **109**(6): p. 409-14.

## **8 GENERAL DISCUSSION AND FUTURE WORK**

### **8.1 General discussion**

#### **8.1.1 Introduction**

The main aim of this thesis was to understand how photo-polymerisation variables, specifically the polymerisation rate, may impact on the structure of model dental RBCs at molecular and micron length scales. The novel application of advanced synchrotron and neutron based techniques, within the context of dental materials research, was explored to characterise these materials to provide new insights and a more complete understanding of their behaviour. In this chapter the main findings presented in chapters' three to seven in this thesis are discussed.

#### **8.1.2 Effect of Polymerisation Rate on the Polymer Structure**

The study presented in chapter three demonstrates how simultaneous time resolved X-ray scattering and FTIR measurements can be used to understand the evolving polymer structure of a model RBC. The molecular scale structure was correlated to photo-polymerisation variables and ultimately the polymerisation rate. The origin of this correlation length and its increase is considered to be intra-monomeric as distances between neighbouring monomers are known to become smaller during polymerisation, due to the exchange of Van der Waals interactions for covalent bonds, which would manifest as a decrease in this correlation length, which was not observed. Weighted least squares fitting confirmed that chain extension occurred predominantly in the TEGDMA monomer for the respective blends. However, this was likely due to a combination of a greater proportion of TEGDMA by molecular weight and differences in molecular structure. Bis-GMA contains a rigid aromatic core which will not deform, but the methacrylate functional groups for each monomer displayed similar magnitudes of chain extension.

In this study light intensity and photo-initiator chemistry were used to achieve a range of polymerisation rates. It was shown that the polymer structure develops very differently for relatively fast and slow polymerisation rates. Accelerating polymerisation generated greater chain extension in a shorter period of time and produced a less ordered structure in comparison with slower polymerisation regimens. It is suggested that rapid polymerisation generates strains, as seen in a 'relaxation' feature in X-ray correlation lengths (chapter three), which are fixed into the polymer structure. In comparison, slower polymerisation delays the onset of chain extension, with respect to DC, and allows for the structure to be modified more slowly during a post-cure period. X-ray scattering is a valuable tool for understanding time dependent structural changes throughout polymerisation. The limitation of this technique and indeed the results in chapter three is that the X-ray scattering feature is formed from several groups of correlation lengths rather than variation about one common correlation length. It is therefore impossible to have an explicit understanding of the structural changes using solely this technique as no single specific structure and/or length scale is observed.

Neutron scattering was used in conjunction with isotopic substitution (as described in chapter four), to address shortcomings of X-ray scattering and to provide complimentary structural information. Partial deuteration of the functional groups was used to select correlation lengths at cross-linking distances, specifically the end to end distance of the TEGDMA monomer. It was found that faster polymerisation generated greater extension of the TEGDMA monomer unit corresponding to a larger cross-link distance. It has been suggested that cross-links with a reduced degree of freedom may exacerbate polymerisation shrinkage, through an increase in packing density, reducing free volume in the polymer. Furthermore, several studies have shown that accelerating polymerisation confers greater shrinkage and inferior mechanical properties in comparison with similarly converted polymers. It is possible that chain extension may act as a secondary mechanism for shrinkage. Furthermore, a more extended chain conformation may provide insight into discrepancies in mechanical properties. An extended cross-link will be less able to re-organise its structure when under load to reduce stress, predisposing the polymer to failure.

### **8.1.3 Inter-Particulate Variability in the Degree of Polymerisation**

The results presented in chapter six illustrate the advantages of using synchrotron light sources to enhance the characterisation abilities of a routine technique such as FTIR to quantify monomer to polymer conversion. To date, inter-particulate heterogeneity with respect to the degree of conversion has only been postulated but never directly shown, under the assumption that a boundary layer with low mobility relative to the surrounding resin matrix surrounds each particle. In this study it has been shown using novel synchrotron FTIR microscopy that conversion varies locally as a function of relative position to a given filler particle. Regions of lower conversion were observed surrounding each filler particle, which strongly implies the existence of a lower mobility boundary layer. Mobility in the boundary layer is likely mediated by polymer drag over the surface of the filler particle surface. Local differences in conversion will define regions of failure in the composite i.e. crack propagation, as paths for stress relief.

Interestingly, it has also been found that the aromatic core of the Bis-GMA monomer demonstrates strain as a function of relative differences in polymerisation rate. This is significant as the aromatic groups are the stiffer portion of the molecular structure, which suggests that other bonds are subjected to strain before strain manifests in the aromatic group. This is further supported by the fact that the ratio of aromatic strain between the relatively fast and slow polymerisation regimes is very similar to the ratio of polymer chain extension seen in chapter three for extreme polymerisation regimes (fast and slow).

#### **8.1.4 Crystallographic Strain**

Cuspal deflection methods are routinely used to ascertain the magnitude of stress generation when an RBC is adhered to the surface of a tooth. However, such measurements cannot discriminate the vector and location of stress generation and indeed any stress relief that occurs within the tooth. Similarly, stress within a specific structure inside the enamel hierarchy cannot be interrogated with traditional laboratory based techniques. The study presented in chapter seven illustrates how synchrotron X-ray diffraction may be used to characterise the spatial distribution of crystallographic strain within a tooth substrate when an RBC is adhered to the surface. It has been shown that the stress response of tooth enamel/dentine with respect to photo-polymerisation is mediated by the orientation of enamel prisms relative to the contraction of the RBC.

Additionally, several studies using cuspal deflection techniques to measure strains have reported no significant differences in strain under a range of photo-polymerisation conditions known to generate different magnitudes of strain. In this study, the polymerisation rate was influenced through two different light intensities, given previous theoretical and experimental work demonstrating that the polymerisation rate is proportional to the intensity of the impinging light. It was shown that faster polymerisation conferred greater strain in the tooth enamel. It is widely reported that composite placement can damage tooth structure, causing the deformation of dentine tubules, crack formation and propagation. Therefore, employing rapid polymerisation techniques, which generate larger strains, in clinical practice to reduce surgical times may not be advisable

## **8.2 Future work**

### **8.2.1 Effect of Polymerisation Rate on the Polymer Structure**

X-ray scattering results presented in this thesis have elucidated how the polymer structure evolves during photo-polymerisation, whilst neutron scattering has provided complimentary information about how polymerisation rate impacts on cross-linking distances with respect to the TEGDMA monomer. The most logical extension of this work would be to investigate how the Bis-GMA cross-link structure evolves during polymerisation as a function of polymerisation rate. This would give a more complete understanding as to how the structure of each monomer is modified. Future research should also focus on correlating microstructural changes to macroscopic properties including polymerisation stress and volumetric shrinkage to further understand the role that the rate dependent polymer structure has on the bulk material. Additionally, the preliminary investigation into how temperature modifies different polymer structure (chapter five) could be continued in greater detail, to understand the effect of thermal cycling on the polymer structure.

### **8.2.2 Inter-Particulate Variability in the Degree of Polymerisation**

Chapter six illustrated the existence of inter-particulate variability in the degree of monomer to polymer conversion in a filled model RBC system. The experimental RBCs were, due to the time constraints of using a synchrotron source, limited to samples with a relatively viscous resin matrix, high filler fraction, highly monodisperse particles which did not incorporate a silane coupling agent. Previous reports have suggested that at higher viscosities i.e. a low mobility resin matrix or high filler fraction, that system mobility is influenced by spatial confinement, interfacial interactions and increased concentrations of radical species. Future research should systematically characterise the effect of reducing the viscosity of the resin matrix and the filler fraction i.e. increasing inter-particulate distances and reducing the effects of light scattering and absorption. It would also be worth characterising the effect of extreme polymerisation rates, using different irradiance protocols, on the

distribution of conversion and particularly the magnitude of chemical bond strain. Additionally, commercial RBCs incorporate a silane agent to increase bonding between the resin and filler phases. The effect of this agent on conversion around filler particles should also be investigated within the context of the aforementioned photo-polymerisation variables.

### **8.2.3 Crystallographic Strain**

Synchrotron X-ray diffraction was used to spatially resolve crystallographic strain induced in the enamel phase of human tooth, by the adhesion of a composite material. In this study relatively high and low light intensities were used to produce different rates of polymerisation, given that the reaction rate is proportional to the square root of the light intensity if other photo-polymerisation variables are fixed. In chapter three it was shown that chain extension and residual strains in the polymer structure, were rate and time dependent. Future work should therefore investigate how crystallographic strain in the tooth enamel/dentine develops during photo-polymerisation i.e. time resolved measurements of crystallographic strain, and correlates to chain extension of the polymer as a function of polymerisation rate.

## 9 CONCLUSIONS

In this thesis the polymer structure, local variation of DC in filled composites and strain transfer have been investigated through the novel application of synchrotron and neutron based techniques.

1. Photo-polymerisation of experimental RBCs generates chain segment extension and changes in short range order within the structures of the constituent monomers Bis-GMA and TEGDMA which form the resin matrix, which to date is unreported. Extension is believed to occur in the functional end groups of both of the monomers as well as in the flexible backbone of the TEGDMA monomer. No structural changes are ascribed to the rigid aromatic core of Bis-GMA.
2. It was shown that different polymerisation rates generate different polymer structures. Accelerating polymerisation through the use of high light intensity sources and modifications to the photo-initiator chemistry conferred greater chain extension and reduced short range order in the aforementioned polymer segments of the Bis-GMA and TEGDMA monomers. RBCs polymerised rapidly demonstrated the greatest chain extension in the shortest period of time, which was followed by a reduction in length not observed in more slowly polymerised systems. This behaviour suggests that residual strains may be stored in the structure as a consequence of relatively fast polymerisation.
3. Neutron scattering combined with isotopic substitution demonstrated that this relationship between polymerisation rate and structure with respect to chain extension and order occurs at longer length scales within the polymer. Specifically, the end to end distance of TEGDMA within the polymer network was greater when polymerisation was driven faster through higher light irradiances. However, faster polymerisation

produced a less ordered structure at these length scales in comparison to lower light irradiance regimens, which is consistent with X-ray observations of polymer segments.

4. The presence of filler particles in a resin matrix was found to introduce local heterogeneity with respect to the degree of monomer to polymer conversion and chemical aromatic bond strain. At small nearest neighbour distances, heterogeneity originates predominantly from a lower converted and reduced bond strain boundary layer surrounding each filler particle, whilst light attenuation and likely, relative monomer mobility effects dominate at longer length scales within the resin matrix
5. Strains generated through the polymerisation of an RBC are transferred to enamel when the composite is adhered to the surface of a tooth. Crystallographic strain within the enamel phase, the result of this strain transfer, can be detected using synchrotron XRD. The spatial distribution of this strain was found to be dependent on the cavity geometry and the orientation of enamel prisms. The magnitude of the strain was also related to prismatic orientation and the inferred polymerisation rate.

## 10 APPENDIX

### 10.1 Chemical Lot Numbers

**Table 10.1.** Lot numbers for monomers and photo-initiators used for resin formulation (where available).

| <b>Chemical Name</b>                              | <b>Company</b>             | <b>Lot No.</b> |
|---|----------------------------|----------------|
| Bisphenol A dimethacrylate                        | Sigma Aldrich (Dorset, UK) | 03924ARV       |
| Diphenyl(2, 4, 6-trimethylbenzoyl)phosphine oxide | Sigma Aldrich (Dorset, UK) | MKBP8673VP     |
| Urethane dimethacrylate                           | Sigma Aldrich (Dorset, UK) | MKBQ7398V      |
| Camphorquinone                                    | Sigma Aldrich (Dorset, UK) | 09003AQV       |
| 2-(Dimethylamino)ethyl methacrylate               | Sigma Aldrich (Dorset, UK) | BCBJ3899V      |
| Ethylene glycol dimethacrylate                    |                            | SHBF7061V      |
| Triethylene glycol dimethacrylate                 | Sigma Aldrich (Dorset, UK) | STBF6453V      |
| Bisphenol A glycerolate dimethacrylate            | Sigma Aldrich (Dorset, UK) | MKBT9132V      |
| Methyl methacrylate                               | Sigma Aldrich (Dorset, UK) | A0354106       |
| Triethylene glycol dimethacrylate                 | Sigma Aldrich (Dorset, UK) | 10186982       |
| Ethylene glycol                                   | Sigma Aldrich (Dorset, UK) | 1413793        |

## 10.2 Effects of X-ray Beam Damage on the Polymer Structure of Dimethacrylate Resins

In chapter three X-ray scattering was used to resolve the structure of Bis-GMA/TEGDMA systems during photo-polymerisation. However, beam damage by the X-rays on the resin is a possibility and may consequently impact on the polymer structure separately to any effects related to photo-polymerisation. Figure 10.1 illustrates the impact that X-rays have on a 60/40 wt% (Bis-GMA/TEGDMA) blend initiated with TPO in the absence of light. TPO was chosen as a control due to its ability to induce a relatively high polymerisation rate. It can be seen in Figures 10.1(a) and 10.1(c) that changes in the correlation length and relative order do not occur until ~ 50 s of X-ray exposure. A TPO initiated system will already have reached a value very close to its terminal conversion long before this point in time (chapter three) and structural effects ascribed to interactions with X-rays are likely to be minimal. In the case of slower polymerisation using a CQ initiator, X-ray interaction effects are still slow in comparison to polymerisation kinetics. Similarly it can be seen that X-ray effects on a pre-polymerised sample are negligible in comparison to the increases in correlation length and relative order described in chapter three.

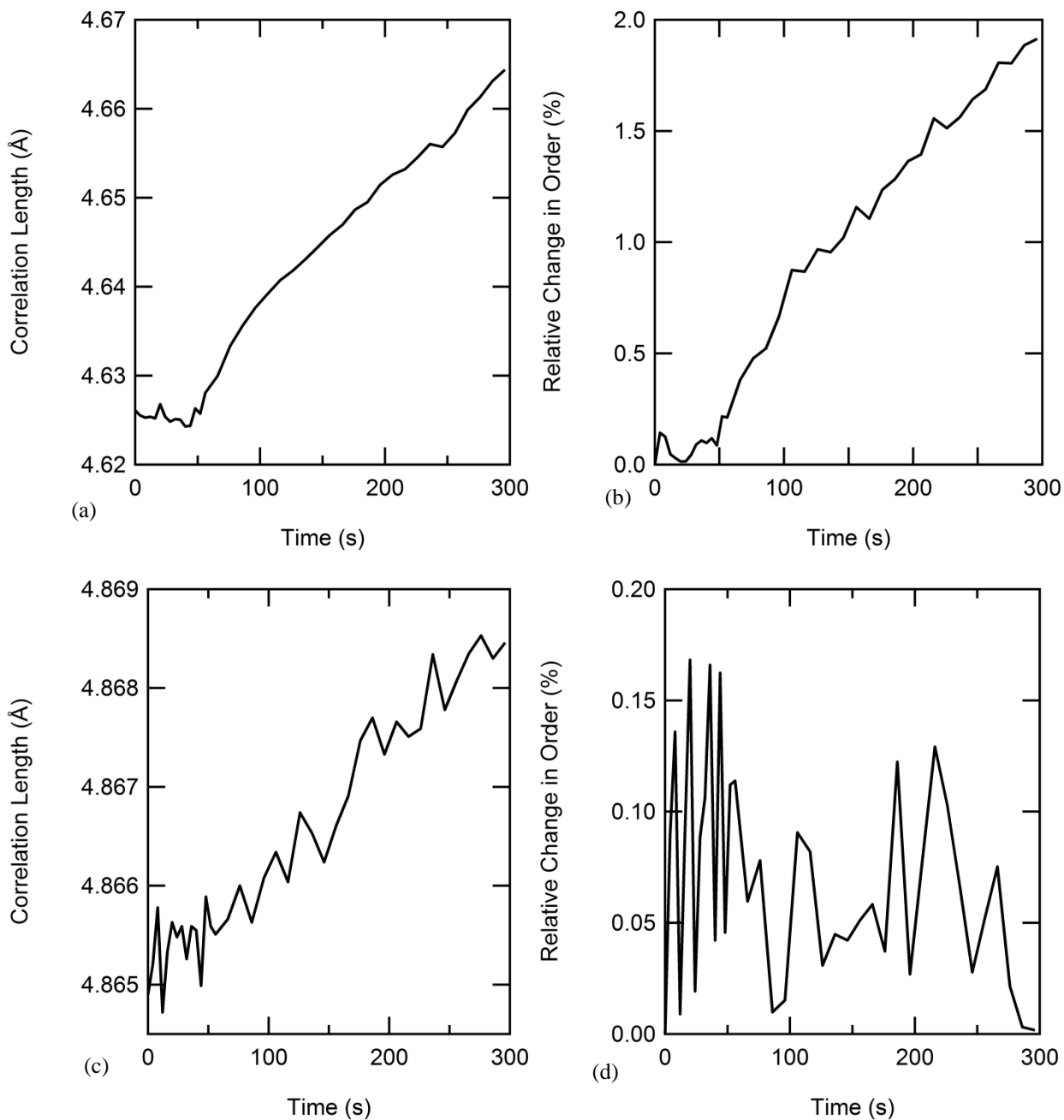


**Figure 10.1.** Real time evolution of the correlation length reported in chapter three when exposed to X-rays for a 60/40 wt% (Bis-GMA/TEGDMA) sample with TPO photo-initiator in the (a) liquid monomer and (c) solid polymer form. Analogous plot for changes in short range order are shown in (b) and (d).

### 10.3 Publications

From results presented in this thesis:

**Sirovica, S.**, Skoda, M.W.A., Thompson, P.B.J., Palin, W.M., Smith, A.J., Addison O. and Martin, R.A. *Novel insight into structural variability of in-situ polymerised biomedical polymers*. Nature Communications, 2017 (submitted).

**Sirovica, S.**, Skoda, M.W.A., Hirschmugl, C.J., Mattson, E.C., Aboualizadeh, E., Martin, R.A. and Addison, O. *Inter-particulate spatial variability in degree of polymerisation of dental composite-filling materials*. Nature Communications, 2017 (submitted).

From results not presented in this thesis:

Watkins, A.J., **Sirovica, S.**, Stokes, B., Isaacs, M., Addison, O., and Martin, A. *Paternal low protein diet programs preimplantation embryo gene expression, foetal growth and skeletal development in mice*. Biochimica et Biophysica Acta, 2016. 1863(1): p. 1371–1381.

Greasley, S.L., Page, S.J., **Sirovica, S.**, Chen, S., Martin, R. A., Riveiro, A., Hanna, J. V., Porter, A.E., Jones, J.R. *Controlling particle size in the Stöber process and incorporation of calcium*. Journal of Colloid and Interface Science, 2016. 469 (1): p.212 – 223.

### 10.4 Conferences

Time resolved X-ray studies of dimethacrylate based biomedical resin systems, *British Society for Research on Ageing*, Liverpool, UK, 2014

Structural evolution of photo-polymerised dimethacrylate resin systems, *International Association of Dental Research Pan European Congress*, Dubrovnik, Croatia, 2014

Microscale spatial variability of monomer conversion in filled dental resin-based-composites, *Academy of Dental Materials annual conference*, Chicago, Illinois, USA, 2016

## **10.5 Invited Talks**

Using structural correlations to inform the development of longer lasting dental restorations,  
Faculty of Medicine and Dentistry, University of Alberta, 2016

## **10.6 Awards**

**2016** Academy of Dental Materials Paffenbarger Award for best student presentation in the field of dental materials